



## Research Activities

## Linewidth Measurements of the UVSOR Free Electron Laser

Kazuhiko KIMURA, Hiroyuki HAMA\*, Jun-ichiro YAMAZAKI\*,  
Toshio KINOSHITA\* and Goro ISOYAMA\*\*

*The Graduate University for Advanced Studies, Myodaiji, Okazaki 444*  
*\*UVSOR Facility, Institute for Molecular Science, Myodaiji, Okazaki 444*  
*\*\*The Institute of Scientific and Industrial Research, Osaka University,*  
*Mihogaoka, Ibaraki 567*

We have carried out experimental studies of storage ring free electron laser (SR-FEL) dynamics. For the case of UVSOR FEL, a quasi-periodic pulsed structure (macropulse) appears when the electron bunch is synchronized with the optical pulse in a resonator. The typical repetition period and the duration of such macropulse are about 8 and 1 msec, respectively[1]. To observe time-dependent properties of the laser macropulse more precisely, a dual-sweep streak camera has been introduced[2]. The streak camera executes a slow ramp deflection on the axis right angle to the fast sweep, so that one can simultaneously observe the micro- and the macro-temporal structure of the laser. We have also investigated spectral evolution of the laser with a time-resolved spectrometer based on the integration of a Fabry-Perot etalon and the slow sweep function of the streak camera.

The UVSOR FEL experiments have been done with two-bunch operation at electron energy of 500 MeV. An optical klystron has been employed for the gain device of the FEL. In experimental studies of the FEL dynamics, the laser wavelength was chosen at a visible wavelength around 470nm. The laser oscillation was normally started at a beam current of 35 mA/bunch, which was a maximum current can be stored in the ring. A threshold beam current for the lasing was approximately 7 mA/bunch.

In the first step, we have measured the time-averaged linewidth of the FEL at various beam currents using the fixed gap etalon. The free spectral range and the finesse of the etalon was 1000 GHz and 50, respectively. The interference pattern of the FEL, which is equivalent to the spectral distribution of the laser, was measured by a CCD linear image sensor (7 $\mu$ m pixel size). A



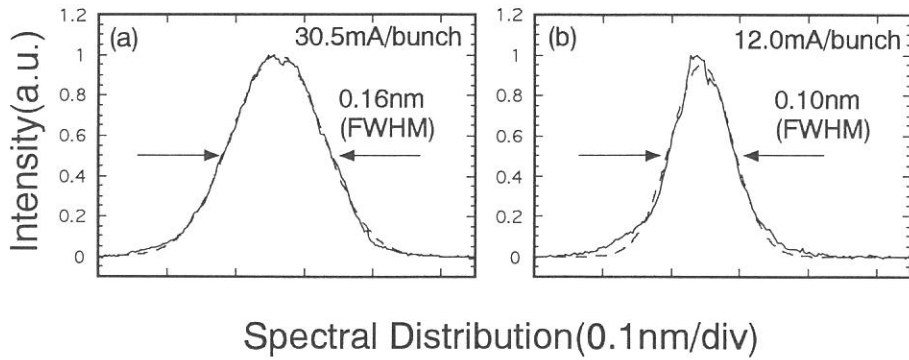


Fig.1 Time-averaged spectral distributions of the FEL. The dashed line represents a Gaussian fitting to the data.

resolution of the spectral measurement system was  $\Delta\lambda/\lambda = 3.5 \times 10^{-5}$ . The output signals of the CCD array were averaged on a digital oscilloscope. Figure 1 shows measured laser spectra under the perfect synchronized condition at two different beam currents. The laser wavelength was 470.0 nm and the integrated time was 0.5 sec. The relative linewidth  $\Delta\lambda/\lambda$  (FWHM) of the laser was  $3.4 \times 10^{-4}$  and  $2.1 \times 10^{-4}$  at 30.5 and 12.0 mA/bunch, respectively. One can notice that the time-averaged lineshape is close to a Gaussian distribution and that the FEL linewidth gets narrow as the beam current decreases.

To investigate the time-dependent behavior of the SR-FEL spectrum, we

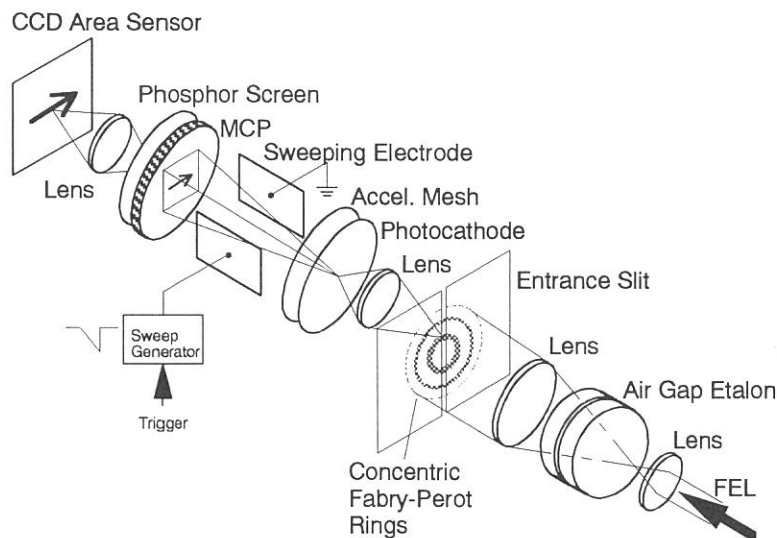


Fig.2 Schematic layout of the time-resolved measurement.

developed a method to measure time-resolved spectral data by sweeping the spatial image of the fringe. The measurement system is schematically shown in Fig.2. The concentric fringe pattern is imaged onto an entrance slit and transferred to a CCD area sensor by relay optics. Electric sweep provides time dependent evolution of the lasing spectrum on the CCD. Figure 3 shows typical time-dependent evolution of the natural lasing spectra obtained at a beam current of 15.3 mA/bunch. It was found that the each macropulse has different lineshape containing considerable internal substructures. Furthermore, one can see that the spectral distribution does not change significantly during one macropulse evolution. Such spectral properties were

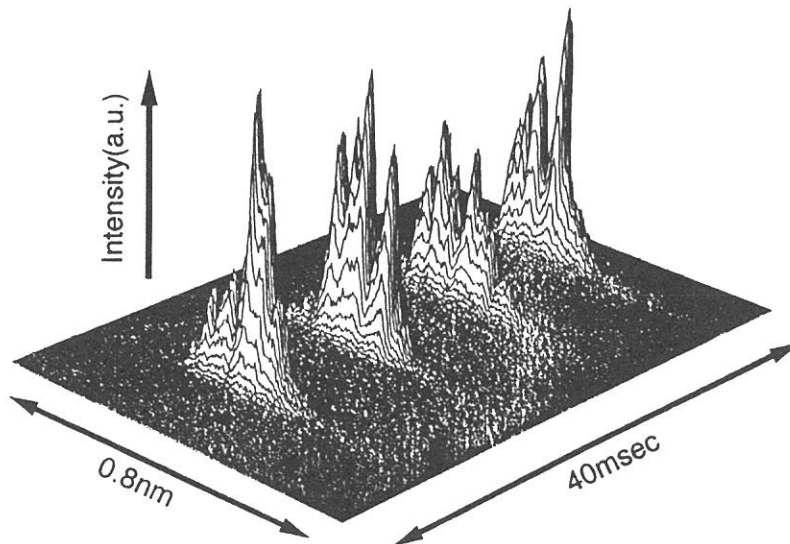


Fig.3 Typical time evolution of the laser lineshape in the natural lasing. The laser wavelength was 467.5nm.

observed at the whole range of the beam current.

Theoretical analysis and further experimental studies such as simultaneous measurements of temporal and spectral distribution of the SR-FEL in both the gain-switched and the natural lasing cases are under way.

#### References

- [1] S. Takano, H. Hama and G. Isoyama, Nucl. Instr. and Meth. A331 (1993) 20.
- [2] H. Hama, J. Yamazaki, T. Kinoshita, K. Kimura and G. Isoyama, Nucl. Instr. and Meth. A (in press).

# Design Concept of New Monochromator for Circularly Polarized Synchrotron Radiation in the Energy Range of 5-250 eV.

Masao Kamada, Kusuo Sakai, Shin-ichiro Tanaka, Shin-ichi Kimura, Atunari Hiraya, Masami Hasumoto, Shigeo Ohara,<sup>a)</sup> Kazumichi Nakagawa,<sup>b)</sup> Kouichi Ichikawa,<sup>c)</sup> Kazuo Soda,<sup>d)</sup> Kazutoshi Fukui,<sup>e)</sup> Yasuo Fujii,<sup>f)</sup> and Eiji Ishiguro<sup>f)</sup>

Institute for Molecular Science,  
a) Nagoya Institute of Technology, b) Kobe University,  
c) University of Osaka Prefecture, d) Nagoya University,  
e) Fukui University, f) Osaka City University

There are several types of glancing incidence monochromators working well in the synchrotron radiation facilities in the world. Among them, the plane grating monochromator SX-700 designed by Petersen (1) is well known to have a good performance, especially resolving power higher than 10,000. The spherical grating monochromator DRAGON designed by Chen (2) also shows high resolution. However, the floor space limitation and the moderate emittance of the UVSOR do not allow the use of these mounts. Therefore we preferred a new Spherical Grating Monochromator with Translational and Rotational Assembly Including a Normal incidence mount (SGM-TRAIN). The SGM-TRAIN is an improved version of a constant deviation monochromator proposed by Ishiguro et al.(3) and Senf et al.(4), and is under construction at BL5A.

The following points have been taken into account in the design: (1) energy range of 5-250 eV, (2) use both of undulator and bending radiations, (3) linear and circular polarizations, (4) spectral purity, (5) resolution, and (6) length of beam line. It should be stressed that the SGM-TRAIN is useful for the experiments where circularly polarized synchrotron radiation is used. Moreover, the SGM-TRAIN has an advantage that small emittance of a storage ring and large space for a long beam line are not necessary.

The SGM-TRAIN consists of two glancing incidence mounts and a normal incidence mount. Its main optical components are three spherical gratings, three sets of plane mirrors, and fixed slits, and the grating and slits are aligned approximately on the Rowland circle. The radii of the gratings (G1 and G2) for the deviation angles of 152° and 172° are 7.3 and 25 m, respectively. The deviation angle of the normal incidence mount is 7° and the radius of the grating (G3) is 2.6 m. Three plane mirrors (M21) coated with different materials (Au, SiC, and Al) and other two plane mirrors coated with Pt (M20) and Au (M22) are interchanged without breaking the vacuum, together with interchanging three gratings. The distance between the entrance and the exit

slits is 3.5 m.

Figure 1 shows the resolving powers of the glancing incidence mount with deviation angles of  $152^\circ$  and  $172^\circ$ , which were estimated with a ray-tracing calculation. In the calculation, the vertical and the horizontal slit sizes are employed to be 0.01 and 10 mm, respectively. The vertical and horizontal divergences of the incident photon beam at the entrance slit for the deviation angle of  $152^\circ$  are set to be 6 mrad and 2 mrad, respectively, and those for the deviation angle of  $172^\circ$  are to be 3 mrad and 2 mrad, respectively. The photon flux with the resolving power of 1,000 is estimated to be  $5 \times 10^{11}$  photons/sec at 10 nm, under the assumption that the diffraction efficiency of G1 is 5% and the horizontal acceptance of the bending radiation is 10 mrad. The good degree of circular polarization is expected in the wide energy range except for around 40 eV.

#### References

- 1 H. Petersen, Opt. Commun. 40, 402 (1982).
- 2 C. T. Chen and F. Sette, Rev. Sci. Instrum. 60, 1616 (1989).
- 3 E. Ishiguro, M. Suzui, J. Yamazaki, E. Nakamura, K. Sakai, O. Matsudo, N. Mizutani, F. Fukui, M. Watanabe, Rev. Sci. Instrum. 60, 2105 (1989).
- 4 F. Senf, F. Eggenstein, and W. Peatman, Rev. Sci. Instrum. 63, 1326 (1992).

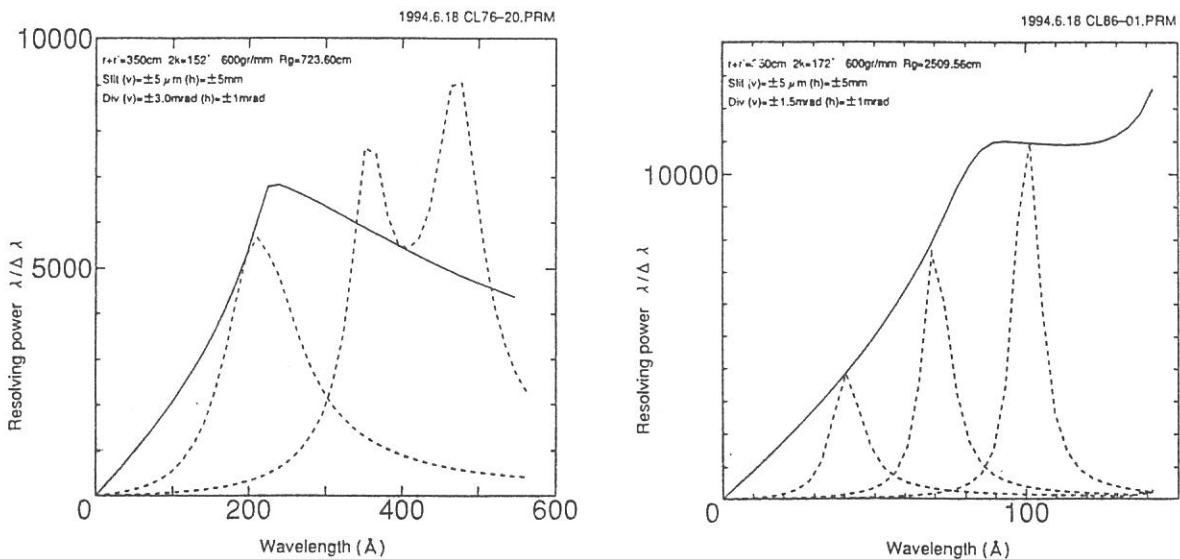


Fig. 1. Calculated resolving power for  $2k=152^\circ$  and  $172^\circ$ . Solid and broken curves correspond to the standard and high-resolution modes, respectively.

## Construction of A New UHV Apparatus for Soft X-Ray Photoemission-Photoabsorption Spectroscopy

Yasutaka TAKATA, Motohiko NAKAMURA and Nobuhiro KOSUGI

*Institute for Molecular Science, Myodaiji, Okazaki 444*

In order to investigate the electronic structure of transition metal compounds by soft x-ray photoemission-photoabsorption spectroscopy, we have constructed a new ultra-high-vacuum (UHV) apparatus. The apparatus has been placed at the soft x-ray double crystal monochromator beamline (BL1A) which covers the photon energy from 830-4000 eV by exchanging the monochromator crystals.

The main component of the apparatus is an electron energy analyzer (SES-200) manufactured by SCIENTA, Uppsala, Sweden[1]. The analyzer is a full hemisphere with a mean radius of 200 mm and equipped with an electron lens and multidetection system. The pass energy can be varied between 1 and 1000 eV. Before the delivery, the energy resolution of the analyzer was estimated from Xe 5p<sub>3/2</sub> photoemission spectra in the gas phase; a typical resolving power ( $E_p/\Delta E$ ) is 1300 and the ultimate resolution ( $\Delta E$ ) is 3.3 meV at the pass energy ( $E_p$ ) of 2 eV.

Figure 1 shows the top view of the whole system. It consists of three vacuum chambers, i.e., an analysis chamber, a preparation chamber, and an air-lock chamber. All the chambers are made of stainless steel and the inner wall is mirror-polished ( $R_{\max}=0.1\mu\text{m}$ ) by electrochemical buffing. A sample is transferred between the chambers. The analysis chamber is equipped with the electron analyzer and a flood gun for compensation of charge up of a sample. The measurement space is shielded magnetically by a  $\mu$ -metal plate. As a result, the magnetic permeability at the center is less than 10 mG. In addition to photoemission spectra, photoabsorption spectra can be measured in total and Auger electron yields in the chamber. The chamber is evacuated by a couple of turbomolecular pumps (TMPs) and a titanium sublimation pump. The analyzer is directly evacuated by a set of TMPs because of its large volume and low conductance. The pressure achieved at present time is  $10^{-11}$  Torr. In the preparation chamber, sample preparation such as evaporating and scraping can be carried out. It is possible to introduce the SR beam to the preparation chamber through a gate valve with 1300 Å Lexan® window so that the absorption spectra also can be measured in the chamber. This arrangement is valuable because the prepared sample can be characterized instantly from the absorption spectra. The chamber has some spare ports with a gas-flow proportional counter for fluorescent x-ray detection and surface analysis components such as LEED optics. The preparation chamber is evacuated by a couple of TMPs and non-evaporable getter pump. The base pressure achieved is  $10^{-11}$  Torr.

The adjustment and performance test of the electron analyzer had been completed. For some Ni compounds, valence, Ni3p and 3s resonant photoemission spectra at Ni L<sub>II,III</sub> edge

have been measured. Preliminary results of NiO is reported in this issue.

### Reference

- [1] N.Mårtensson, P.Baltzer, P.A.Brühwiler, J.-O.Forsell, A.Nilsson, A.Stenberg, and B.Wannberg, *J.Electron.Spectrosc.Relat.Phenom.*, **70** (1994) 117.

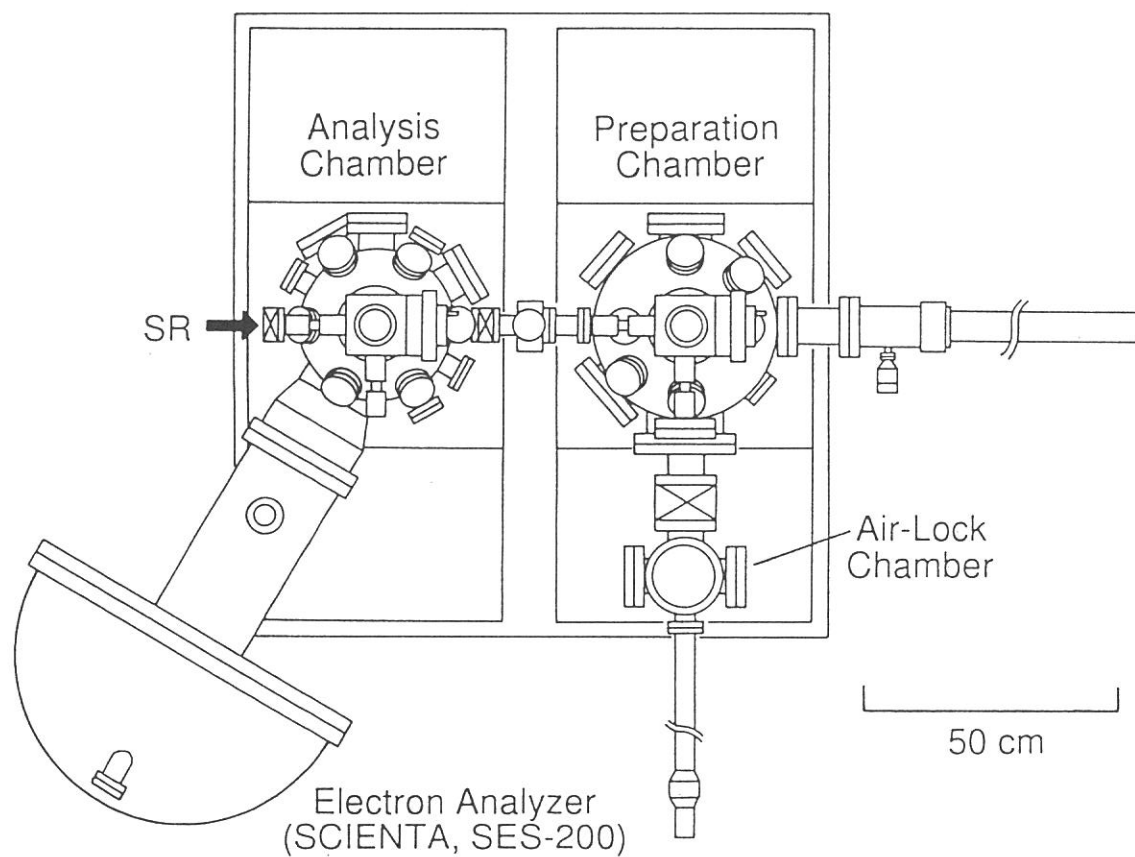


Fig.1. Top view of the UHV apparatus for photoemission-photoabsorption spectroscopy.

## Resonant Ni 3p and 3s Photoemission for the Ni 2p Core-Excitation in NiO

Motohiko NAKAMURA, Yasutaka TAKATA and Nobuhiro KOSUGI

*Institute for Molecular Science, Myodaiji, Okazaki 444*

Resonant photoemission is a technique based on the effect that the photoemission is enhanced by Auger decay after the photon excitation at the core-level absorption edge [1]. In case of 3d transition metal compounds, resonant photoemission in 2p core excitation shows a strong resonance in comparison with that in 3p core excitation [2]. The 2p resonant photoemission, therefore, has been a powerful means to investigate the electronic character of unidentified peaks in x-ray absorption (XAS) and photoemission (XPS) spectra.

We have performed Ni 3p and 3s photoemission study in the Ni 2p core excitation region for NiO using a new UHV apparatus at BL-1A [3]. NiO is a classical example of the Mott insulators. NiO was prepared by oxidation of nickel rod (99.99%,  $\phi 10\text{mm} \times 15$ ) at 950 °C in air for 5 hours [4]. The Clean surface was obtained *in situ* by scraping the sample with a diamond file under the pressure of  $\sim 10^{-10}$  Torr. XAS spectrum was measured by the total electron yield. XPS spectra were measured with a hemispherical electron analyzer (SES-200) manufactured by SCIENTA. The total energy resolution was about 0.7 eV for the analyzer pass energy of 300 eV. The calibration of the binding energy was made by measuring Au 4f level. Each spectrum was normalized using the total electron yield of an Au mesh.

Figure 1 shows the Ni 2p XAS spectrum of NiO. Figure 2 shows the photoemission spectra of the Ni 3p and 3s core-level of NiO at various photon energies indicated in Fig. 1. It took  $\sim 3$  hours (30 scan) to obtain one spectrum. The peaks of 1 and 5 in Fig. 2 are the main peaks of Ni 3p<sub>3/2</sub> and 3s, and the other peaks are mainly enhanced resonant peaks. The Ni 3p and 3s photoemission spectra change drastically above the photon energy of the Ni 2p<sub>3/2</sub> absorption edge. These resonant peaks can be described by 2p3d3p, 2p3d3s and 2p3p3p Auger decays [5]. The peak of 3 shift only toward the higher binding energy with increasing the photon energy; that is, the resonant peak of 3 corresponds to the spectator Auger decay which changes a final ionic state depending on the photon energy. The other resonant peaks correspond to the participant Auger decay which does not change final ionic states. In order to make this change of spectra more clear, we show the contour map of these photoemission spectra in Fig. 3. The spectra of j, k, and l were created by shifting the binding energy of normal 2p3d3p, 2p3d3s and 2p3p3p Auger spectra. The horizontal axis and the vertical axis represent an electron binding energy and a photon energy, respectively. Normal Auger peaks such as 10 in Fig. 3 shift toward higher binding energy with increasing the photon energy, but the peak of 3 does not shift similarly. This feature suggests that a final state of this peak is affected by the electron correlation or the screening of the conduction band.



## References

- [1] L.C. Davis, J. Appl. Phys. **59**, R25 (1986).
- [2] L. H. Tjeng, C. T. Chen, J. Ghijsen, P. Rudolf, and F. Sette, Phys. Rev. Lett. **67**, 501 (1991).
- [3] Y. Takata, M. Nakamura and N. Kosugi, in this issue.
- [4] K. S. Kim and R. E. Davis, J. Electron Spectrosc. **1**, 251 (1972).
- [5] A. Tanaka and T. Jo, J. Phys. Soc. Jpn. **63**, 2788 (1994).

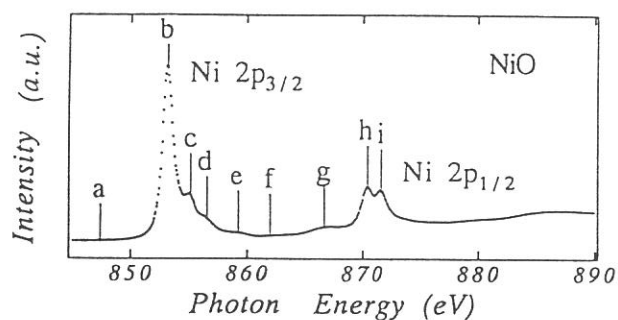


Fig. 1. Ni 2p XAS spectrum of NiO. The vertical bars indicate the photon energies chosen for the XPS spectra.

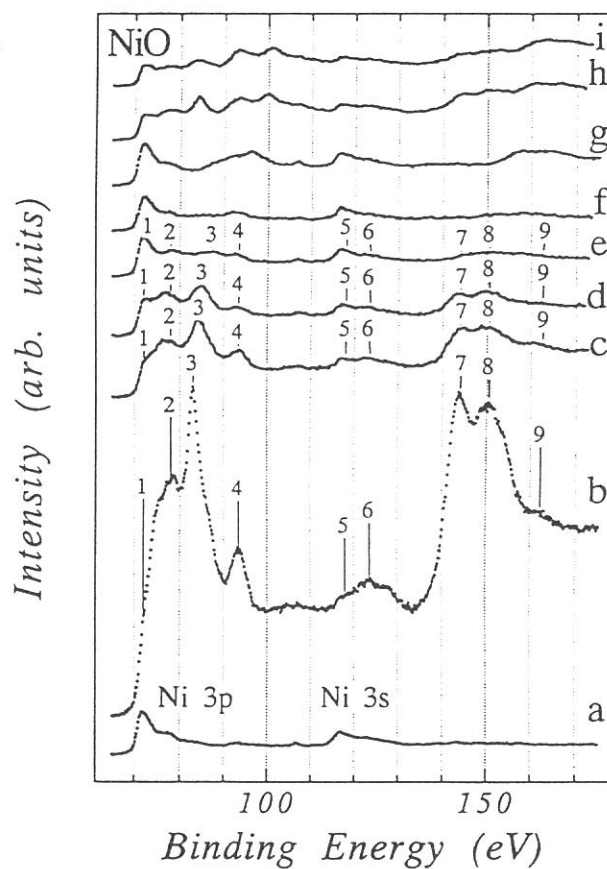


Fig. 2. Ni 3p and 3s XPS spectra in the Ni 2p core excitation region.

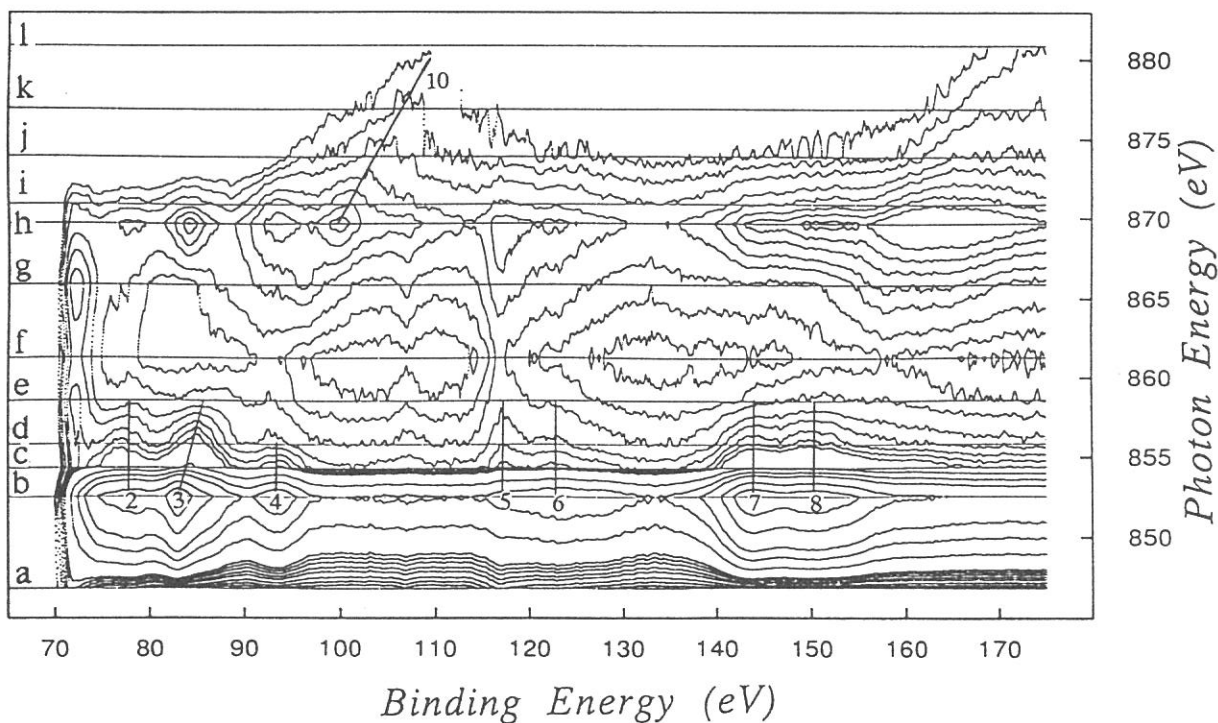


Fig. 3. Contour map of Fig. 2. The dotted horizontal lines corresponds to the photon energies shown in Fig. 1.



## A Soft X-ray Core-Absorption Study on the Conduction Bands of the Cu and Ag Photodoped Amorphous GeSe<sub>2</sub>

Shinya HOSOKAWA, Tsuyoshi KOUCHI, Izumi ONO, Akihito FURUTA,  
Masaki TANIGUCHI, Yasutaka TAKATA\* and Nobuhiro KOSUGI\*

*Department of Materials Science, Hiroshima University,  
Kagamiyama, Higashi-Hiroshima 724*

*\*Institute for Molecular Science, Myodaiji, Okazaki 444*

When an amorphous (a-) chalcogenide thin film is deposited onto a clean surface of Cu or Ag metal and irradiated by visible light, metal atoms rapidly diffuse into the amorphous films. It is a very interesting phenomenon that takes place only in amorphous chalcogenides, not in crystal ones. This photodoping phenomenon has been well-known since the discovery in 1966 [1]. The atomic structure of the Ag photodoped a-GeSe<sub>2</sub> was investigated by the EXAFS and the anomalous x-ray scattering measurements and it was found that Ag atoms are surrounded by four Se atoms and there are no pronounced correlations of Ag-Ag or Ag-Ge [2]. Recently we have measured the inverse-photoemission (IPES) spectra of Ag and Cu photodoped a-GeSe<sub>2</sub> in our laboratory, and found that the prominent two peaks of the unoccupied density of states (DOS) of a-GeSe<sub>2</sub> smears out by the photodoping of Ag or Cu metals [3]. The core-absorption spectroscopy also provides information on the conduction-band DOS, especially including the selection rule of angular momentum on the optical transitions. By comparing IPES spectra with core-absorption spectra, we can extract the contribution of each orbital component from the DOS and obtain information on the effect for such partial DOS's by the photodoping.

We have measured the Ge, Se and Cu 2p<sub>3/2</sub> core-absorption spectra for the Ag and Cu photodoped a-GeSe<sub>2</sub> at the beam line BL-1A of UVSOR at Institute for Molecular Science. The measurements were performed in the total electron yield mode at room temperature using the double Beryl monochromator. The sample film of a-GeSe<sub>2</sub> with the thickness of 1000 Å was evaporated onto a clean Au substrate in a preparation chamber under the base pressure below 8×10<sup>-10</sup> Torr, that was taken into UVSOR from our laboratory. The photodoped samples were prepared by evaporating Ag or Cu metals onto the a-GeSe<sub>2</sub> films and irradiating by visible light emitted from a 1000-W tungsten lamp through a viewing window of the chamber for more than 10 minutes. The samples were *in situ* transferred into an analyzer chamber under base pressure below 5×10<sup>-10</sup> Torr.

Figure 1 (a) shows the Ge 2p<sub>3/2</sub> core-absorption spectra of photodoped a-GeSe<sub>2</sub>Ag<sub>0.5</sub> and a-GeSe<sub>2</sub>Cu<sub>0.5</sub>, and undoped a-GeSe<sub>2</sub>. Each spectrum of the photodoped samples is very

similar to that of undoped a-GeSe<sub>2</sub>. This result is in consistent with the information on the local structure around the Ge atoms [2]. The Se 2p<sub>3/2</sub> core absorption spectra shown in Figure 1 (b) reveal a little doping effect that the Se 4s contribution at 1432-1439 eV becomes slightly large for each photodoped sample. However, the Ge and Se 3d core-absorption spectra are strongly affected by the photodoping of Ag metal [4]. In conclusion, the prominent change of the conduction-band DOS by Ag or Cu photodoping is caused mainly through the Ge and Se 4p contributions.

This study was partly supported by The Japan Securities Scholarship Foundation and Nissan Science Foundation.

- [1] M. T. Kostysin, E. V. Mikhailovskaya and P. F. Romanenko, *Sov. Phys.* **8**, 351 (1966).  
 [2] A. Fischer-Colbrie, A. Bienenstock, P. H. Fuoss and M. A. Marcus, *Phys. Rev. B* **38**, 12388 (1988).  
 [3] S. Hosokawa, Y. Hari, I. Ono, K. Nishihara, M. Taniguchi, O. Matsuda and K. Murase, *J. Phys.: Condens. Matter* **6**, L207 (1994).  
 [4] K. Inoue, T. Katayama, K. Kawamoto and K. Murase, *Phys. Rev. B* **35**, 7496 (1987).

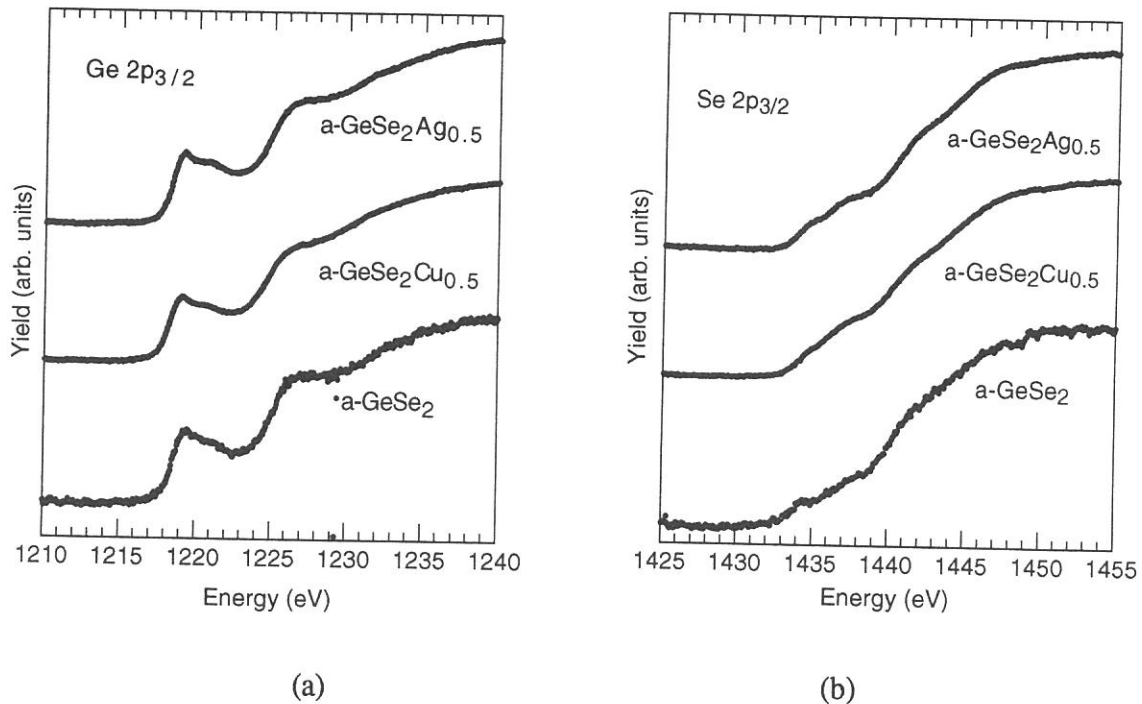


Figure 1. The Ge (a) and Se (b) 2p<sub>3/2</sub> core-absorption spectra of photodoped a-GeSe<sub>2</sub>Ag<sub>0.5</sub> and a-GeSe<sub>2</sub>Cu<sub>0.5</sub>, and undoped a-GeSe<sub>2</sub>.

## Polarized Vacuum-UV Absorption and Reflection Spectra of Poly(tetrafluoroethylene) and Its Model Compound

Kouhei NAGAYAMA, Takayuki MIYAMAE, Ryuichi MITSUMOTO, Hisao ISHII,  
Yukio OUCHI and Kazuhiko SEKI

*Department of Chemistry, Faculty of Science, Nagoya University,  
Furocho, Chikusa-ku, Nagoya 464-01, Japan*

Poly(tetrafluoroethylene)(CF<sub>2</sub>)<sub>n</sub>, is one of the most fundamental organic polymers. Its electronic structure for occupied states has been studied by X-ray photoelectron spectroscopy (XPS)[1-3] and uv photoemission spectroscopy (UPS)[4]. The results of agreed well with the density of states (DOS) obtained by the *ab initio* band calculation [4]. As for the unoccupied states, the general trend of the calculated results are consistent with those by electron transmission spectroscopy [5] and near-edge X-ray absorption fine structure (NEXAFS) spectroscopy [6,7]. However, the reliability of calculation is not so good, and further confirmation was desired. A way of performing this is to study the polarization dependence of the absorption spectra. The absorption spectrum of PTFE was measured by us [4], but the polarization dependence was not performed, partly due to the difficulty of the preparing well-oriented film of PTFE.

We have recently found that well oriented films of PTFE can be prepared by mechanical rubbing of evaporated films of PTFE, with the molecular axes parallel to the rubbing direction [7]. Also we reported that evaporated films of a short model compound of PTFE *n*-C<sub>24</sub>F<sub>50</sub> shows good molecular orientation vertical to the substrate surface. In this work we report the polarized optical spectra of PTFE and *n*-C<sub>24</sub>F<sub>50</sub> with these films, including the comparison with the band calculation.

The sample materials of PTFE (*n*=100-400, with maximum at *n*=172) and *n*-C<sub>24</sub>F<sub>50</sub> were obtained from Central Glass Co., and Aldrich, respectively. The spectra were measured both in absorption and reflection modes at the beamline 1B at UVSOR using a Seya-Namioka type monochromator. For absorption spectra, samples were prepared as evaporated films on LiF substrates with a thickness of 100 nm as measured by a quartz oscillator. The sample of PTFE was further mechanically rubbed with a cloth under a pressure of 20 g/cm<sup>2</sup>. For reflection measurements we used (i) the surface of a PTFE bar after sliding on a heated glass plate and (ii) a PTFE sealing tape after uniaxial elongation.

In Fig. 1, the absorption spectra of rubbed PTFE film and evaporated film of *n*-C<sub>24</sub>F<sub>50</sub> are shown. For PTFE film, a peak is observed at 7.7 eV. This peak in the spectrum with the electric vector of incident light *E* parallel to the rubbing direction is stronger than that in the spectrum with *E* vertical to the rubbing direction. Since it is known that the molecular axes are oriented parallel to the rubbing direction, this absorption is allowed for *E* parallel to the molecular axis. Since the rubbing process will lead to the molecular alignment only at the surface region, transmittance through the remaining bulk part may lead to the incomplete disappearance of this peak in the spectrum with *E* vertical to the rubbing direction. On the other hand, the spectrum of evaporated *n*-C<sub>24</sub>F<sub>50</sub> shows no absorption around this photon energy. When we consider that molecules are aligned vertically to the substrate, this shows that the transition is forbidden for *E* vertical to the molecular chain. When we incline the LiF substrate to the incident beam, we observed a peak at 8.1 eV, with increasing intensity for increasing inclination angle.

Corresponding results were obtained for reflection spectra. As shown in Fig. 2, the absorption spectra of oriented PTFE obtained by the Kramers-Kronig transformation of the reflection spectra gave a peak at 7.6 eV, with the transition moment parallel to the molecular chain. The band calculation predicts that the transition from the highest occupied crystal orbital (or the top of the valence band) to the lowest unoccupied vacant level (or the bottom of the conduction band) is allowed for *E* parallel to the chain

direction. Other combinations for the topmost region of the occupied states and the lowest unoccupied states do not give allowed transition. Thus the present result strongly supports the validity of the band calculation.

The calculation indicates that both the topmost occupied and the lowest unoccupied orbitals show strong dispersion, *i.e.* there should be a significant carbon-number dependence of the orbital energies. For examining this point, in Fig. 3 we plot the reported[7] and presently observed peak energies as a function of the inverse of the carbon number  $n$ . We see a good straight relation between the transition energy and  $1/n$ . This can be explained by assuming a simple 1-dimensional bands predicted for units interacting through nearest-neighbor interactions. These results have given a rather clear picture about the electronic structure of PTFE.

- [1] D.T. Clark and D. Kilcast, *Nature Phys. Sci.* **233**, 77 (1971).
- [2] J.J. Pireaux, J. Riga, R. Caudano, J.J. Verbist, J.M. Andre, J. Delhalle, and S. Delhalle, *J. Electron Spectrosc.*, **5**, 531 (1974).
- [3] J. Delhalle, S. Delhalle, J.M. Andre, J.J. Pireaux, J. Riga, R. Caudano, and J.J. Verbist, *J. Electron Spectrosc.*, **12**, 293 (1977).
- [4] K. Seki, H. Tanaka, T. Ohta, Y. Aoki, A. Imamura, H. Fujimoto, H. Yamamoto, and H. Inokuchi, *Phys. Scripta*, **41**, 167 (1990).
- [5] I. Ishii, R. McRalen, A.P. Hitchcock, K.D. Jordan, Y. Choi, and M.B. Robin, *Can. J. Chem.*, **66**, 2104 (1988).
- [6] T. Ohta, K. Seki, T. Yokoyama, I. Morisada, and K. Edamatsu, *Phys. Scripta*, **41**, 150 (1990).
- [7] K. Nagayama, R. Mitsumoto, T. Araki, Y. Ouchi, and K. Seki, *Physica B*, in press.
- [8] G. Belanger, P. Sauvateau, and C. Sandorfy, *Chem. Phys. Lett.*, **3**, 649 (1969).

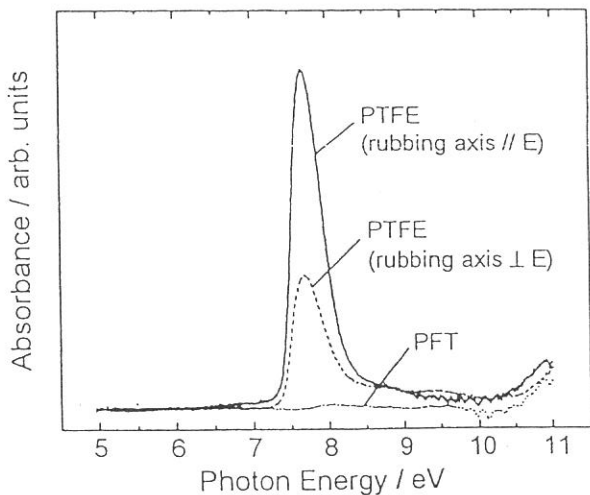


Fig. 1. Polarized absorption spectra of oriented films of PTFE and  $n$ -C<sub>24</sub>F<sub>50</sub>.

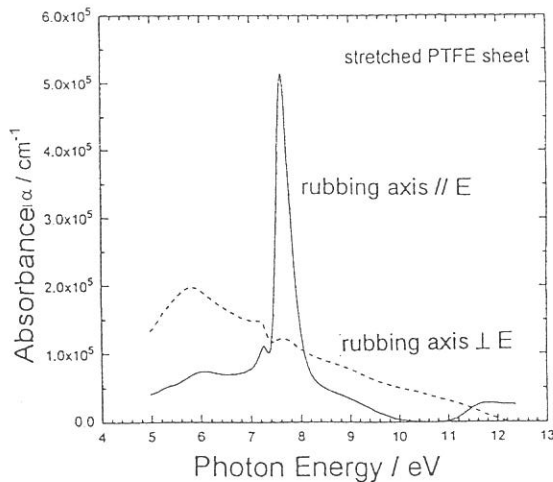


Fig. 2. Polarized absorption spectra of elongated PTFE tape obtained by K-K transformation of the reflection spectra.

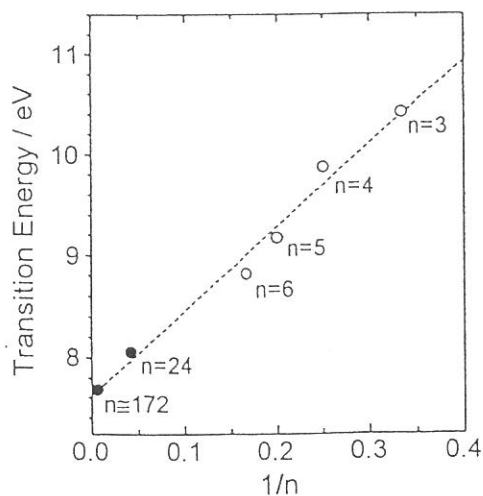


Fig. 3. Carbon number dependence of the energy of the lowest excitation for perfluoroalkanes.

## Two Types of STE Luminescence in PbCl<sub>2</sub> Crystal

M. Kitaura, H. Nakagawa, K. Fukui, M. Fujita\*, and T. Miyanaga\*\*

*Department of Electrical and Electronics Engineering, Fukui University, Fukui 910*

*\*Maritime Safety Academy, Kure 737*

*\*\*Department of Physics, Faculty of Education, Wakayama University, Wakayama 640*

Lead chloride (PbCl<sub>2</sub>) belonging to orthorhombic system, has been well known as a typical material which shows photochemical decomposition with UV irradiation. In this study, luminescence (EMISSION, EXCITATION) spectra have been investigated at BL-1B of UVSOR.

Figure 1 shows emission spectra of PbCl<sub>2</sub> at 6.5K under excitation in (a) the lowest exciton and (b) the band-to-band absorption region. The observed four emission bands are in good agreement with the previously reported ones<sup>1)</sup>. The UV emission band locates in the highest energy region and is excited in the lowest exciton band at 9K. On the other hand, the BG emission is dominant under excitation in the region above the band gap energy where the electron trapping centers (STEL) of (Pb<sub>2</sub>)<sup>3+</sup> type are optically created<sup>2)</sup>.

Excitation spectra for the observed emission bands are shown in figure 2. All excitation spectra were measured at 6.5K. The Excitation spectrum for the UV emission rises at the low energy tail of the lowest exciton band and exhibits two dips at 4.51eV and 4.78eV, which correspond to the structures found in the reflection spectra for E // b<sup>3)</sup>. Therefore, the UV emission is regarded as that arising from the direct relaxed states of the lowest exciton band which consists of sub-levels separated from the <sup>3</sup>P<sub>1</sub> state of the Pb<sup>2+</sup> ion. The B and the BG emission are scarcely excited at 4.51eV where the UV emission is strongly excited. In Fig. 2 (b) and (c), it is not possible to distinguish real excitation spectra for B and BG owing to the strong overlap between B and BG emission bands. It may be safely noticed, however, that the BG emission is excited only in the band-to-band absorption region at 6.5K. Excitation spectrum for the R emission has structures in the region below the lowest exciton band. It is plausible that the origin of R is extrinsic due to impurity or defects.

Figure 3 shows the temperature dependence of the excitation spectrum for the B emission. As elevating temperature, the B emission comes to be strongly observed with excitation at 4.51eV and 4.78eV, while the UV emission is diminished. The result suggests that the initial state of the B emission is connected with that of the UV emission. Enhancement of the B emission and quenching of the UV emission is explained by considering the thermal activation of STE's (self-trapped excitons) from the initial state of the UV emission into that of the B emission. The initial states of the UV emission and the B emission are to be well described by the STE states localized at the Pb<sup>2+</sup> ion.

Several emission bands are observed at low temperature in  $\text{PbCl}_2$ . Among these emission bands, only the BG emission appears under excitation in the region above the band gap energy. It was confirmed that the temperature dependence of the BG emission intensity is in good agreement with that of ESR signals of the STEL centers<sup>2)</sup>. Thus, the BG emission is connected to the recombination luminescence due to radiative annihilation of STE's consisting of  $[(\text{Pb}_2)^{3+} + \text{hole}]$ , in which a STEL center captures a hole. This type of STE is in contrast with that of  $[(\text{X}_2)^- + \text{electron}]$  type well-known in alkali halides, where  $\text{X}^-$  is the halogen ion.

Finally, we conclude that two kinds of STE's coexist in  $\text{PbCl}_2$ : the one is a monomer type-STE localized at the  $\text{Pb}^{2+}$  ion, giving rise to the UV emission below 15K and the B emission above 15K, and the other is a dimer type-STE consisting of  $[(\text{Pb}_2)^{3+} + \text{hole}]$  giving the BG emission.

1) W. C. De Gruijter: Phys. Letter **34A** (1971) 251.

2) S. V. Nistor, E. Goovaerts and D. Schoemaker: Phys. Rev. **B48** (1993) 9575.

3) M. Fujita, H. Nakagawa, K. Fukui, H. Matsumoto, T. Miyanaga and M. Watanabe: J. Phys. Soc. Jpn. **60** (1991) 4393.

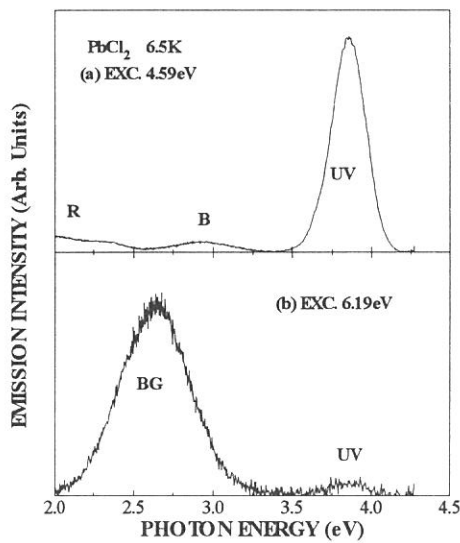


Fig. 1

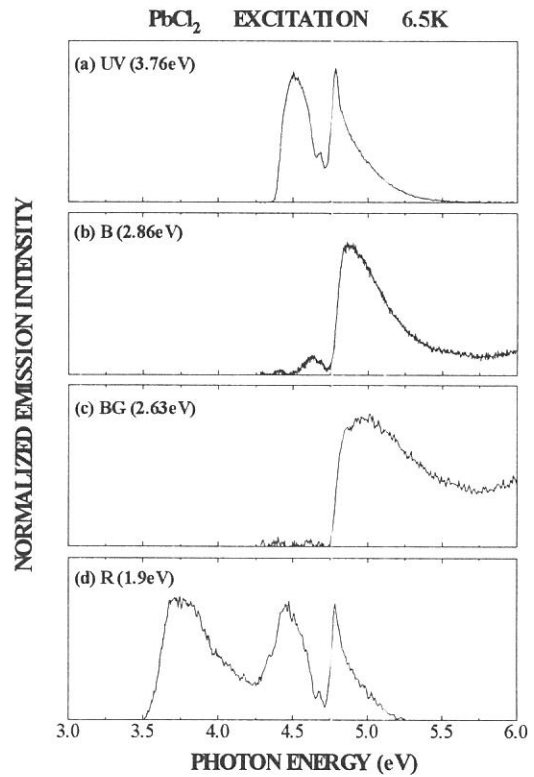


Fig. 2

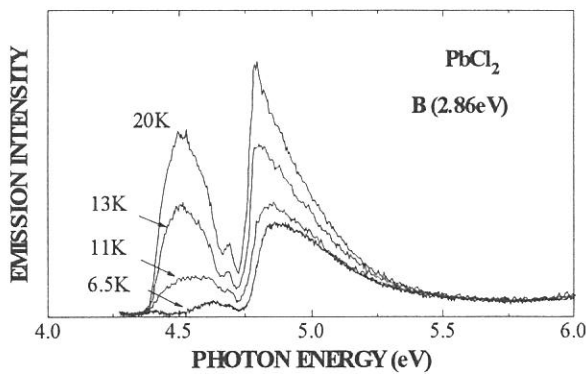


Fig. 3



## Photoionization Potentials of Fullerenes( $C_{60}\sim C_{84}$ ) in nonpolar liquid

Iwao SHIMOYAMA, Kazumichi NAKAGAWA, <sup>1</sup>Chiemi FUJIKAWA,  
<sup>1</sup>Katsuyuki MORII, <sup>1</sup>Tadaaki MITANI, <sup>2</sup>Ryuzi KATOH

Faculty of Human Development, Kobe University, Tsurukabuto, Nada-ku, Kobe 657,  
Japan

<sup>1</sup>Japan Advanced Institute of Science and Technology, Hokuriku, Tatsuguchi,  
Noumi-gun, Ishikawa 923-12, Japan

<sup>2</sup>Faculty of Science, Gakushuin University, Mejiro, Tokyo 171, Japan

Although fullerenes were investigated so hardly in many fields, the data of gas phase ionization potential  $I_g$  were measured for only  $C_{60}$  and  $C_{70}$ . Data of  $I_g$  for higher fullerenes are not available because evaporation temperature of higher fullerenes is so high that experiment is very difficult. Therefore, instead of gas-phase UPS measurement, we tried to estimate  $I_g$  values of higher fullerenes from the result of measurements of photocurrent threshold energy  $I_p$  of fullerenes ( $C_{60}$ ,  $C_{70}$ ,  $C_{76}$ ,  $C_{78A}$ ,  $C_{78B}$ ,  $C_{82}$ ,  $C_{84}$ ) doped in 2,2,4-trimethylpentane(TMP). It is established that ionization potential  $I_p$  of aromatic molecules doped in nonpolar liquid is well described by an equation  $I_p = I_g + P + V_0$  (Eq. (1)), where  $V_0$  is conduction band energy of liquid TMP,  $P$  is the polarization energy of fullerene ions in TMP[1]. Since  $V_0$  of TMP is reported to be  $-0.24\text{eV}$ [1],  $I_g$  should be estimated from Eq. (1), when we measure  $I_p$  and estimate  $P$  value. On the basis of this idea, we started experiment to measure  $I_p$  values.

Fullerenes were prepared and purified in Japan Advanced Institute of Science and Technology, Hokuriku. Highly purified TMP were offered by Dr. Kengo Itoh of the University of Tokyo.

Experiments were performed at the BL-1B beamline of the UVSOR in the Institute for Molecular Science, Okazaki, Japan. Monochromatized synchrotron radiation (SR) in the energy region of  $2.4 < h\nu < 12.4\text{eV}$  was introduced between two parallel-plate electrodes in the cell through the  $\text{MgF}_2$  front window. After filling cell with TMP doped with fullerenes, we measured photocurrent  $i(h\nu)$  between the electrodes, and transmitted light intensity  $T(h\nu)$  through the  $\text{MgF}_2$  rear window of the cell.

An example of a photocurrent spectrum of  $C_{78B}$  are shown in the Fig. 1. Because of strong absorption by the TMP above  $6.7\text{eV}$ , we analyzed  $i(h\nu)$  and  $T(h\nu)$  in the region of  $h\nu < 6.7\text{eV}$ . We determined  $I_p$  values using semi-empirical power law [2]  $\eta(h\nu) = C(h\nu - I_p)^{5/2}$  (Eq. (2)), where  $C$  is a constant,  $h\nu$  is incident light energy, and  $\eta(h\nu)$  is photoionization quantum yield. Figure 4 shows obtained values

of  $I_p(\square)$  vs. numbers  $N$  of carbon atoms of fullerenes.

We estimated experimental  $I_\infty$  values via eq.(1), using the reported value of  $V_0$  ( $-0.24\text{eV}$ )[1].  $P$  values of fullerenes were estimated via the Born formula[3];  $P = -e^2(1-1/\epsilon)/2R$  (Eq. (3)), where  $e$  is the elementary charge,  $R$  the ion radius, and  $\epsilon$  the dielectric constant of TMP, which is reported to be 1.936 at room temperature. Values of  $R$  were calculated by a simple relation  $R=0.355\sqrt{N}/60$  (Eq.(4)), reported by Y.Saito et al.[3], where  $N$  is the carbon number. Values of  $I_\infty$  estimated via Eq.(1), (3) and (4) are shown in the Fig. 4 by a symbol  $\circ$ . It is clear that with the increase of carbon number  $N$ ,  $I_\infty$  values decrease at first and turns into increase at  $N>78$ . This result shows similar tendency to the theoretical  $I_\infty$  values calculated by Cioslowski et.al.[4], which are shown in the figure by a symbol  $\triangle$ .

References [1]Holroyd R.A. et. al., J.Chem.Phys.79(1983)1. [2]Yakovlev B.S. and Lukin L.V., Advances in Chem.Phys. 60(1985)99. [3]Born M., Z.Physik. 1(1920)45. [4]Saito Y. et. al., Phys.Rev.B 48(1993)12. [5]Cioslowski J. et. al., J.Chem.Phys. 98(1992)11.

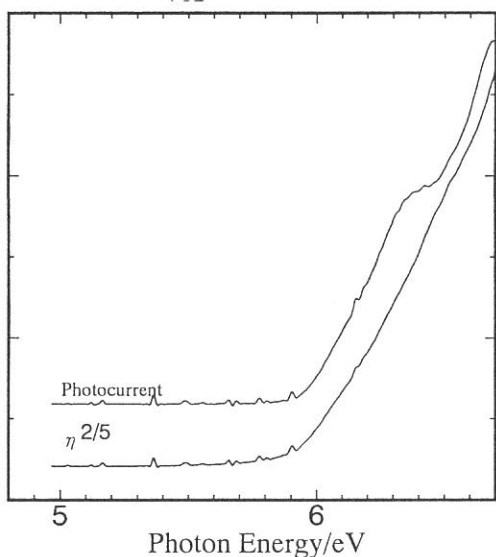


Fig.1 Photocurrent spectrum and quantum yield spectrum  $\eta$  of  $C_{7.8B}$ .  $\eta^{2/5}$  is shown.

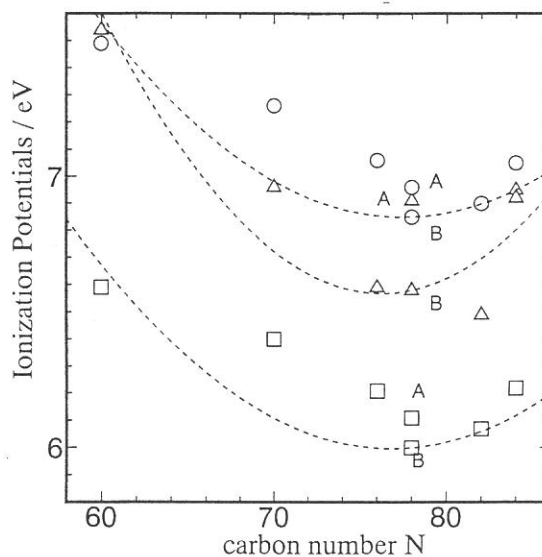


Fig.2 Ionization potentials of fullerenes.  $\square$ :Our  $I_p$  data in TMP.  $\circ$ : $I_\infty$  data estimated from our  $I_p$  data.  $\triangle$ : $I_\infty$  data calculated by Cioslowski et al.[5].



## Emission and Excitation Spectra of (C<sub>n</sub>H<sub>2n+1</sub>NH<sub>3</sub>)<sub>2</sub>CdCl<sub>4</sub>: n=1,2,3

Akimasa OHNISHI, Takeyoshi YAMADA, Takehisa YOSHINARI,  
Ken-Ichi KAN'NO\*, Ikuko AKIMOTO\* and Tomoyoshi KAMIKAWA

*Department of Physics, Yamagata University, Yamagata 990*

*\*Department of Physics, Kyoto University, Kyoto 606*

Alkylammonium metal halides, (C<sub>n</sub>H<sub>2n+1</sub>NH<sub>3</sub>)<sub>2</sub>MX<sub>4</sub>: n=1,2,3; M=Cd, Cu, Mn; X=Cl, Br, I are layered (two dimensional) crystals. They show the novel phenomena, for instance, the metal precipitation and the halogen gas release with X-ray or  $\gamma$ -ray irradiation.<sup>1)</sup> The formation of the self-trapped hole centers and the electron trap centers were also confirmed.<sup>2,3)</sup> The formation mechanism of the hole center and the electron center is classified to the type III (off center type) proposed by Kan'no.<sup>4)</sup> Both of the formation yields of the hole centers and the electron centers are high, hence the yield of intrinsic luminescence is supposed to be very low. That is the reason why the intrinsic luminescences have not been reported yet. We suggested that the electron trap centers<sup>3)</sup> would be self-trapped in the present compounds. It is open to the further investigation.

We observed two emission bands in alkylammonium cadmium chlorides by using the UVSOR light. The peak energies of them are 2.50 eV and 2.25 eV with half height widths of 0.8 eV and 0.7 eV each in (C<sub>2</sub>H<sub>5</sub>NH<sub>3</sub>)<sub>2</sub>CdCl<sub>4</sub>. The emissions are so weak that we used the photon counting system with multi-channel analyzer and multi-channel plate tube. The 2.25 eV emission was not observed in other blocks of crystals, therefore, it was attributed to impurities. It is excited by the band-to-band energy light and not strongly excited with the light of exciton absorption region. The 2.50 eV emission is the intrinsic luminescence which is strongly excited with 5.90 eV light. In the cadmium compounds holes are quickly self-trapped and can not move long distance. On the other hand, electrons migrate through conduction bands and happen to be trapped to the impurities when they are excited with band-to-band energy light. When excitons created with light directly, they migrate and relax to the self-trapped excitons, after then, emit intrinsic luminescence.

The emission spectra are shown in Fig. 1. The excitation spectrum of 2.50 eV emission are also exhibited in Fig. 1. The excitation spectrum shows that the 2.50 eV emission is excited in the exciton and the band-to-band energy region and there is no apparent impurity absorption at the lower energy side of the exciton.

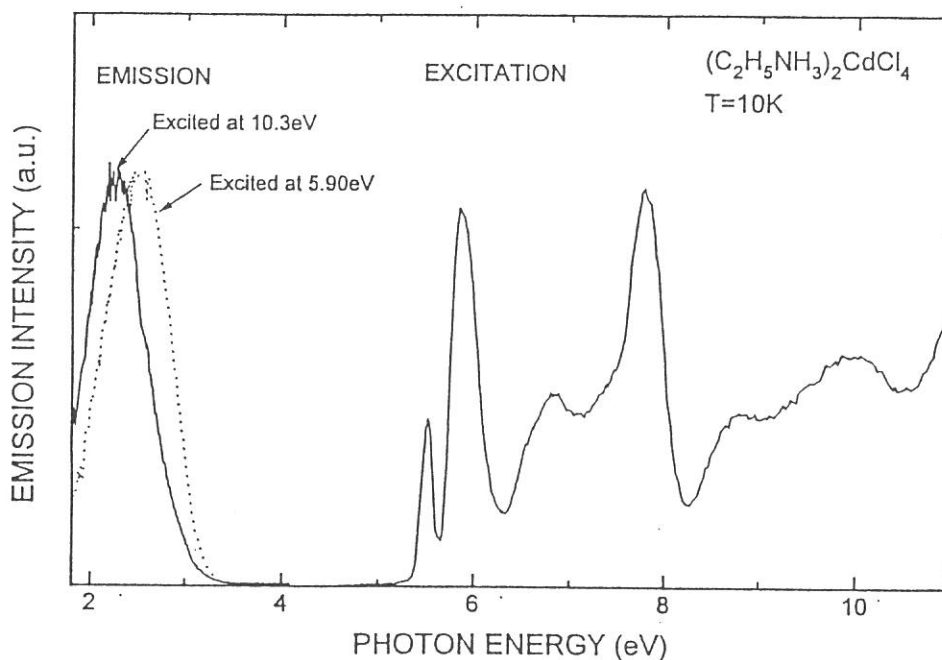


Fig. 1

The 2.25 eV emission intensity is weaker than that of 2.50 eV emission. The emission intensity of 2.25 eV is normalized to that of 2.50 eV thus the S/N ratio of former is smaller than that of latter one. The impurity absorption band is observed in the lower energy region than that of the exciton absorption in other crystals which show the strong emission of 2.25 eV.

There are two decay components in 2.50 eV emission. The intensity of the fast component decays in about 50 ns and the slow one shows the decay too long to measure with our equipment. The emission spectra of the fast decay component and the slow component are separated by setting the time window open at each component. The emission band peak energy of the slow component is lower than that of the fast component. It means that the emission level is splitted to the singlet and the triplet states, and the triplet state is located under the singlet level.

#### References.

- 1) T. Yoshinari, T. Matsuyama, H. Yamaoka and K. Aoyagi: Jpn. J. Appl. Phys. **24** (1985) L720.
- 2) T. Yoshinari, T. Matsuyama, N. Achiwa, H. Yamaoka and K. Aoyagi: J. Phys. Soc. Jpn. **56** (1987)3354.
- 3) T. Yoshinari, T. Matsuyama, H. Yamaoka and K. Aoyagi: J. Phys. Soc. Jpn. **58** (1989) 4222.
- 4) K. Kan'no, K. Tanaka and T. Hayashi: Rev. Solid State Sci. **4** (1990) 383.

# Photoyield Measurements of CVD Diamond

Nobuhiro EIMORI, Akimitsu HATTA, Toshimichi ITO and Akio HIRAKI

*Department of Electrical Engineering, Osaka University, 2-1 Yamadaoka, Suita, Osaka 565*

## 1 Introduction

In this study, we report detailed features of photoyield from homoepitaxial diamond surfaces near the photothreshold energy, which have been investigated using ultraviolet synchrotron radiation light with energies close to the band-gap energy of diamond (5.5eV), and discuss the electron affinity of (111) and (100) surfaces of single-crystalline diamond grown homoepitaxially on single-crystalline high-pressure-synthesis diamond by a CVD method. Specimen surfaces were treated with hydrogen or oxygen after homoepitaxial growth in order to investigate the effect of atoms adsorbed on the diamond surface.

## 2 Experimental

Diamond films were synthesized by means of microwave plasma CVD on (111) and (100) diamond substrates. A dilute B<sub>2</sub>H<sub>6</sub> gas (100ppm in H<sub>2</sub>) was used for boron doping in order to prevent the specimens from charging during photoemission measurements.

H-adsorbed surfaces were obtained for specimens exposed to hydrogen plasma after the diamond growth. The surface exposed to hydrogen plasma has diamond structure, and there are no peaks originating from surface states in electron energy loss (EEL) spectra for the hydrogen-plasma-treated surface, while the surface-state-induced peaks appeared in EEL spectra when the specimen was heated to 900 °C. This means that the diamond surface with the hydrogen plasma treatment is covered with hydrogen atoms. Some of the diamond films were annealed in oxygen atmosphere to obtain the O-adsorbed surface. Oxygen atoms exist only on the specimen surface, and the surface structure has diamond structure, as determined from Auger spectra and Rutherford backscattering.

Photoyield measurements were carried out at room temperature in 10<sup>-8</sup>Torr using synchrotron radiation from the 750 MeV storage ring of the Institute for Molecular Science. Specimens were biased to -240V to collect emitted electrons. A 5-mm-thick quartz window was used to eliminate higher-order light of  $h\nu > 8$  eV. Photoyield spectra were corrected by relative beam intensity of incident photons including the effects of the wavelength-sensitive grating used and time-dependent storage ring current.

## 3 Results and Discussion

Figure 1 shows photoemission yields taken in the energy range of  $4.5 \leq h\nu \leq 7$ eV from the (111) and (100) single-crystalline CVD diamond surfaces treated with hydrogen and oxygen. In Fig. 1, the photoemission yield from the H-treated diamond surface (curve a and c) appears just above 5.4, 5.0 eV and shows a small structure around 5.5eV, which corresponds to the fundamental band-gap energy of diamond. The fact that the onset of band-to-band transitions

is well correlated to the onset of photoelectron emissions signifies that the electron affinity of the H-treated surface is negative.

The H-treated surface (curve a and c) can emit more electrons than the O-treated surface (curve b and d). In the case of the O-treated surface, the onset of photoyield shifts to the higher-energy side, compared to the H-treated surface. The origin of the shift is concluded to be an increase in the work function after the oxygen treatment. This is because the line shape around the threshold energy of photoyield from the O-treated surface is similar to that from the H-treated surface. On the other hand, the threshold energy of photoyield from the O-adsorbed surface is 5.6, 6.0eV and larger than the band-gap energy, indicating that the electron affinity of the O-adsorbed surface is positive. A high electronegativity of oxygen atoms may play the major role in the increase of work function.

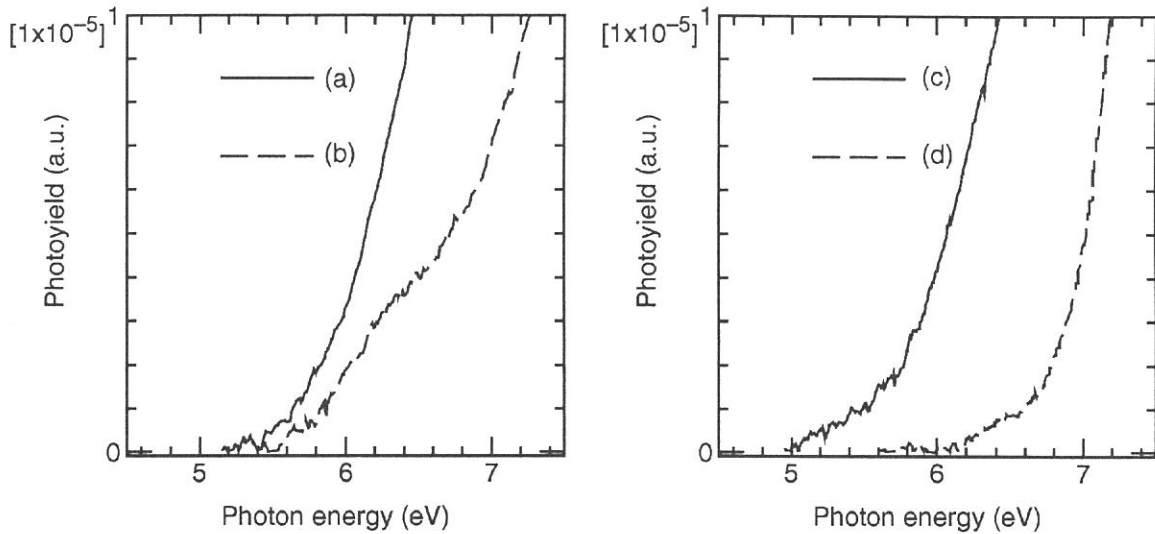


Figure 1:

In comparison with the H-treated (111) surface, the threshold energy of photoyield from the H-treated (100) surface is closer to the band-gap energy of diamond (5.5eV). This suggests that the vacuum level measured from the valence band maximum is higher at the (100)-oriented surface than at the (111)-oriented surface. The dependence of the work function on crystal directions has been reported for other materials. The work function is determined by the total electrostatic potential, which is related to the cohesive energy and the shape of the electron wave function from the surface. The difference in the threshold of photoyield between the (111)- and (100)-oriented surfaces seems to originate from the difference in the shape of the spilling wave function of the two surfaces.

The threshold energy of photoyield from the (100)-oriented surface with O treatment is close to 5.5eV. This value is lower than that from the (111)-oriented surface with O treatment. This difference suggests that the oxygen atoms bonding to carbon atoms at the diamond surface differ between (111)- and (100)-oriented surfaces. The increase of photoyield from the (100)-oriented surface differs from that from the (111)-oriented surface. This also suggests a difference in the C-O bond between the (100)- and (111)-oriented surfaces.

# Impurity-Induced Quenching of Auger-Free Luminescence in Mixed $\text{CsCl}_{1-x}\text{I}_x$ System

M. Itoh,<sup>1</sup> H. Hara,<sup>1</sup> N. Ohno,<sup>2</sup> H. Yoshida,<sup>2</sup> K. Kan'no<sup>3</sup> and S. Hashimoto<sup>4</sup>

<sup>1</sup>Department of Applied Science, Shinshu University, Nagano 380

<sup>2</sup>Department of Solid State Electronics,

Osaka Electro-Communication University, Neyagawa 572

<sup>3</sup>Department of Physics, Kyoto University, Kyoto 606

<sup>4</sup>Department of Physics, Kyoto University of Education, Kyoto 612

When the band-gap energy  $E_g$  is smaller than the energy difference  $E_{vc}$  between the tops of the valence band and the outermost-core band, the Auger process resulting in valence electron excitation is a dominant decay channel of core holes. On the other hand, if  $E_g > E_{vc}$ , a core hole decays primarily through the radiative recombination with a valence electron, leading to Auger-free luminescence (AFL). CsI belongs to the former case, and CsCl to the latter case. Therefore, it is likely that introduction of even small amounts of  $\text{I}^-$  ions into CsCl quenches the AFL of pure CsCl, owing to the competition between luminescence process and Auger process. This situation is schematically depicted in Fig. 1.

Figure 2(a) shows the luminescence spectrum of undoped CsCl measured at RT under core-level excitation with 21.4-eV photons. Two emission bands

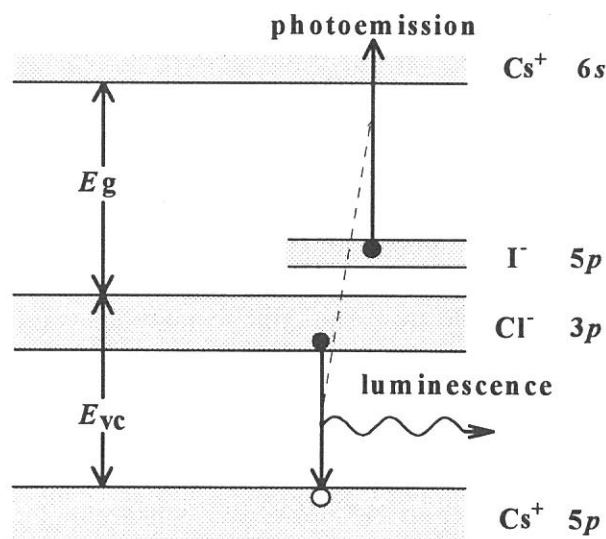


Fig. 1. Schematic energy-level diagram of  $\text{CsCl}_{1-x}\text{I}_x$  system.

peaking at 4.6 and 5.2 eV are the AFL between the  $\text{Cl}^- 3p$  valence band and the  $\text{Cs}^+ 5p$  core band in  $\text{CsCl}$ . In the mixture, two additional bands take place under photo-excitation of the absorption band due to  $\Gamma^-$  ions; the 3.9-eV emission is ascribed to  $\Gamma^-$  monomer and the 4.8-eV emission to  $\Gamma^-$  dimer. Figure 2(b) shows the luminescence spectrum of  $\text{CsCl}_{1-x}\text{I}_x$  ( $x=0.002$ ) excited with 21.4-eV photons at RT. The spectrum is decomposed into the AFL bands and the monomer band, as shown by solid curves. In this figure, excitation spectra for the monomer and dimer bands are also represented by broken and dotted curves, respectively. It is emphasized that the high-energy tail of the AFL band overlaps slightly with the low-energy region of the  $\Gamma^-$ -impurity absorption.

The decay behaviors of the AFL in  $\text{CsCl}_{1-x}\text{I}_x$  crystals with different concentration  $x$  were examined under the single-bunch operation of synchrotron radiation at 21.4 eV. Typical examples are depicted in Fig. 3. It is clearly seen that the decay time decreases from 1.3 to 0.95 ns when  $x$  increases from 0 to 0.002. This result is to be expected from Fig. 1.

The obtained results were complicated in heavily doped crystals, which suggests the need for further experiments.

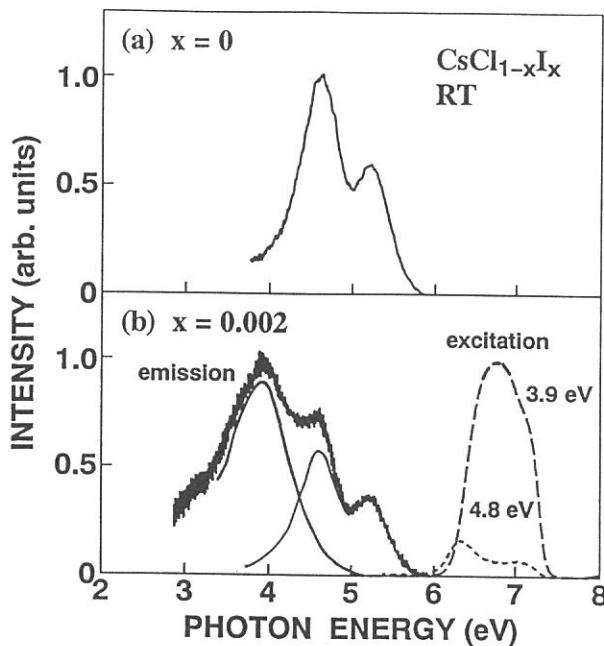


Fig. 2. Luminescence and excitation spectra of  $\text{CsCl}_{1-x}\text{I}_x$ ; (a)  $x=0$  and (b)  $x=0.002$ .

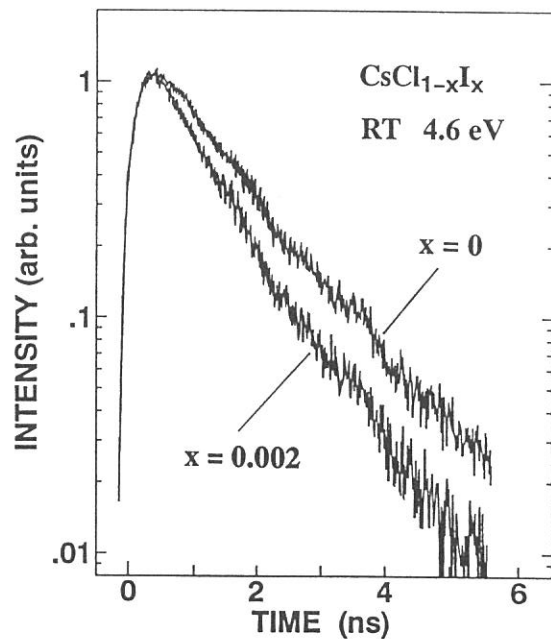


Fig. 3. Decay profiles of the AFL in  $\text{CsCl}_{1-x}\text{I}_x$  ( $x=0$  and 0.002).



## Recombination Luminescence from Self-Trapped Excitons in BaFCl

Akimasa OHNISHI \*, Ken-ichi KAN'NO, Yasuo IWABUCHI<sup>A</sup> and Nobufumi MORI<sup>A</sup>

*Department of physics, Kyoto University, Kyoto 606*

<sup>A</sup> *Fuji Photo Film Co., Ltd., Miyanodai, Kaisei-machi, Kanagawa 258*

Barium-fluoro-halides (BaFX, X=Cl, Br, I) are known as important host materials for application to photo-stimulated luminescence phosphors<sup>1)</sup>. In these materials, there exists the possibility for hole self-trapping in a variety of different kinds of  $V_k$  centers, i.e.  $X_2^-$  in-plane,  $X_2^-$  out-of-plane,  $F_2^-$  and  $(FX)^-$ . This would also cause the possibility for the number of self-trapped excitons (STE). We previously reported that only the  $Br_2^-$  out-of-plane is responsible for intrinsic luminescence in BaFBr<sup>2)</sup>. In the present study, recombination luminescence from BaFCl, in which a hole self-traps as out-of-plane  $V_k(Cl_2^-)$ <sup>3)</sup>, has been investigated under vacuum ultra-violet excitation at BL1B of UVSOR.

Figure 1(a) shows emission spectra obtained at 11K (solid curve) and 70K (broken curve) under band-to-band excitation with 10.3eV light. Two emission bands are observed at 5.5 and 3.4eV at low temperatures. Figure 1(b) shows excitation spectra for the 5.5eV (solid curve, 11K) and 3.4eV band (broken curve, 70K), along with positions of halogen doublet due to  $Cl^-$  spin-orbit splitting (arrows at 8.6 and 8.7eV). Both emission bands show high excitation yield in the intrinsic absorption range above 8.6eV. As for the 3.4eV band, however, intensive excitation structures are observed also in the lower energy side of the absorption edge.

In Fig. 2 is shown the temperature dependence of emission intensities at 5.5eV (●) and 3.4eV(▲) measured under excitation with 10.3eV light. The 5.5eV band quenches in the range of 20~60K, where emission intensity of the 3.4eV band increases. Luminescence decay measurements under single bunch operation made clear that both the 5.5eV and 3.4eV bands are of phosphorescence with a lifetime longer than 1  $\mu$  s.

We have reported that the intrinsic luminescence (5.1eV) in BaFBr originates from STE of on-center type<sup>2)</sup>. The 5.5eV band in BaFCl, which is most likely of intrinsic

---

\* *Present address ; Department of physics, Yamagata University, Yamagata 990*

luminescence, has a similar characteristic to that of the 5.1eV band in BaFBr. We suppose that the STE in BaFCl is also of on-center type. On the other hand, the 3.4eV band is efficiently excited in the lower energy side than the fundamental absorption, and is still observed at temperatures higher than 115K, where  $V_k(\text{Cl}_2^-)$  centers become unstable<sup>3)</sup>. This suggests that the 3.4eV band may come from perturbed STEs attached by impurity ions or point defects.

## References

- 1) M. Sonoda, M. Takano, J. Miyahara and H. Kato ; *Radiology*, **148** (1983) 833
- 2) A. Ohnishi, K. Kan'no, Y. Iwabushi and N. Mori ; *Nucl. Instr. and Meth. in Phys. Res. B* **91** (1994) 210
- 3) M. Yuste, L. Tarel and M. Rahmani ; *Solid State Commun.* **17** (1975) 1435

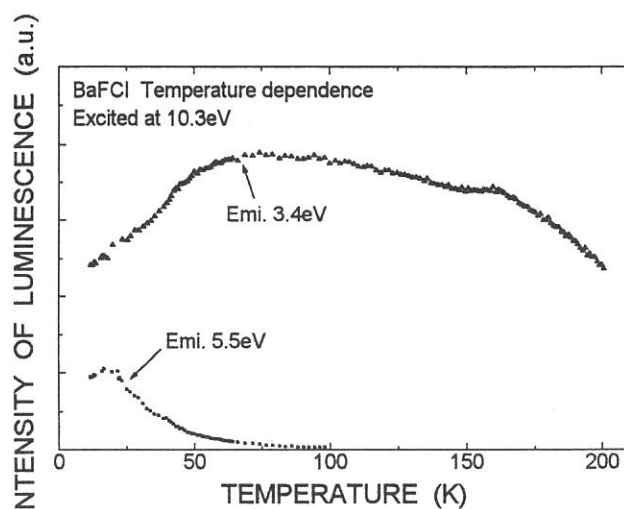
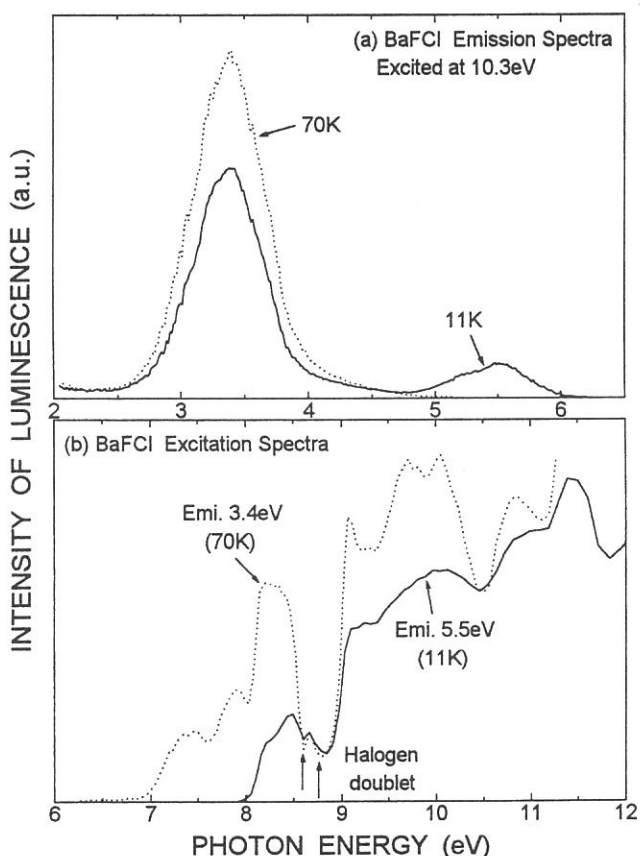


Fig. 1 (left side) (a) Emission spectra at 11K and 70K under excitation at 10.3eV. (b) Excitation spectra for bands at 5.5eV (11K) and 3.4eV (70K).

Fig. 2 (upper side) Temperature dependence of emission intensities at 5.5eV and 3.4 eV under excitation at 10.3eV.



## A Fast Decay Component of the BG-Emission in KCl:I

Masahiro ABE\* , Tamao MATSUMOTO and Ken-ichi KAN'NO

*Department of Physics, Kyoto University, Kyoto 606, Japan*

Photo-excitation into the absorption bands due to  $I^-$  monomers in KCl:I gives rise to several emission bands. Two bands located at 2.60eV (BG-emission) and at 5.88eV (NE-emission) appear at temperatures below 20K, and there is a thermally-activated process from the NE-state to the BG-state.<sup>1</sup> While the NE-emission disappears above 20K, the BG-emission still remains up to temperatures around 230K. The BG-emission has been attributed to radiative decay from the relaxed excited state of hetero-nuclear excitons of two-center type;  $[(ClI)^- + e]$ . On the other hand, the NE-emission has been attributed to radiative decay from the relaxed excited state of one-center type, in which the exciton is localized mainly on the central site of a substituted  $I^-$  ion with small lattice relaxation. In the present work, we have measured the temperature dependence of intensities and lifetimes of the BG-emission under single-bunch operation of UVSOR. A sample crystal was cleaved from the KCl:I ingot which contained  $3 \times 10^{-3}$  mole fraction of  $I^-$  ions.

Decay curves of the BG-emission were measured at temperatures above 30K using the time-correlated single photon counting technique. The excitation photon energy was 6.73eV which is located in the lowest absorption band due to  $I^-$  monomer. Figure 1 shows decay curves at temperatures between 30 and 230K in a linear scale. One can see slow and fast components. The slow component, shown by shade, is major at low temperatures and decreases with increasing temperature. On the other hand, the fast decay component begins to appear around 70K, and it still remains at higher temperatures around 230K.

The lifetime of the fast decay component versus the reciprocal temperature is shown in Fig. 2. It starts to decrease around 100K. The initial intensity of the fast decay component is also plotted. It increases with temperatures above 70K. A good agreement of the calculated line with the data points could be obtained, when we assumed a thermally-activated process: The activation energy was found to be about 30 meV.

It is natural to suppose that fast and slow decay components of the BG-emission arise from the singlet and triplet manifolds of the lowest orbital state of  $[(ClI)^- + e]$ . In accordance with the existence of the thermally-activated process from the NE-state to the BG-state, the above-mentioned activation energy may correspond to the height of a

---

\* On leave from OLYMPUS OPTICAL CO.,LTD., Tokyo 192, Japan

potential barrier on the singlet adiabatic potential energy surface. However, further investigation is necessary to clarify the mechanism to explain this fast component.

### REFERENCES

1. K. Kan'no, M. Itoh and Y. Nakai; J.Phys.Soc.Jpn., 47, pp. 915-921, 1979.

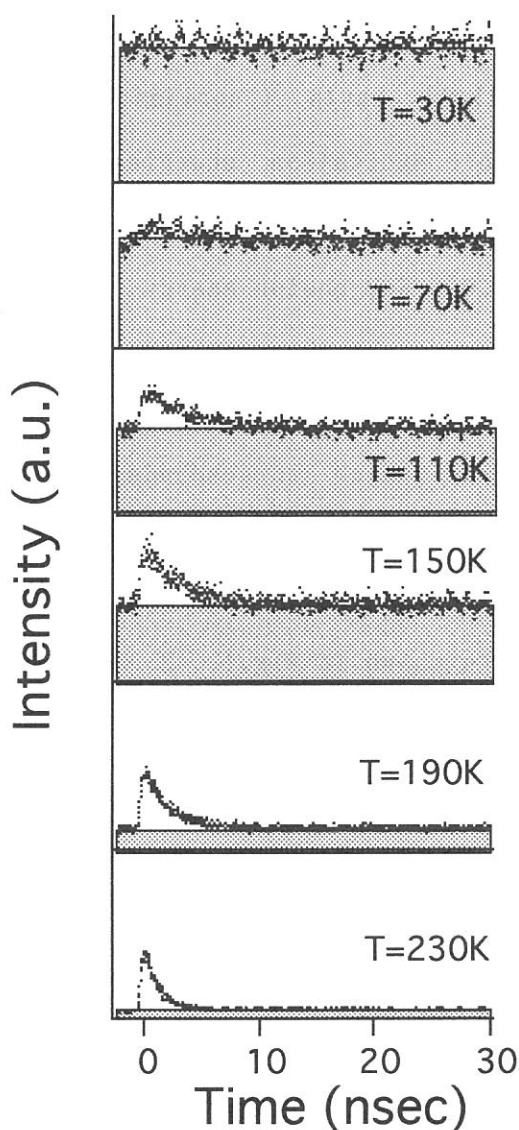


Fig.1 Decay curves of the BG-emission in KCl:I at temperatures between 30 and 230K. The excitation photon energy was 6.73eV. The emission was detected at 460nm.

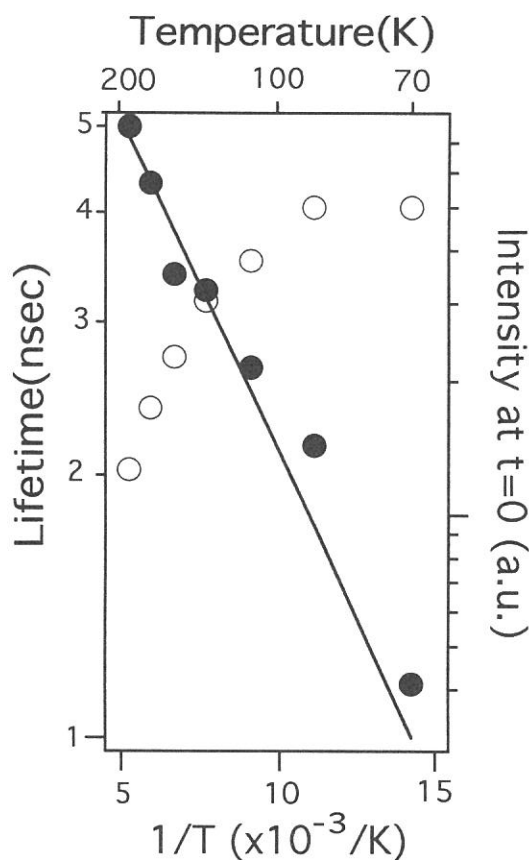


Fig.2 Lifetime (○) and initial intensity (●) of the fast decay component as a function of temperature. A solid line was obtained by assuming a thermally-activated process with the activation energy of about 30meV.

## Photo-luminescence in Alkali Earth Fluorides

A. EJIRI, A. HATANO<sup>A</sup>, and K. NAKAGAWA<sup>B</sup>

Faculty of Education, University of Ryukyus, Senbaru 1, Nishihara, Okinawa 903-01

A:Department of Pure and Applied Sciences, University of Tokyo, Meguroku Tokyo 153

B:Faculty of Human Development, Kobe University, Tsurukabuto, Nada-ku, Kobe 657

Photo-luminescence spectra in alkali earth fluorides;

CaF<sub>2</sub>, SrF<sub>2</sub>, and BaF<sub>2</sub> excited at the core excitation energies (32eV, 25eV, and 20eV, respectively) and at the valence excitation energy (10eV) were investigated in the 2.0-6.5eV photon energy region at the BL-1B. The luminescence was measured at the room temperature and 23K by the use of a Spex monochromator with a slit width of 1.0mm for the both of entrance and exit slits which corresponds to a wavelength of approximately 5nm. The results of apparent luminescence spectra excited at the core excitation energies at the room temperature and 23K for each material are shown in Fig.1, 2, and 3, respectively.

It is well known that BaF<sub>2</sub> has a character emitting the Auger free luminescence (AFL) at 5.7eV<sup>1)</sup>, and that AFL should become weak below 150K<sup>2)</sup>. Whereas a broad band around 4eV which is considered to be due to STE (self trapped exciton) abruptly increases its intensity for the cooling.

In SrF<sub>2</sub>, luminescence bands are appeared at 3.7 and 4.4eV, but weak still at 23K. In CaF<sub>2</sub>, luminescence bands (3.5eV and 4.5eV) are appeared and weak similarly with SrF<sub>2</sub>. In these three materials, for the valence excitation (10eV), a very strong luminescence was observed (not shown) at around 4.5eV, however, for core excitation, luminescence yields are very weak in CaF<sub>2</sub> and SrF<sub>2</sub>. These phenomena are likely due to the effect of Auger process<sup>3)</sup> which produces two valence holes and two conduction electrons in the final state.

This final state seems to make some effects different from the final state of the valence excitation where is one valence hole and one conduction electron.

References:

- 1) Yu. M. Aleksandrov, V. N. Makhov, P. A. Rodnyi, T. I. Syerischikova and M. N. Yakimenko; Sov. Phys. Solid State 26 (1984) 1734.
- 2) C. shi, Y. Dong, and X. Ln; Vacuum Ultraviolet Rad. Phys. World Scientific (1993) 501.
- 3) A. Ejiri, S. Kubota, A. Hatano, K. Nakagawa, and K. Yahagi; Act. Rep. SRL(ISSP) 1993, Tokyo, (1994) 34.

Fig.1. Photo-luminescence intensity in  $\text{CaF}_2$  excited at 32eV.

o: RT, ●: 23K

Fig.2. Photo-luminescence intensity in  $\text{SrF}_2$  excited at 25eV.

o: RT, ●: 23K

Fig.3. Photo-luminescence intensity in  $\text{BaF}_2$  excited at 20eV.

o: RT, ●: 23K

Fig. 1

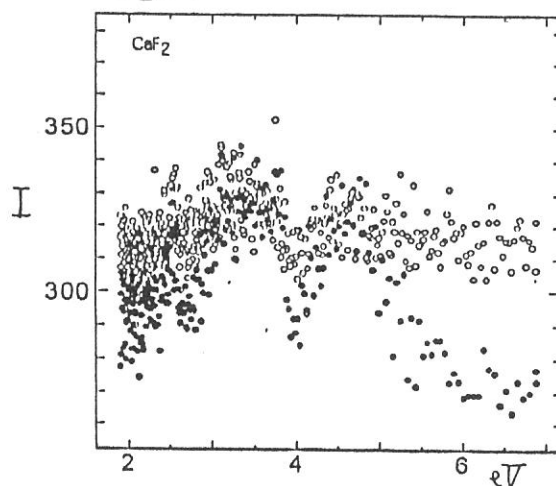


Fig. 2

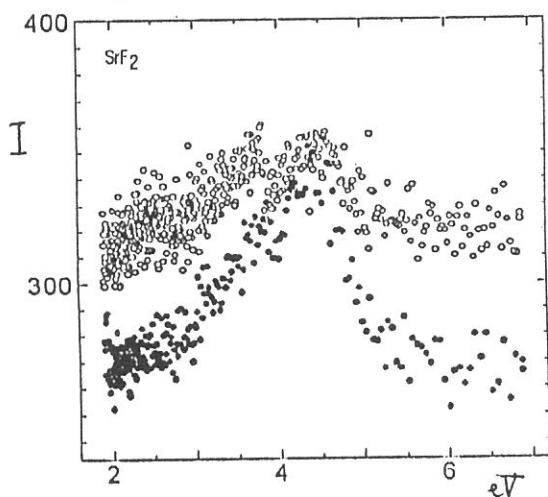
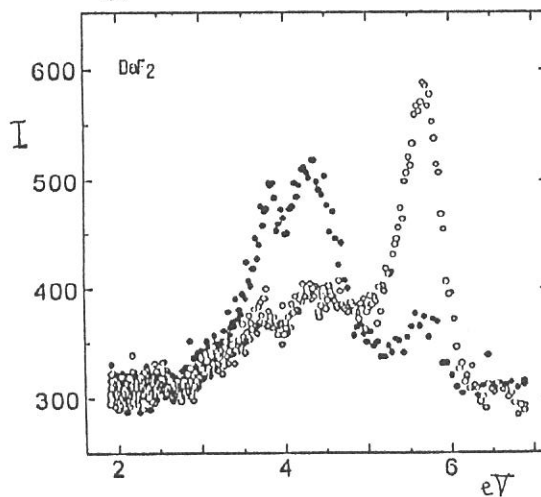


Fig. 3



## Relaxation Dynamics of Free Excitons in Alkali Iodides

Tetsusuke HAYASHI, Toru TSUJIBAYASHI\*, and Masayuki WATANABE

*Faculty of Integrated Human Studies, Kyoto University, Kyoto 606-01*

*\*Department of Physics, Osaka Dental University, Makino, Hirakata, Osaka 573*

Luminescence of self-trapped excitons (STE) in many alkali halides consists of two emission bands,  $\sigma$  and  $\pi$ [1]. The  $\sigma$  band is known to arise mainly from the singlet state of an on-center type STE, and the  $\pi$  band from the triplet state of an off-center type one. In alkali iodide crystals free exciton (FE) luminescence is observed in addition to the STE luminescence. The main line of the FE luminescence in KI and RbI is attributed to radiative decay of spin-triplet paraexcitons ( $J=2$ ) accumulated via phonon scattering from orthoexciton ( $J=1$ ) state. It has been clarified recently that the STE state responsible for the  $\sigma$  emission is connected to the orthoexciton state of FE and that for the  $\pi$  emission to the paraexciton state as far as excitation is made in the  $n=1$  exciton band[2]. However, the intensity of the  $\sigma$  band under the  $n=1$  exciton is extremely weak. The fact was referred to as " $n=1$  anomaly" by Hayashi *et al.*[3] Two explanations might be possible on this effect; (1) nonradiative annihilation rate of orthoexcitons is much larger than that of paraexcitons, or (2) orthoexcitons are scattered efficiently into the paraexciton state. In order to clarify this point, accurate measurement of the luminescence efficiency with various excitation photon-energies may be useful.

Measurements were performed with BL1B of UVSOR. A sample was kept at 72 K in order to reduce impurity luminescence caused by exciton diffusion at lower temperatures. The sample was irradiated with light from a Seya-Namioka type vacuum monochromator in an angle of  $58^\circ$  from the normal of the sample surface. The band-pass of the excitation light was about 8 Å. The luminescence from the sample was observed in an angle of  $13^\circ$ , and was dispersed by a single-path monochromator (Spex 270M) attached with a CCD camera cooled by liquid nitrogen (Princeton Instruments). Reflectivity at the sample surface was measured with a photomultiplier equipped inside the sample chamber.

Figure 1(a) shows the reflection spectrum of KI. A peak due to the  $n=1$  exciton and a small hump due to the  $n=2$  excitons are observed at 5.85 eV and 6.15 eV, respectively. Excitation spectra of  $\sigma$  and  $\pi$  emission bands are shown in Fig. 1(b) by crosses and closed squares. The sum of the intensities of the two bands is also plotted by the solid line. The intensity of  $\sigma$  band relative to that of  $\pi$  band (S/T) is depicted in Fig. 1(c). S/T is almost constant under excitation with higher energies. It decreases with decrease in the excitation energy and reaches a minimum around 6.15 eV. Then it increases again toward 5.85 eV.

We can see that the reflectivity loss is very small in the energy range between 6.6 eV and 6.0 eV, and in this range the total luminescence intensity is nearly kept constant. On the other hand, the intensity of the  $\sigma$  band decreases steeply at the edge of the  $n=2$  exciton energy, at 6.15

eV ( $n=1$  anomaly). The decrease is compensated by the increase in the intensity of  $\pi$  band. The fact supports the explanation (2). That is,  $n=1$  anomaly is due to a large scattering rate of orthoexcitons into paraexcitons.

We previously reported that the decay time of FE luminescence in RbI is 1.2 ns at 15 K[4]. Further investigation of the temporal behavior of the FE luminescence has clarified that the luminescence has a component with a short decay time less than 0.4 ns. Figure 2 shows the decay profile of the luminescence under excitation with 6.05 eV by solid circles. The solid curve represents the component with the decay time of 1.2 ns. The intensity of the fast component depends on the excitation photon-energy and temperature, suggesting the dynamical behavior of exciton polaritons near the crystal surface. Efforts of precise measurements are in progress.

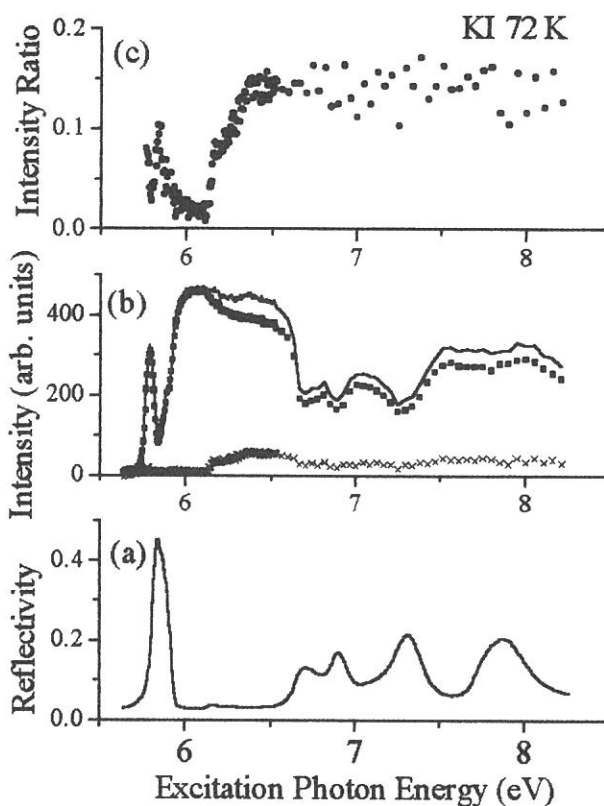


Fig. 1

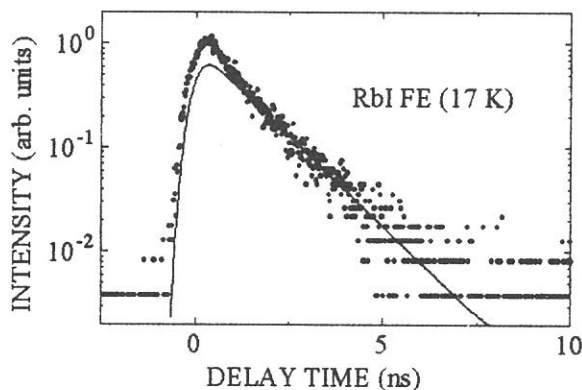


Fig. 2

## REFERENCES

- [1] K. S. Song and R. T. Williams, *Self-trapped Excitons* (Springer, Berlin, 1993), and references therein.
- [2] T. Tsujibayashi-Kishigami, *J. Phys. Soc. Jpn.* **63** (1994) 335.
- [3] T. Hayashi, T. Yanase, T. Matsumoto, K. Kan'no, K. Toyoda, and Y. Nakai, *J. Phys. Soc. Jpn.* **61** (1992) 1098.
- [4] T. Hayashi *et al.* UVSOR Activity Report 1992. T. Tsujibayashi *et al.* *J. Lumines.* **58** (1994) 368.



# Silicon precipitation in surface layers of amorphous Si<sub>3</sub>N<sub>4</sub> films with ArF excimer laser irradiation

Kazuo Nakamae, Kou Kurosawa<sup>1</sup> and Ryoichi Sonouchi<sup>1</sup>

Department of Physics and Electronics, University of Osaka Prefecture, Sakai, Osaka 593

<sup>1</sup>Photonics Application Laboratory, University of Miyazaki, Miyazaki 889-21

High energy photons above 5eV have attracted much attention, because of their feasibility for opening doors towards new phenomena in material processings. In fact, we have recently shown that VUV photons have an ability to break bonds between Si-O in quartz and further to lead oxygen desorption and silicon precipitation. The phenomenon requires photons having high energy enough to induce the direct band-to-band transition (9eV). The similar phenomenon has been confirmed to occur in Si<sub>3</sub>N<sub>4</sub> film with the band gap energy of 5eV. The silicon precipitation on the surface of Si<sub>3</sub>N<sub>4</sub> film has been observed mainly with X-ray photoemission (XPS) and Raman scattering spectroscopy<sup>1)</sup>. It seems to us that the photochemical reactions proceed within several tens to hundred nm beneath the surface. With these techniques, it is easy to check the presence of silicon but difficult to measure the amount and the depth profile. Analyzing the reflectivity and/or transmission spectra, we have tried to estimate the amount and depth profile of silicon in Si<sub>3</sub>N<sub>4</sub> films after the ArF excimer laser irradiation.

Si<sub>3</sub>N<sub>4</sub> films are fabricated from SiH<sub>4</sub> and NH<sub>3</sub> gases on silicon wafers using a plasma enhanced chemical vapor deposition (CVD) technique. The thickness is 900nm. The laser-irradiation experiments are carried out in vacuum at room temperature with an ArF excimer laser whose photon energy of 6.4eV exceeds the band-gap energy. The laser beam is focused with a lens to provide a pulse having an energy of 0.8J/cm<sup>2</sup>. Reflectivity is measured with the BL-1B beam line of UVSOR at IMS in the spectral range from 50 to 6000 Å.

The reflectivity spectra are reproduced in Fig.1 for an original film of silicon nitride, in Fig.2 for a film exposed with the laser-pulse, and in Fig.3 for a film exposed with the 10 laser-pulses. In these figures, the reflectivity spectra for a silicon single crystal are plotted together with the calculated ones for Si<sub>3</sub>N<sub>4</sub> film based upon the optical constants in Palik's handbook<sup>2)</sup>.

In Fig.1 the spectrum from an original surface of the film shows peaks around 800 and 2000 Å, whereas the calculated one has a peak around 1000 Å. In the measured one, we can see an oscillatory behavior above 3000 Å, which is due to an interference effect of the film. The laser-irradiation induces the degradation of the 800 Å peak and also of the oscillation. Such tendency is enhanced with the multiple shots of the laser pulses as shown in Fig.3. The spectra in Figs. 2 and 3 have peaks around 3000 Å and are similar to the spectra of silicon single crystal, and furthermore the amplitudes are found to decrease.

We estimate the thickness of silicon layer based upon the oscillation due to the interference effect. The silicon layer induced with the 10 laser-shots is seen to be six times thicker than that with the 1 laser shot.

We can see at least qualitatively that the ArF laser irradiation induces the silicon precipitation in the surface of silicon nitride films. The next step for us is to estimate quantitatively the amount of silicon and further the depth profile based upon the reflectivity spectra.

1) K.Nakamae et al.: Nucl. Instrum. Meth. **B91**(1994) 659.

2) E.D.Palik : *Handbook of Optical Constants of Solids*, Academic Press

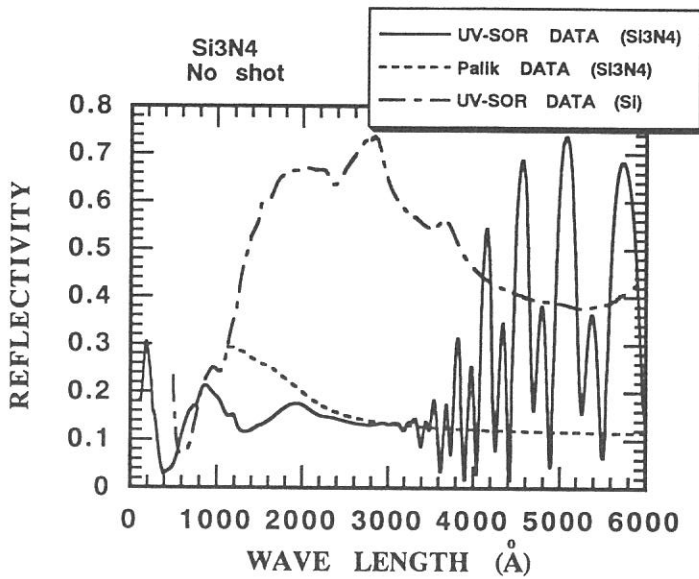


Fig.1 Reflectivity spectra for a silicon nitride film (solid line) and silicon single crystal (dashed line) together with the calculated one for silicon nitride (dotted line).

Fig. 2 Reflectivity spectra for a silicon nitride film after irradiation of one pulse of an ArF excimer laser (solid line) and silicon single crystal (dashed line) together with the calculated one for silicon nitride (dotted line).

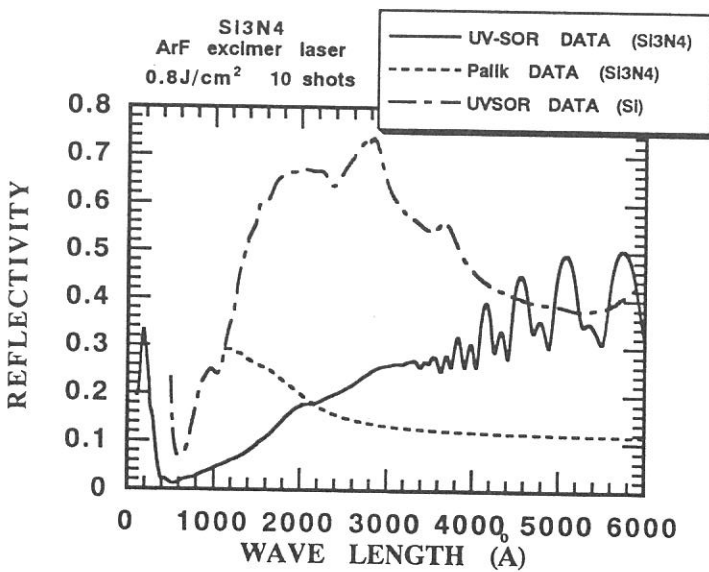
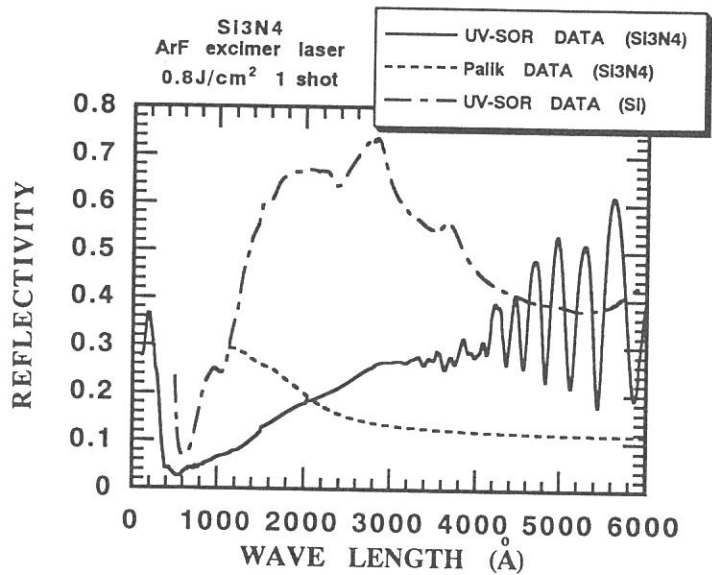


Fig. 3 Reflectivity spectra for a silicon nitride film after irradiation of ten pulses of an ArF excimer laser (solid line) and silicon single crystal (dashed line) together with the calculated one for silicon nitride (dotted line).



Photochemistry of Cyanogen Bromide  
in the 40 - 120 nm Region

Kazuhiro Kanda, Takashi Nagata<sup>1</sup>, Mitsuhiko Kono<sup>2</sup>,  
Atsunari Hiraya<sup>2</sup> and Kosuke Shobatake<sup>3</sup>

*Department of Fundamental Science, College of Science and  
Engineering, Iwaki Meisei University, Iwaki 970*

<sup>1</sup> *Department of Chemistry, College of Arts and Sciences,  
The University of Tokyo, Komaba, Meguro-ku 153*

<sup>2</sup> *Institute for Molecular Science, Myodaiji, Okazaki 444*

<sup>3</sup> *Department of Materials Chemistry, School of Engineering,  
Nagoya University, Chikusa-ku, Nagoya 464-01*

Recently we have reported on the photochemistry of cyanogen bromide, BrCN, in the 105-155 nm region.<sup>1</sup> For the wavelength range shorter than 105 nm, however, little has been known about the high-lying electronic states of BrCN because of the lack of a radiation source available for the photoabsorption measurements. In the present study, by taking advantage of the window-less experimental configuration at UVSOR, absolute cross sections for the formation of CN(B) are determined in the wavelength range 40-120 nm. A gas filter, instead of a LiF window, was mounted in front of the absorption cell in the shorter wavelengths below the LiF cut-off.

Figure 1 shows the absorption spectrum of BrCN in the 90-120 nm region. A broad, structureless continuum was observed below 91 nm. The ionization potentials (IPs) of BrCN are reported to be 11.88 eV (104.4 nm) and 12.07 eV (102.7 nm) for the production of BrCN<sup>+</sup> in the <sup>2</sup>Π<sub>3/2</sub> and <sup>2</sup>Π<sub>1/2</sub> manifolds, respectively. The second IP associated with the <sup>2</sup>Σ<sup>+</sup> ionic state is located at 13.58 eV (91.3 nm). The Rydberg series converging to these first and second IPs are identified in the absorption spectrum. As shown in

Fig. 2, the quantum yield for the CN(B) production was observed to increase with the excitation energy from  $\sim 0.05$  at 120 nm up to  $\sim 0.1$  at 105 nm. The sudden drop observed around 104 nm is ascribed to the opening of the ionization channel.

#### Reference

- [1] K. Kanda, S. Katsumata, T. Kondow, K. Kuchitsu, A. Hiraya and K. Shobatake, Chem. Phys. 175 (1993) 399.

Figure 1.  
The absorption spectrum of BrCN. The cross sections were measured at a vapor pressure of 20 mTorr.

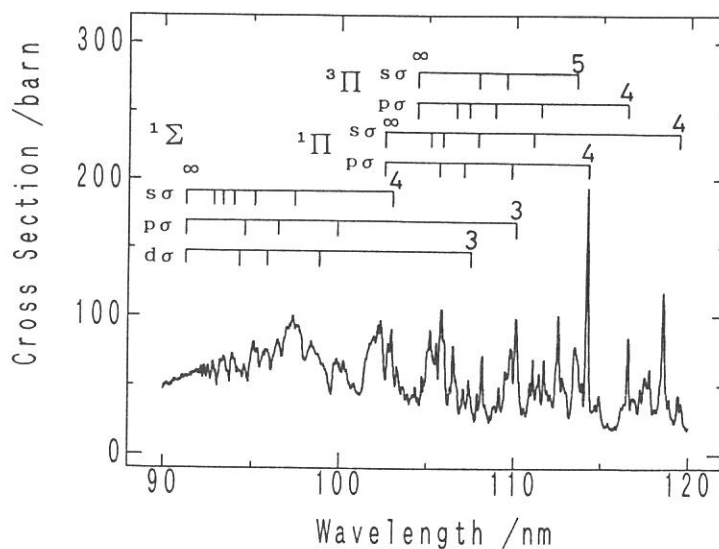
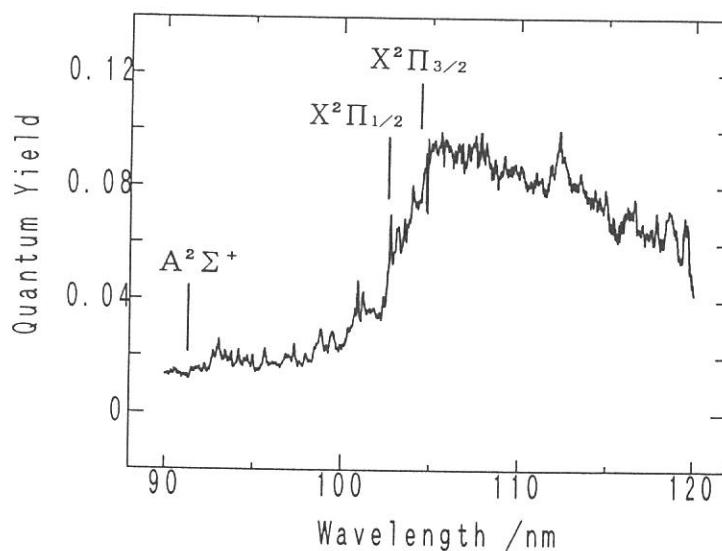


Figure 2.  
The quantum yield for the CN(B) formation in the photodissociation of BrCN.



## Photoabsorption and Fluorescence Cross Sections of $\text{SiCl}_4$ in the 40-120 nm Region

Toshio IBUKI,<sup>1</sup> Mitsuhiko KONO,<sup>2</sup> and Kosuke SHOBATAKE<sup>3</sup>

<sup>1</sup>*Kyoto University of Education, Fukakusa, Fushimi-ku, Kyoto 612*

<sup>2</sup>*Department of Functional Molecular Science,*

*The Graduate University of Advanced Studies, Myodaiji, Okazaki 444*

<sup>3</sup>*Institute for Molecular Science, Myodaiji, Okazaki 444 and Department of Material Chemistry, School of Engineering, Nagoya University, Chikusa-ku, Nagoya 464-01*

Photoabsorption and fluorescence cross sections of  $\text{SiCl}_4$  have been measured in the region 40-120 nm using a newly developed argon gas filter. At photon energies longer than 80 nm, a considerably high intensity of the higher order light from the 1-m Seya VUV monochromator installed at the BL2A station of UVSOR prevented us from obtaining reliable photoabsorption and fluorescence excitation spectra in the wavelength region below LiF cutoff of 105 nm. In the present project we have developed a gas filter filled with argon in a long channel with a cross section of 2.5 mm  $\times$  5.0 mm and 170 mm long, which was placed before monochromatized SR enters a windowless sample cell. The argon gas effusing out from the filter placed in a vacuum chamber was evacuated by a 5000 l/s diffusion pump.

Figure 1 shows the transmitted light intensities ( $I_0$ ) with and without Ar gas, both of which are normalized to the ring current. These spectra indicate that monochromatized SR is practically usable at exciting wavelengths,  $\lambda_{\text{ex}}$ , longer than 40 nm and the higher order light in the  $\lambda_{\text{ex}} \geq 80$  nm region can be removed since the observed  $I_0$  curves are very close at  $\lambda_{\text{ex}} \approx 80$  nm. The difference in the transmitted light intensities with Ar at 0.3 Torr and without an Ar filter gas for  $\lambda_{\text{ex}} \geq 80$  nm can be considered to be due to unfiltered higher order light. Some Rydberg transition bands are observed.

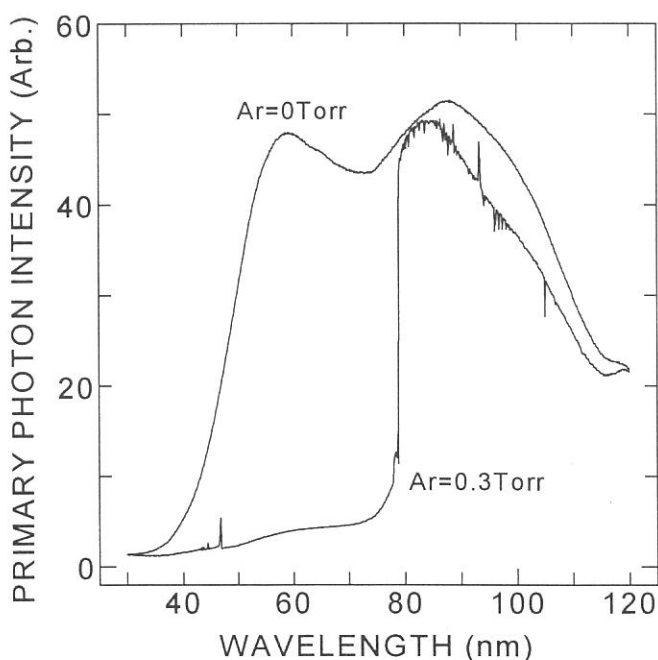


Fig. 1. Transmitted primary photon intensities with and without Ar gas filter

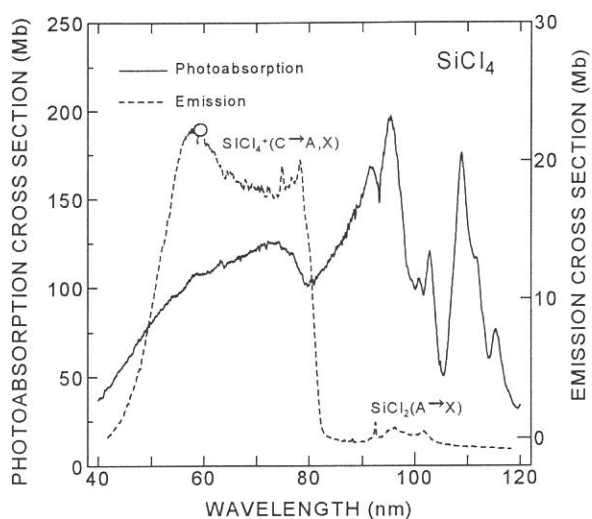


Fig. 2. Photoabsorption and fluorescence cross sections of  $\text{SiCl}_4$ .  $\circ$  indicates the absolute fluorescence cross section determined by use of He I resonance line (58.4 nm).

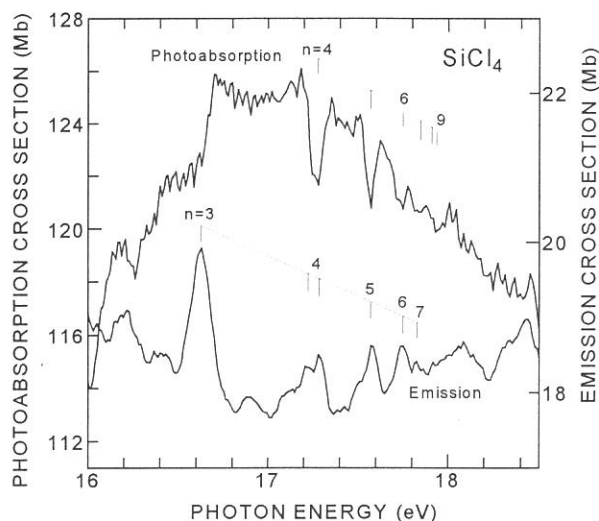


Fig. 3. Rydberg transitions observed in the photoabsorption and fluorescence excitation spectra.

Preliminary results of photoabsorption and fluorescence cross sections of  $\text{SiCl}_4$  measured using the Ar gas filter are given in figure 2 in the wavelength region  $\lambda_{\text{ex}}=40\text{-}120$  nm. The fluorescence has been assigned as  $\tilde{C}^2T_2 \rightarrow \tilde{X}^2T_1$  and  $\tilde{C}^2T_2 \rightarrow \tilde{A}^2T_2$  transitions of  $\text{SiCl}_4^+$  cation.<sup>1)</sup> The total fluorescence cross section has been independently determined as  $22.4 \pm 3.6$  Mb by using He I resonance line (58.4 nm) and it is marked with an open circle in figure 2.

Figure 3 shows the Rydberg series which have been assigned as  $np \leftarrow 7a_1$  converging to the ionic  $\tilde{D}^2A_1$  state,<sup>1,2)</sup> are observed both in the photoabsorption and fluorescence excitation spectra. This series observed in photoabsorption spectrum shows the windowlike Fano-profile while the emission spectrum exhibits convex peaks.

## References

- 1) I. R. Lambert, S. M. Mason, and R. P. Tuckett, *J. Chem. Phys.* **89**, 2675 (1988).
- 2) K. Kameta, M. Ukai, T. Numasawa, N. Terazawa, Y. Chikahira, N. Kouchi, Y. Hatano, and K. Tanaka, *J. Chem. Phys.* **99**, 2489 (1993).

Absorption and Fluorescence Studies of  $\text{CCl}_3\text{CN}$  in the  
Vacuum Ultraviolet Region.

Kiyohiko TABAYASHI, Yohko SHIMOMURA, Munenori AKAO, Koh SAITO,  
Mitsuhiko KONO\*, Haruhiko OHASHI\*, and Kosuke SHOBATAKE\*

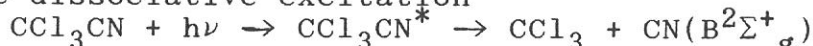
*Department of Chemistry, Faculty of Science, Hiroshima University,  
Kagamiyama, Higashi-Hiroshima 724*

*\*Department of Functional Molecular Science,  
The Graduate University for Advanced Studies,  
and Institute for Molecular Science,  
Myodaiji, Okazaki 444*

Cross sections for absorption and fluorescence excitation spectra of  $\text{CCl}_3\text{CN}$  have been first measured using synchrotron radiation source over the spectral range 105 ~ 200 nm.

Fig.1 shows the spectra observed in the 105 ~ 150 nm region with resolution of 0.3 nm. Absorption bands appeared are relatively broad and the strongest peak cross section at 129 nm has ~ 120 Mb ( $\text{Mb} = 10^{-18} \text{ cm}^2$ ), which is compared with those of usual  $\text{RCN}$  ( $\text{CH}_3\text{CN}$  and  $\text{CF}_3\text{CN}$ ) molecules. In the assignment of VUV bands of  $\text{CCl}_3\text{CN}$ , electronic structure in the ground state was simply checked by ab initio calculation with HF/3-21G basis set. The valence shell configuration of  $\text{CCl}_3\text{CN}$  is represented as  $-(8e)^4(12a_1)^2(9e)^4(10e)^4(2a_2)^2$ . According to population analysis, outermost  $2a_2$  and degenerate  $10e$  MO's represent chlorine lone pairs ( $n_{\text{Cl}}$ ) character, respectively,  $9e$  orbital corresponds to  $\pi_{\text{CN}}$  bond and  $n_{\text{Cl}}$  in nature, and  $12a_1$  is attributed to  $\sigma_{\text{CN}}$  bond character. Details of the ionization potentials (IP) of  $\text{CCl}_3\text{CN}$  have not yet been settled. Lake and Thompson[1] measured photoelectron spectra (PES) of chlorinated acetonitriles, no assignment was given. Here, we tentatively proposed IP assignment for the PES peaks of  $\text{CCl}_3\text{CN}$ , based upon the above the electronic configuration analysis. The observed absorption bands are then interpreted in terms of excitation to Rydberg states. The results of are also indicated in Fig. 1.

Fluorescence dispersed spectrum, recorded with excitation of  $\text{CCl}_3\text{CN}$  at the strongest absorption peak of 129 nm, is shown in Fig. 2. Emission peaks in the 340-460 nm region are identified as  $\Delta v = 0, \pm 1$ , and  $+2$  sequence of  $\text{CN}(\text{B-X})$  transition. A weak and broad  $\text{CN}(\text{A-X})$  band appears in the longer wavelength and extends to IR region, but fluorescence measurement was limited due to low response of PMT (R585) above ~ 600 nm. No other emission bands such as from  $\text{CCl}_n^*$  have been discernible for  $\text{CCl}_3\text{CN}$  excitation. The dissociative excitation



is thus concluded as the predominantly UV fluorescent-step following VUV photo-excitation.

Fluorescence excitation spectrum is also shown by dotted curve in Fig. 1. Here, total fluorescence intensity ( $\lambda_{\text{obs}} = 180 - 650 \text{ nm}$ ) was converted to absolute cross section by comparing it with that of  $\text{CH}_3\text{CN}$  for which fluorescence cross section has been determined. Although absolute cross section is generally lower than 1 Mb,  $\text{CN}(\text{B}^2\Sigma_g^+)$  is found to be formed prominently via  $2a_2 \rightarrow np$  transitions. This is indicative of strong coupling of the excited states with precursor state leading to  $\text{CCl}_3 + \text{CN}(\text{B}^2\Sigma_g^+)$  fragments.

[1] R.F. Lake and H. Thompson, Proc. Roy. Soc. Lond. A317, 187 (1970).

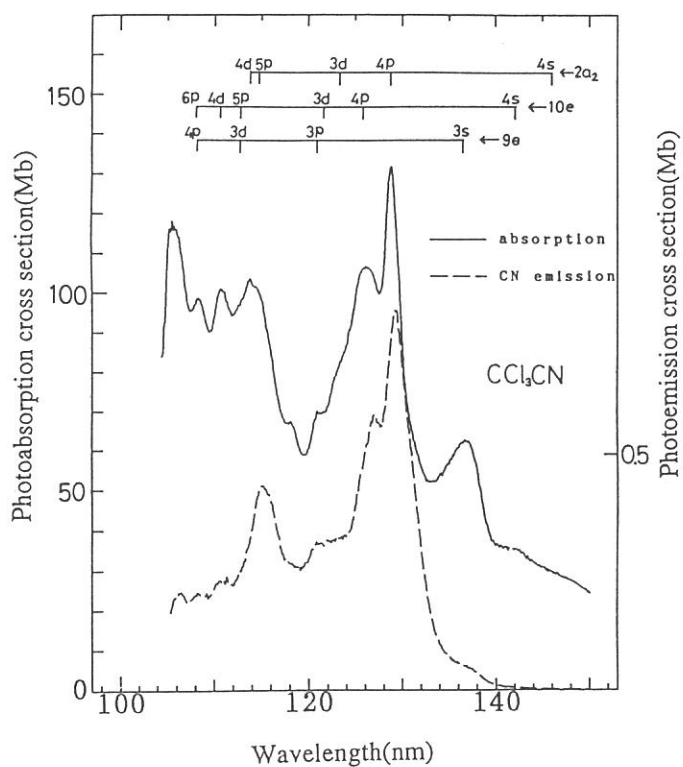


Fig. 1. Absorption and fluorescence excitation cross sections for  $\text{CCl}_3\text{CN}$  in the 105 - 150 nm region. The spectral resolution was 0.3 nm. Sample pressure was 20 mTorr.

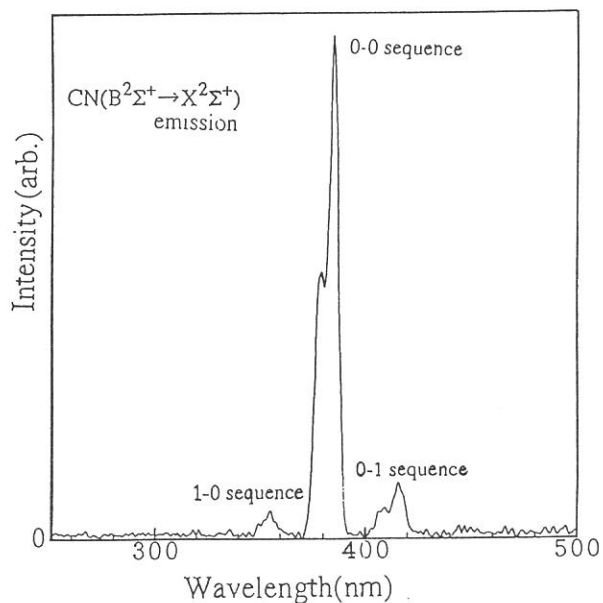


Fig. 2. Dispersed fluorescence observed with excitation of  $\text{CCl}_3\text{CN}$  at  $\lambda_{\text{exct}} = 129.5$  nm with  $\Delta\lambda_{\text{exct}} = 1$  nm. The spectral resolution was about 6 nm. The sample pressure was 30 mTorr.

VUV Absorption and  $CN(B^2\Sigma_g^+)$  Excitation Spectra of  
Chlorinated Acetonitriles.

Munenori AKAO, Kiyohiko TABAYASHI, Yohko SHIMOMURA, Koh SAITO,  
Mitsuhiko KONO\*, Haruhiko OHASHI\*, and Kosuke SHOBATAKE\*

Department of Chemistry, Faculty of Science, Hiroshima University,  
Kagamiyama, Higashi-Hiroshima 724

\*Department of Functional Molecular Science,  
The Graduate University for Advanced Studies,  
and Institute for Molecular Science,  
Myodaiji, Okazaki 444

Previously, we have studied photo-excitation of  $CCl_3CN$  in the VUV energy region, dissociative excitation process  $CCl_3CN + h\nu \rightarrow CCl_3CN^* \rightarrow CCl_3 + CN(A, B)$  has been found to be prominent fluorescent decay channel. It is thus of particular interest to examine substituent effect of chlorine atoms on the excited states and excited state dynamics of chloro-acetonitrile. Here, we report preliminary results on the measurements of absorption and fluorescence excitation spectra for chloro-acetonitriles  $CH_nCl_mCN$ .

The spectroscopic measurements were performed in a gas-cell apparatus constructed at the Beamline BL2A of UVSOR. Figures 1 and 2 show absorption (solid line) and fluorescence excitation (dotted line) spectra of  $CH_2ClCN$  and  $CHCl_2CN$ , observed in the excitation wavelength region of 105 - 160 nm. The absolute scale for the fluorescence cross section was determined by comparing the emission intensities with that of  $CH_3CN$  photo-dissociation. Separate dispersion fluorescence measurements showed that present fluorescence cross sections are largely due to that of  $CN(B^2\Sigma_g^+)$  radical formation. Based upon our MO analysis and PES data for the nitriles, their IP's values are settled and absorption bands have been assigned to excited Rydberg states as indicated in the Figures.

General inspection of excitation cross sections for these nitriles, including trichloro-acetonitrile, reveals as follows. Quantum yield for the  $CN(B)$  formation is found to decrease in the order  $CCl_3CN > CH_2ClCN > CHCl_2CN$ . They are all lower than 0.01. In the case of  $CH_nCl_mCN$ , strong interaction is not found between the excited states and precursor state of  $CN(B)$  formation channel.  $CH_2ClCN$ , for example, has no strong excitation peaks in the region of 125 - 130 nm in spite of similar intense absorption bands ( $n_p \leftarrow n_{C1}$ ) as  $CCl_3CN$ . Lower values of the quantum yield for  $CH_nCl_mCN$  than  $CCl_3CN$  are considered to be due to the opening of new  $HCl$  elimination process as one of the dominant neutral decay channels following the photoexcitation.

Thermochemical data for the chlorinated acetonitriles are not known. Threshold energies of the  $CN(B^2\Sigma_g^+)$  formation were examined to obtain upper limits for the bond dissociation energies  $D_0(R-CN)$ . The results determined are summarized and compared with those of other nitriles in Table I.

Table I.

R-CN	$D_0(R-CN)$	$\Delta H_{f298}^0$
$CH_2ClCN$	$\leq 123.6$	$\geq 8.8$
$CHCl_2CN$	$\leq 127.0$	$\geq 1.1$
$CCl_3CN$	$\leq 129.7$	$\geq 7.9$
$CF_3CN$	110.6	---
$CH_3CN$	122.6	---

\*in Kcal/mole.



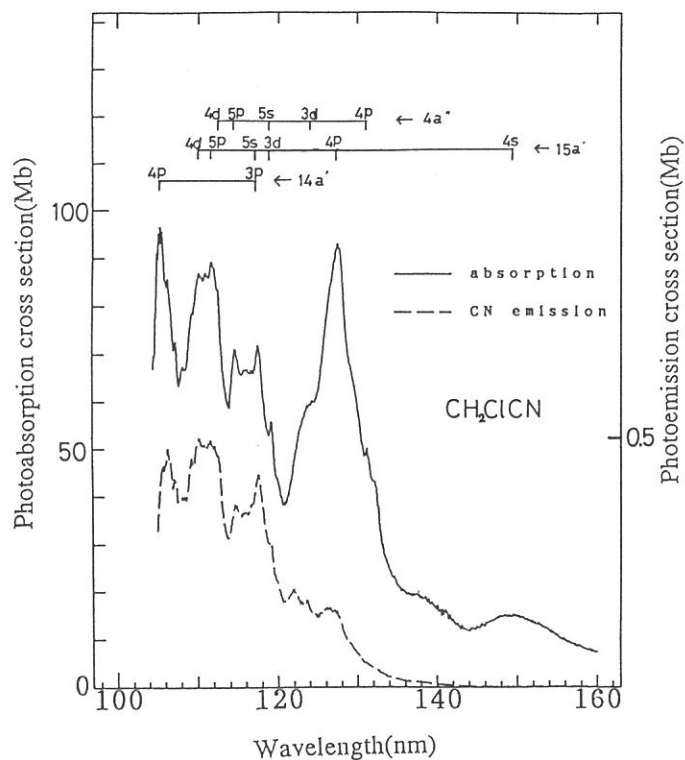


Fig. 1. Absorption and fluorescence excitation cross sections for  $\text{CH}_2\text{ClCN}$  in the 105 - 160 nm region. The spectral resolution was 0.3 nm. Sample pressure was 20 mTorr.

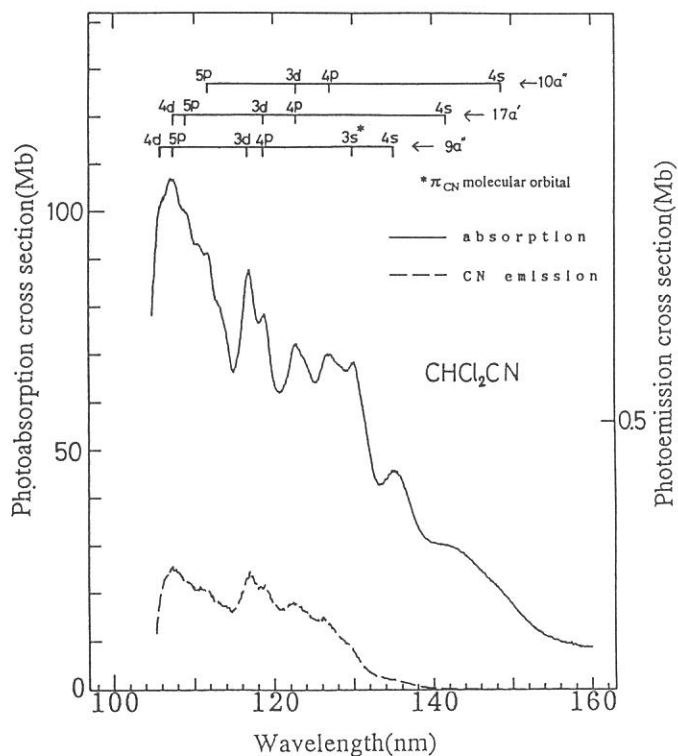


Fig. 2. Absorption and fluorescence excitation cross sections for  $\text{CHCl}_2\text{CN}$  in the 105 - 160 nm region. The spectral resolution was 0.3 nm. Sample pressure was 30 mTorr.

# Photodissociation dynamics of HNCO studied by photofragment fluorescence polarization measurements

Yoshihisa Matsushita, Yasumasa Hikosaka, Mitsuhiro Kono\*,  
Kosuke Shobatake\*, and Takumi Hikida

*Department of Chemistry, Tokyo Institute of Technology, Ohokayama,  
Meguro 152*

*\*Institute for Molecular Science, Myodaiji, Okazaki 444*

It has been known that the photolysis of HNCO forms NH and NCO radicals in various electronic states. In the far VUV photolysis, the emission from both singlet NH ( $c^1\Pi \rightarrow a^1\Delta$ ) and triplet NH ( $A^3\Pi \rightarrow X^3\Sigma$ ) as well as that from NCO ( $A^2\Sigma, B^2\Pi$ ) have been observed. The time-resolved emission intensity measurements of Hikida *et al.*<sup>(1)</sup> have shown that both singlet and triplet NH\* molecules are formed within the duration of the excitation light pulse (~10 ns). They have concluded that both NH\* molecules are formed as primary photoproducts from the excited HNCO molecules, and the spin-forbidden formation of NH ( $A^3\Pi$ ) is not due to the secondary reaction between the photoproducts, CO ( $a^3\Pi$ ) and NH ( $X^3\Sigma$ ). Using UVSOR as a light source, they have reported photodissociative excitation spectra of NH ( $c^1\Pi, A^3\Pi$ ) radicals and quantum yields for the formation of radicals in the wavelength region 107-180 nm.<sup>(2)</sup> In this study, fluorescence polarization of NH ( $c^1\Pi, A^3\Pi$ ) radicals were measured under near collision-free conditions.

Theoretical basis for fluorescence polarization was originally presented by Fano and Macek<sup>(3)</sup>, and the relation between the lifetime of excited molecule and the degree of fragment polarization has been established for triatomic molecules.<sup>(4)</sup> The purposes of this work are to clarify the mechanism of HNCO photodissociation, and also to develop the analytical method for the photofragment fluorescence polarization spectroscopy of four atomic molecules.

An absorption and fluorescence measurement apparatus constructed in the beamline BL2A was used. The monochromated polarized VUV light was introduced to a gas cell filled with HNCO from 20 to 50 mTorr. The NH ( $c^1\Pi \rightarrow a^1\Delta$ ) and ( $A^3\Pi \rightarrow X^3\Sigma$ ) fluorescence parallel and perpendicular to the vector of the excitation light were observed with equipped plate polarizers. The degrees of polarization for the fluorescence were measured using a photoelastic modulator at several reference wavelengths.

The fluorescence intensities of parallel and perpendicular components of the NH( $c^1\Pi \rightarrow a^1\Delta$ ) and ( $A^3\Pi \rightarrow X^3\Sigma$ ) transitions are shown in figure 1 (a)

and (b), respectively. No significant difference was found between the spectral shapes of the parallel and perpendicular components for both the  $\text{NH}(c^1\Pi \rightarrow a^1\Delta)$  and  $(A^3\Pi \rightarrow X^3\Sigma^-)$  fluorescence. Moreover the degrees of polarization obtained by the measurements using photoelastic modulator were equal to zero at all reference wavelengths within the observational errors. As our result, the anisotropy for both the  $\text{NH}(c^1\Pi \rightarrow a^1\Delta)$  and  $(A^3\Pi \rightarrow X^3\Sigma^-)$  fluorescence was not observed in the photodissociative excitation process of HNCO and the excited HNCO molecule may have a long life time.

Since the photoexcited state of HNCO is expected to be singlet, the primary photodissociation process into  $\text{NH}(A^3\Pi)$  and  $\text{CO}(X^1\Sigma)$  is spin forbidden. Hikida *et al.* have concluded that triplet radicals may be formed via triplet HNCO produced by the intersystem crossing. Although the details yet to be clarified, their conclusion and the result of photofragment fluorescence polarization spectroscopy agree that the excited HNCO molecule may have a long life time, which allows a part of the excited molecules to cross to the triplet state.

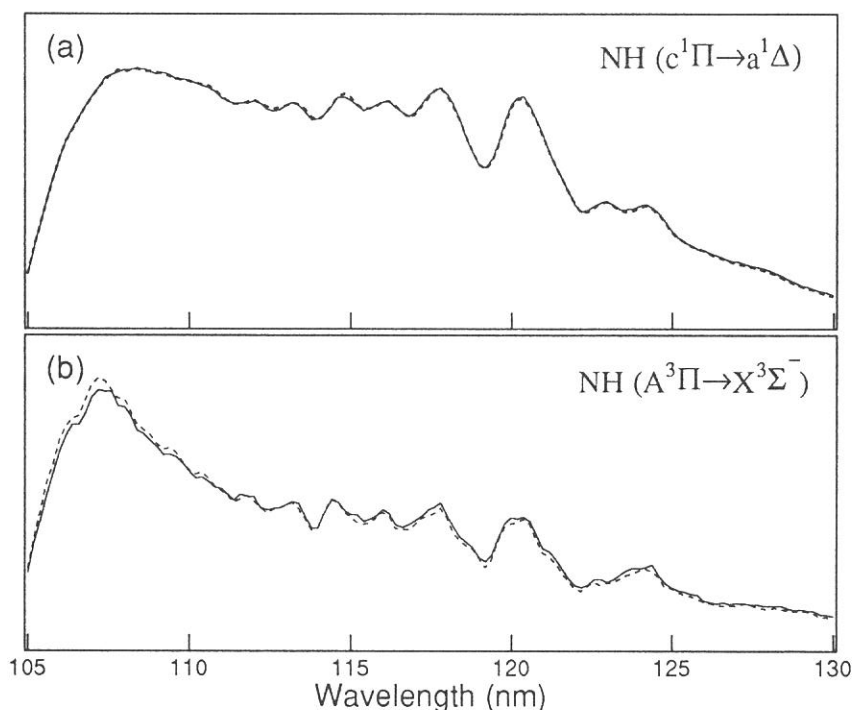


**Figure 1** Observed fluorescence polarized parallel (solid line) and perpendicular (dashed line) to the polarization vector of the incident light in the photolysis of HNCO.

- 
- (1) T. Hikida, Y. Maruyama, Y. Saito, Y. Mori, *Chem. Phys.*, **121** (1988) 63.
  - (2) K. Uno, T. Hikida, A. Hiraya, K. Shobatake, *Chem. Phys. Lett.*, **166** (1990) 475.
  - (3) U. Fano, and J. H. Macek, *Rev. Mod. Phys.*, **45** (1973) 553.
  - (4) T. Nagata, T. Kondow, K. Kuchitsu, G. W. Loge, and R. N. Zare, *Mol. Phys.*, **50** (1983) 49.

## CORE ELECTRON ABSORPTION SPECTRA OF UNDRAWN AND DRAWN POLYESTER FILMS

Isuke OUCHI, Ikuo NAKAI, Masao KAMADA\*, Shin-ichiro TANAKA\* and Tsuneo HAGIWARA<sup>†</sup>

Faculty of General Education, Tottori University, Koyama, Tottori 680

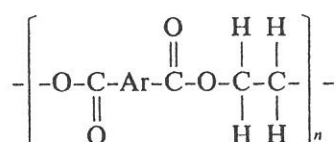
\*Institute of Molecular Science, Myodaiji, Okazaki 444


†Teijin Seiki Co., Kanagawa Science Park, Kawasaki 213

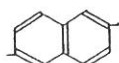
In the previous report,<sup>1)</sup> we described core electron absorption spectra of polyethylene terephthalate (PET) films obtained by total electron yield method. These data were combined with the results obtained by transmission method reported a year earlier.<sup>2)</sup> In these experiments, PET and polyethylene 2,6-naphthalate (PEN) films were used; these

polymers can be prepared in the shape of a film of the thickness less than 1  $\mu\text{m}$  and be measured by either two methods mentioned above.

From optical densities obtained by transmission method, overall oscillator strengths were roughly estimated using a formula:<sup>3)</sup>



where Ar =  : PET,

 : PEN.

$$f = \left\{ 10^3 \cdot \ln 10 \cdot mc^2 / (\pi e^2 N_A) \right\} \int \epsilon(\sigma) d\sigma \\ = 4.32 \times 10^{-9} \int \epsilon(\sigma) d\sigma$$

For simplicity, the integral was taken between 280 eV and 520 eV for carbon and between 520 eV and 680 eV for oxygen. The integrated values of  $f$  were 9.1 for PET and 12.2 for PEN per repeat unit or 0.9 per carbon atom for both films. These particular films were biaxially drawn and not isotropic three dimensionally. However, the errors caused by use of above formula in the calculation for the  $\pi^*$  and for the  $\sigma^*$  transition would cancel each other to some degree from the consideration of their relative directions. Integrated  $f$  values for oxygen were 0.8 per O atom.

Although optical density is not be obtained from the total electron yield method directly, polarization effects are more clearly observed by total electron yield method than by transmission method; thickness of the frame to hold a film interrupts the incident or transmitted light path and a film may not be tilted deeper in the transmission method. Fig. 1 shows the tilt angle dependency of total electron yield signal of a uniaxially drawn PEN film near oxygen K-edge. Peak OA increases with incidence angle (angle between the incident beam and the normal of the film plane) and peak OB decreases with it. From this behaviour, together with the published data of XPS<sup>4)</sup> and EELS<sup>5)</sup> of PET, the peak OA is attributed to  $0\text{ }1s \rightarrow \pi^*$  transition and peak OB is assigned to  $0\text{ }1s \rightarrow \sigma^*$  transition.<sup>6)</sup>

The spectra shown in Fig. 1 were taken by use of a grating of 1200 lines/mm. Replacing this grating by that of 2400 lines/mm brought a significantly better resolution; this is demonstrated in fig. 2, in which the absorption spectra of biaxially drawn PET with incident angle  $45^\circ$  are compared. More structures are revealed also in the carbon K-edge spectra. Detailed results are still to be

worked out.

Fig. 1. Absorption spectra, by total electron yield method, near oxygen K-edge of a uniaxially drawn (3x) PEN film; a 1200 lines/mm grating was used. The ordinate is adjusted at 580 eV.

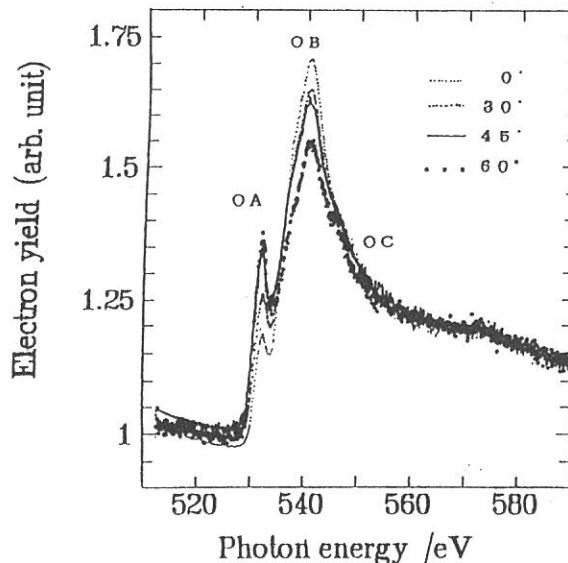
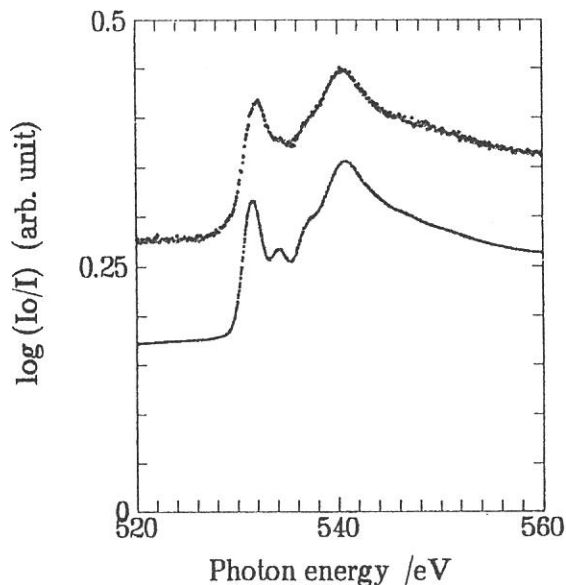


Fig. 2. Comparison of the resolution due to different gratings. Above: 1200 lines/mm. Bottom: 2400 lines/mm.



- 1) I. Ouchi, I. Nakai, M. Kamada and S. Tanaka: UVSOR Activ. Rep. (1993) 104.
- 2) I. Ouchi, I. Nakai, M. Kamada, S. Tanaka and T. Hagiwara: *ibid* (1992) 88.
- 3) H. Baba: Jikken Kagaku Koza vol.3, Chap. 7 (Chem. Soc. Jpn.) (1957) p.386.
- 4) ex. D.W. Wright, J.E. McGrath and J.P. Wightman: J. Appl. Polym. Sci., Symp. 34 (1978) 35.
- 5) A.P. Hitchcock, S.G. Urquhart and E.G. Rightor: J. Phys. Chem. 96 (1992) 8736.
- 6) I. Ouchi, I. Nakai, M. Kamada, S. Tanaka and T. Hagiwara: Polym. J., 27 (1995) No. 2. (in press)

**$3p \rightarrow 3d$  resonant photoemission spectra of  $\text{LaTO}_3$  ( $T=\text{Co, Ni}$ )**

Y. Taguchi, M. Kageyama, K. Soda,\* T. Katsumi, S. Tanaka, K. Ichikawa, Wu Quing,  
K. Okuda, and O. Aita

*College of Engineering, University of Osaka Prefecture, Gakuen-cho 1, Sakai 593*

*\*School of Engineering, Nagoya University, Nagoya, 464-01*

The electronic structures of perovskite oxides  $\text{LaTO}_3$  ( $T=3d$  transition metal) have been studied extensively, since they have various electrical and magnetic properties depending on the  $T$  element. However, there are still unsettled problems in their electronic states: an apparent discrepancy between spectroscopic data and magnetic measurements regarding the spin state of the Co ion in  $\text{LaCoO}_3$  at room temperature (RT),<sup>1,2</sup> an uncertainty of the ground-state electronic configuration of  $\text{LaNiO}_3$ ,<sup>3</sup> and so on. We have investigated the valence-band photoemission spectra of  $\text{LaCoO}_3$  and  $\text{LaNiO}_3$  in the  $T3p \rightarrow 3d$  absorption region, in order to obtain the information on the  $3d$  state involved in the valence band.

The experiments were carried out at the BL2B1 beamline. The samples used were a single crystalline  $\text{LaCoO}_3$  and a sintered polycrystalline  $\text{LaNiO}_3$ . The sample surfaces were scraped with diamond files at RT in a vacuum chamber before measurements. All the photoemission measurements were made at RT.

Figures 1 and 2 show the photon-energy dependences of the peak intensities in the valence-band spectra of  $\text{LaCoO}_3$  and  $\text{LaNiO}_3$ , respectively. The intensities are shown after the background due to secondary electrons is subtracted. The insets of the figures show typical valence-band spectra at off-resonance.

In  $\text{LaCoO}_3$ , peaks a and b show resonant behavior clearly (Fig. 1). In the previous study,<sup>1</sup> it has been considered that the peak a is characteristic of the low-spin state of the Co ion, and has large  $3d$ -spectral weight. The resonant enhancement of the peak b is comparable to that of the peak a, which suggests the coexistence of the low- and high-spin states of the Co ions at RT. The resonances of peaks c and d are less clear. The peak c is attributed to the O  $2p$  emission. In Ref. 1, the peak d was considered to arise from many-body satellites. However, it is hard to distinguish between the intrinsic feature and the well-known “dirty peak”, which comes about frequently by filling an oxide sample at RT. A more careful sample preparation, e.g., cleavage at liquid nitrogen temperature, should be required.

In  $\text{LaNiO}_3$ , peaks b and e show resonant enhancement clearly (Fig. 2). Comparison between the present soft X-ray and the Mg  $K\alpha$  X-ray photoemission spectra<sup>4</sup> also indicates that the peak b has mainly the Ni  $3d$  character. It is worth noting here that the many-body satellite, the peak e, is distinguished. There is not yet a theoretical analysis for the valence-band spectra of  $\text{LaNiO}_3$ , which treats many-body effects explicitly. Here we only point out that the calculated  $3d$ -electron-removal spectrum of a hole-doped NiO ( ${}^2E_g$ ) seems to reproduce the observed features qualitatively.<sup>5</sup> This may indicate that  $\text{LaNiO}_3$  in the ground state has a negative charge-transfer energy  $\Delta$ .

Further investigation of these compounds with more careful sample preparation is now undertaken.

## References

1. M. Abbate *et al.*, Phys. Rev. B **49**, 7210 (1994).
2. K. Asai *et al.*, Phys. Rev. B **50**, 3025 (1994).
3. M. Medarde *et al.*, Phys. Rev. B **46**, 14 975 (1992).
4. T. Katsumi *et al.*, unpublished work; S. R. Barman *et al.*, Phys. Rev. B **49**, 8475 (1994).
5. J. van Elp, Ph.D. thesis, University of Groningen, 1991.

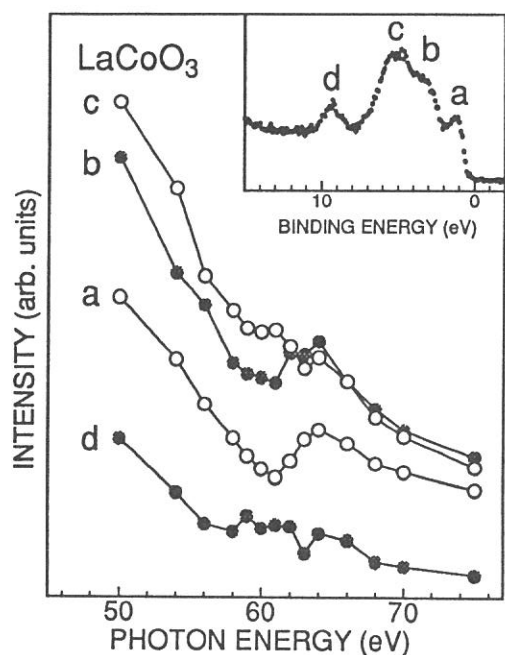


Fig. 1

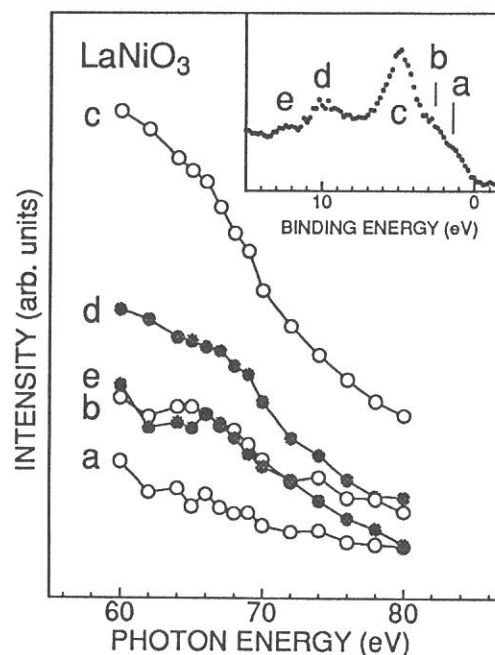


Fig. 2

Fig. 1. Photon-energy dependence of the peak intensities in the valence-band spectra of LaCoO<sub>3</sub>. Peak intensities are shown after the background due to secondary electrons is subtracted. The inset shows the spectrum taken with  $h\nu = 50$  eV.

Fig. 2. Photon-energy dependence of the peak intensities in the valence-band spectra of LaNiO<sub>3</sub>. The inset shows the spectrum taken with  $h\nu = 72$  eV.



## Orientation and desorption of oxygen admolecules on a Pt(113) stepped surface

Toshiro Yamanaka, Tatsuo Matsushima, Shin-ichiro Tanaka\*  
and Masao Kamada\*

Catalysis Research Center, Hokkaido University, Sapporo 060 Japan,  
\*Institute for Molecular Science, Myodaiji Okazaki 444, Japan.

Oxygen admolecules on stepped Pt(113) or (s)2(111)x(001) were characterized with thermal desorption spectroscopy (TDS) and near-edge X-ray absorption fine structure (NEXAFS). Their molecular axis was determined to be parallel to both the step edge and the bulk surface plane, from the dependence of Auger electron yield initiated with  $\sigma^*$  resonance on the electric vector orientation of incident X-ray.

The O-O bond in O<sub>2</sub> admolecules on platinum surfaces is remarkably weakened and verges into the dissociation. Its orientation is important in the oxidation process, since it can be broken easily by being heated or by being radiated with ultra-violet light. The resultant atoms are emitted along the bond axis and highly reactive towards co-adsorbed species. The NEXAFS of oxygen molecules consists of two parts labeled by  $\pi^*$  and  $\sigma^*$  resonance according to the symmetry of the related valence orbital. The former is initiated by X-ray absorption due to the transition of a 1s electron into the unfilled anti-bonding  $1\pi^*$  orbital ( $1\sigma_u \rightarrow 1\pi^*_g$ ). This resonance is maximized when the electric vector,  $\mathbf{E}$ , of the X-ray is perpendicular to the molecular symmetry axis and vanishes when  $\mathbf{E}$  is parallel to it. The  $\sigma^*$  resonance due to the transition of ( $1\sigma_g \rightarrow 3\sigma^*_u$ ), on the other hand, is maximized when  $\mathbf{E}$  is parallel to the molecular axis.

Experiments were separately performed in two ultra-high-vacuum apparatuses. The first is a conventional UHV system with LEED-AES, which was used for TDS measurements. The other is on the Beam Line 2B1 at UVSOR with the use of grass-hopper monochromator (Mark XV). The intensity of the incident X-ray beam was monitored by measuring photoemission from a gold mesh set in the beam and used to normalize the spectra. The photon energy was calibrated with the sharp photoemission spectrum of the Pt(4f) level located 73 eV below the Fermi level. The spectra were recorded by a partial electron yield mode with the kinetic energy of the oxygen KLL Auger electrons. A cylindrical mirror electron energy analyzer (CMA) was operated in a non-retarding mode yielding an energy resolution of 4 eV. A Pt(113) crystal was positioned in the focal point of CMA and rotatable vertically, where the photon beam was also focused. The crystal was set so that the  $\mathbf{E}$  vector was oriented parallel, perpendicular or inclined to the step edge as shown in Fig.1. It was mounted on a round sapphire plate by spot-welded it to thin tantalum heater wires. The plate was coupled to a copper stage connected with a liquid nitrogen reservoir and can be rotated to change the crystal azimuth.

The desorption at low temperatures shows three peaks due to the molecular adsorption states at 235 K ( $\alpha_1$ ), 190 K ( $\alpha_2$ ), and 160 K ( $\alpha_3$ ) as shown in Fig.2. These peaks are originated from adsorption sites on steps ( $\alpha_1$ ,  $\alpha_2$ ) and terraces ( $\alpha_3$ ). Each peak can be separately observed by annealing and modifying the surface with oxygen adatoms. The NEXAFS spectra of  $\alpha_3$ -O<sub>2</sub> were recorded as follows. The surface was annealed to 260 K after O<sub>2</sub> exposure at 130 K to accelerate the dissociation of oxygen and remove remaining admolecules. The step sites are covered at this stage by oxygen adatoms. The desorption shows a single  $\alpha_3$ -O<sub>2</sub> peak around 160 K in heating after further O<sub>2</sub> exposure at

130 K. Typical NEXAFS of  $\alpha_3$ -O<sub>2</sub> are shown in Fig.3 in the difference spectrum form between the  $\alpha_3$ -O<sub>2</sub> covered surface prepared above and oxygen atom-covered surface prepared for  $\alpha_3$ -O<sub>2</sub> adsorption.

Both  $\pi^*$  and  $\sigma^*$  resonance are significant when  $\mathbf{E}$  is parallel to the step edge (Fig.3a). On the other hand, the  $\sigma^*$  resonance is attenuated for  $\mathbf{E}$  perpendicular to it (Fig.3b). This indicates the molecular axis of oxygen admolecules parallel to the step edge. This orientation is consistent with the spectrum when  $\mathbf{E}$  inclines 80° from the  $[1\bar{1}0]$  direction, where significant  $\pi^*$  resonance and a small signal assigned to the  $\sigma^*$  resonance are found as shown in Fig.3c. The spectra of  $\alpha_1$ -O<sub>2</sub> and  $\alpha_2$ -O<sub>2</sub> show features similar to those of  $\alpha_3$ -O<sub>2</sub>. The molecular axis of oxygen admolecules yielding each desorption peak is commonly parallel to the step edge. Such oriented adsorption may be caused by narrow terraces where admolecules are hardly oriented perpendicular to them by steric hindrance.

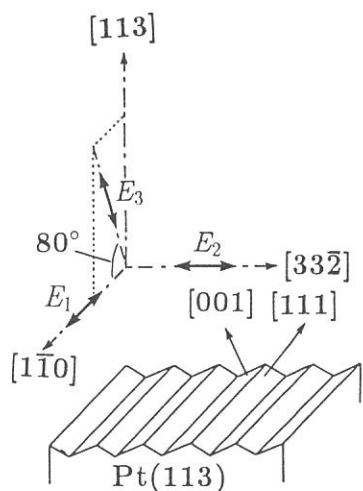


Fig.1 Surface structure of Pt(113) and orientation of X-ray electric vector.

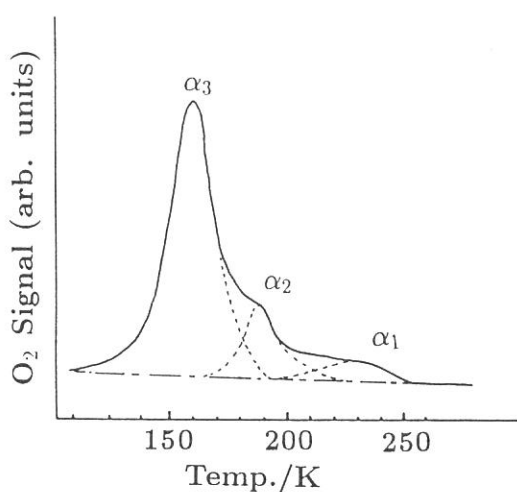
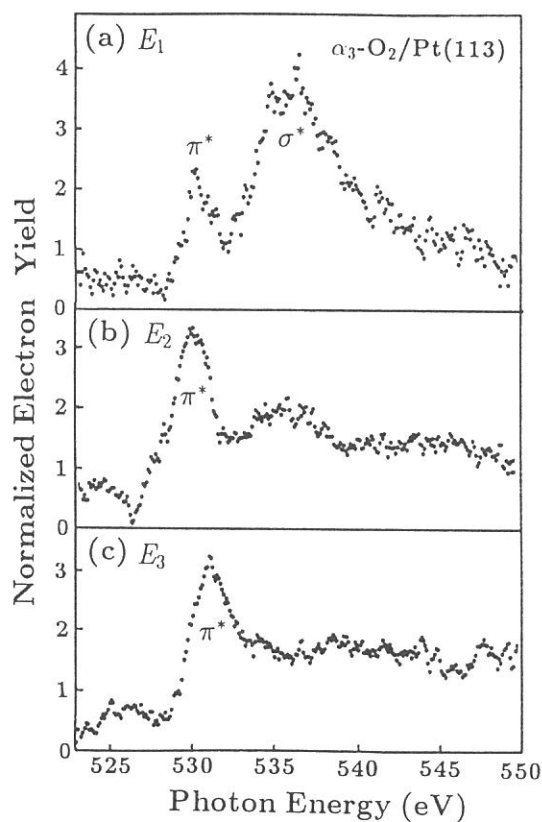


Fig.2 TDS of oxygen adatoms on Pt(113).



Figs.3 NEXAFS in differential form of  $\alpha_3$ -O<sub>2</sub>.

## NEXAFS Study on the Adsorption Structure of N<sub>2</sub>O on Si(100)(2×1) Surface

Kyoichi SAWABE and Yoshiyasu MATSUMOTO  
*Institute for Molecular Science, Myodaiji, Okazaki 444*

Determining the orientation of adsorbed species is important in understanding whether structure or dynamics is related with angle distribution of the photo-stimulated desorption. Photo-stimulated dissociation of N<sub>2</sub>O on Si(100) surface shows two distinct angular distributions in Time of Flight (TOF) measurements<sup>1</sup>; one has a sharp angular distribution at ~32° from the surface normal and another a much broader distribution peaked at surface normal. The former sharp distribution was mainly gained by the photodissociation of N<sub>2</sub>O adsorption at 95 K. Thus, if this distribution reflects the orientation of adsorbed structure, the tilt angle of adsorbed N<sub>2</sub>O at 95 K will be ~60° from the surface plane. Near edge x-ray absorption fine structure (NEXAFS) spectra provide information on the orientation of the adsorbed molecule, since the intensity of resonance peak is proportional to the dipole transition between core levels and unoccupied molecular orbitals (MO). Therefore, we have measured the NEXAFS spectra of N<sub>2</sub>O adsorbed on Si(100) surface at 95 K as a function of incidence angles of light.

The measurements have been performed in a UHV system of the BL2B1 of UV-SOR facility. A Si sample (Sb-doped, 0.005-0.01Ω, 9×20 mm<sup>2</sup>) was mounted on a copper block by clamping the side edges and cooled down to 90 K by the contact to the liquid N<sub>2</sub> reservoir or resistively heated above 1300 K. The NEXAFS spectra were taken measuring the Partial Electron Yield (E<sub>r</sub>=200V) with a micro-channel plate (MCP). The MCP was located about 4 cm below the sample in order to set the same solid angle for electron detection at various incidence angles of photon.

Fig. 1 shows a set of NEXAFS spectra taken at the nitrogen K-edge as a function of incidence angles of light from the surface plane. Each spectrum was normalized by the height of edge jump. The photon energy was calibrated by comparing the position of edge jump with the binding energy of terminal N(1s) peak in XPS spectrum. There are two resonance peaks at 401.1 eV and 404.6 eV which are the resonance from 1s orbitals of terminal and center N of N<sub>2</sub>O to the unoccupied π\* MO, respectively. The peak separation, 3.5 eV corresponds to the shift of 1s binding energies of terminal and center nitrogen. Fig. 2 shows the intensity of π\* resonance at each incidence angle. In order to analyze the orientation of N<sub>2</sub>O, we assumed that the N<sub>2</sub>O was aligned to the direction of Si dimer of surface. Furthermore, its structure is assumed to be linear and the direction of dipole transition (1s→π\*) is perpendicular to the molecular axis. Then, the intensity of π\* resonance is proportional to the following equation,

$$P[(2 \sin^2 \theta + (2 - 3 \sin^2 \theta) \cos^2 \alpha) + (1 - P)(1 + \sin^2 \alpha)]$$

Here,  $\theta$ ,  $\alpha$  and  $P$  are the incidence angle of light from surface plane, the tilt angle of N<sub>2</sub>O from surface plane and the degree of linear polarization of light, respectively. Nonlinear least squares fitting of the data gives the tilt angle  $\alpha = 41^\circ \pm 4^\circ$  and  $39^\circ \pm 7^\circ$  for the resonance of terminal and center nitrogen K-edge, respectively. We assumed the polarization factor  $P$  is 0.85, but if  $P$  is 1.0, the result was not much changed. Since the dynamic range of π\* resonance around  $\alpha = 40^\circ$  is narrow as shown in fig. 2, we can not determine the tilt angle precisely. Now, our conclusion is that N<sub>2</sub>O on Si(100) inclines at  $40^\circ \pm 10^\circ$  from the surface plane and the obtained angle is different from the expected angle 60° by the TOF measurements. Thus, the angular

distribution of photo-stimulated dissociation of  $N_2O$  depends on its dynamics, as well as the adsorbed structure.

## Reference

[1 ] J. Lee, H. Kato, K. Sawabe and Y. Matsumoto, to be submitted.

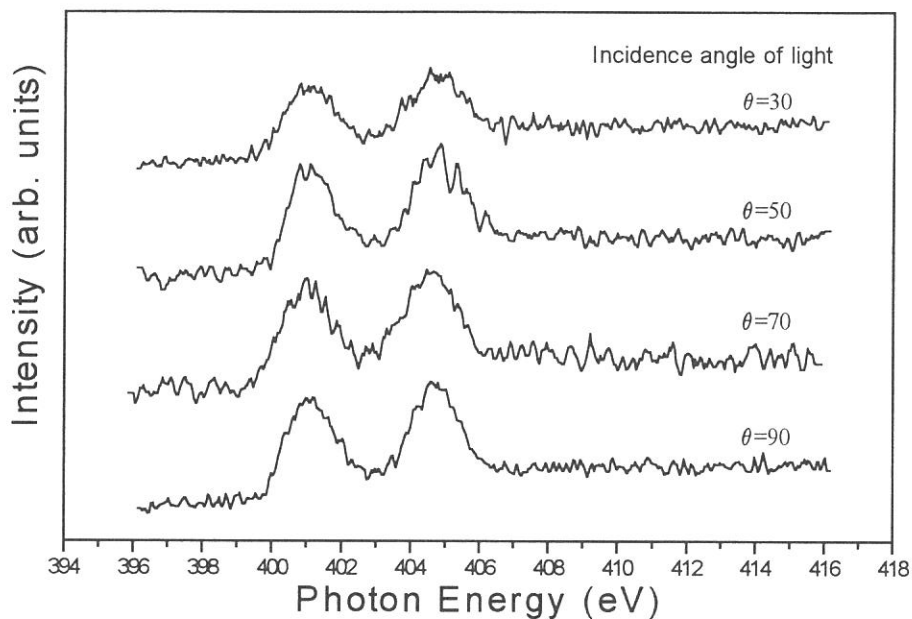


Fig.1 NEAFS spectra of  $N_2O$  adsorbed on  $Si(100)(2\times 1)$  surface at 95 K. Series of spectra were taken as a function of incidence angle of light.

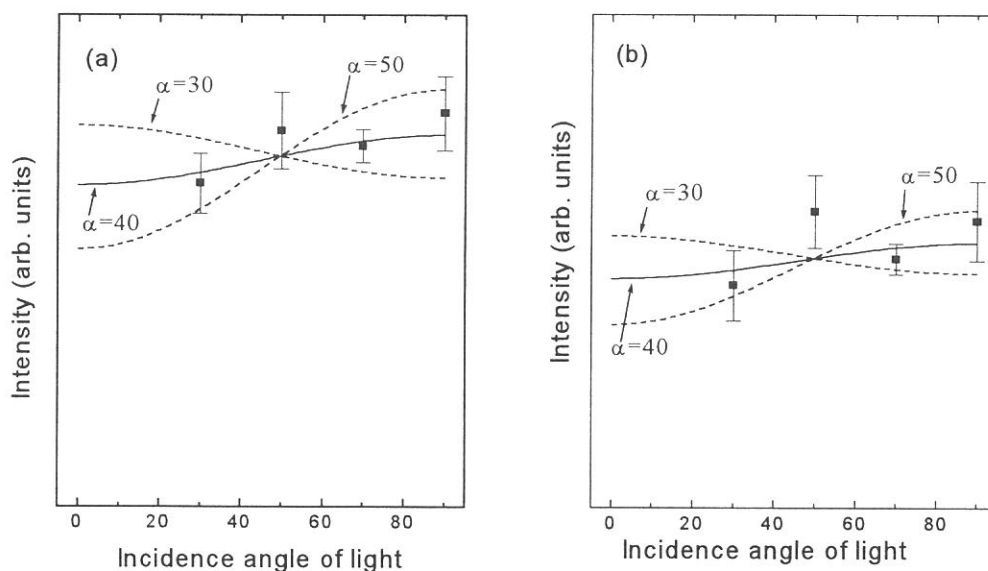


Fig.2 Intensities of the  $1s \rightarrow \pi^*$  resonance of (a) terminal and (b) center N. Calculated curves are shown for tilt angles  $\alpha = 30^\circ, 40^\circ$  and  $50^\circ$ .

# The Studies on the Core-Excitonic Effect of Aromatic Hydrocarbons in NEXAFS Spectroscopy

Hiroshi OJI, Ryuichi MITSUMOTO, Eisuke ITO, Hisao ISHII, Yukio OUCHI,  
Kazuhiko SEKI, and Nobuhiro KOSUGI\*

*Department of Chemistry, Nagoya University, Chikusa-ku, Nagoya 464*

*\*Institute of Molecular Science, Myodaiji, Okazaki 444*

It has been the subject of interest to obtain the density of unoccupied states (DOUS) for relatively large organic molecules. We have been studying the applicability of the technique of near edge X-ray absorption fine structure (NEXAFS) spectroscopy, in which electronic excitations from core orbitals (e.g. C1s) to various vacant orbitals are observed. Since the NEXAFS spectrum, however, may be significantly deformed from DOUS due to the excitonic effect caused by the interaction between core-hole and the excited electron[1,2], it is necessary to assess the magnitude of the excitonic effect systematically. Our previous paper has evaluated the variation of the magnitude of the excitonic effect among various delocalized  $\pi$ -electron systems, such as fullerenes, naphthacene and *p*-sexiphenyl[3]. In this work, we extend our study to other  $\pi$ -electron systems, chrysene, perylene and coronene, whose degree of  $\pi$ -conjugation is estimated between fullerenes and naphthacene.

The samples were prepared by vacuum evaporation to be 2000Å in thickness. C K-edge NEXAFS spectra were measured at the beamline 2B1 with grasshopper monochromator (1200 line/mm) at UVSOR. Analysis of the observed spectra was performed by *ab initio* MO calculation program, GSCF3 coded by one of the authors (N. K.), with use of hole-potential method[4]. While convoluting the delta functions at each transition energy with Gaussian function to obtain NEXAFS spectra, we have taken account of the difference among the C1s binding energies,  $\Delta IP$ , for each atom in the molecule.

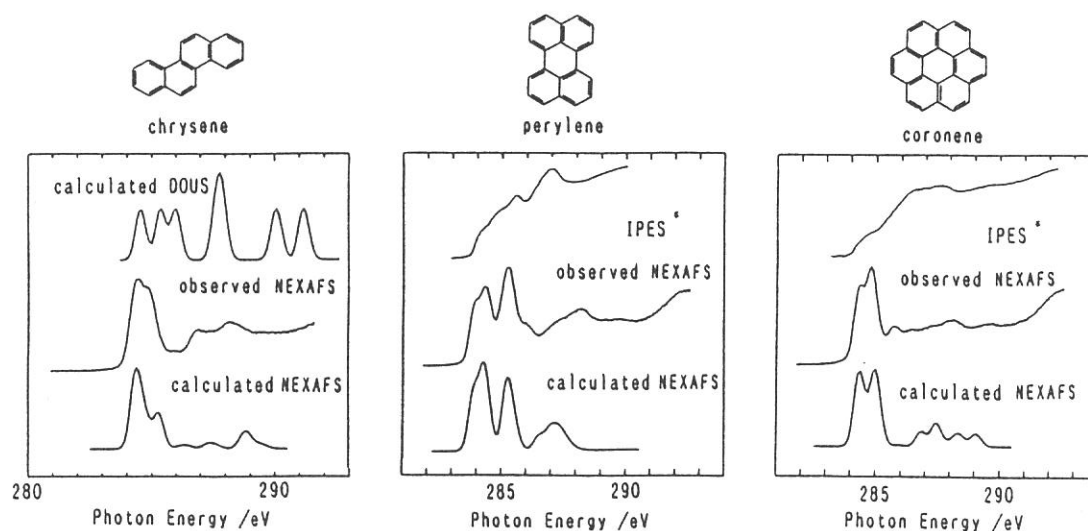
In Fig. 1, we show the C K-edge NEXAFS spectra of chrysene, perylene and coronene with the results of inverse photoemission spectroscopy (IPES) [5] and calculated NEXAFS spectra. Since IPES spectrum of chrysene is not available in the literature, we have used the result from *ab initio* calculation for ground-state instead. As is clear from the figure, the resemblance between IPES and NEXAFS spectra are rather poor, as has been observed in the case of naphthacene[3].

In order to evaluate how large the excitonic effect reflects upon the MO and hence the NEXAFS spectra, we have depicted the details of MO calculation for perylene in Fig. 2 as an example. Abscissa represents the number of atom whose 1s orbital is excited as is shown in the inset. Schematic views of unoccupied MO of ground-state are illustrated in conjunction with the energy levels of unoccupied MO for each excited atom which, in hole-potential method, correspond to the core excitation energies. Delta function of each energy level is

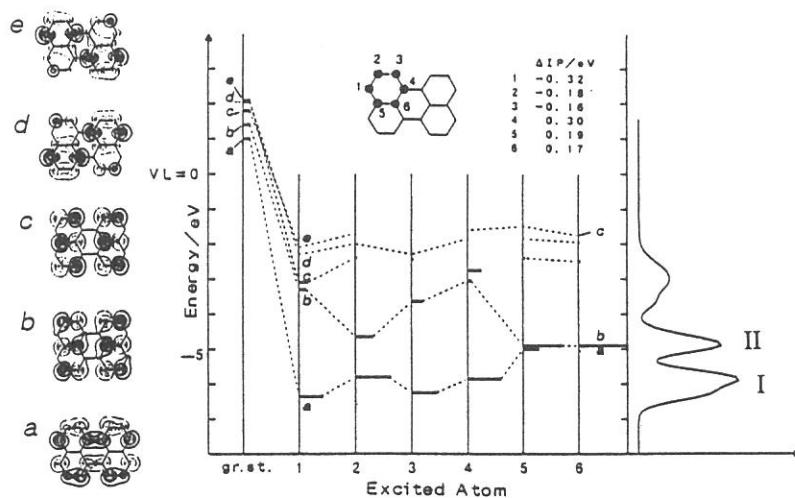
convoluted and their weighted sum over the C atoms gives the simulated NEXAFS spectrum (right). The first peak (I) consists of the excitations from the C1s orbitals of atoms 1, 2, 3 and 4 to the MO-a. Though the peak seems to have a shoulder, it is evident that the shoulder has the same final MO. The second peak (II), on the other hand, is contributed from both MO-a and MO-b with the excitation of atoms 5 and 6. Taking into account of the variation of the energy levels of MO with each atom-excitation, we can conclude that DOUS information of this size of  $\pi$ -conjugated system is hardly obtainable from NEXAFS spectra itself.

## References

- [1] J. Stöhr, NEXAFS Spectroscopy, Springer, Berlin, 1992.  
 [2] T. Yokoyama, K. Seki, I. Morisada, K. Edamatsu and T. Ohta, *Phys. Scr.*, **41**, 189 (1990).  
 [3] K. Seki, R. Mitsumoto, T. Araki, E. Ito, Y. Ouchi, K. Kikuchi and Y. Achiba, *Synthetic Metals*, **64**, 353 (1994).  
 [4] S. Huzinaga and C. Annau, *Phys. Rev. A***1**, 1280 (1970).  
 [5] K.H. Frank, P. Yannoulis, R. Dudde and E. E. Koch, *J. Chem. Phys.*, **89**, 7569 (1988).



↑ Fig. 1 Comparison of Carbon K-edge NEXAFS spectra and IPES spectra or calculated DOUS for chrysen, perylene, and coronene.



← Fig. 2 Details of MO calculation for perylene. Abscissa represents the number of atom whose 1s orbital is excited as is shown in the inset. The energy levels of unoccupied MO for each excited atom correspond to the core excitation energies in hole-potential method.



# Photoemission Studies on Valence Band Structure of $\text{AgSbO}_3$ (BL2B1)

Masahiro YASUKAWA, Hideo HOSONO, Naoyuki UEDA, \* and Hiroshi KAWAZOE\*

Research Laboratory of Engineering Materials, Tokyo Institute of Technology,  
Nagatsuta, Midori-ku, Yokohama 226

\* Institute for Molecular Science, Myodaiji, Okazaki 444

$\text{AgSbO}_3$  has defect pyrochlore structure in which  $\text{AgO}_6$  and  $\text{SbO}_6$  octahedra are connected by sharing their vertex oxygens, respectively. In addition, since both  $\text{Ag}^+$  and  $\text{Sb}^{5+}$  cations have  $d^{10}s^0$  electronic configuration, upper valence bands of  $\text{AgSbO}_3$  are considered to be composed of Ag-4d and O-2p orbitals. Since the atomic energy levels of these orbitals are closely located, it is expected that these orbitals form broad band at the top of valence band in  $\text{AgSbO}_3$  through the chemical bonding. If holes are doped in this material, p-type conduction may be caused by the delocalization of the doped holes. The purpose of this study is to examine the valence band structure of  $\text{AgSbO}_3$  using ultra-violet photoemission spectroscopy(UPS) technique and to make sure of the possibility of p-type conduction in  $\text{AgSbO}_3$ .

The sintered pellet of  $\text{AgSbO}_3$  was prepared by solid state reaction of  $\text{AgNO}_3$  and  $\text{Sb}_2\text{O}_3$  powders. The sintering was performed at 1000°C for 48 h in  $\text{O}_2$  gas flow and the formation of a single phase of  $\text{AgSbO}_3$  was confirmed by powder X-ray diffraction. N-type conduction was confirmed on the obtained sample. The UPS measurements were performed at BL2B1 beam line. The monochromatized lights with the photon energy of 60 - 200 eV were used. The kinetic energy of photoelectrons was analyzed in a double-pass cylindrical mirror analyzer(CMA). Constant initial state(CIS) spectra were measured by scanning the photon energy. The total resolution was  $\sim 0.5$  eV for each measurement. The Fermi level of all the UPS spectra was corrected to that measured on an in-situ evaporated Au. The number of photoelectrons was corrected with respect to both intensity of the monochromatized light and collecting efficiency of CMA. All measurements were performed at room temperature under a vacuum of  $\sim 6 \times 10^{-8}$  Pa. Surface filing of the sintered specimen and the evaporations of metallic Au and Ag were performed under a vacuum of  $\sim 2 \times 10^{-7}$  Pa just before the measurements.

Figure 1(a) shows the photoemission spectra of  $\text{AgSbO}_3$  measured in photon energy region of 60 - 200 eV. These spectra indicate that the upper valence band of  $\text{AgSbO}_3$  has a structure in which the top of valence band and the peaks are located at the energies marked with A, B, C, and D, respectively. The subject is to confirm the distribution of Ag-4d orbitals over these peaks. Fig.1(b) shows the photoemission



spectra of metallic Ag measured in photon energy region of 60 - 170 eV. A small bump due to metallic Ag-5s orbital is seen at the rising edge of Fermi level. Ag-4d peaks which were splitted by the spin-orbit interaction are clearly seen at the binding energies of 4.5 eV and 6.5 eV. Fig.2(b) shows the CIS spectra of metallic Ag measured at the fixed binding energies of 4d peaks. Both CIS spectra indicate intensity minimum around 130 eV. This intensity minimum called as "Cooper minimum" has been previously observed in metallic Ag<sup>1)</sup> and has been indicated by a theoretical calculation on photon energy dependence of photoionization cross section for Ag-4d orbital,<sup>2)</sup> as shown in the inset of Fig.2(b). Fig.2(a) shows the CIS spectra of AgSbO<sub>3</sub> measured at each fixed binding energy for the peaks A, B, C, and D in Fig.1(a). The peak D indicated the monotonous decrease with increasing photon energy. On the other hand, the peaks A, B, and C indicated the inflection around 130 eV. This inflection is attributed to the appearance of Cooper minimum for Ag-4d orbital. Therefore, the top of valence band in AgSbO<sub>3</sub> is mainly composed of the broadly distributed 0-2p and Ag-4d components. This result suggests that if holes are successfully doped in this material, they can delocalize.

1) P. S. Wehner et al., Phys. Rev. B 14(1976)2411.

2) J. J. Yeh and I. Lindau, Atomic Data and Nucl. Data Tables 32(1985)1.

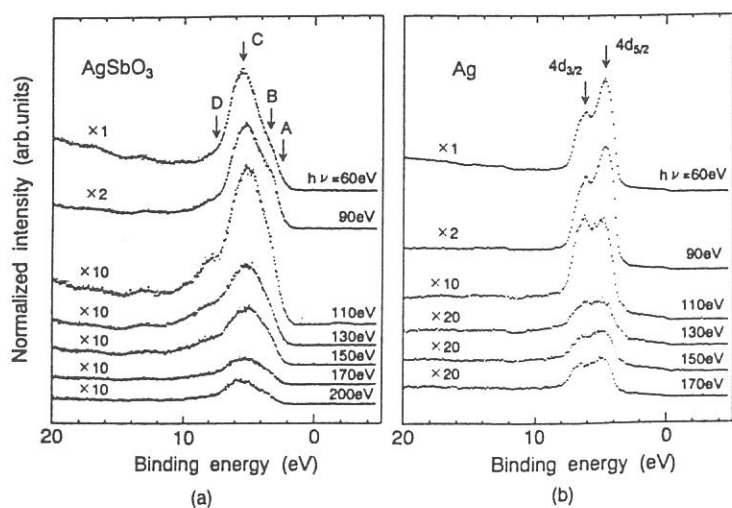


Fig.1 Photoemission spectra of AgSbO<sub>3</sub> (a) measured in photon energy region of 60 - 200 eV and of metallic Ag (b) measured in the region of 60 - 170 eV.

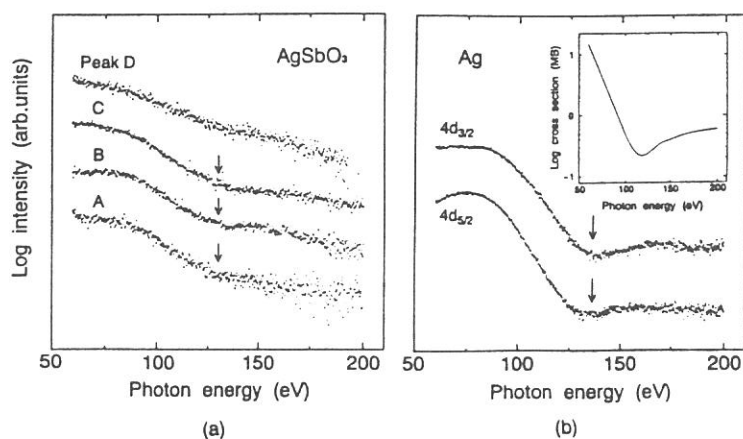


Fig.2 CIS spectra of AgSbO<sub>3</sub> (a) measured for the peaks A, B, C, and D and of metallic Ag (b) measured for the 4d peaks.

H. Mizoguchi, T. Omata and H. Hosono

Research Laboratory of Engineering Materials, Tokyo Institute of Technology  
Nagatsuta, Midori-ku, Yokohama 226, Japan

N. Ueda and H. Kawazoe

Institute for Molecular Science, Myodaiji, Okazaki 444, Japan

Thallus halides are attractive semiconductors especially from the structure of valence band. But, most of them are very hygroscopic, therefore these materials are not useful in the view of practical application.

On the other hand,  $\text{TlAlF}_4$  is expected to less hygroscopic and more hard in strength, because  $\text{Al}^{3+}$  ion which is one of the hard cations are introduced to the thallus halide lattice and because fluoride is not more hygroscopic than chloride or bromide, generally. The structure of the valence band, especially contribution of Tl 6s, was estimated by photoemission measurement.

The angle-integrated ultraviolet photoemission measurements were performed at the beam line BL2B1. Thin film samples were prepared by vacuum evaporation onto a Molybdenum sample holder in a preparation chamber with a base pressure of  $2 \times 10^{-9}$  Torr, and the holder was transferred as soon as possible to an analyzing chamber with a base pressure of  $1 \times 10^{-10}$  Torr.

Figure 1 and 2 show valence band photoemission spectra for various excitation photon energies in TlF and  $\text{TlAlF}_4$ , respectively.

The peaks observed in UPS spectra are labeled from A to G. The deeper two peaks, G and F are ascribed to spin orbit splitted  $\text{Tl}5d_{5/2}$  and  $5d_{3/2}$  emission because of their binding energies, large splitting and the ratio of emission intensities. The large spin orbit splitting is a feature of 5d inner shell of heavy metallic cations,  $\text{Hg}^{2+}$ ,  $\text{Tl}^+$ ,  $\text{Pb}^{2+}$  and  $\text{Bi}^{3+}$ . In an assignment of the observed peaks, the data of dependences of ionization cross sections<sup>1</sup> of the related Tl6s, Tl5d and F2p electrons on the excitation photon energies are very helpful. Using it, the cross section ratios of Tl6s relative to the F2p at 60, 130 and 1486.7 eV excitation are 0.02, 0.04 and 1.3, respectively. Then, at photon energy level of UV-light excitation, the contribution of F2p is expected to dominate a photoemission spectrum. On the other hands, at the photon energy of X-ray(1486.7 eV), that of Tl6s is comparable to that of F2p.

The spectra of TlF will be discussed. The separation between A and B is much clearer, compared with that of  $\text{TlCl}$  and  $\text{TlBr}$ <sup>2, 3</sup>. The reason is explained as follows: Because the energy level of F2p is much deeper than Cl3p and Br4p, the mixing of Tl6s with F2p is probably smaller than outermost p orbitals of other halogens. Taking into consideration the dependences of ionization cross sections, the Tl6s fractions in the

peaks A, B, C, D and E are estimated roughly to be 0.8, 0.9, 0.0, 0.9 and 0.0, respectively, in comparison with a XPS spectrum. This result indicates that the mixing between Tl6s and F2p is very small, although Tl6s orbital splits into three bands, A, B and D. The assignment of the feature A, B, C and E are considered trialily to be Tl6s-F2p $\sigma^*$ , Tl6s-F2p $\pi^*$ , Tl6s-F2p $\pi$  and Tl6s-F2p $\sigma$ , respectively. Considering in this way, the splitting between  $\sigma$  and  $\sigma^*$  is 5.4 eV. This value is consistent with that of PbF<sub>2</sub>, 6.3 eV.<sup>4</sup> Since An energy level of Pb6s orbital is closer a little to that of F2p than that of Tl6s, the larger interaction between Pb6s and F2p causes the large splitting. The PES spectra of TlAlF<sub>4</sub> will be discussed in the same way.

#### Reference

- 1 J. J. Yeh and I. Lindau, At. Data Nucl. Data Tables, 32, 1(1985)
- 2 D. R. Williams, R. T. Poole, J. Electron. Spectrosc. 9, 11(1976)
- 3 L. Porte and A. Tranquard, Chem. Phys. Lett. 56, 466 (1978)
- 4 V. Chab, B. Kawalski and B. A. Orłowski, Solid State Commun. 548, 667(1986)

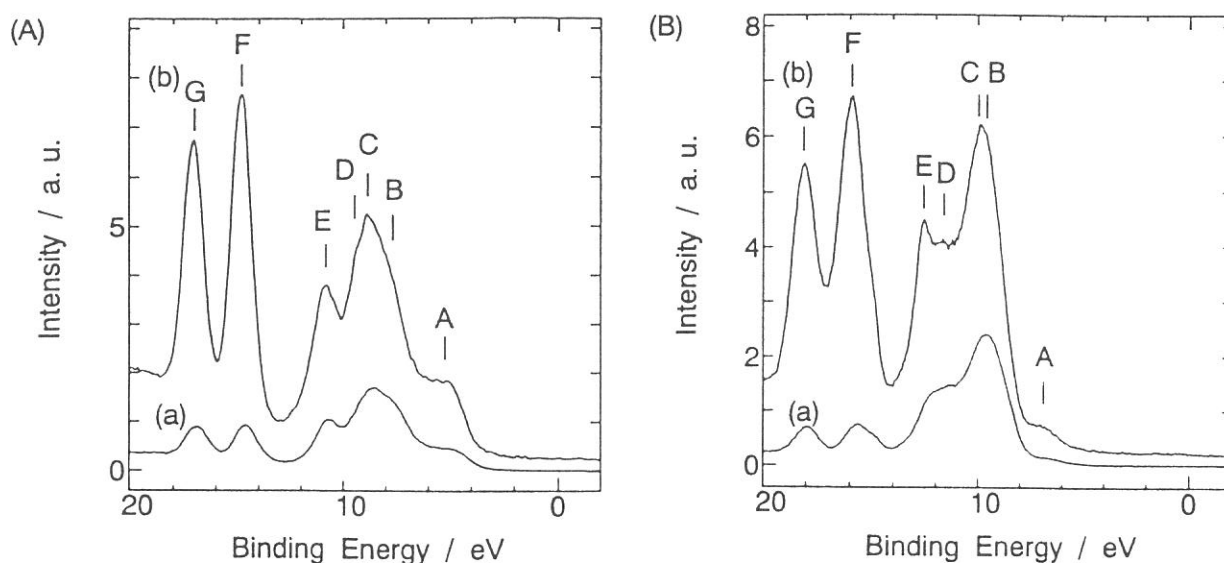


Figure 1 Photoemission Spectra of evaporated thin film of (A)TlF and (B)TlAlF<sub>4</sub> in the region of valence bands for photon energy (a)60 eV and (b)130 eV. Binding energy is measured from the Fermi level. The bars indicate the peak positions.

## Surface core exciton of Alkali Chloride film on Si(100) (BL2B1)

S. Tanaka, N. Takahashi, M. Kamada and K-P. Lee\*

UVSOR Facility, Institute for Molecular Science, Okazaki 444, Japan

\*Kyungpook National University, Taegu 702-701 Korea

Alkali halide is typical Ionic crystal, and has been extensively studied experimentally and theoretically for long years. However, its surface properties are not well known, because it is an insulator, and cannot be investigated using usual techniques in surface analysis of conducting material. We produced the thin film on the well-ordered Si(100)(2x1) in UHV, and observed the surface optical properties of alkali chloride.

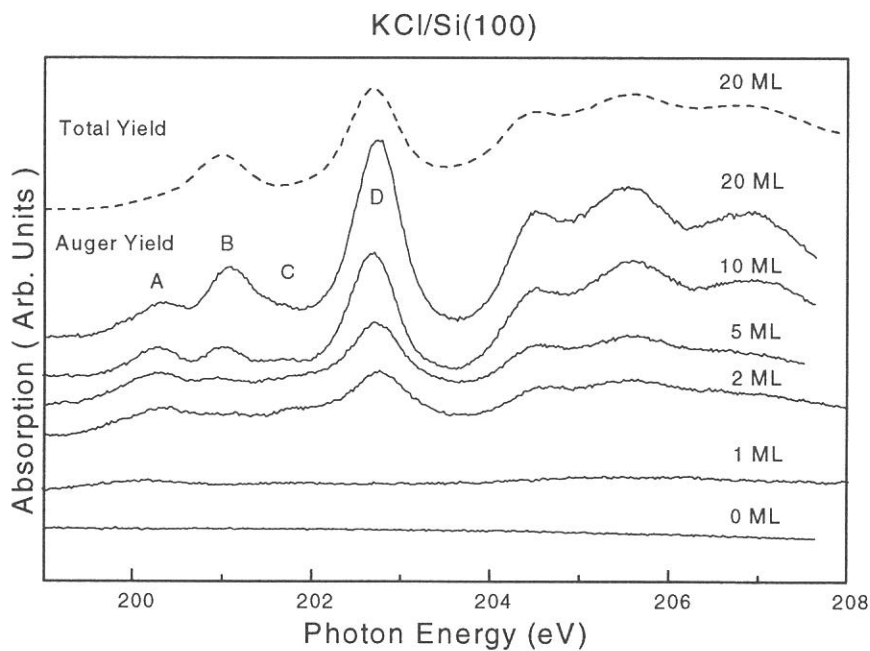


Figure 1

Figure 1 shows the absorption spectra at Cl-L<sub>2,3</sub> edge of KCl/Si(100) as a function of thickness (indicated in ML) of the film at RT. Dotted line is the total photoelectron yield which indicates the “bulk” spectrum, and solid lines are Auger-yield, which indicate the “surface” spectra. In the “bulk” spectrum, peaks B and D (splitting is due to the spin-orbit interaction of initial Cl-2p state) had been observed and assigned to be due to core exciton, previously. Peaks A and C (spin-pair) have not been observed until this study to our knowledge, and ascribed to surface-excitons of the KCl film. The reasons are (a) peaks A and C were not observed in “bulk” spectrum; (b) the peaks A and C have larger or similar intensities compared with peaks B and D when thickness are small (< 5ML), that is, when the relative number of surface atoms to bulk atoms are larger than that in thicker film; and (c) peaks A and C were drastically decreased in intensities after exposure to a lot of residual gases (maybe, H<sub>2</sub>O, CO<sub>2</sub>, etc.). The surface core excitons are located at photon energy of 0.7 eV below the bulk excitons. Similar surface core excitons shifted by 0.7 eV from bulk core exciton were observed in the case of NaCl/Si(100) (Figure 2).

We also measured the Cl-2p photoelectron spectrum for KCl/Si(100) and NaCl/Si(100), and it was shown that no “surface core level shifts” in these systems.

Peak energies of core exciton are determined by energy-gap from the core level state to the empty state, and relaxation energy due to the interaction between core-hole and excited electrons ( mainly, Coulomb interaction ). It is considered that the surface shifts in absorption spectra are ascribed to the latter term. It may be due to the difference of dielectric function in the surface region from that in the bulk region.

Figures 2 show the “surface” absorption spectrum of NaCl/Si(100) at 105K( upper part ) and photoelectron spectra (lower part). The photon energies used in photoelectron spectra are indicated as a-f in the absorption spectra. Peaks are ascribed to Cl-LVV Auger electrons ( $2p^5 3p^6 \rightarrow 2p^6 3p^4 + e^-$ ), except peaks indicated by open triangles which are shifted as much as photon energies, which are ascribed to the direct photoelectron

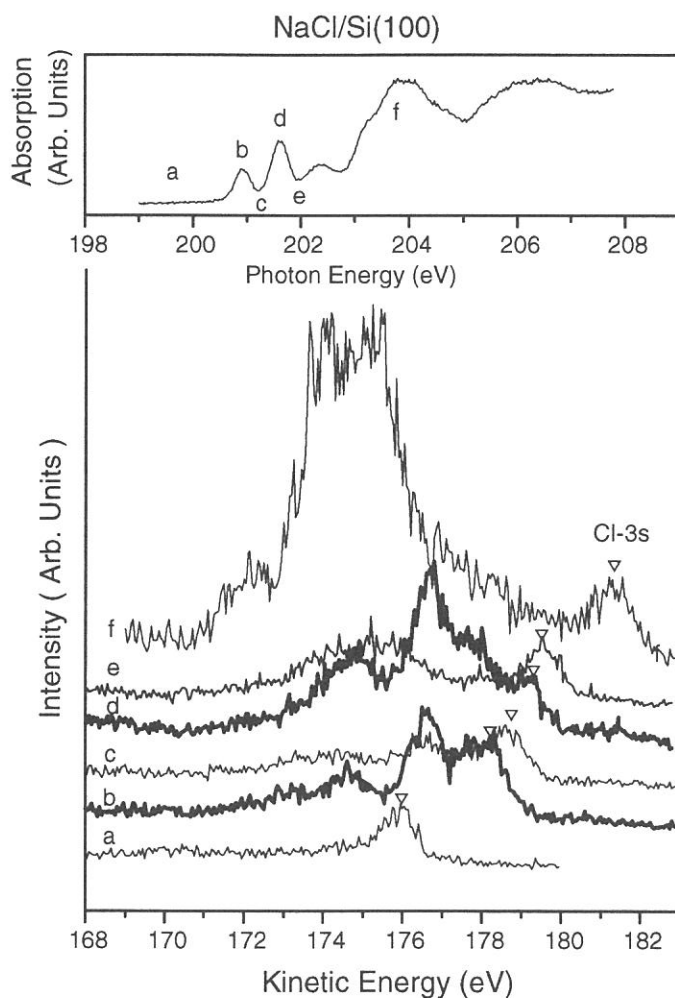


Figure 2

process. It makes additional screening to Cl 3p electrons from the outer potential, and thus, the Auger spectra are similar to the atomic one, not valence-like.

In conclusion, surface core exciton at Cl-L<sub>2,3</sub> edge on alkali chloride film were observed. Its excitation energy was shifted by 0.7eV compared to bulk core exciton. The photoelectron spectroscopy have shown that the “spectator” model is valid during the Auger-decay of these exciton.

photoelectron excitation from Cl-3s level. The spectra b and d correspond to the decay process of surface core exciton and bulk core exciton, respectively. 3 peaks are observed at similar energies ( overlapped with Cl-3s ) in the spectra b and d although the energies of exciton are different by 0.7 eV. These peaks were interpreted as <sup>1</sup>S, <sup>1</sup>D, <sup>3</sup>P configurations of final 3p<sup>4</sup> state of Cl atom. These interpretation suggest that the excited electron ( trapped near Cl atoms due to the interaction with core-hole ) stay as “spectator” and do not directly interact with 3p electrons during the decay

## Annealing effect of NaCl film on Si(100) surface (BL2B1)

S. Tanaka, M. Kamada and K-P. Lee\*

UVSOR Facility, Institute for Molecular Science, Okazaki 444, Japan

\*Kyungpook National University, Taegu 702-701 Korea

The growth of insulating film on the semiconductor surface is technologically important, and also interesting as a basic material science. In this study, we have investigated the NaCl film deposited on the Si(100)(2x1) surface. The lattice constant of NaCl crystal is 5.63 Å, and that of Si(100) surface is 5.43Å, therefore, the lattice misfit of NaCl/Si(100) interface is 3.7%. Recently, NaCl film on Ge(100) have been studied by Henzler et.al.<sup>1)</sup> and shown that epitaxial layer of NaCl was obtained at low temperature after annealing. It was ascribed to the fact the lattice constant of Ge(100) is 5.66 Å. and the lattice misfit is fairly small (~0.5%) for NaCl/Ge(100) interface. For NaCl/Si(100), the lattice misfit is larger than the NaCl/Ge(100), and it may be interesting to compare NaCl/Si(100) and NaCl/Ge(100).

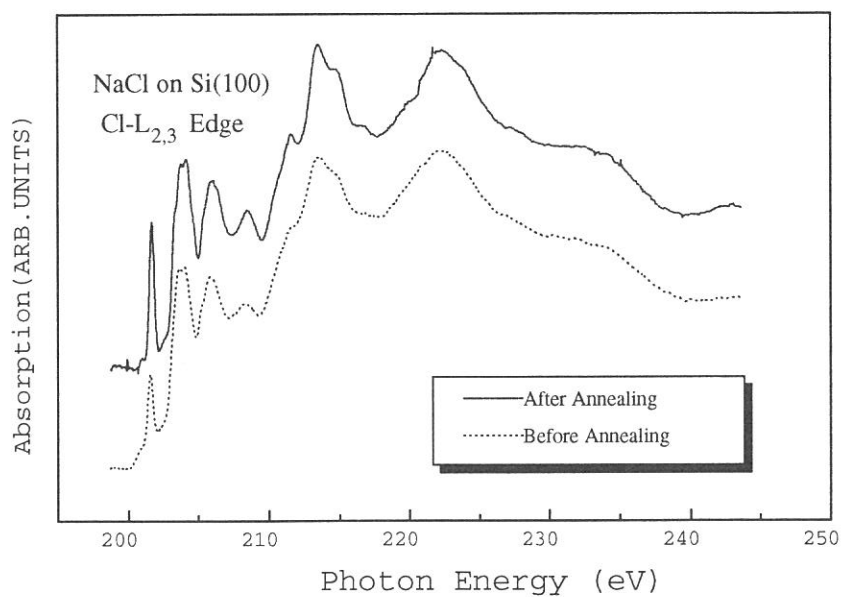
The experiments were performed at BL2B1. Si(100) surface has been prepared after several cycles of Ar-sputtering and annealing, until a sharp (2x1) LEED ( Low Energy Electron Diffraction ) pattern was observed. AES spectrum showed that there were no contamination. NaCl film were produced by thermal evaporation on the Si(100) surface kept at 105K. We used the Knusen-Cell (KC-3, WA Technology ) as the evaporator. The evaporation rate was very small ( estimated as ~0.3nm/min ), and the background pressure was  $1 \times 10^{-10}$  Torr. The thickness was estimated from the AES and the photoabsorption spectra. We observed the absorption spectrum ( via a total photoelectron yield ) and LEED. Charge-up effect was not observed in these measurements.

Figure 1 shows the Cl-L<sub>2,3</sub> edge absorption spectra of NaCl film on Si(100) ( thickness was estimated as 15nm ) as deposition and after annealing at 560K for 3min. The feature of the spectrum were not drastically changed, but every peaks became obviously sharpened after annealing. Figures 2 show LEED images of NaCl/Si(100) as deposition (a) and after annealing (b). Only diffused background was observed for NaCl/Si(100) without annealing [Fig.2(a)], while broad but clear (1x1) LEED pattern were observed for the surface after annealing. The spots were observed at nearly the same positions as the integral spots of (2x1) LEED pattern which had been observed for clean Si(100) in the same condition.

The change in absorption spectra and LEED images are interpreted to be due to the change of the structure in the NaCl film. Before annealing, no diffraction pattern was observed, and absorption spectra has a broad feature. These indicate that there is no long-range order and the amorphous-like configuration near Cl atoms in NaCl film before annealing. After annealing, film was crystallized, and LEED pattern was observed. However, the spot profile was broader than the case of NaCl/Ge(100)<sup>1)</sup>, which indicates that the crystalline portions are smaller in NaCl/Si(100). This is considered to be due to lager lattice misfit in NaCl/Si(100).

In conclusion, we have investigated the NaCl film evaporated on the Si(100) film, and shown that the annealing was effective to get a crystalline film, and better absorption spectrum.





**Figure 1.**  
 The Cl-L<sub>2,3</sub> absorption spectrum for the NaCl ( 30ML ) film deposited on Si(100) at 105K. Dotted line shows the spectra without annealing, and solid line shows that after annealing at 560 K for 3 minuets.

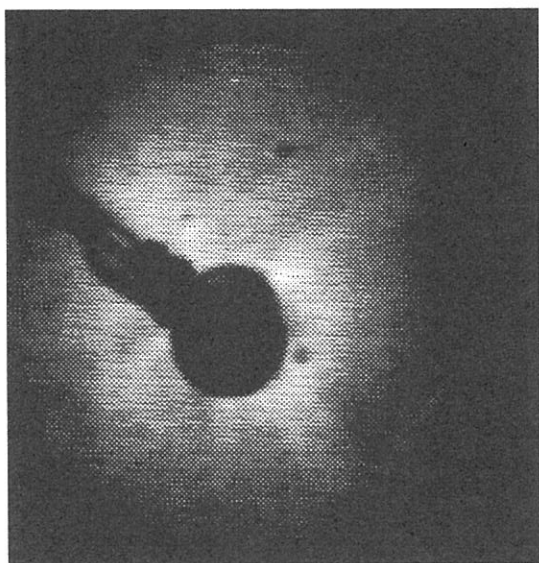


Figure 2(a)  
 LEED image from the Si(100)/NaCl before annealing



Figure 2(b)  
 LEED image from the Si(100)/NaCl after annealing

1) U. Barjenbruch, S. Fölsch and M. Henzler, *Surf. Sci.* 211/212(1989)749

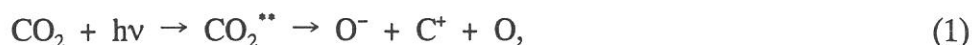


## Observation of Doubly Excited Rydberg States of CO<sub>2</sub> by Positive Ion–Negative Ion Coincidence Spectroscopy

Hiroaki YOSHIDA and Koichiro MITSUKE

*Department of Vacuum UV Photoscience, Institute for Molecular Science,  
Myodaiji, Okazaki 444*

Ion–pair formation processes of CO<sub>2</sub> are studied using synchrotron radiation to observe superexcited states CO<sub>2</sub>\*\* lying in the 25–37 eV excitation energy range. Positive ion–negative ion coincidence (PINICO) spectroscopy makes it possible to distinguish dissociation into three bodies,



or



from dissociation into two bodies,



Figure 1 shows the photodissociation efficiency curves for processes (1) and (3) in 25–37 eV. The efficiency for process (2) is negligibly small since no coincidence signals for O<sup>−</sup> and O<sup>+</sup> are observed. The curve for process (3) slowly falls with the increase of the photon energy, while that for process (1) makes a maximum at about 29.8 eV and then gradually fades out with showing some peak structures. A detection efficiency of an ion pair in a three–body dissociation is not so different from that in a two–body dissociation.<sup>1)</sup> It is, thus, concluded that the three–body dissociation (1) is dominant in the ion–pair formation from CO<sub>2</sub> above 26.6 eV.

Several resonance–like peaks are observed in the efficiency curves in Fig.1. Peaks appearing in the two curves are numbered from 1 to 16. The positions of the ionic satellite states (SAT) with multiple electron being excited are also indicated using previous photoelectron spectroscopy data.<sup>2)</sup> It is highly likely that most of the peaks are ascribed to transitions to superexcited states with double–electron excitation, judging from the electronic configurations of the satellite states which exist in this particular energy region. There are a number of doubly excited Rydberg

states in which an electron is promoted to an unfilled valence orbital and another electron to a Rydberg orbital. Excitation energy  $E_R$  for the Rydberg state is related to the vertical ionization energy  $E_I$  for the corresponding doubly excited ionic state by the Rydberg formula

$$E_R = E_I - R/(n-\delta)^2, \quad (4)$$

where  $R$ ,  $n$ , and  $\delta$  are the Rydberg constant, the principal quantum number, and the quantum defect, respectively. Comparing  $E_R$  obtained using eq. (4) with the peak energies in Fig.1, we will make tentative assignments of Peaks 1–16. Analysis of the shape of coincidence signals show that the three-body dissociation (1) results from a transition to a superexcited state  $\text{CO}_2^{**}$  with  ${}^1\Sigma_u^+$  symmetry. With this symmetry restriction, a possible configuration of the involved Rydberg state converging to SAT VI is  $(3\sigma_u)^{-1}(1\pi_u)^{-1}(2\pi_u)^1(ns\sigma_g)^1 {}^1\Sigma_u^+$ . As shown in Fig.2, the positions of Peaks 4,8–10 are in fair agreement with those expected from  $E_R$  values for several doubly excited Rydberg states.

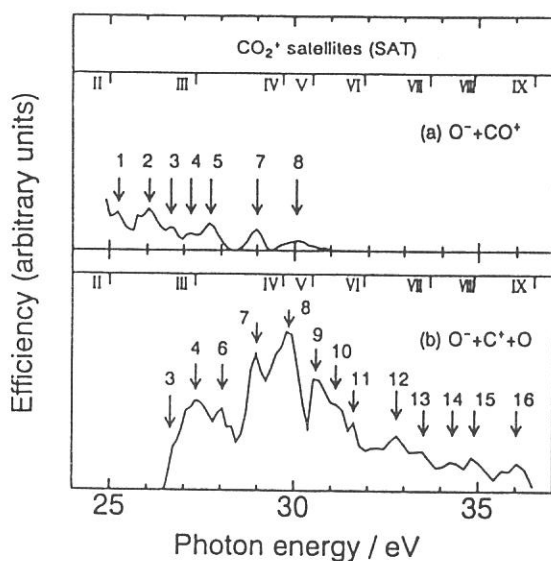


Fig.1 Photodissociation efficiency curves for the ion-pair formation from  $\text{CO}_2$  as a function of the photon energy. (a) the two-body dissociation  $\text{CO}_2+h\nu\rightarrow\text{O}^-+\text{CO}^+$  and (b) the three-body dissociation  $\text{CO}_2+h\nu\rightarrow\text{O}^-+\text{C}^++\text{O}$ .

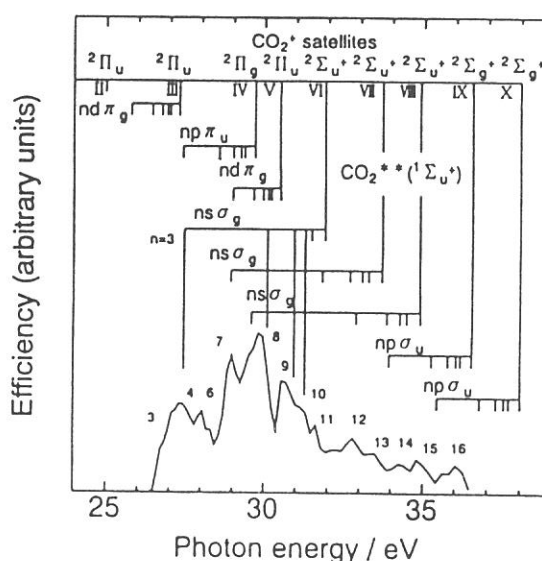


Fig.2 Photodissociation efficiency curve for the three-body dissociation  $\text{CO}_2+h\nu\rightarrow\text{O}^-+\text{C}^++\text{O}$  in the photon energy range of 25–37 eV.

#### References

- 1) H. Yoshida and K. Mitsuke, *J. Chem. Phys.* **100**, 8817 (1994).
- 2) P. Roy et al., *J. Chem. Phys.* **84**, 2050 (1986).

## Photodarkening Phenomena in Amorphous Chalcogenide Films

Koji HAYASHI, Daisaku KATO\*, and Koich SHIMAKAWA\*

*Institute for Molecular Science, Okazaki 444*

*\*Department of Electronics and Computer Engineering, Gifu University, Gifu 501-11*

Amorphous chalcogenide semiconductors, such as  $\text{As}_2\text{S}_3$ , is presenting variety of photoinduced phenomena, and is expected as a potential material for photofunctional devices. However, the details of the mechanism are still unknown. We have been investigating for what kind of photoinduced effects in those materials occurs by exciting inner core electron with the irradiation of the vacuum ultra-violet (VUV) light. We reported that photodarkening is caused with the irradiation of the VUV light. In this report, we investigate the difference between the irradiation of the VUV light and that of the light with the energy corresponding to the optical bandgap.

Thin films of amorphous  $\text{As}_2\text{S}_3$  were prepared onto Corning 7059 substrates by the conventional evaporation technique. After evaporation, samples were annealed at near the glass-transition temperature for two hours in vacuum with a pressure of  $1 \times 10^{-6}$  Torr. The experiments of the VUV light were performed at BL3A1 beam line of the UVSOR facility in Okazaki. The VUV light was used the light that is filtered through a Al film from undulator line and have 45 eV photon energy. The bandgap light was obtained from a high pressure mercury lamp with water filter. These irradiation were performed in a vacuum at room temperature.

Figure 1 shows the growth kinetics of the energy shift in the absorption edge. As in the figure, the photodarkening phenomenon has the different growth kinetics between two light sources. The growth rate in the VUV light is extraordinary bigger than that in the bandgap light.

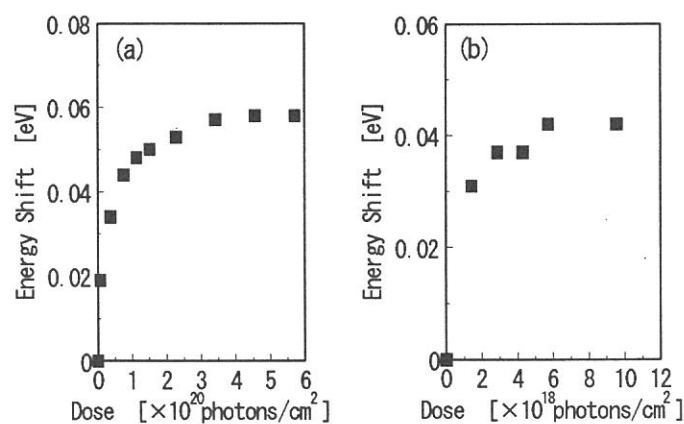


**Figure 1** The energy shift in the absorption edge (a)for the bandgap light and (b)for the VUV light.



Prof. K. Nakagawa of Kobe Univ. is working at BL1B with two students.



Prof. T. Ibuki (left) and Dr. A. Hiraya are analyzing the data obtained at BL8B1.

## Preparation of ZnO thin films from DEZn at various temperatures using undulator radiation (UR)-excited CVD

A. Ganjoo, S. Ikeda, K. Maeda and A. Yoshida  
*Toyohashi University of Technology, Toyohashi 441*

Recently, ZnO thin films have gained much attention as a window material for solar cells due to high transparency. We have already prepared ZnO films using UR excited photo CVD at room temperature. In the present work, we have deposited thin films of ZnO from DEZn (diethyl-zinc) and O<sub>2</sub> on Si substrates at various substrate temperatures and by varying the O<sub>2</sub>/DEZn ratio. UR light has been used in the deposition of ZnO thin films due to its high photon energy, changeable wave length, quasi monochromatic behavior and clean environment. The films were characterized by in-situ XPS and Auger Electron Spectroscopy (AES).

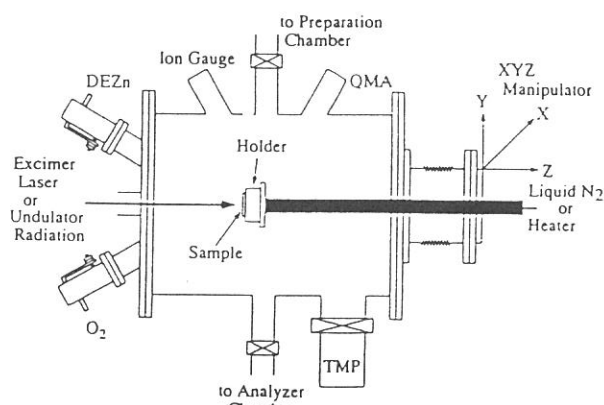
The experimental set up for the deposition of ZnO films consists of three chambers, namely, preparation, growth and analyzer chambers. The block diagram of the set up is shown in Fig. 1. The substrate temperature was varied from -100 ~ 150°C. Oxygen and DEZn were used as the source gases and their ratios were varied as 10, 100 and 1000. The UR light from beam line BL-3A1 was used as the light source. The spectrum of UR with gap length of 60 mm has a peak at 36.0 eV. The compositional analysis was carried out using XPS and AES.

Fig. 2 shows the change in oxygen content in the films as a function of source gas ratios at various substrate temperatures as observed by AES. As the substrate temperature is increased, the oxygen content is found to increase. However, as the gas ratio increases, the change becomes less prominent and for the gas ratio 1:1000, nearly no change is observed. As the partial pressure of DEZn and O<sub>2</sub> is constant for all the temperatures for a particular gas ratio the behavior of oxygen inclusion can be explained on the basis of the available sites on the growing film.

Fig. 3 shows the variation of carbon content as a function of initial gas ratios at various substrate temperatures. As can be seen from the figure, with increase in the oxygen content, carbon atoms are reduces considerably in the films for all substrate temperatures. We attribute this behavior to the fact that since UR has a high photon energy, it can break all the bonds and carbon is easily produced. That may be the reason for having high carbon contents with low initial oxygen ratios. For high oxygen ratios, carbon atom easily reacts with oxygen to form CO<sub>x</sub> and thus the carbon content decreases to nearly zero.

The thickness of the films was estimated as a function of substrate temperature and the activation energy has been calculated. The variation of thickness is shown in Fig. 4. The activation energy is found to be  $-0.019$  eV. The negative activation energy indicates that the surface reactions are prominent than the gas phase reactions. At low temperatures, since the residence time of the adsorbed DEZn molecules is long, there are many DEZn molecules on the substrate surface, resulting in a high deposition rate. However, at high temperatures, the residence time becomes short, and the number of Zn atoms on the surface for the film is reduced.

Thus, we have deposited carbon-free thin films of ZnO at  $150^{\circ}\text{C}$  and/or for various higher gas ratios. We consider that variation of substrate temperature results in the variation of residence time of DEZn, which influences the change in the oxygen and carbon content and deposition rate of the films.



**Fig. 1**

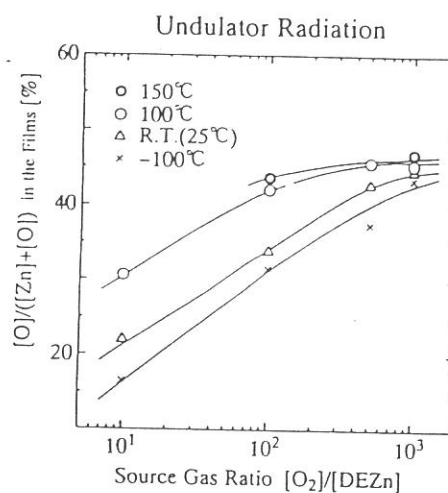


**Fig. 2**

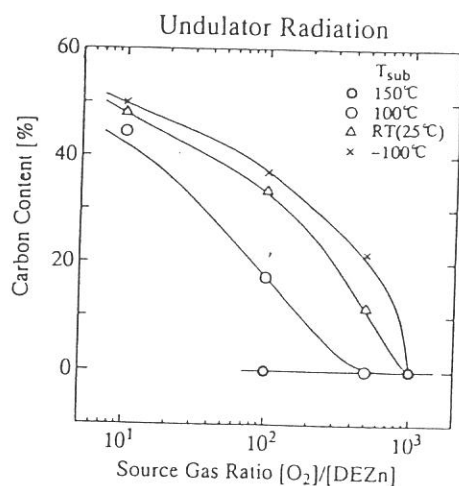


**Fig. 3**

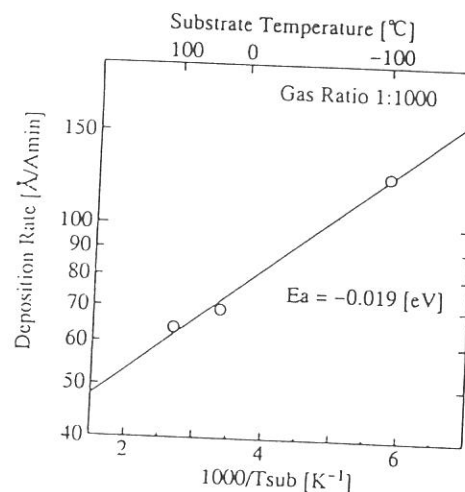


**Fig. 4**



## Time Response of Excited-State Na Desorption from NaCl (Temperature Dependence)

Sayumi Hirose and Masao Kamada

*Institute for Molecular Science, Myodaiji, Okazaki 444*

Bombardment of solids by energetic electrons and photons induces the desorption of constituents from the surface. Although there have been reported many desorption studies in alkali halides, the desorption mechanism is not definite since dynamics have not been investigated in detail yet. Time response of ground-state alkali desorption from alkali halides has been reported to be in the scale of ms to  $\mu$ s by Loubriel *et al.*,<sup>1)</sup> Green *et al.*,<sup>2)</sup> and Kanzaki and Mori,<sup>3)</sup> but there is no data about time-response of photon-stimulated desorption (PSD) of excited-state alkali atoms except our reports. We have reported that the time response of excited-state alkali desorption consists the fast component in the ns range and the slow component between 178 ns and 3 ms.<sup>4,5)</sup> We have also proposed two desorption mechanism of excited-state alkali atoms. On the basis of the substance dependence, it becomes evident that the substance having a larger Rabin-Klick parameter shows a larger efficiency of the fast desorption. This result indicates that the lattice instability due to the electronic excitation in the surface layers may play an important role on the fast PSD of excited-state alkali atoms. On the other hand, the slow component of excited-state alkali desorption is seemed to be in the time scale of ground-state alkali desorption. The desorption process of ground-state alkali atoms is related to the diffusion of F or  $V_K$  centers and the surface reaction of F centers and alkali ions. Therefore, the slow PSD may be due to the thermal instability of surface defects. In order to know the validity of the desorption mechanism as mentioned above, we have measured the temperature dependences of two components.

The experiments were carried out with a time-correlated single photon counting method by using synchrotron radiation pulses under a single-bunch operation at a undulator beam line 3A1. The undulator radiation was used as an excitation source through a 1300-Å-thick aluminum filter. The time width of incident photon pulse including the detector system was about 480 ps and the interval of successive pulses was 178 ns. Any component slower than the time interval shows up as pileup in the background. The time response of excited-state alkali desorption was also measured in the range of 3 - 300 ms by using a mechanical chopper. Single crystals of NaCl were

cleaved with a knife edge in a sample chamber, base pressure of which was about  $2 \times 10^{-7}$  Pa.

Figure 1 shows the temperature dependences of the fast and slow components for excited-state Na desorption from NaCl. The ratio between the fast and slow components at each temperature was estimated from the integrated intensities in the time range of 0 to 178 ns. By using the ratio between the fast and slow components at each temperature and the temperature dependence of the total desorption yield, the temperature dependences of the fast and slow components were derived. As seen in Fig. 1, the fast component does not strongly depend on the sample temperature, while the slow component increases above 200 K and disappears about 420 K, with having a prominent peak at 285 K. The present results of the temperature dependences support our two desorption model, where the fast and slow desorptions are due to the electronic transition in the surface layer and the thermal instability of surface defects, respectively.

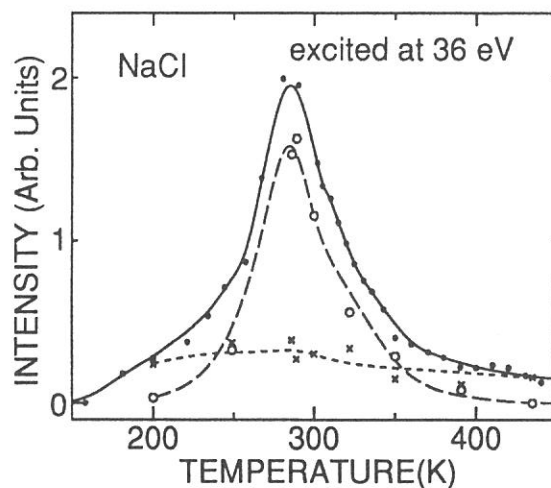


Fig. 1. Temperature dependence of excited-state Na desorption from NaCl. Solid circles, crosses and open circles are total desorption yield, the fast and slow components, respectively. Curves were drawn as a guide.

## References

- 1) G. M. Loubriel, T. A. Green, P. M. Richards, N. H. Tolk, R. H. Albridge, R. F. Haglund, K. J. Snowden, L. T. Hudson, D. W. Cherry, R. K. Cole, M. H. Mendenhall, D. M. News, and P. M. Savundararaj, *Phys. Rev. Lett.* 57, 1781 (1986).
- 2) T. A. Green, G. M. Loubriel, P. M. Richards, N. H. Tolk, and R. F. Haglund, Jr., *Phys. Rev. B* 35, 781 (1987).
- 3) H. Kanzaki and T. Mori, *Phys. Rev. B* 29, 3573 (1984).
- 4) S. Hirose and M. Kamada, *Phys. Rev. B* 48, 17641 (1993).
- 5) S. Hirose and M. Kamada, *J. Phys. Soc. Jpn.* 63, 1053 (1994).

## Observation and investigation of solid C<sub>60</sub>F<sub>48</sub> and C<sub>70</sub>F<sub>58</sub> luminescence

A. Kolmakov, V. Stankevitch, V. Bezmelnitsin, A. Rizkov, V. Sokolov,  
and N. Svechnikov

RRC "Kurchatov Institute" Moscow, Russia

I. Akimoto, T. Matsumoto, and K. Kan'no

Kyoto University, Japan

S. Hirose and M. Kamada

IMS UVSOR Okazaki, Japan

The highly fluorinated C<sub>60</sub> continues the new family of high symmetric topologically unusual carbon based molecules. However, very little is known about electronic structures of these materials. We have investigated the luminescence properties of halogenated fullerenes at BL3A1 in order to understand the electronic structures of these materials.

C<sub>60</sub>F<sub>48</sub> (C<sub>70</sub>F<sub>58</sub>) were synthesised by fluorination of the proper fullerene with KrF<sub>2</sub> in anhydrous HF solution under normal conditions. The powder of C<sub>60</sub>F<sub>48</sub> was deposited on the copper plates and put on the sample holder of the cryostat in the vacuum chamber. Two different light sources were used for luminescence excitation: the undulator light 36 eV 10<sup>14</sup> phot/sec mm<sup>2</sup> and eximer ArF-6.4 eV (KrF-5 eV) laser.

The typical solid C<sub>60</sub>F<sub>48</sub> luminescence spectrum is shown in Fig. 1, with the absorption spectrum of C<sub>60</sub>F<sub>x</sub> (38 < x < 48) dissolved in C<sub>6</sub>F<sub>6</sub>(1). For comparison the solid C<sub>60</sub> luminescence spectrum is also included as a curve C. Using C<sub>60</sub> as a reference C<sub>60</sub> luminescence signal one can roughly estimate the quantum yield of C<sub>60</sub>F<sub>48</sub> emission to be in the order of 10<sup>-4</sup>. The luminescence spectra obtained at different excitation energies 36, 6.4, and 5.5 eV are similar with each other. It is also necessary to note that C<sub>70</sub>F<sub>58</sub> luminescence spectra are similar to those of C<sub>60</sub>F<sub>48</sub>.

The luminescence kinetics of C<sub>60</sub>F<sub>48</sub> (C<sub>70</sub>F<sub>58</sub>) were measured in nanoseconds range by using synchrotron radiation pulses under the single bunch operation. As shown in Fig. 2, the decay curve can be fitted by two exponents with the time constants T<sub>1</sub> < 1 ns and T<sub>2</sub> being in the order of 100 ns. There is no temperature dependence of the decay curves.

The similarity of the luminescence spectra obtained at different excitation energies and the luminescence kinetic behaviour show that the relaxation from the highest electronic states to the emitting one is rather fast. Moreover, the dose-dependence and photodesorption data indicate that the CF-group could be responsible for absorption and luminescence behaviour of C<sub>60</sub>F<sub>48</sub>

and C<sub>70</sub>F<sub>58</sub>. Further experiments with other halogenated fullerenes should be carried out to confirm this interpretation.

## REFERENCES

1. A.A.Tuinman, P.Mukherjee, J.L.Adcock, R.L.Hettich and R.N.Compton, J.Phys. Chem. 1992, 96, 7584-7589

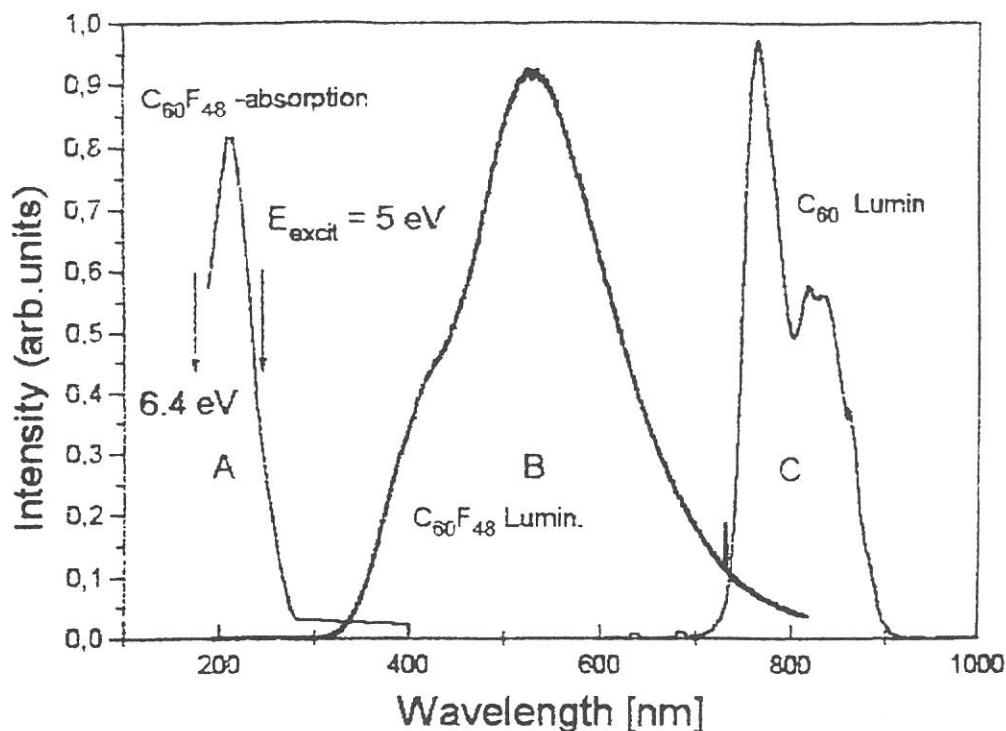


Fig.1. Absorption and luminescence spectra: curve {A}- C<sub>60</sub>F<sub>x</sub> - absorption (38<x<48) dissolved in C<sub>6</sub>F<sub>6</sub> [1], {B}- C<sub>60</sub>F<sub>48</sub> - uncorrected luminescence; for comparison {C}-C<sub>60</sub>- luminescence

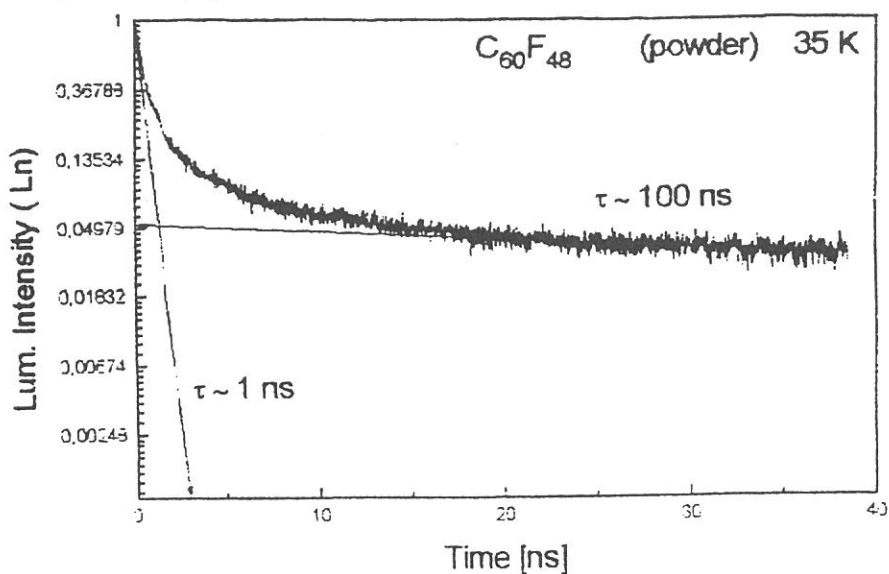


Fig.2 Luminescence kinetics for C<sub>60</sub>F<sub>48</sub> at nanoseconds range

## Radiative Transitions in C<sub>60</sub> Thin Films under SR Excitation.

M.A.Terekhin, N.Yu.Svechinikov, M.Kamada\*, K.Kan'no#, V.G.Stankevitch, A.A.Kolmakov, V.A.Stepanov, V.N.Bezmelnitsin, T.Matsumoto#, I.Akimoto#, A.Ohnish# and M.Ashida#.

*Russian Resarch Center "Kurchatov Institute", Moscow, Russian Federation*

*\*) Institute of Molecular Science, Myodaiji, Okazaki, Japan*

*#) Department of Physics, Kyoto University, Kyoto 606, Japan*

Photoluminescence properties of pure C<sub>60</sub> thin solid films have been investigated in the emission range of 1.2-2.4 eV over a wide temperature interval under excitation with 36 eV photons from the undulator at BL3A1. The 0.6-1.0 μm solid films of pure C<sub>60</sub> on quartz substrate were prepared at Kurchatov Institute.<sup>1)</sup> The samples were annealed at 250 C for 10 h under ultra-high vacuum of 10<sup>-9</sup> Torr, and were cooled down to 13 K to measure emission spectra, luminescence degradation, temperature dependence, photoluminescence decay, and ambient gas pressure influence on luminescence. The decay time measurements were performed in the single-bunch operation mode using a conventional TAC method of a photon counting mode.

The luminescence spectrum at 13 K is presented in Fig. 1, along with a near edge absorption spectrum of the same film measured at 77 K. Besides a broad main peak at 1.67 eV, a vibronic structure of a C<sub>60</sub> molecule is demonstrated on the low energy side of the luminescence spectrum; a shoulder at 1.60 eV and a second peak at 1.50 eV. A similar vibronic structure is recognized in the absorption spectrum, from which one may deduce a value of E<sub>g</sub>=1.85 eV. This threshold energy may correspond to the zero-phonon transition of the singlet Frenkel exciton, which originates from the parity-forbidden H<sub>1u</sub> --> T<sub>1u</sub> (HOMO-LUMO) transition of an isolated C<sub>60</sub> molecule.<sup>2)</sup> The decay curve of integrated emission intensity at 13 K, obtained after extracting the background signal, exhibited approximately a single exponent with the lifetime of 1.2 ns. Temperature dependence of luminescent intensity exhibited a step-like peculiarity in the vicinity of the structural phase transition near T<sub>C</sub> ~ 260K.

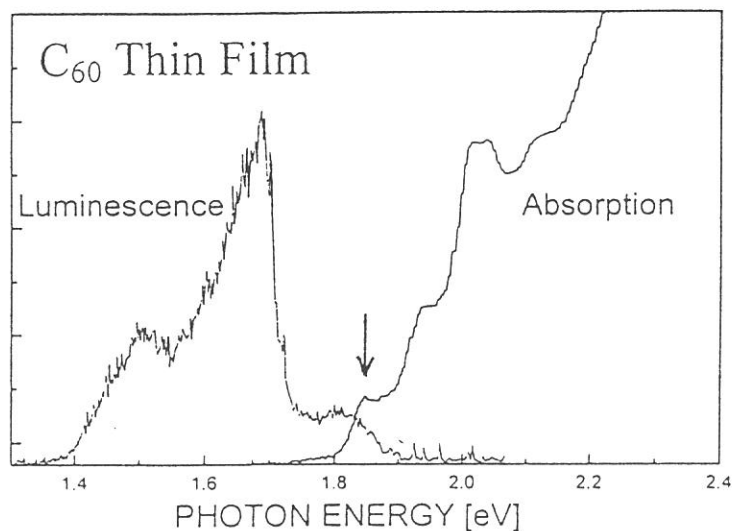


Fig. 1.

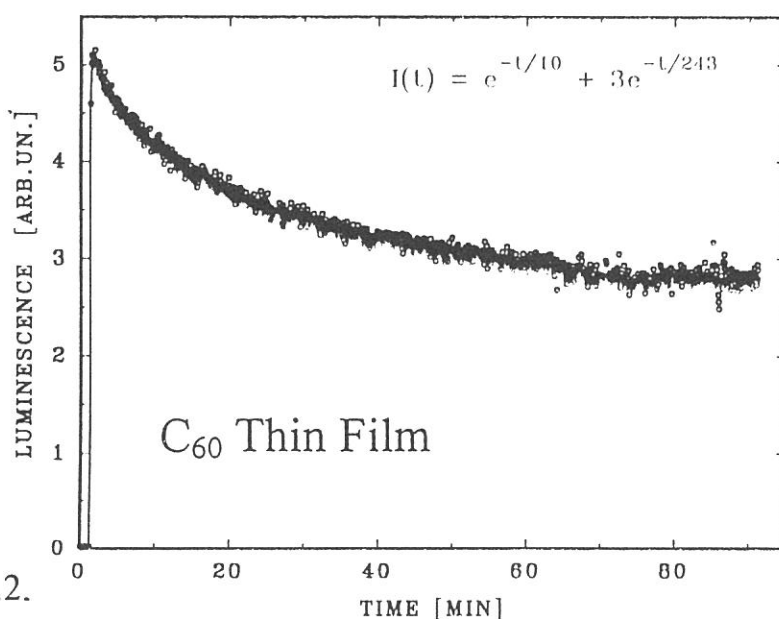


Fig.2.

As shown in Fig.2, degradation of a photoluminescence intensity during long time irradiation has manifested in all the experiments in ultra-high vacuum conditions, though almost no visual defects were observable under microscope on the film surface. One of the explanations for the degradation may be attributed to the polymerization process.

### References

- 1) M.A.Terekhin, N.Yu.Svechnikov, V.G.Stankevitch, A.A.Kolmakov, V.A.Stepanov, V.N.Bezmelnitsin, M.Kamada and K.Kan'no: Optics and Spectroscopy (1994, in press)
- 2) M.Matus, H.Kuzmany, E.Sohmen: Phys. Rev.Lett. 68, (1992), 2822. □



**DISSOCIATIVE PHOTOIONIZATION OF IRON PENTACARBONYL IN THE  
RANGE 30–120 eV. I. OBSERVATION OF NEW MOLECULAR  
DICATIONS AND C–O BOND RUPTURE IN THE LIGAND**

Yusuke TAMENORI and Inosuke KOYANO

*Department of Material Science, Himeji Institute of Technology,  
Kamigohri, Hyogo 678–12*

Photodissociation and dissociative photoionization of transition metal carbonyls, especially those of iron pentacarbonyl, have received considerable attention over the past decade, since it has been widely recognized that the study of such processes are important in understanding the unique bonding properties and reactivity of these compounds. However, almost all previous studies, regardless of the wavelength range used, or whether they utilized a single photon or multiphoton process, concerned only with the scission of the metal–carbonyl coordination bonds, as is also the case with electron impact and metastable neutral impact studies. Although the breakage of the covalent C–O bond(s) in the ligand is energetically possible above ~11.2 eV (in the case of neutral fragmentation) or above ~20 eV (in the case of ionic fragmentation), no such studies have been reported in the past, in both neutral and ionic dissociations, except an inner-shell excitation/ionization study of  $\text{Cr}(\text{CO})_6$ .<sup>1</sup> Detailed studies of such processes, if occur at all, over a wide range of excitation energies are expected to provide a unique opportunity to investigate intramolecular energy transfer between the weak coordination and strong covalent bonds.

We have initiated a series of detailed studies of dissociative photoionization of metal carbonyl vapor in the energy range 30–120 eV, using a TOF mass spectrometry and a photoion–photoion coincidence technique. The apparatus used is that installed on the BL3A2 beamline with a constant deviation grazing incidence monochromator, the details of which have been described elsewhere.<sup>2</sup> All measurements were carried out at the angle of  $55^\circ$  with respect to the polarization vector of the incident photon (so-called "magic angle") to avoid the effect of the anisotropic angular distribution of photoelectrons. The present paper reports a mass spectrometric observation of ionic fragmentation products, which provides a clear evidence for the occurrence of C–O bond rupture in the ligand without breaking the coordination bond.

Figure 1 shows an example of TOF mass spectrum taken at an incident photon energy of 70 eV and a drift tube length of 25.2 cm. As can be seen, the most abundant ions are those corresponding to the formula  $\text{Fe}(\text{CO})_n^+$  ( $n=0-5$ ) with  $n=0$  and 1 peaks being especially strong, and  $\text{CO}^+$ . These ions are evidently produced by simple scission of (a) Fe–CO coordination bond(s) in a single or multiple charged parent ion. In addition to these, however, many interesting fragment ions are seen to be formed, although the abundances are much smaller than those of the ions formed by the Fe–CO bond scission. These include  $\text{FeC}(\text{CO})^{2+}$  and  $\text{FeC}^+$ , which definitely indicate the occurrence of C–O bond breakage in the ligand without breaking the weak coordination bond, and  $\text{CO}_2^+$  which indicates a drastic rearrangement occurring before or during the fragmentation process of parent ions. It is also noteworthy that many previously unknown doubly charged molecular ions, *i.e.*,  $\text{Fe}(\text{CO})_n^{2+}$  ( $n=0-4$ ) as well as the above-mentioned ones, have been observed here for the first time. However, it is to be noted that the occurrence of  $\text{Fe}(\text{CO})_n^{2+}$  ions with  $n=0, 2$  and  $4$  cannot be conclusive from the mass spectrometric measurements alone, since the  $m/z$  values of these dications coincide with those of  $\text{CO}^+$ ,  $\text{Fe}^+$ , and  $\text{Fe}(\text{CO})^+$  monocations, respectively.

It should also be emphasized that the singly charged parent ions  $\text{Fe}(\text{CO})_5^+$  have been observed, demonstrating the existence of non-dissociating ionic states, *i.e.*, states with a lifetime

of  $\sim 5 \mu\text{s}$  or more even at 70 eV of ionizing photons. On the other hand, the appearance energy of doubly charged ions, has been estimated to be around 38 eV, which corresponds to the binding energy of the  $\text{CO}:3\sigma$  inner valence electron. Further analysis is in progress to find out the dissociation pathways to these interesting ions.

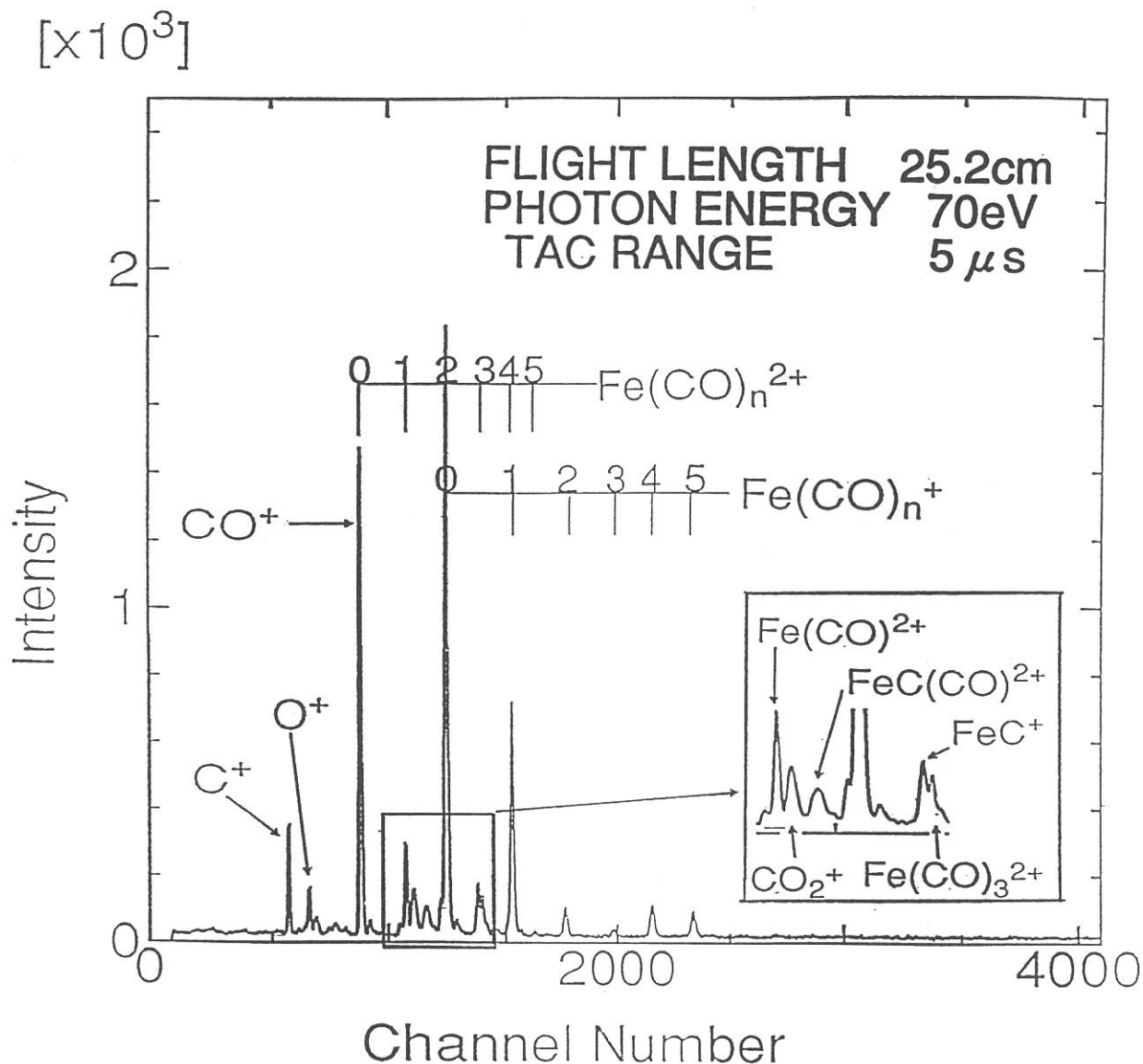


Figure 1. TOF mass spectrum of  $\text{Fe}(\text{CO})_5$  at 70 eV of incident photons.

## REFERENCES

1. C.-T. Chen, Dissertation, University of Pennsylvania, 1985.
2. T. Masuoka, T. Horigome, and I. Koyano, *Rev. Sci. Instrum.* **60**, 2179 (1989); T. Masuoka and I. Koyano, *J. Chem. Phys.* **95**, 909 (1991).

## DISSOCIATIVE PHOTOIONIZATION OF IRON PENTACARBONYL IN THE RANGE 30–120 eV. II. A PHOTOION–PHOTOION COINCIDENCE STUDY OF THE DISSOCIATION OF DOUBLY AND TRIPLY CHARGED PARENT IONS

Yusuke TAMENORI and Inosuke KOYANO

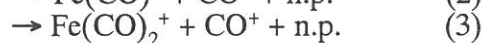
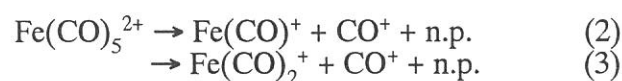
*Department of Material Science, Himeji Institute of Technology,  
Kamigohri, Hyogo 678–12*

In order to elucidate dissociation pathways to various fragment ions observed mass spectrometrically (preceding report), we have performed a TOF photoion–photoion coincidence (PIPICO) measurements among fragment ions resulting from irradiated iron pentacarbonyls in the photon energy range 30–120 eV. The apparatus and procedure have been described elsewhere.<sup>1</sup> Branching ratios for various ion–pairs was determined as a function of photon energy and their appearance potentials estimated.

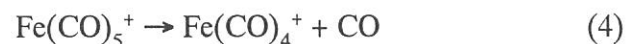
Figure 1 shows a PIPICO spectrum taken at an incident photon energy of 100 eV with a drift tube length of 25.2 cm. A novel feature here is the observation of the dissociation of triply charged molecular ions into dication–monocation pairs as evidenced by the  $\text{CO}^+ + \text{Fe}(\text{CO})_2^{2+}$  and  $\text{CO}^+ + \text{FeC}(\text{CO})_2^{2+}$  coincidence peaks. Unfortunately, however, only these two weak peaks provide conclusive evidence for such processes, because, in this system, all other peaks that are assignable as a dication–monocation coincidence are exactly overlapped by a peak corresponding to a monocation–monocation coincidence, as indicated in the figure, owing to the fact that the mass of Fe is exactly twice the mass of CO. Judging from the above–mentioned two peaks, there may be still other dication–monocation channels, but their branching ratios may not be large. Thus, if we assume that other peaks consist dominantly of the monocation–monocation contribution indicated for each peak in Fig. 1, then we find that the overwhelmingly dominant disociation channel of  $\text{Fe}(\text{CO})_5^{2+}$  at 100 eV is



where n.p. represents neutral products. It is to be noted that coincidence between  $\text{CO}^+$  and  $\text{Fe}(\text{CO})_2^+$ , as well as that between  $\text{CO}^+$  and  $\text{Fe}(\text{CO})_3^+$  has been observed but no coincidence occurred between  $\text{CO}^+$  and  $\text{Fe}(\text{CO})_3^+$  nor between  $\text{CO}^+$  and  $\text{Fe}(\text{CO})_4^+$ . The intensity of  $\text{Fe}(\text{CO})_3^+$  in mass spectrum is extremely weak but that of  $\text{Fe}(\text{CO})_4^+$  is as strong as that of  $\text{Fe}(\text{CO})_2^+$  (preceding report). Thus the above fact conclusively indicates that the following two reactions occur in addition to reaction (1),



but  $\text{Fe}(\text{CO})_4^+$  exclusively originates from singly charged parent ion:



It is also interesting to note that the fragment ion  $\text{FeC}^+$ , which must have been produced in a process involving a C–O bond fission in the ligand (leaving the C atom on Fe), gives coincidence with both  $\text{O}^+$  and  $\text{C}^+$  with almost equal intensity. The  $\text{FeC}^+ - \text{C}^+$  coincidence evidently requires fission of at least two C–O bonds; one in a state bonded to Fe, and another probably in the dissociated free  $\text{CO}^+$  state. Thus it may be concluded that the  $\text{O}^+$  ion coincident with  $\text{FeC}^+$  is of the same origin as the  $\text{C}^+$  ion giving the  $\text{FeC}^+ - \text{C}^+$  coincidence, *i.e.*, free  $\text{CO}^+$ :

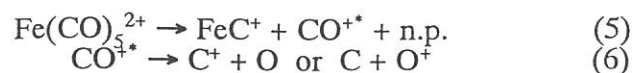
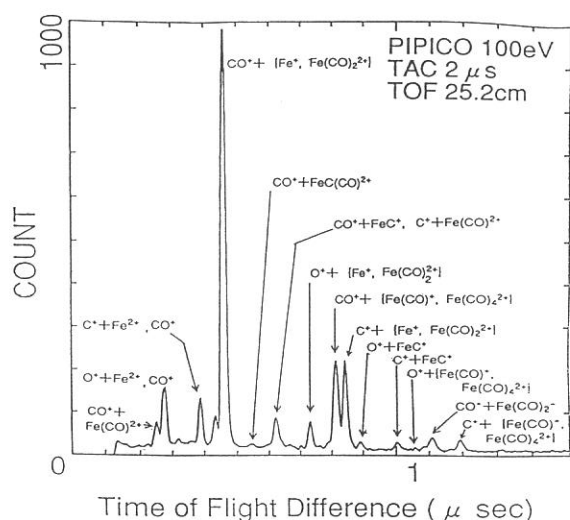
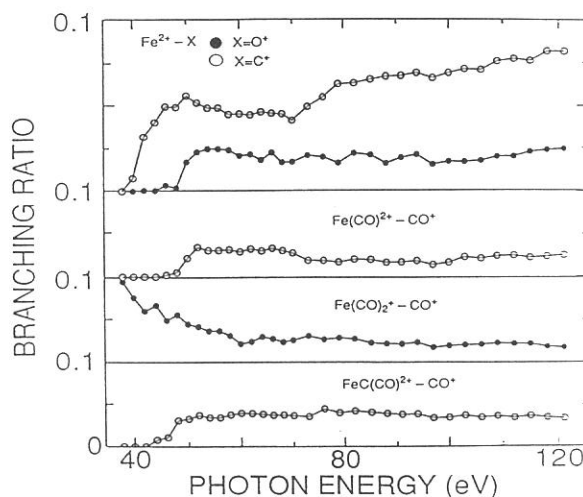
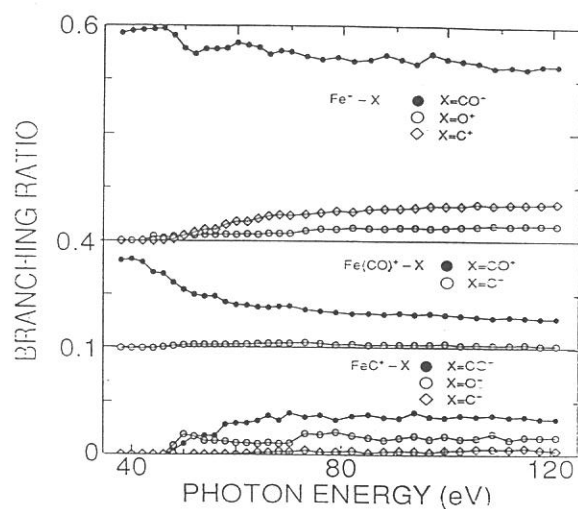


Figure 2 shows the PIPICO branching ratios as a function of the incident photon energy. For the ions that have a threshold in the energy range studied, appearance potentials (APs) have been estimated. It has been found that the ion pairs are divided into two groups according to the APs, one having the AP of around 38 eV and the other around 44 eV. The former AP approximately corresponds to the IP of  $\text{CO}:3\sigma$  inner-valence electron and the latter AP lies slightly above the  $\text{CO}^{2+}$  threshold energy.



**Figure 1** A PIPICO spectrum of  $\text{Fe}(\text{CO})_5$  taken at 100 eV of incident photons.



**Figure 2** PIPICO branching ratios for various ion pairs from  $\text{Fe}(\text{CO})_5$  as a function of incident photon energy.

## REFERENCES

1. T. Masuoka, T. Horigome, and I. Koyano, *Rev. Sci. Instrum.* **60**, 2179 (1989); T. Masuoka and I. Koyano, *J. Chem. Phys.* **95**, 909 (1991).

DISSOCIATIVE SINGLE AND DOUBLE PHOTOIONIZATION OF CS<sub>2</sub>

Toshio MASUOKA

Department of Applied Physics, Faculty of Engineering  
Osaka City University, Sugimoto 3, Sumiyoshi-ku, Osaka 558

In order to study dissociative single and double photoionization of CS<sub>2</sub>, time-of-flight (TOF) mass and photoion-photoion-coincidence (PIPICO) spectra were measured in the region 37-120 eV by the use of a constant-deviation grazing incidence monochromator together with synchrotron radiation. Aluminum optical filters were used to eliminate higher-order radiation. The drift tube of the TOF mass spectrometer was 2.9 cm long and the TOF mass and PIPICO spectra were measured at an angle of about 55° with respect to the polarization vector where the second-order Legendre polynomial is close to zero, thus minimizing any effects of anisotropic angular distribution of fragment ions.

The TOF mass spectrometer was operated in two modes for the measurement of TOF mass spectra. In mode A, the photoelectron signal detected by a channel electron multiplier was fed into the start input of a time-to-amplitude converter (TAC). The storage ring was operated in a multi-bunch mode. In this mode of operation of the TOF mass spectrometer, the relative ion yields in single and double photoionization are affected by the different kinetic energies of individual photoelectrons and by the different numbers of photoelectrons in the two processes. At  $h\nu=60$  eV, for example, the kinetic energy of a photoelectron ejected from CS<sub>2</sub> (forming the ground state of CS<sub>2</sub><sup>+</sup>) is about 50 eV, whereas that of a photoelectron (forming the ground state of CS<sub>2</sub><sup>2+</sup>) is about 33 eV as a maximum. These more energetic photoelectrons produced by single photoionization are more easily discriminated in the TOF mass spectrometer than those produced by double photoionization, resulting in an underestimation of the number of ions produced in single photoionization. Furthermore, the different numbers of ejected electrons in single and double photoionization causes an overestimation of the number of the ions produced in double photoionization because the probability of forming one output pulse in the electron detector is higher for two electrons hitting simultaneously than that for one electron.

In mode B, the rf frequency (90.115 MHz) of the storage ring was used as the start signal of the TAC by reducing it to 1/32 through a frequency demultiplier. The storage ring was operated in a single-bunch mode, which was essential to obtain meaningful TOF mass spectra. In mode B, it is believed that the observed mass spectra are free from the discrimination effects mentioned above because the ratio of the partial cross sections  $\text{Ar}^{2+}/\text{Ar}^+$  measured in the region from the double-photoionization threshold to 100 eV was in good agreement with previous reports.<sup>1</sup> The collection efficiencies of energetic fragment ions in the TOF mass spectrometer were calculated with a computer program. The results show that the collection efficiency for the S<sup>+</sup>+CS<sup>+</sup> ion pair having 8.5-eV kinetic energy is 90 % and that with 20-eV kinetic energy is 84 %. This discrimination effect against energetic ions is not corrected in the present study.

The TOF mass spectra showed a small O<sup>+</sup> peak caused by impurity which necessitated a correction of the S<sup>+</sup> peak intensity due to underlying O<sub>2</sub><sup>+</sup> signal prior to computation of the ion branching ratios in each TOF mass spectrum. Such a correction has been performed using the photoion branching ratios of O<sub>2</sub> [2]. The ion branching ratios measured in mode B are shown in Fig. 1 together with those reported by Carnovale, Hitchcock, Cook, and Brion<sup>3</sup> who used the electron impact (e, e<sup>+</sup>-ion) technique which simulates

photoionization mass spectrometry. The present results obtained in mode B in the 37-40 eV region where both data sets overlap are in good agreement (within 12 % discrepancy) with those reported by Carnovale et al. for all types of ions except for  $\text{CS}_2^{2+}$ , for which about 30 % discrepancy exist.

#### References

- 1) D.M.P.Holland, K.Codling, J.B.West, and G.V.Marr, *J.Phys.B* 12, 2465 (1979).
- 2) J.A.R.Samson, G.H.Rayborn, and P.N.Pareek, *J.Chem.Phys.* 76, 393 (1982).
- 3) F.Carnovale, A.P.Hitchcock, J.P.D.Cook, and C.E.Brion, *Chem.Phys.* 66, 249 (1982).

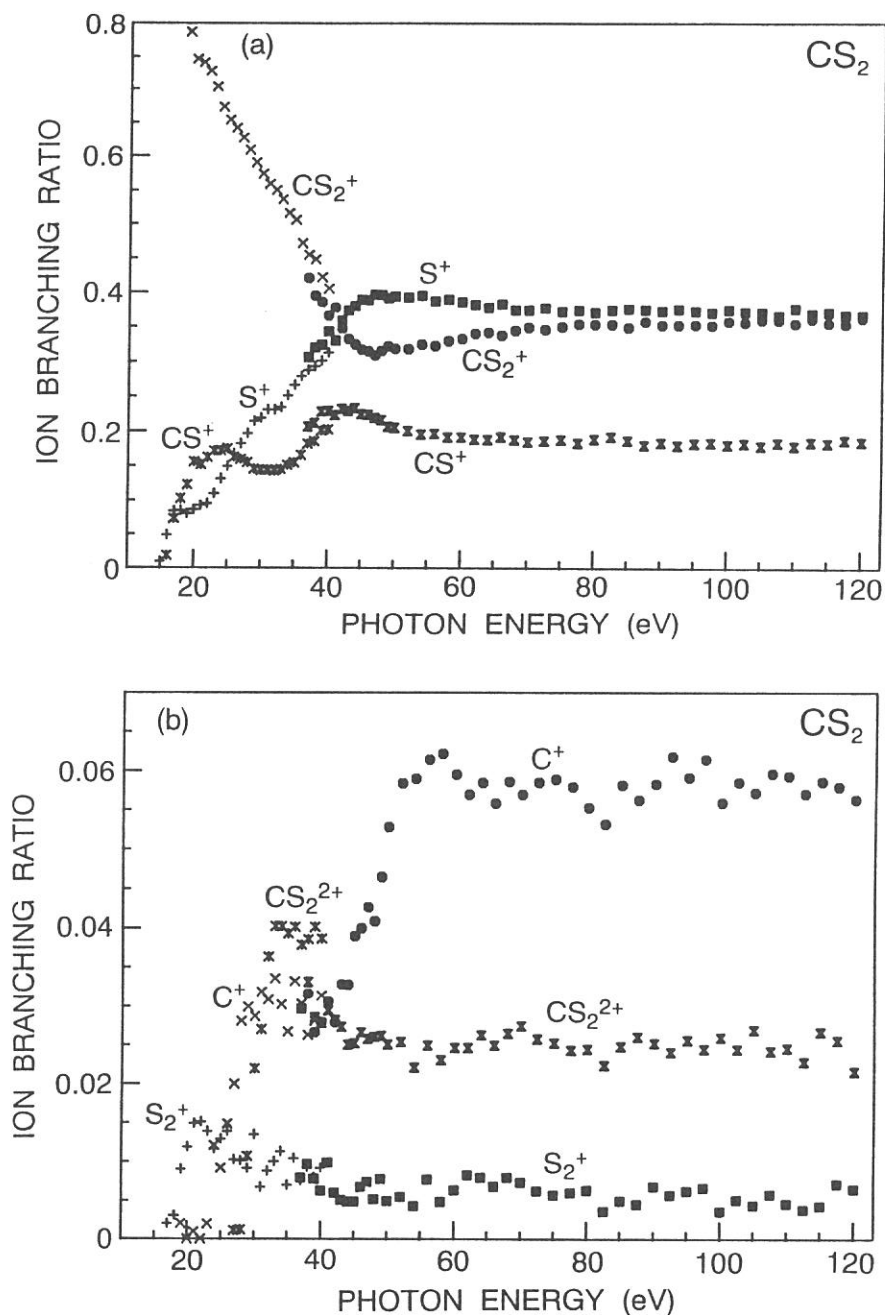


FIG. 1 Apparent ion branching ratios for  $\text{CS}_2$  directly obtained from the TOF mass spectra as a function of photon energy. ●, ■, and x, present data; x, +, and \*, from Carnovale et al. (ref. 3).



Kinetic-Energy Release in the Dissociation of  $\text{SO}_2^{2+}$ 

Toshio MASUOKA

Department of Applied Physics, Faculty of Engineering  
Osaka City University, Sugimoto 3, Sumiyoshi-ku, Osaka 558

Kinetic-energy release distributions (KERDs) of the fragment ion pairs ( $\text{O}^+ + \text{SO}^+$  and  $\text{O}^+ + \text{S}^+$ ) produced in dissociative double photoionization of sulfur dioxide have been determined by analyzing photoion-photoion coincidence (PIPICO) spectra measured in the region 37-130 eV by use of a time-of-flight mass spectrometer and synchrotron radiation. The PIPICO spectra were measured at an angle of about  $55^\circ$  with respect to polarization vector where the second-order Legendre polynomial is close to zero, thus minimizing any effects of anisotropic angular distribution of fragment ions.

In the simple framework whereby a doubly charged molecular ion ( $\text{AB}^{2+}$ ) is produced directly from absorption of a single photon and then  $\text{AB}^{2+}$  dissociates into  $\text{A}^+$  and  $\text{B}^+$ , the kinetic-energy release (KER),  $K(E)$ , is given by

$$K(E) = \text{AB}^{2+}(\text{M}\Lambda, \nu) - [\text{A}^+(\text{M}\text{L}) + \text{B}^+(\text{M}\text{L}) + D_0],$$

where  $\text{AB}^{2+}(\text{M}\Lambda, \nu)$  is the internal energy of the precursor,  $\text{A}^+(\text{M}\text{L})$  and  $\text{B}^+(\text{M}\text{L})$  are the internal energies of the two ionic fragments, all measured from the respective neutral ground states, and  $D_0$  is the dissociation energy of the neutral. The values in the bracket correspond to the various dissociation limits of  $\text{AB}^{2+}$ . In almost all studies of the KERs so far reported, this simple model was assumed explicitly or implicitly. However, as reported by Becker et al.<sup>1</sup> for CO, dissociative double photoionization is not that simple. Autoionization of valence-excited  $\text{CO}^{2+}$  states in the molecule and after dissociation plays an important role, particularly at low excitation energies.

Two dissociation channels of  $\text{SO}_2^{2+}$ ,  $\text{SO}^+ + \text{O}^+$  with the threshold at  $34.3 \pm 0.5$  eV and  $\text{S}^+ + \text{O}^+ + \text{O}$  with the threshold at  $37.7 \pm 0.5$  eV, were observed. The  $\text{SO}^+ + \text{O}^+$  channel is dominant below 50 eV, whereas the  $\text{S}^+ + \text{O}^+ + \text{O}$  channel is more intensive above 50 eV. The average, minimum, and maximum KERs in the  $\text{SO}^+ + \text{O}^+$  channel are shown in Fig. 1 and those in the  $\text{S}^+ + \text{O}^+ + \text{O}$  channel in Fig. 2 as a function of excitation energy.

 **$\text{SO}^+ + \text{O}^+$  channel**

The average KER in this channel at 39 eV is 4.7 eV (with 2.8 eV FWHM), which is in good agreement with 4.7 eV at 38 eV (the  $\alpha$  state in their notation) reported by Dujardin et al.<sup>2</sup> and 4.7 eV (with 1.6 eV FWHM) at 40.8 eV reported by Curtis and Eland.<sup>3</sup> Dujardin et al.<sup>2</sup> observed a 7 eV KER component in this channel with the threshold at 41 eV. This high-energy component was not observed in the present study. Since in their PIPICO spectra two peaks corresponding to the  $\text{SO}^+ + \text{O}^+$  and  $\text{S}^+ + \text{O}^+ + \text{O}$  dissociation are not well resolved and further it has been observed for the dissociation of  $\text{NO}^{2+}$  (Ref. 4) and  $\text{CO}^{2+}$  (Ref. 5) that the KER increases continuously as the excitation energy increases, we believe that the threshold, partial cross sections, and KERs of the  $\beta$  and  $\gamma$  states reported by them are not reliable. As shown in Fig. 1, the average, minimum, and maximum KERs in this channel do not change appreciably as the excitation energy increases. At the lowest excitation energy of 37 eV, the KERD extends from 2.4 to 7.6 eV with the 4.8 eV average KER. The maximum KER corresponds to  $h\nu$  (37 eV) minus the lowest dissociation limit of  $\text{SO}_2^{2+}$ ,  $\text{SO}^+(\text{X}^2\Pi) + \text{O}^+(\text{4S}_u)$ , at 29.52 eV and the average KER corresponds to the energy difference between the  $\text{SO}_2^{2+}$

( $X^1\Sigma_g^+$ ) state at 34.4 eV and the lowest dissociation limit. From the results shown in Fig. 1, it is concluded that the dissociation of  $SO_2^{2+}$  into  $SO^+ + O^+$  is due to the low-lying states of  $SO_2^{2+}$  which correlate with the low-lying dissociation limits of  $SO_2^{2+}$  in the range 29.5-34.5 eV.

**$S^+ + O^+ + O$  channel**

The average KER in this channel increases considerably at the low excitation energies up to about 60 eV and then gradually above 60 eV. This trend is in sharp contrast to the results for the  $SO^+ + O^+$  channel. At the low excitation energies, the average, minimum, and maximum KERs are smaller than those in the  $SO^+ + O^+$  channel. As the excitation energy increases, the KERD becomes wider and wider, extending up to about 17.4 eV at a photon energy of 130 eV. However, the increase of the KER is not as much as the increase in the excitation energy. This means that the high-lying electronic states of  $SO_2^{2+}$  that dissociate into  $S^+ + O^+ + O$  result in  $S^{++}$ ,  $O^{++}$ , and/or  $O^*$  with higher levels of excitation and with larger KER than those resulting from the low-lying states. In other words, the potential-energy surfaces of the high-lying states are steeper and more repulsive than those of the low-lying states.

**References**

- 1) U. Becker, O. Hemmers, B. Langer, A. Menzel, and R. Wehlitz, Phys. Rev. A 45, R1295 (1992).
- 2) G. Dujardin, S. Leach, O. Dutuit, P. M. Guyon, and M. Richanrd-Viard, Chem. Phys. 88, 339 (1984).
- 3) D. M. Curtis and J. H. D. Eland, Int. J. Mass Spectrom. Ion Processes, 63, 241 (1985).
- 4) T. Masuoka, J. Chem. Phys. 100, 6422 (1994).
- 5) T. Masuoka, J. Chem. Phys. 101, 322 (1994).

FIG. 1 Average-, minimum-, and maximum-kinetic energy releases in the dissociation of  $SO_2^{2+}$  into  $SO^+ + O^+$  as a function of excitation energy.

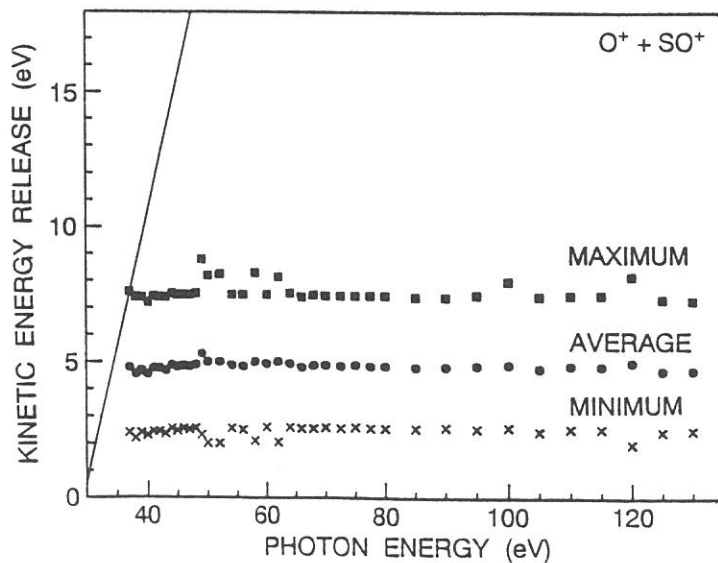
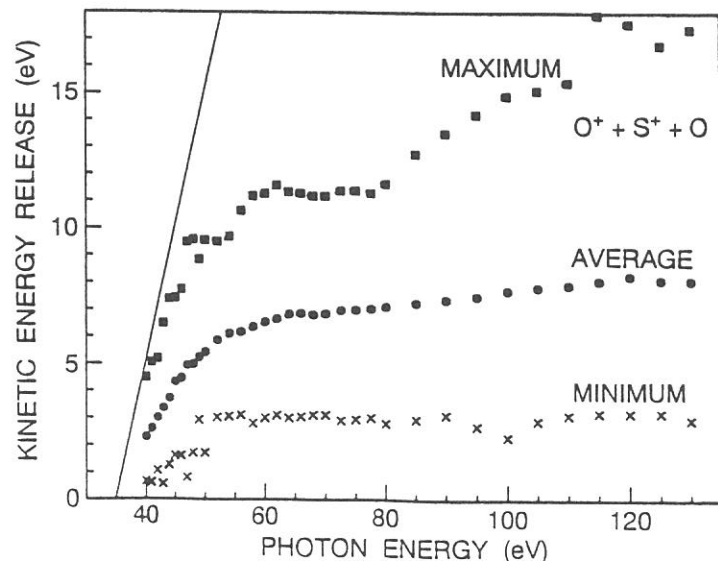


Fig. 2 Average-, minimum-, and maximum-kinetic energy releases in the dissociation of  $SO_2^{2+}$  into  $S^+ + O^+ + O$  as a function of excitation energy. The KERs of  $O^+$  and  $S^+$  are shown.



Kinetic-Energy Release in the Dissociation of  $\text{CO}_2^{2+}$ 

Toshio MASUOKA

Department of Applied Physics, Faculty of Engineering, Osaka City  
University, Sugimoto 3, Sumiyoshi-ku, Osaka 558

Eiken NAKAMURA and Atsunari HIRAYA

Ultraviolet Synchrotron Orbital Radiation Facility,  
Institute for Molecular Science, Myodaiji, Okazaki 444

Many doubly charged molecular ions are unstable because of Coulomb repulsion between two positive charges and dissociate into ionic fragments with a concomitant kinetic-energy release (KER). In order to elucidate the production and dissociation dynamics of doubly charged molecular cations, it is necessary to understand the mechanism of the KER. The KER is related to the shape of the potential surface of the precursor-ion states and the energy partitioning among the internal degrees of freedom of the ionic fragments in the framework of direct double photoionization of molecules and subsequent dissociation.

Kinetic-energy release distributions (KERDs) of the fragment ion pairs ( $\text{O}^+ + \text{CO}^+$  and  $\text{C}^+ + \text{O}^+$ ) produced in dissociative double photoionization of carbon dioxide have been determined by analyzing photoion-photoion coincidence (PIPICO) spectra measured in the region  $h\nu = 40\text{--}100$  eV by use of a time-of-flight mass spectrometer and synchrotron radiation. The mechanism of the three-body dissociation ( $\text{CO}_2^{2+} \rightarrow \text{C}^+ + \text{O}^+ + \text{O}$ ) has been examined to take place sequentially via  $\text{CO}^+$  by a triple photoelectron-photoion-photoion coincidence experiment. The KERDs observed for the  $\text{O}^+ + \text{CO}^+$  and  $\text{C}^+ + \text{O}^+$  channels at low excitation energies cannot be explained by a simple framework whereby a doubly charged molecular ion is directly produced on single photon absorption followed by the dissociation of  $\text{AB}^{2+}$  into ionic fragments. Some of the ion pairs are produced through indirect processes in which highly excited  $\text{CO}_2^{**}$  and  $\text{CO}_2^{**}$  (double Rydberg) states converging to the high-lying  $\text{CO}_2^{2+}$  electronic states autoionize before and after dissociation. From the observed KERDs for the  $\text{O}^+ + \text{CO}^+$  and  $\text{C}^+ + \text{O}^+$  channels of  $\text{CO}_2^{2+}$ , the range of the intercharge distances of two positive holes is estimated by assuming that the KER is given purely by Coulomb repulsion.

The threshold for the  $\text{O}^+ + \text{CO}^+$  ion-pair formation is at  $39.2 \pm 0.3$  eV.<sup>1</sup> The total KERDs of the  $\text{O}^+ + \text{CO}^+$  ion pair obtained by analyzing the PIPICO spectra at various energies between 40 and 100 eV are shown in Fig. 1. At the excitation energies between 40 and 55 eV, the KERD becomes slightly wider and shifts toward the higher energy side with increasing photon energy. However, the increase of the KER is much less than the increase in the excitation energy. This is in sharp contrast to nitric oxide<sup>2</sup> and carbon monoxide<sup>3</sup> for which considerable increase in the KER was observed with increasing photon energy. This means that the high-lying electronic states of  $\text{CO}_2^{2+}$  result in  $\text{O}^{*+}$  and/or  $\text{CO}^{*+}$  with much higher levels of excitation. Above 55 eV, the KERDs are almost identical. That is, most of the internal energy of  $\text{CO}_2^{2+}$  is transferred to the internal energies of the excited ion pair. In the case of NO and CO, the potential-energy curves of the high-lying states are steeper and more repulsive than those of the low-lying

states.<sup>2,3</sup> For  $\text{CO}_2$ , however, this trend is weakened.

Curtis and Eland<sup>4</sup> reported the total KER for the  $\text{O}^+ + \text{CO}^+$  channel at the excitation energy 40.8 eV to be  $6.0 \pm 0.4$  eV with 3 eV FWHM, which contrasts strongly with the narrow distribution of 0.5-1.0 eV FWHM reported by Dujardin and Winkoun.<sup>5</sup> The average KER in the present work is 4.4 eV with 2.6 eV FWHM at 41 eV. The 2.6 eV FWHM is in good agreement with that reported by Curtis and Eland. The discrepancy between the average KER in the present work and that reported by Curtis and Eland is rather large, which may be caused by the assumption of a single-valued KER in Ref. 4.

#### References

- 1) T. Masuoka, Phys. Rev. A 50, 3886 (1994).
- 2) T. Masuoka, J. Chem. Phys. 100, 6422 (1994).
- 3) T. Masuoka, J. Chem. Phys. 101, 322 (1994).
- 4) D. M. Curtis and J. H. D. Eland, Int. J. Mass Spectrom. Ion Processes 63, 241 (1985).
- 5) G. Dujardin and D. Winkoun, J. Chem. Phys. 83, 6222 (1985).

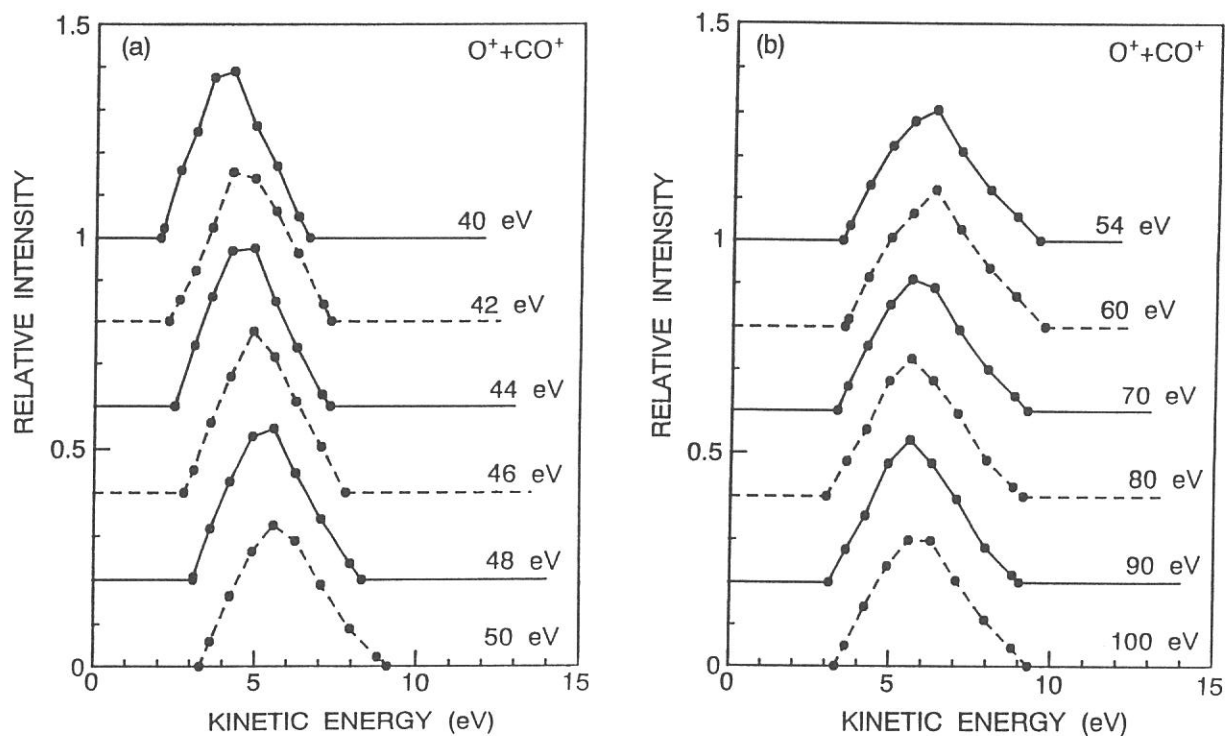


FIG. 1 Kinetic-energy release distributions in the  $\text{O}^+ + \text{CO}^+$  channel of  $\text{CO}_2^{2+}$  at excitation energies of 40-100 eV.

Single- and Double-Photoionization Cross Sections of Carbon  
Dioxide ( $\text{CO}_2$ ) and Ionic Fragmentation of  $\text{CO}_2^+$  and  $\text{CO}_2^{2+}$

Toshio MASUOKA

Department of Applied Physics, Faculty of Engineering,  
Osaka City University, Sugimoto 3, Sumiyoshi-ku, Osaka 558

Single- and double-photoionization processes of carbon dioxide ( $\text{CO}_2$ ) have been studied in the photon-energy region of 30-100 eV by use of time-of-flight mass spectrometry and the photoion-photoion-coincidence method together with synchrotron radiation.<sup>1</sup> The single- and double-photoionization cross sections of  $\text{CO}_2$  are determined by a newly developed method.<sup>2</sup> The results are shown in Fig. 1 as a function of photon energy assuming that  $\sigma_t = \sigma^+ + \sigma^{2+}$ . The total cross section is from Ref. 3. It is emphasized that the double photoionization cross section shown in Fig. 1 includes both the dissociative and nondissociative processes of the precursor  $\text{CO}_2^{2+}$ . Dujardin and Winkoun<sup>4</sup> reported the value of  $\sigma^{2+}/\sigma_t$  to be 0.027 at 52 eV, which is much lower than the present data of 0.077 at the same energy. The  $\sigma^{2+}/\sigma_t$  ratios for several molecules reported by this group are systematically much lower than other literature values.

The threshold for molecular double photoionization was found to be  $37.6 \pm 0.3$  eV. The thresholds for the  $\text{CO}^+ + \text{O}^+$  and  $\text{C}^+ + \text{O}^+$  channels of  $\text{CO}_2^{2+}$  are at  $39.2 \pm 0.3$  and  $47.2 \pm 0.5$  eV, respectively, both of which are in close agreement with  $39.7 \pm 0.5$  and  $46.4 \pm 1.5$  eV reported by Millie et al.<sup>5</sup>

Ion branching ratios and the partial cross sections for the individual ions respectively produced from the precursors  $\text{CO}_2^+$  and  $\text{CO}_2^{2+}$  are determined separately at excitation energies where the molecular and dissociative single- and double-photoionization processes compete. It is found that in the single photoionization the production of the stable  $\text{CO}_2^+$  ions is a dominant process throughout the energy region examined. The partial cross sections for the respective channels of the  $\text{CO}_2^{2+}$  precursor separately determined from those for  $\text{CO}_2^+$  are shown in Fig. 2. The  $\text{O}^+ + \text{CO}^+$  and  $\text{C}^+ + \text{O}^+$  ion-pair formation is dominant because of Coulomb repulsion between two positive holes. However, the metastable  $\text{CO}_2^{2+}$  ion is also observed due to the presence of attractive chemical forces at smaller internuclear distances. The charge-localized dissociation of  $\text{CO}_2^{2+}$  forming  $\text{C}^{2+}$  becomes appreciable at higher excitation energies, where two electrons in the atomic orbitals of carbon are ejected.

Separate determinations of the ion branching ratios for the precursors  $\text{CO}_2^+$  and  $\text{CO}_2^{2+}$  were used to obtain the dissociation ratios of the singly and doubly charged precursors. The dissociation ratio of  $\text{CO}_2^{2+}$  is larger than 0.90 above 50 eV. This trend is very similar to the results obtained for  $\text{OCS}^{2+}$  [1],  $\text{NO}^{2+}$  [6], and  $\text{CO}^{2+}$  [7]. Although the dissociation ratio of molecular dications has been examined for only four molecules such as OCS, NO, CO, and  $\text{CO}_2$  so far, the high dissociation ratio of dications can be regarded as a general phenomenon even if some metastable dications are produced. This is because only a few low-lying electronic states of molecular dications are quasibound, if any. Conversely, the dissociation ratio of molecular cations ( $\text{AB}^+$ ) splits into two groups: a high dissociation ratio in the

case of OCS [1] and a low dissociation ratio (say less than 40%) for NO [6], CO [7], and  $\text{CO}_2$  below 100 eV, although details of differentiating these two groups cannot be clearly determined at present.

For the production of the stable  $\text{CO}_2^+$  and  $\text{CO}_2^{2+}$  ions at higher photon energies, it is pointed out that the bound-type  $\text{CO}_2^+$  and  $\text{CO}_2^{2+}$  do exist and/or the Rydberg states play an important role through autoionization.

## References

- 1) T. Masuoka, Phys. Rev. A 50, 3886 (1994).
- 2) T. Masuoka and H. Doi, Phys. Rev. A 47, 278 (1993).
- 3) J. A. R. Samson and G. N. Haddad (unpublished).
- 4) G. Dujardin and D. Winkoun, J. Chem. Phys. 83, 6222 (1985).
- 5) P. Millie, I. Nenner, P. Archirel, P. Lablanquie, P. G. Fournier, and J. H. D. Eland, J. Chem. Phys. 84, 1259 (1986).
- 6) T. Masuoka, Phys. Rev. A 48, 1955 (1993).
- 7) T. Masuoka and E. Nakamura, Phys. Rev. A 48, 4379 (1993).

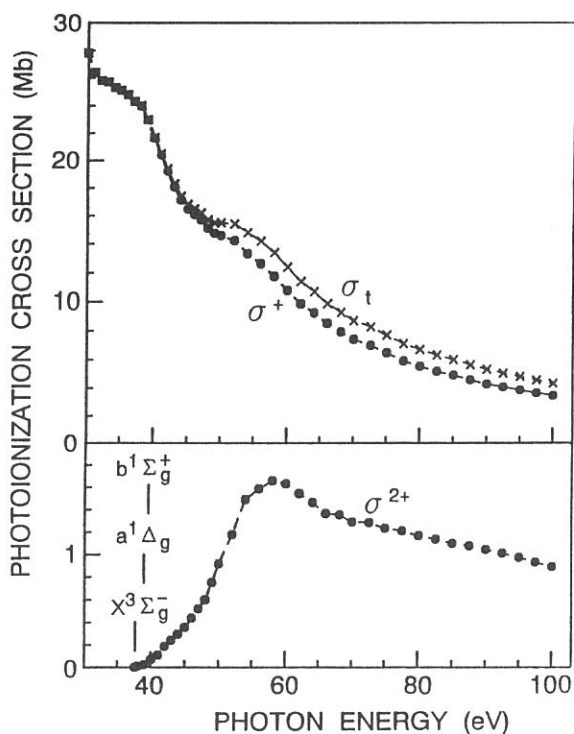


FIG. 1 Cross sections for single ( $\sigma^+$ ) and double ( $\sigma^{2+}$ ) photoionization of  $\text{CO}_2$ . The total cross section ( $\sigma_t$ ) is from Ref. 3.

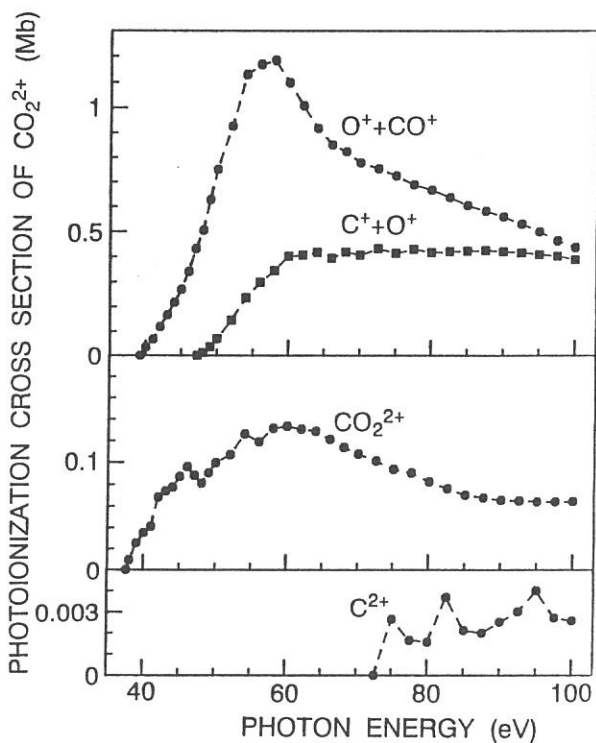


FIG. 2 Partial photoionization cross sections for the ions produced from the precursor  $\text{CO}_2^{2+}$ . For details, see Ref. 1.



## Photodissociation of CF<sub>3</sub>Br induced by Br(3d) excitation.

T. Senga, M. Kawasaki, A. Hiraya\*, T. Ibuki\*\*

*Graduate School of Environmental Earth Science, Hokkaido Univ., Hokkaido*

*\*Institute for Molecular Science, Myodaiji, Okazaki 444*

*\*\*Department of Chemistry, Kyoto University of Education, Sumizome, Fusimi-ku 612, Japan*

We have investigated the photodissociation of CF<sub>3</sub>Br within  $h\nu=40\text{--}130$  eV, using TOF-MASS, and PIPICO method on BL3A2. Figure 1 shows photoabsorption spectrum of Br(3d), inner-shell of CF<sub>3</sub>Br. Observed peaks at 70.5 and 71.5 eV are assigned to the transitions,  $\sigma^* \leftarrow 3d_{5/2}$  and  $\sigma^* \leftarrow 3d_{3/2}$ , respectively[1]. Peaks at 75.1 and 76.1 eV are attributed to the Rydberg transitions of  $5p \leftarrow 3d_{5/2}$  and  $5p \leftarrow 3d_{3/2}$ , respectively[1].

With Excitation at 40–130 eV, singly charged fragment ions detected by TOF-MASS were C<sup>+</sup>, F<sup>+</sup>, CF<sup>+</sup>, CF<sub>2</sub><sup>+</sup>, CF<sub>3</sub><sup>+</sup>, Br<sup>+</sup>, CBr<sup>+</sup>, CF<sub>2</sub>Br and CF<sub>3</sub>Br<sup>+</sup>. Quantum yields of doubly charged fragment ions F<sup>2+</sup>, CF<sup>2+</sup>, and Br<sup>2+</sup> were also observed. Small singly charged fragment ions, such as C<sup>+</sup>, F<sup>+</sup>, Br<sup>+</sup> and CF<sup>+</sup>, and doubly charged fragment ions increased with photon energy, while those of other singly charged ions decreased.

Figure 2 shows the photon energy dependence of the branching ratios. The doubly charged ion pairs of (F<sup>+</sup>+C<sup>+</sup>) and (F<sup>+</sup>+CF<sup>+</sup>) increased when Br(3d) was excited. However, the corresponding change was not observed in the photoabsorption spectrum (Fig.1).

To our knowledge, the excitation of Br( $\sigma^* \leftarrow 3d$ ) induces bond break in HBr[2], C<sub>2</sub>H<sub>3</sub>Br and C<sub>2</sub>H<sub>5</sub>Br[3], while I( $\sigma^* \leftarrow 4d$ ) does not for HI, CH<sub>3</sub>I[4], nor Si( $\sigma^* \leftarrow 2p$ ) for Si(CH<sub>3</sub>)Cl<sub>3</sub>: the present results for CF<sub>3</sub>Br are similar to those of the I and Si cases.

[1] D. A. Shaw, D. Svejanojic, G. C. King, and F. H. Read, J. Phys. B 17, 1173 (1984).

[2] P. Morin and I. Nenner, Phys. Rev. Lett, 56, 1913 (1986).

[3] P. Morin, T. LeBrun, and P. Lablanquie, Bull. Soc. R. Sci. Liege, 58, 135 (1989).

[4] P. Morin and I. Nenner, Phys. Scri. T17, 171 (1987).

[5].S.Nagaoka,J.Oshima,M.Ishikawa,T.Masuoka,and I.Koyano,J.Phys.Chem.97,1488(1993).

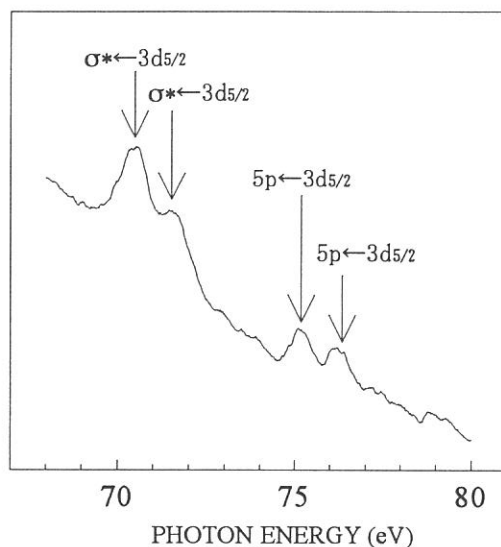


Figure 1. Photoabsorption spectrum of Br(3d), inner-shell of CF<sub>3</sub>Br.

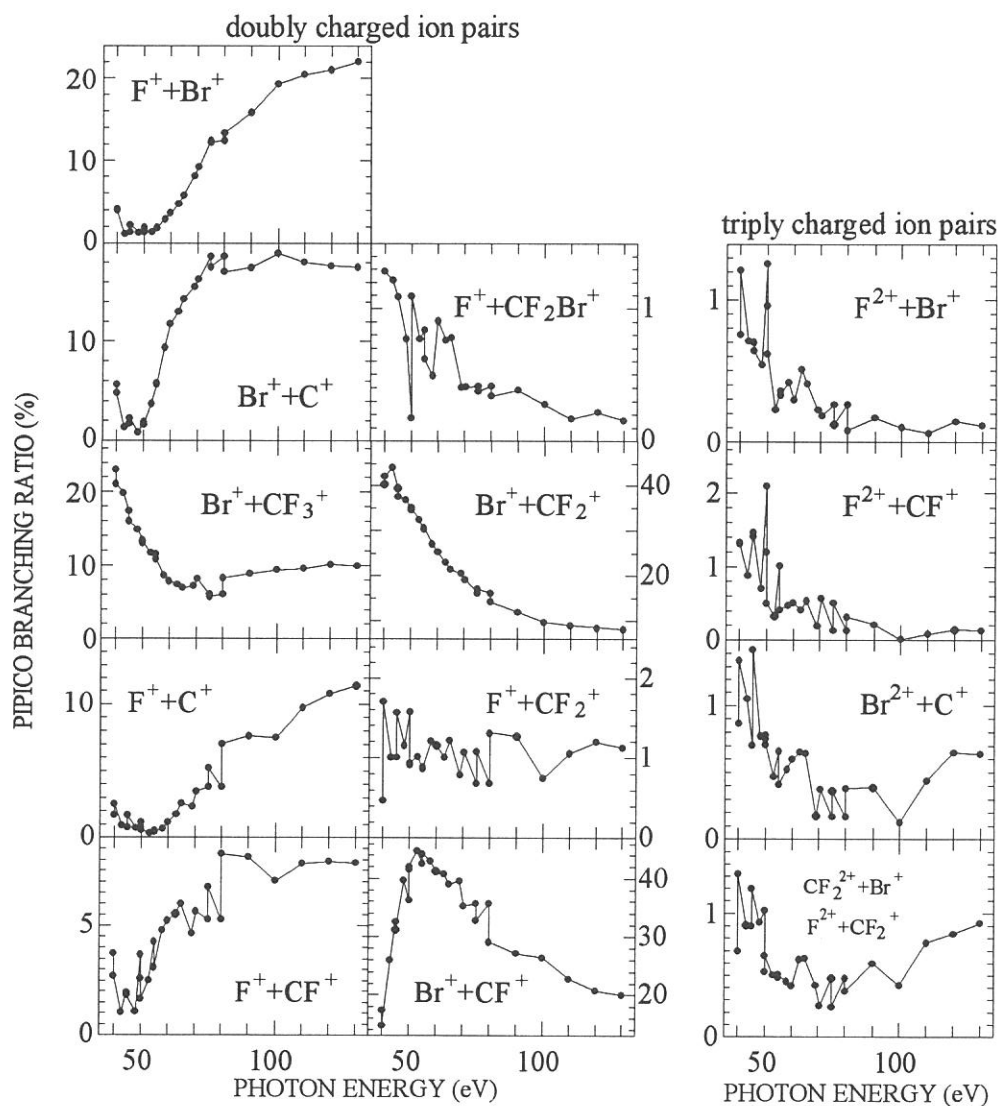


Figure 2. The photon energy dependence of the branching ratios.

Development of a Position-Sensitive Detection System  
for VUV Photoelectron Spectroscopy

Koichiro MITSUKE, Yasumasa HIKOSAKA,\* Hideo HATTORI, and Takumi HIKIDA\*

*Department of Vacuum UV Photoscience,  
Institute for Molecular Science, Myodaiji, Okazaki 444*  
\**Department of Chemistry, Tokyo Institute of Technology,  
Ohokayama, Meguroku, Tokyo 152*

The machine constructed on the beam line BL3B is devoted to gas-phase photoelectron spectroscopy to obtain knowledge on fundamental electron-core interactions in a molecule through photoionization phenomena. This year, we have developed a new electron detection system to get a higher count rate and better spectral resolution.

The crux of the system is a position sensitive detector (PSD) composed of dual microchannel plate (MCP) multipliers and a two-dimensional resistive anode encoder. An exit slit and a single channel MCP detector so far used are removed from a 160° spherical electron energy analyzer and then fitted PSD on the end of the analyzer. Great improvement in detection efficiency has been realized by this alteration as described below.

The former single channel detector collects the electrons whose kinetic energy falls within a narrow energy range determined from the size of the exit slit (typically 1.5 - 2 mm $\phi$ ). In contrast, PSD can detect all of the energy-dispersed electrons simultaneously that can pass through between the two spherical sector surfaces; the range of the electron kinetic energy is about 10 % of a transmission energy for the analyzer. The kinetic energy can be precisely determined from a displacement of the location of the incident electron along the coordinate of energy dispersion. When the incident electron strikes the input MCP, a pulse of a 0.1 - 1 picocoulomb is deposited on the anode encoder. The anode itself is a square distributed resistive network with collection electrodes at the four corners. Charge pulses from the electrodes are sent to a position analyzer which performs

a fast computation of the incident position of the electron using sums and ratios of the four charges.

The spatial resolution of PSD is 10 times as high as that of the single channel detector. Consequently, a photoelectron spectrum with much better resolution can be obtained in a short period by using this system. At the energy resolution of 70 meV FWHM, for example, the accumulation time is reduced to 1/50 of that required in a previous measurement, as far as other conditions are the same. When the energy resolution of the incident light is set to about 28 meV, the highest overall resolution is estimated to be 30 meV.

The photoelectron spectrum obtained at the resolution of 40 meV is shown in Figure 1a). The electron energy is dispersed in the horizontal direction of this image. Summing all signal counts at a given horizontal position over a range of vertical axis leads to a one-dimensional spectrum in Figure 1b). We are now studying autoionizing and shape resonances in molecular photoionization processes and the properties of involved superexcited states (see reports on  $C_2H_2$  and NO in this journal).

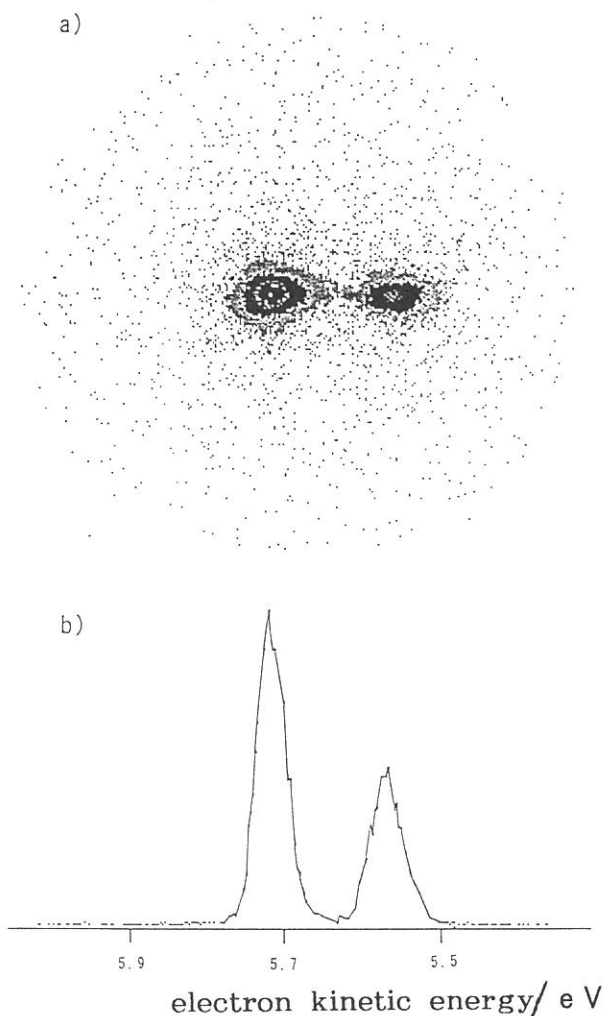


**Figure 1.** Photoelectron spectrum of  $Ar^+(^2P_{3/2}, ^2P_{1/2})$  at the energy resolution of 40 meV FWHM. a) Image on the position-sensitive detector, and b) a one-dimensional spectrum obtained by conversion of the image data (see the text).

## Two-dimensional photoelectron spectroscopy of NO

Yasumasa HIKOSAKA, Hideo HATTORI\*, Takumi HIKIDA and Koichiro MITSUKE\*

*Department of Chemistry, Tokyo Institute of Technology, Ohokayama, Meguro 152*

*\*Institute for Molecular Science, Myodaiji, Okazaki 444*

Two-dimensional photoelectron spectroscopy of NO is performed at the beam line BL3B to study superexcited states lying in the 11-13 eV excitation energy range. It is well known that a number of autoionizing resonances appear in a photoabsorption or photoionization cross section curve in this energy range. They can not be accounted for by Rydberg states converging to  $\text{NO}^+(\tilde{a}^3\Sigma^+)$ , judging from the peak positions expected from the term values of the Rydberg states. Sobolewski<sup>1)</sup> proposed theoretically that these features result from interaction between an excited valence state and Rydberg states converging to  $\text{NO}^+(\tilde{X}^1\Sigma^+)$ . The equilibrium bond length and vibrational frequency of the excited valence state are estimated by Erman et al.<sup>2)</sup> to be 1.3 Å and 1610  $\text{cm}^{-1}$ , respectively. They identified the resonance peaks as the vibrational levels  $v_1=7-17$  of the excited valence state by comparing photoionization efficiency curves between  $^{14}\text{NO}$  and  $^{15}\text{NO}$ .

Figure 1 shows a two-dimensional photoelectron spectrum of NO. The vertical axis is the photon energy and the horizontal one is the ionization energy. Patterns running parallel to the photon energy axis correspond to the final vibrational levels ( $v_1=0-15$ ) of  $\text{NO}^+(\tilde{X}^1\Sigma^+)$ . Horizontal intense patterns superimposed on direct ionization continua are due to the autoionizing resonances. Figure 2 shows photoelectron spectra at (a) 11.64 eV and (b) 12.16 eV, sectional views taken on horizontal lines of Fig. 1. The peak intensity of the vibrational levels of  $\text{NO}^+(\tilde{X}^1\Sigma^+)$  increases with  $v_1$  to a maximum at  $v_1=2$  or 3. Then, it decreases and reaches one or two minima, *i.e.* a minimum at  $v_1=6$  and two minima at  $v_1=5$  and 8 in the spectra of 11.64 and 12.16 eV, respectively. The number of the minimum positions tends to increase with the photon energy: three minima ( $v_1=5, 7$  and 10) at about 12.4 eV, and four minima ( $v_1=4, 7, 9$  and 12) at about 12.6 eV.

From Franck-Condon analysis using RKR potentials, this trend can be interpreted by assuming a single bound or repulsive excited valence state. Nevertheless, Fig. 1 contains complex structures with irregularly spaced peaks in each vertical pattern along the photon energy axis. We consider that perturbation from Rydberg states converging to  $\text{NO}^+(\tilde{X}^1\Sigma^+)$  enlarges the electric transition dipole moment from the ground state  $\text{NO}(\tilde{X}^2\Pi)$  to the excited valence state. Thus, the vibrational levels of the Rydberg states emerge in Fig. 1, in consistent with the resonance peaks in the photoabsorption or photoionization cross section curve.

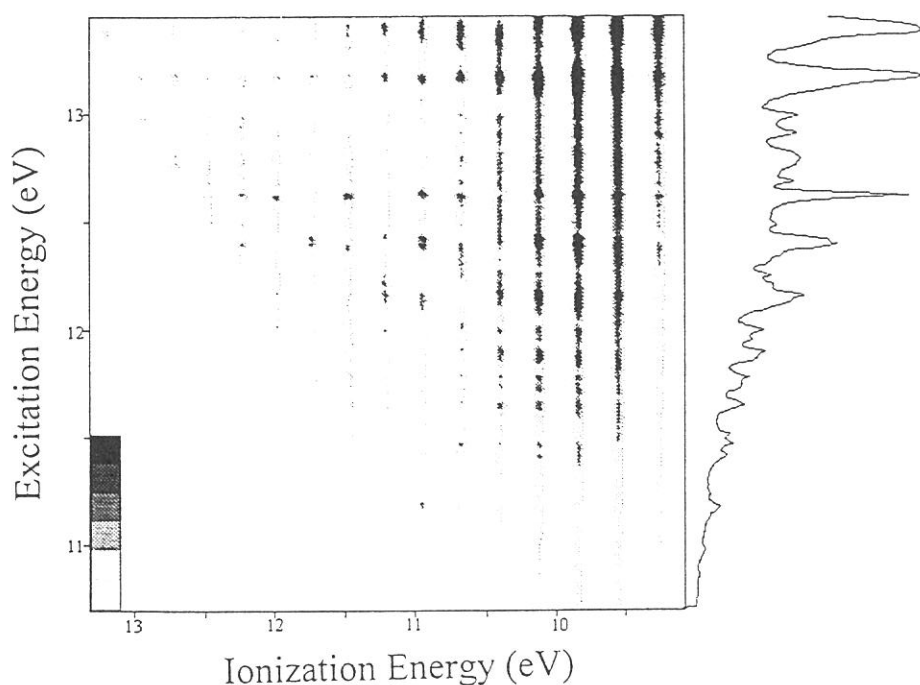
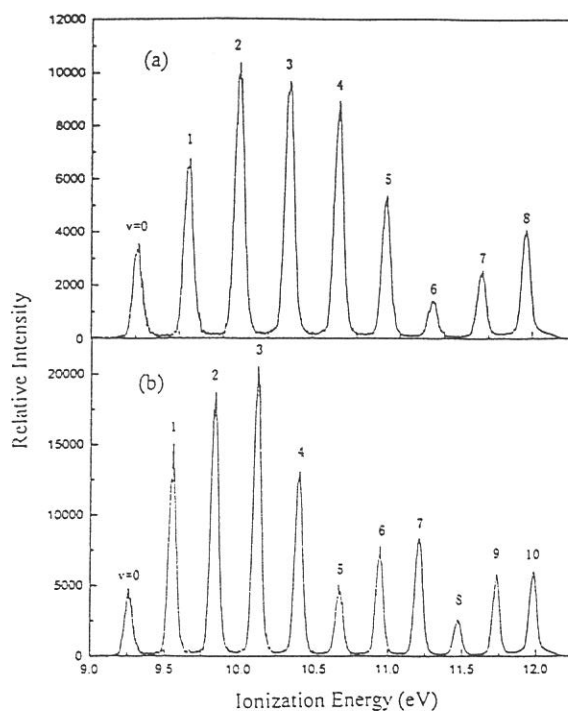


Fig. 1. Two-dimensional photoelectron spectrum of NO as a function of both ionization energy and photon energy. The electron intensity is shown increasing from light to dark on a linear scale. A single dimensional excitation spectrum, the right curve, is given by summing electron counts at a fixed photon energy.

Fig. 2. Photoelectron spectra of NO excited at photon energies of (a) 11.64 eV and (b) 12.16 eV.

- 1) A. L. Sobolewski, J. Chem. Phys., **87**, 331 (1987).
- 2) P. Erman, A. Karawajczyk, E. Rachlew-Källne and C. Strömholm, J. Chem. Phys., in press.



## Autoionization of an Excited Valence State of $C_2H_2$

Hideo HATTORI and Koichiro MITSUKE

*Department of Vacuum Photoscience, Institute for Molecular Science,  
Myodaiji, Okazaki 444*

The photoionization cross section curve of  $C_2H_2$  has two broad maxima around 13.3eV and 15.5eV. The maximum of 15.5eV has been attributed to an excitation to the valence state,  $2\sigma_u \rightarrow 1\pi_g$ . In contrast, there are still some controversies about the origin of the 13.3eV maximum: a local maximum in the  $1\pi_u \rightarrow \varepsilon\delta_g$  continuum, shape resonance, autoionizing resonance, or some combination of such resonances. In this work, autoionization process of  $C_2H_2$  is investigated by photoelectron spectroscopy using synchrotron radiation in the energy region from 12.8 to 14.1eV.<sup>1)</sup> Measurements were performed at the beamline BL3B and the details of the experimental system were described elsewhere.<sup>2)</sup>

Figure 1 shows photoelectron spectra of  $C_2H_2$ . All features can be assigned to vibrational levels of the electronic ground state of  $C_2H_2^+$ . Asterisks denote peaks assigned as a vibrational ground state and  $\nu_2=1$  and 2 states of the C–C stretching mode  $\nu_2$  (the vibrational spacing =  $0.22_3 \pm 0.004$ eV). In addition, we can observe two progressions with average spacings of  $0.37_6 \pm 0.006$ eV in the entire photon energy range. This pronounced vibrational excitation is considered to arise from autoionizing resonance which contributes to the 13.3eV maximum in the photoionization cross section curve.<sup>3)</sup>

To assign the progressions, we examine the possible influence of the isotope on their spacings. A photoelectron spectrum of  $C_2D_2$  in Fig. 2 indicates two progressions  $0.20_3 \pm 0.004$ eV apart with spacings of  $0.30_2 \pm 0.010$ eV. From the considerable isotope shift between  $C_2H_2$  and  $C_2D_2$ , we conclude that the C–H (or C–D) symmetric stretching mode  $\nu_1$  is excited. This result indicates that autoionization occurs via a superexcited state with equilibrium C–H distances much different from those of the ground state  $C_2H_2$  and  $C_2H_2^+$ . We assign the autoionizing state as an excited valence state  $(3\sigma_g)^{-1}(3\sigma_u)^1$ , because Hayaishi *et al.*<sup>3)</sup> suggest that this state lies at about 14eV and has longer C–H bond lengths.

We attempt to observe vibrational levels in the valence state using the CIS (Constant-Ionic-State) measurement of the  $(\nu_1, \nu_2)=(3,0)$  vibrational state of  $C_2H_2^+(\tilde{X}^2\Pi_u)$  to exclude contribution of direct ionization (Fig.3). In this method, the difference between the exciting photon energy and the observed electron kinetic energy is kept constant while a monochromator is scanning. Observed intensity enhancement corresponds to the  $3\sigma_g \rightarrow 3\sigma_u$  intravalence transition. Furthermore, there are weak structures constituting two progressions



$0.12_5 \pm 0.027\text{eV}$  apart with average spacings of  $0.19_5 \pm 0.027\text{eV}$ , labelled P1 and P2 in Fig.3. They are attributable to vibrational levels of this valence state, probably combination bands of the C-H and C-C stretching modes. This implies that the  $(3\sigma_g)^{-1}(3\sigma_u)^1$  state has a lifetime with respect to autoionization longer than the periods of the above vibrational motions.

#### References

- 1) K. Mitsuke and H. Hattori, *J. Chem. Phys.*, in press.
- 2) H. Hattori and K. Mitsuke, UVSOR Activity Report 1993, p.15.
- 3) T. Hayaishi, S. Iwata, M. Sasanuma, E. Ishiguro, Y. Morioka, Y. Iida, and M. Nakamura, *J. Phys. B* **15**, 79 (1982).

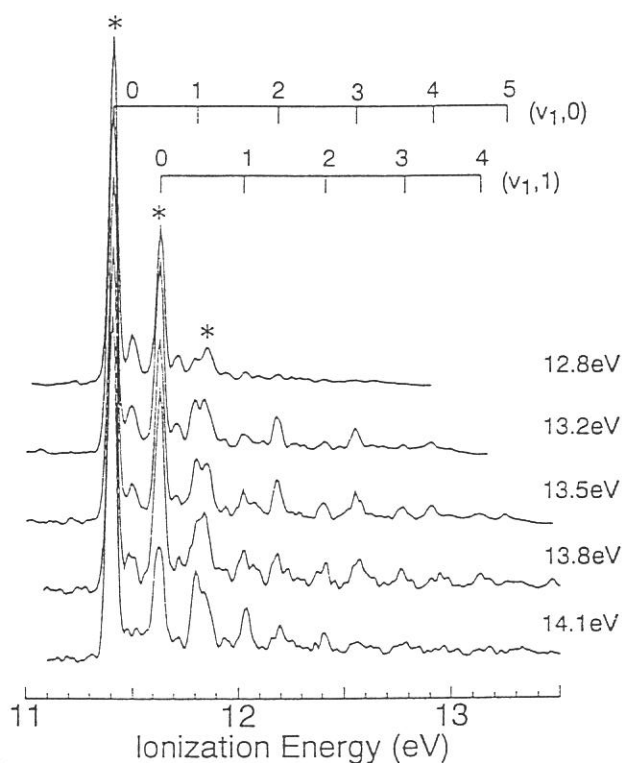


**FIG.1.** Photoelectron spectra of  $\text{C}_2\text{H}_2$  at the excitation energy from 12.8eV to 14.1eV. The  $(v_1, v_2)$  mark denotes the vibrational state in which  $v_1$  and  $v_2$  quanta of the C-H and C-C stretching modes, respectively, are simultaneously excited. The overall resolution is 60meV (FWHM).

**FIG.3.** CIS spectrum for the  $(v_1, v_2) = (3, 0)$  vibrational state of  $\text{C}_2\text{H}_2^+(\tilde{X}^2\Pi_u)$ . The overall resolution is approximately 110meV (FWHM).

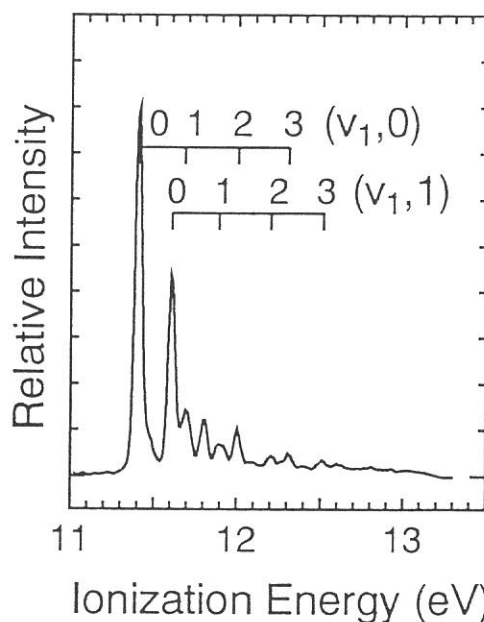
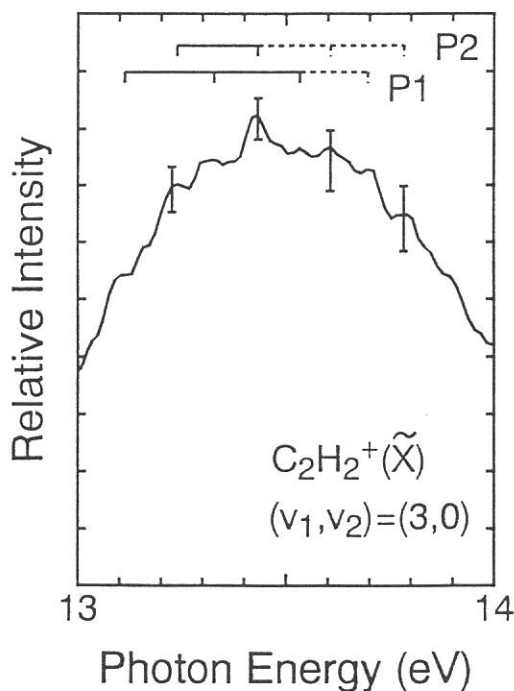


**FIG.2.** Photoelectron spectrum of  $\text{C}_2\text{D}_2$  at the excitation energy of 13.3eV.



**Synchrotron Radiation Photochemistry in Low-Temperature Condensed Layers of Organo-Aluminum Compounds on SiO<sub>2</sub> Surface Investigated by Buried-Metal-Layer Infrared Reflection Absorption Spectroscopy**

Yoshiaki Imaizumi <sup>a</sup>, Yoshiyuki Tsusaka <sup>b</sup>, Tsuneo Urisu <sup>b</sup>

<sup>a</sup> *The Graduate University for Advanced Studies and* <sup>b</sup> *Institute for Molecular Science, Myodaiji, Okazaki, 444 Japan*

Synchrotron radiation ( SR ) irradiation effects on the low-temperature condensed layer of trimethyl aluminum ( TMA ) and dimethyl aluminum hydride ( DMAH ) on an SiO<sub>2</sub> surface were investigated by infrared reflection absorption spectroscopy ( IRAS ) using a buried metal layer ( BML ) substrate. The low-temperature condensed layer of these compounds on semiconductor materials is expected to be useful for area-selective deposition of aluminum thin films by laser [ 1, 2 ] or synchrotron radiation ( SR ) beam induced processes. The adsorbed or condensed layers have attracted more attention in recent years [ 3 - 5 ], but fundamental knowledge of not only photochemistry but also molecular structures and orientations remains very insufficient.

TMA was a dimer at the experimental temperature range of 110 K < T < 160 K. The molecular orientation varied depending on the deposition temperature. The condensed layer of DMAH as-deposited at the temperature ranging from 110 to 130 K was a mixture of trimers and dimers. A dimer changed to a trimer as the temperature increased, practically disappearing above 130 K. This temperature dependence was not reversible. The trimer did not change to a dimer below 130 K. The ordered orientation of the trimer molecules was a stable DMAH condensed layer structure on the SiO<sub>2</sub> surface. Another noticeable point in the temperature dependence shown in Fig. 1 is concerned with the irreversibility of the spectral change with the temperature from 112 to 130 K. From this fact and the absence of any significant change in the molecular orientation with temperature, we conclude that the condensed layer containing both the dimer and trimer molecules as-deposited at 112 K has an already-ordered orientation. This is, however, a metastable structure. It changes to a more stable structure of an ordered orientation having almost exclusively trimeric forms as the temperature increases from 112 to 130 K.

The spectral changes induced by the single-bunch SR (  $\lambda > 1$  nm ) irradiation are shown in Fig. 2. This shows that as-deposited condensed layer containing the dimer and

trimer forms change to the only trimer forms by SR irradiation. Of course, photo-stimulated desorption also occur. The substrate temperature increase by SR irradiation is measured to be about 4 degrees for 30 sec irradiation in the case of single bunch ( $\sim 15$  mA ring currents). So, the thermal effects by the SR irradiation can be ignored in the present case. No drastic spectral change was induced by the multi-bunch SR beam using sapphire filter ( $\lambda > 150$  nm). These data indicate that the inner-shell or valence electron excitation of aluminum by SR induces the change from the mixture of the dimer and trimer forms to only trimer forms.

## References

- [1] T. Motooka, S. Gorbatkin, D. Lubben, Djula Eres, and J. E. Greene, *J. Vac. Sci. Technol.*, **A4** (1986) 3146.
- [2] T. Cacouris, G. Scelsi, P. Shaw, R. Scarmozzino, R. M. Osgood, and R. R. Krchnavek, *Appl. Phys. Lett.*, **52** (1988) 1865.
- [3] W. R. Salaneck, R. Bergman, J. E. Sundgren, A. Rockett, T. Motooka and J. E. Greene, *Surface Science*, **198** (1988) 461.
- [4] Y. Zhou, M. A. Henderson and J. M. White, *Surface Science*, **221** (1989) 160.
- [5] D. R. Strongin and P. B. Comita, *J. Phys. Chem.*, **95** (1991) 1329.

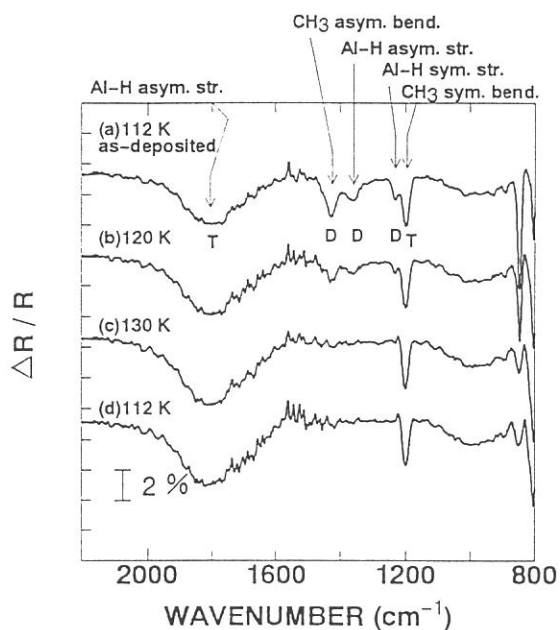


Fig. 1 Observed IRAS spectra of DMAH, (a) as deposited at the substrate temperature of 112 K and 30 L dose, (b) then the temperature was increased to 120 K, (c) then to 130 K and (d) then cooled to 112 K.

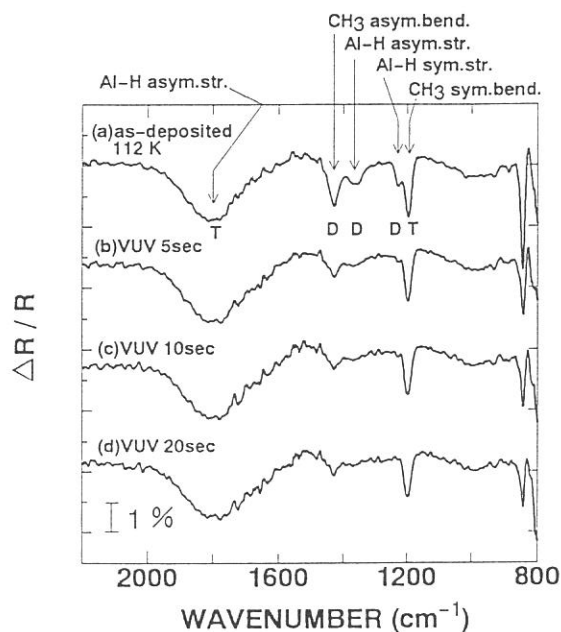


Fig. 2 Observed IRAS spectra of DMAH, (a) as deposited at the substrate temperature of 112 K and 30 L dose, (b) then VUV ( $> 1\text{nm}$ ) 5 sec irradiation, (c) then more 5 sec, total 10 sec, (d) total 20 sec irradiation.

Synchrotron radiation excited growth of ZnTe by atomic layer epitaxial technique using metalorganic sources.

Toshihiro OGATA, Syed Irfan GHEYAS, Hiroshi OGAWA\* and Mitsuhiro NISHIO

Institute for Molecular Science, Myodaiji, Okazaki 444, Japan

\*Department of Electronic Engineering, Faculty of Science and Engineering, Saga University, Honjo-1, Saga 840, Japan

In our previous studies on ZnTe deposition, diethylzinc and diethyltelluride were fed simultaneously into the reaction chamber using hydrogen as a carrier gas. The quantum yield for forming ZnTe molecules by photons is higher than 0.7% at room temperature. Thus, SR will be a powerful light source for the low temperature growth of ZnTe. However, a strong thickness profile of the deposited film was always recognized in the vertical direction. The non-uniformity of the film may be attributed to the deposition by simultaneous gas supply. Alternative gas supply of metalorganic sources, i.e., atomic layer epitaxial technique may bring out excellent uniformity and lead to ultimate control of film thickness.

In this experiment, room temperature epitaxial growth of ZnTe has been studied on the (100) oriented GaAs substrate using SR as a light source by atomic layer epitaxial technique, i. e., by supplying diethylzinc and diethyltelluride alternatively. The growth experiments have been carried out using the beam line, BL-4A. Time sequences for the gases and synchrotron radiation irradiation used here are shown in Fig.1. The source gases of diethyltelluride and diethylzinc were introduced alternatively into the chamber with an interval of 60 s between each other to prevent mixing of the gases by switching air-operated valves controlled by a personal computer. SR irradiation onto the sample was synchronized with the introduction of both source gases. Figure 2 shows the result of the stylus step profiler. Here, the thickness profile of the film deposited by simultaneous gas supply is shown in the same figure. It is seen that the film with excellent uniformity can be obtained by alternative gas supply. Such a plateau shape in the deposition profile is similar to the characteristic of atomic layer epitaxy. Figures 3 (a) and (b) show the dependence of the growth rate upon the metalorganic flux.

The growth rate increases with diethylzinc or diethyltelluride flux and becomes almost saturated at one monolayer per cycle. This tendency seems to be quite similar to the characteristic of atomic layer epitaxy. Thus, we can control successfully the growth rate corresponding to almost one monolayer per cycle with the irradiation of SR.

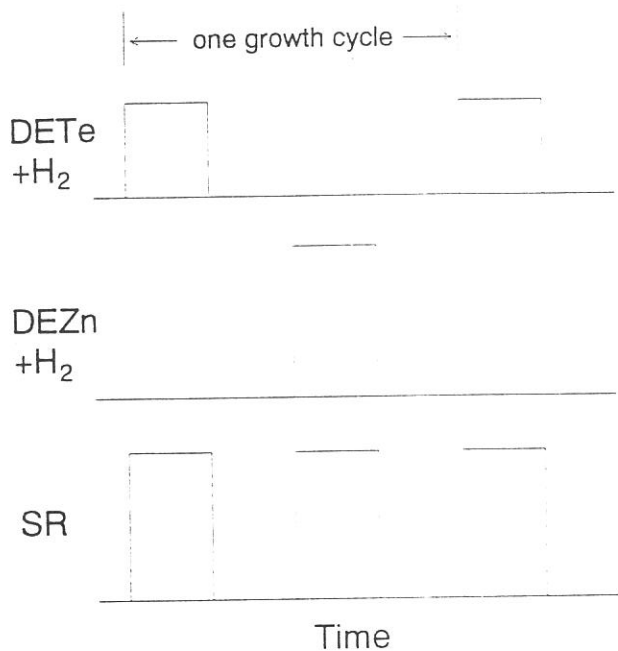


Fig. 1. Time sequence for gases and SR irradiation.

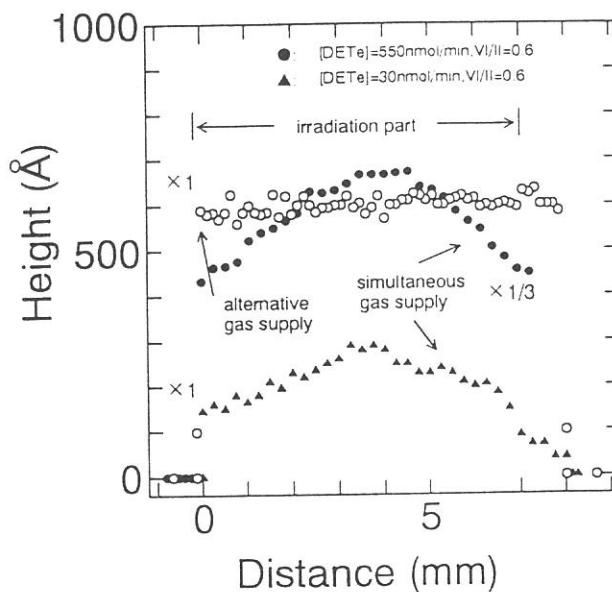


Fig. 2. A typical thickness distribution measured with a stylus step profiler. The results on the films deposited by simultaneous gas supply are also shown in the figure.

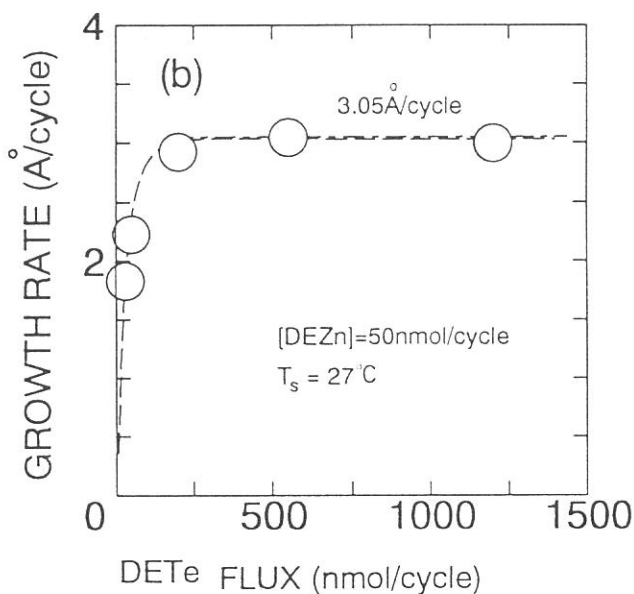
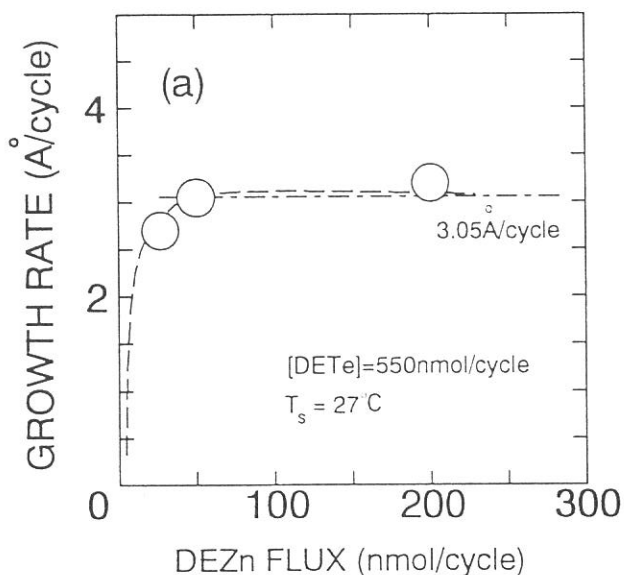


Fig. 3. Growth rate of deposited film versus flux of DEZn (a) or DETe (b).

## Synchrotron radiation assisted surface process of adsorbed diethylzinc on GaAs(100)

Syed Irfan GHEYAS, Toshihiro OGATA, Hiroshi OGAWA\* and Mitsuhiro NISHIO

Institute for Molecular Science, Mydaiji, Okazaki 444, Japan

\*Department of Electronic Engineering, Faculty of Science and Engineering, Saga University, Honjo-1, Saga 840, Japan

Studying the effects of photon illumination on the decomposition of diethylzinc adsorbed on GaAs (100) surface should give useful information about the photon-assisted surface process at the initial growth stage of II-VI compounds using GaAs substrate, since diethylzinc is one of the most widely used group II alkyl sources. In this study, the effects of white light synchrotron radiation (SR) and greater than 150 nm photons on the diethylzinc adsorbed GaAs (100) surface have been studied by x-ray photoelectron spectroscopy. The experiments have been carried out in the beam line, BL-4A.

Figure 1 shows Zn  $2p_{3/2}$  XPS spectra taken for adsorbed DEZn at 115 K and following exposure to SR. For DEZn covered GaAs (100), Zn  $2p_{3/2}$  peak is mainly due to molecular DEZn (curve a). Exposing the adsorbed DEZn to longer than 150 nm photons even (1500 mA·min SR transmitted through a sapphire window) does not alter the peak position (curve b). Exposing DEZn at 115 K to 400 mA·min of SR results in an approximately 0.8 eV downward shift of the Zn  $2p_{3/2}$  peak to 1022.2 eV (curve c). So it is considered that SR decomposes adsorbed DEZn even at a very low temperature such as 115 K but light in the longer than 150nm region seems to have no visible effect on the adsorbed state of this metalalkyl. A very conservative estimate shows the average quantum efficiency for dissociating DEZn to be better than 0.005 per photon over the 0.5 to 150 nm region. Figure 2 shows C 1s and Ga  $L_{3}M_{23}M_{45}(^1P)$ . Clean surface shows almost no trace of carbon and the Ga  $L_{3}M_{23}M_{45}$  Auger peak appears at 282 eV (curve a). This peak becomes almost totally obscure after exposure of the GaAs surface to 100 L of DEZn (curve b). Instead a very strong C 1s peak appears at 285 eV. This peak loses more



than 40% of its intensity after 400 mA·min of SR illumination and FWHM increases by 0.4 eV. The desorption of molecular DEZn is found to be very low as suggested by Zn 2p peak intensity. So it seems that substantial amount of carbon gets desorbed during SR illumination even at 115 K. XPS data reveals that SR illumination at room temperature has no effect on adsorbed DEZn as far as dissociation of this metalalkyl is concerned, since DEZn is supposed to dissociate completely into Zn and ethyl species by 300 K (without photoassistance). XPS data related to C 1s at 300 K, on the other hand, makes some important revelation (Figure 3). C 1s signal becomes hardly traceable after the DEZn adsorbed GaAs (100) surface at 300 K is SR illuminated.

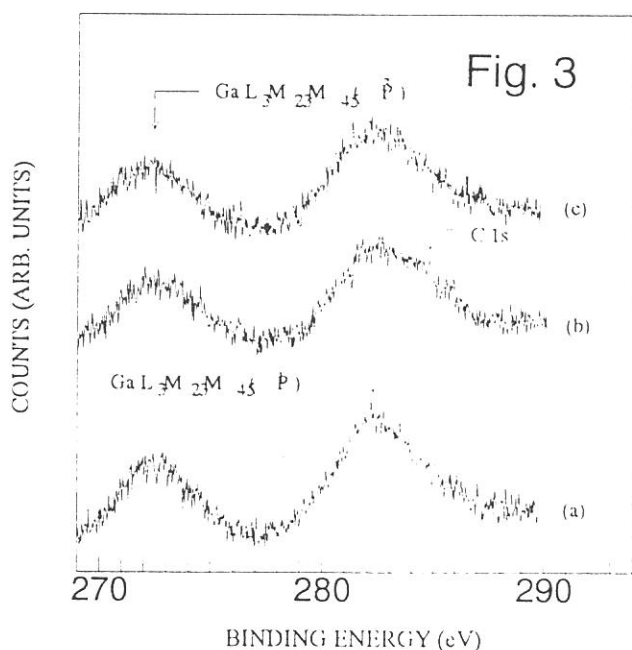
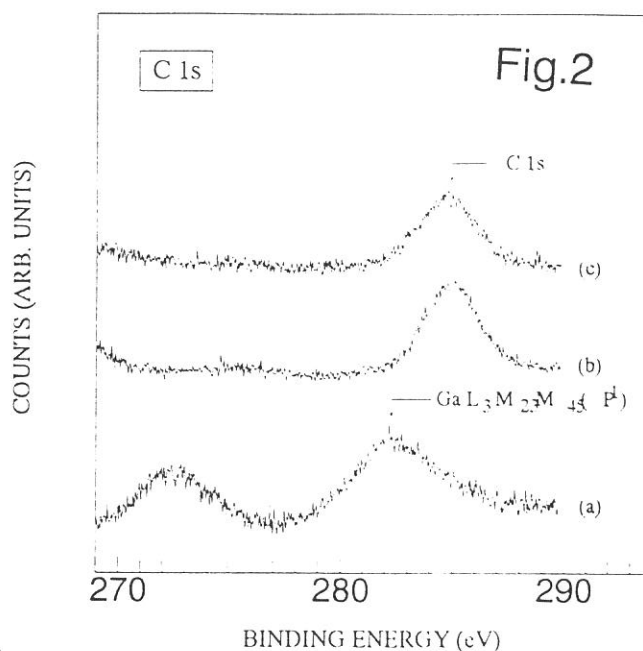
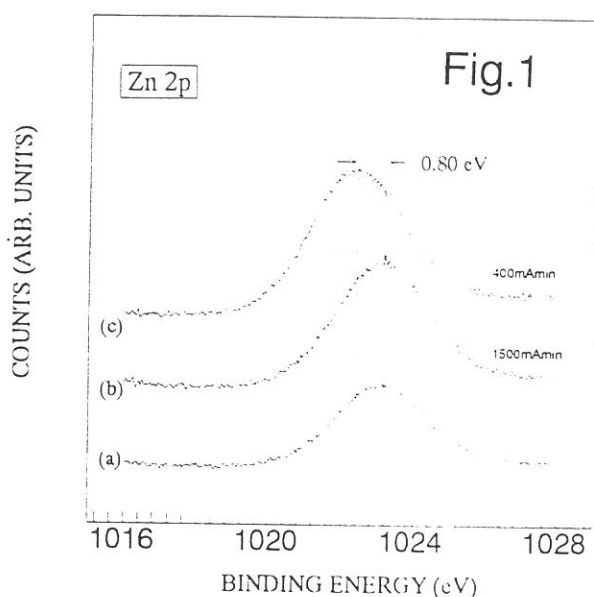


Fig.1. Zn 2p<sub>3/2</sub> XPS spectra (100L DEZn exposure at 115K).

Fig.2. XPS spectra in the 269–290 eV (100L DEZn exposure at 115K).

Fig.3. XPS spectra, in the 269–290 eV range, of (a) the clean GaAs (100) surface, (b) the same surface dosed with 600L DEZn at 300K, and following 625 mAmin SR illumination at 300K.

## Low temperature growth of II–VI compound semiconductors by synchrotron radiation using metalorganic sources

Toshihiro OGATA, Syed Irfan GHEYAS, Hiroshi OGAWA\* and Mituhiro NISHIO

Institute for Molecular Science, Myodaiji, Okazaki 444, Japan

\*Department of Electronic Engineering, Faculty of Science and Engineering, Saga University, Honjo–1, Saga 840, Japan

Low temperature growth is one of the important factors for preparing II–VI compounds of high quality. Synchrotron radiation (SR) will provide a powerful light source for a novel low–temperature growth technique of semiconductors. In this study, the deposition of ZnSe on (100) GaAs substrate has been carried out in the beam line, BL–4A, at very low pressure of  $10^{-5}$  Torr using diethylzinc and diethylselenide as the precursor sources and hydrogen as carrier gas. The deposited films are characterized by XPS and RHEED. The effect of the transport rate of source materials upon the growth rate of ZnSe film has been investigated. Furthermore, similar effect has been studied for ZnTe film by using diethylzinc and diethyltelluride as source materials, and the process associated with the SR excited growth is given here.

The formation of the film can be recognized only in the region exposed to SR for ZnSe and ZnTe depositions, indicating that the surface excitation process is the dominant growth mechanism. The epitaxial growth of ZnSe occurs even at room temperature when the film thickness is less than  $100\text{\AA}$ . When the film thickness exceeds around  $100\text{\AA}$ , the simultaneous growth of the epitaxial layer and micro–crystals takes place, very different from the case of ZnTe deposition where the epitaxial layers can be obtained independent of film thickness. Figures. 1 (a) and (b) show the dependence of ZnSe deposition rate upon the transport rate of metalorganic source. The growth rate is almost independent of diethylzinc transport rate, while it varies greatly with diethylselenide transport rate. Accordingly, the growth rate of ZnSe is governed by the supply of diethylselenide. Similar tendency is observed in the SR excited growth of ZnTe using diethylzinc and diethyltelluride, as shown in Figures. 2 (a) and (b). Thus, the process in ZnSe deposition might resemble that in the ZnTe growth, although the value of ZnTe growth rate is higher

than that of ZnSe growth rate by a factor of around 10 under the same growth condition. The results obtained here suggest that the adsorbed species related with VI-group followed by the decomposition due to the surface excitation plays an important role in the growth of II-VI compounds.

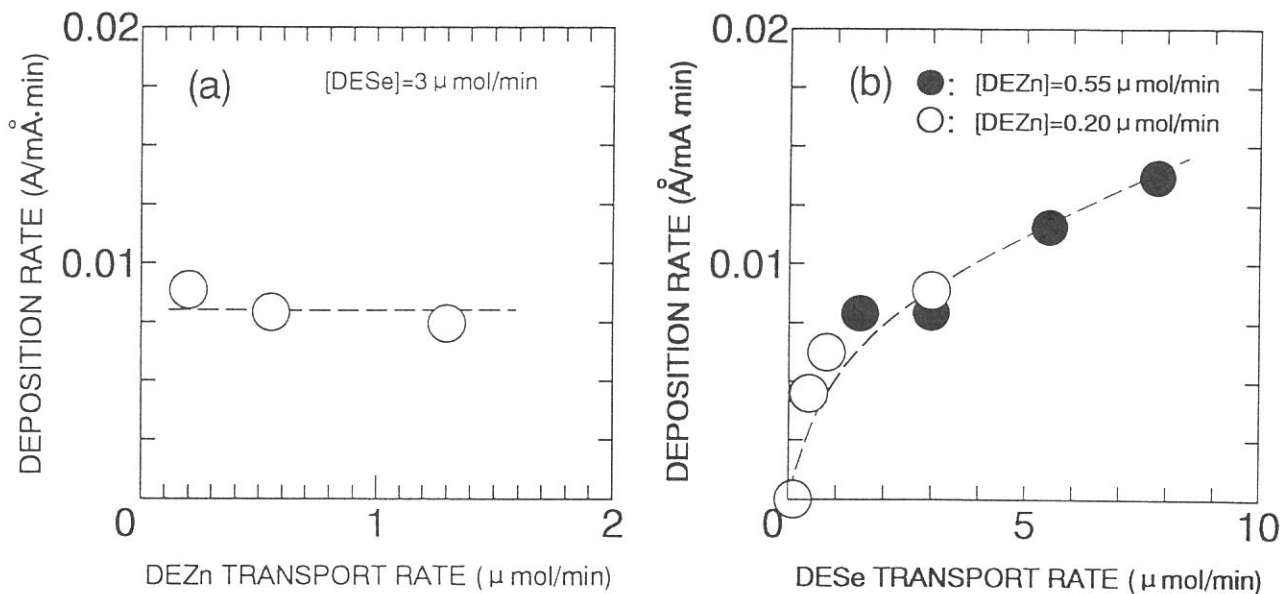


Fig. 1. Deposition rate of ZnSe versus transport rate of DEZn (a) or DESe (b).

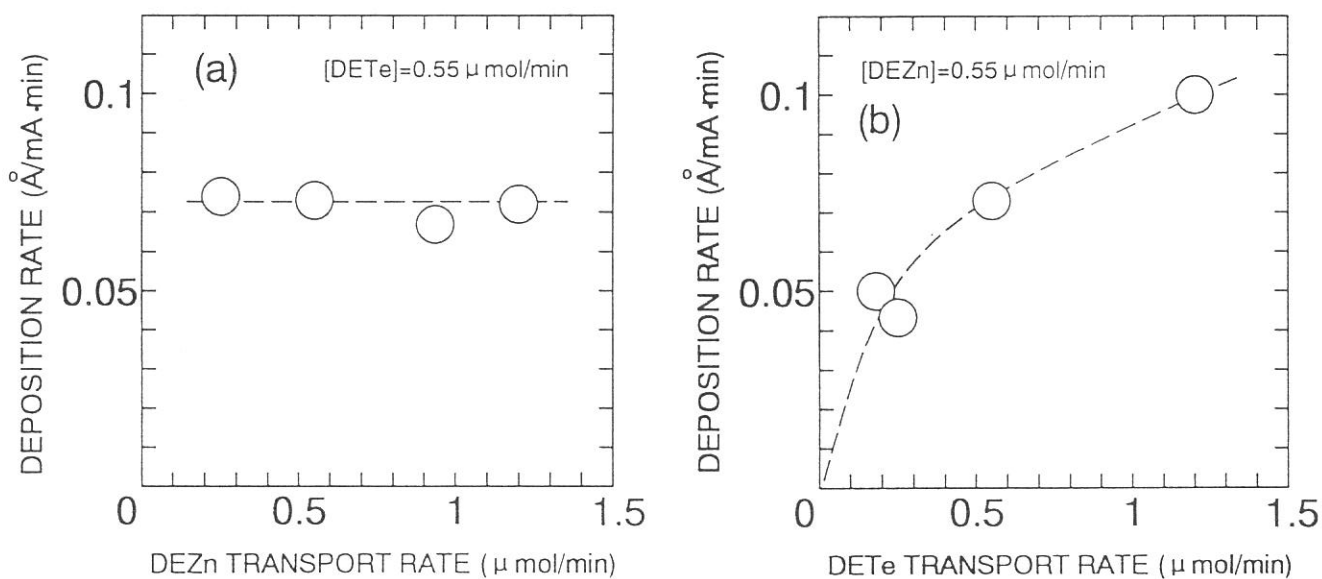


Fig. 2. Deposition rate of ZnTe versus transport rate of DEZn (a) or DETe (b).

# In situ observation of SR-induced a-Si deposition by using BML-IRAS

A.Yoshigoe\*, M.Nagasono\*\*, K.Mase\*\* and T.Urisu\*\*

*\*The Graduate University for Advanced Studies, Institute for Molecular Science, Myodaiji, Okazaki 444*

*\*\* Institute for Molecular Science, Myodaiji, Okazaki 444*

By applying infrared reflection absorption spectroscopy ( IRAS ) using buried metal layer ( BML ) substrate<sup>1)</sup> to the in situ observation of SR induced a-Si chemical vapor deposition ( CVD ), vibrational spectra of surface SiH<sub>n</sub> species in this reaction system are observed with sufficient sensitivity for the submonolayer coverage.

Experiments are carried out using an apparatus of surface photo-chemical reaction chamber equipped with an optical system for IRAS<sup>2)</sup>. This system is set at beam line 4B. The calculated photon wavelength distributes from 1 nm to more than 100 nm with its peak at about 10 nm, and the flux is  $1.6 \times 10^{16}$  photons/s for 100mA ring current on the 15 mm<sup>2</sup> sample surface. Spectra were measured using FT - IR spectrometer ( JIR7000 of JEOL Co.Ltd ) equipped with MgCdTe ( MCT ) detector by 4 cm<sup>-1</sup> resolution and 1000 scans. The p-polarization of IR beam was selected by a wire - grid polarizer using barium fluoride substrate. The optical path was purged with dry N<sub>2</sub>. The spectra were recorded as  $\Delta R/R_0$  (  $\Delta R = R' - R_0$  ) where R' and R<sub>0</sub> are the reflectance for the substrate with and without a deposited layer, respectively. N - type Si(100) substrates with a 200 - nm - thick Al layer buried under a 15 -nm - thick SiO<sub>2</sub> thin film were used as BML substrate. The sample washed by acetone and deionized water was set on the Mo sample holder in the reaction chamber ( base pressure was  $4 \times 10^{-10}$  Torr ). The a-Si was deposited on the surface of the SiO<sub>2</sub> BML substrate by an SR beam irradiation at 150°C under the Si<sub>2</sub>H<sub>6</sub> gas of  $1 \times 10^{-3}$  Torr.

Fig. 1 shows the IRAS spectra of a-Si observed in situ after deposition for several doses ( = storage ring current  $\times$  exposure time ). Peaks at around 2100, 908, and 866 cm<sup>-1</sup> are assigned to SiH<sub>n</sub> vibrations. The 950 cm<sup>-1</sup> peak is assigned to the Si-O-Si stretching vibration

in the O doped amorphous Si. This peak is considered to appear due to the SR induced reactions between surface  $\text{SiO}_2$  and  $\text{Si}_2\text{H}_6$ . The main component of the  $2100\text{cm}^{-1}$  band is  $\text{SiH}_2$  vibrational mode. So the observed bands at  $908$ , and  $866\text{cm}^{-1}$  are assigned to  $\text{SiH}_2$  bending vibrations. The deposition rate was measured to be about  $0.1\text{nm}/100\text{mA} \cdot \text{min}$  by using a step profile meter. If it is assumed that this value is valid for the thin film of a monolayer order, the spectra shown in Fig. 1 correspond to thin films of  $0.02$  to  $0.5\text{nm}$  thickness. This indicates that the present BML - IRAS technique has sufficient sensitivity for submonolayer adsorbates of  $\text{SiH}_n$ .

1) A. Yoshigoe, A. Nagasono, K. Mase, and T. Urisu, UVSOR Activity Report (1993)72.

2) M. Nagasono, A. Yoshigoe, K. Mase, and T. Urisu, UVSOR Activity Report (1993)19.

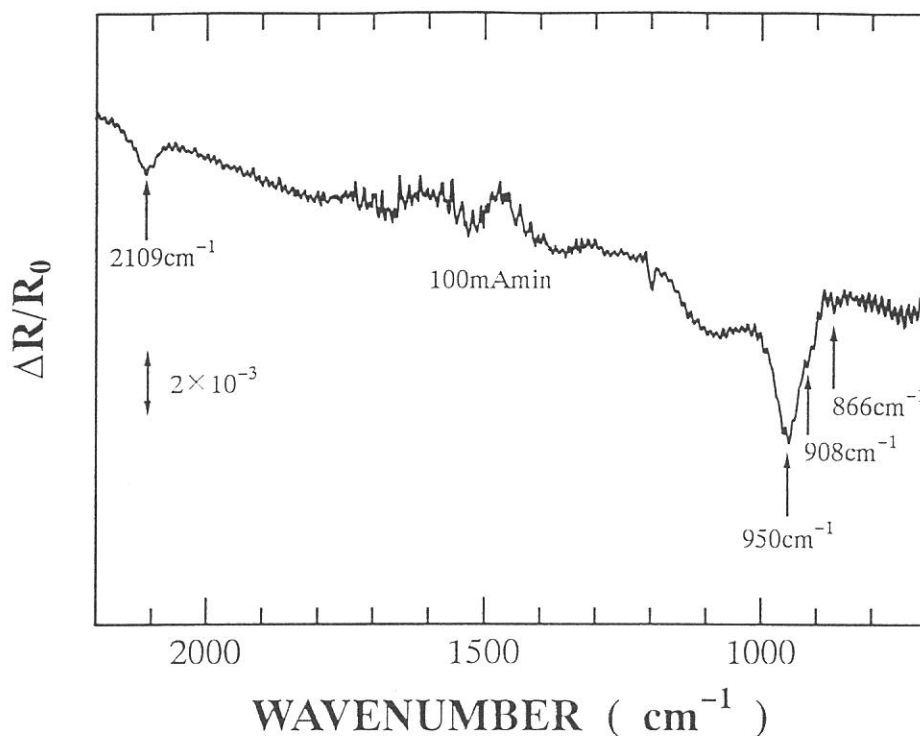


Fig.1 In situ measurement IRAS spectra of the a-Si deposited by the SR-CVD on the  $\text{SiO}_2$  BML substrate.

# SYNCHROTRON RADIATION EXCITED ETCHING OF SILICON SURFACE STUDIED BY VELOCITY DISTRIBUTION MEASUREMENTS OF DESORBED SPECIES (III)

Haruhiko OHASHI<sup>1</sup> and Kosuke SHOBATAKE<sup>1,2</sup>

*Institute for Molecular Science<sup>1</sup>, Myodaiji, Okazaki 444, Japan*  
*Nagoya University<sup>2</sup>, Nagoya 464-01, Japan*

Synchrotron radiation (SR) excited etching of Si surface with XeF<sub>2</sub> are studied. The velocity distributions of the desorbed neutral species from etched Si surface have been measured using a time-of-flight (TOF) technique and an electron bombardment ionization mass spectrometer detector (EBIMS)<sup>1,2</sup>. In the case of thermal or undulator light excited etching by XeF<sub>2</sub> at room temperature, the desorbed species were SiF<sub>4</sub> and more large molecules such as Si<sub>2</sub>F<sub>x</sub> (3 ≤ x ≤ 6). The velocity distributions are Maxwell Boltzmann ones and the translational temperatures are approximately equal to surface temperatures. On the other hand when focused white SR light from a bending magnet was irradiated upon the Si sample in the XeF<sub>2</sub> atmosphere above a few tens of thousands of doses (mA·min), the desorbed neutral species were SiF<sub>3</sub> or SiF<sub>2</sub>.

Depending on the experimental conditions one or two peaks appear in the velocity distribution. Figure 1 shows the TOF spectra observed at detected ion mass m/e=85(SiF<sub>3</sub><sup>+</sup>). Though the slow peaks for accommodated species depend on sample temperatures, the fast one is independent of the surface temperature. Although the additional peak for the fast moving species was not only always observed even when Si was irradiated with focused white SR light, it is distinctly observed only when SR is shone upon Si. The desorbed molecules and the number of peaks depended upon the experimental conditions such as irradiation time, SR beam intensity and XeF<sub>2</sub> gas doses. It is known that there are thick Si<sub>x</sub>F<sub>y</sub> layers on Si surface etched by XeF<sub>2</sub>. It is considered that the condensed layer of Si<sub>x</sub>F<sub>y</sub> is decomposed into smaller molecules by focused SR light.

To clarify the variation of the condensed

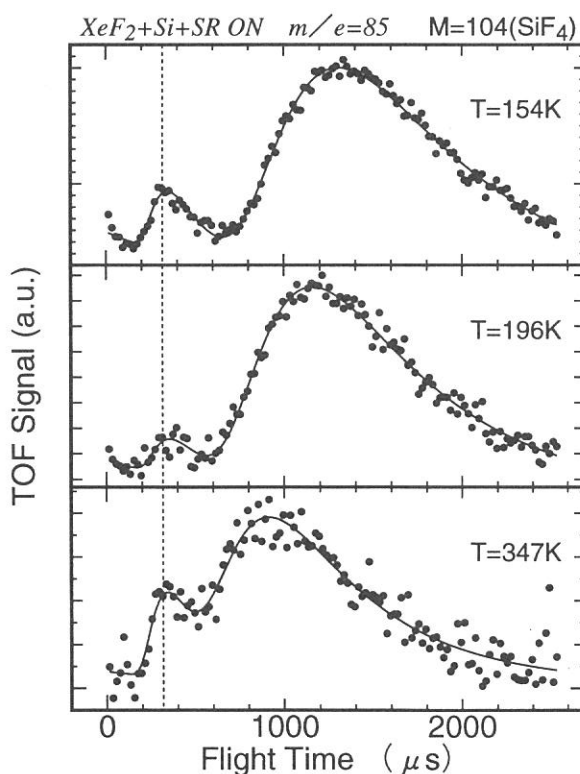


Figure 1. TOF spectra of desorbed species detected at mass m/e=85(SiF<sub>3</sub><sup>+</sup>) with focused SR beam. The curve corresponds to the calculated SMB and MB distribution.



Si<sub>x</sub>F<sub>y</sub> layer with and without SR irradiation, thermal desorption spectra (TDS) were measured. Figure 2 shows TDS observed at a detected ion mass  $m/e=85$  (SiF<sub>3</sub><sup>+</sup>) after SR excited etch and after thermal etching and SR dose without etchant. The upper curve shows that there exist two types of Si<sub>x</sub>F<sub>y</sub> species in the condensed layer formed from focused white SR excited etching using XeF<sub>2</sub> as etchant gas. The ratio of their intensity depends upon SR as well as XeF<sub>2</sub> doses. After Si was exposed XeF<sub>2</sub> for 16 min at room temperature without SR light (thermal etching) and the etchant gas was exhausted, SR was shone upon for 460 mA·min or 5473 mA·min (see the lower two curves). Both structures of layer seen in the upper curve are decomposed by SR irradiation while the etchant is not present. The low temperature component is more easily dissociated than the high temperature component under SR irradiation without etchant. As TOF spectra show that detected SiF<sub>3</sub><sup>+</sup> ion is the fragment of the desorbed neutral SiF<sub>4</sub> or Si<sub>2</sub>F<sub>x</sub> ( $3 \leq x \leq 6$ ) which species are observed while thermal etching. On the other hand other TOF results show that the smaller molecules (SiF<sub>x</sub>,  $x < 4$ ) are also desorbed under this condition while SR is irradiated upon the surface. The low temperature component seemed to be the fragment of larger molecules such as Si<sub>2</sub>F<sub>x</sub>. It is considered that the former component is the secondary thermal reaction on the surface.

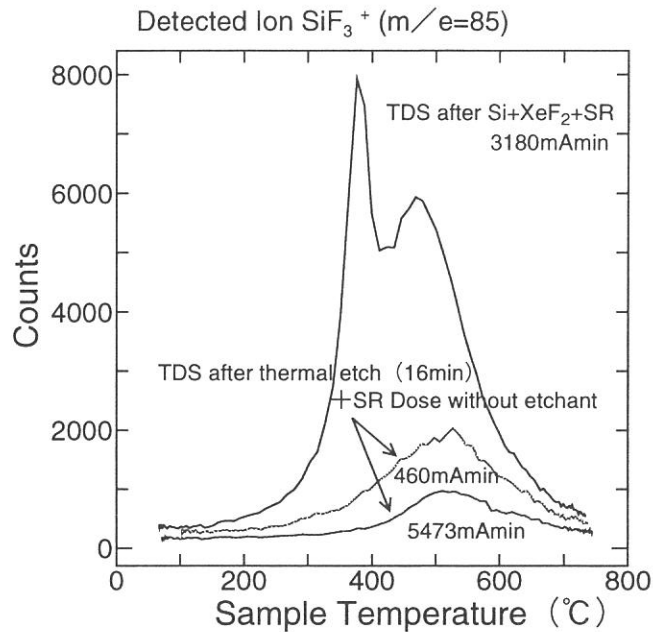


Figure 2. TDS spectra of detected ion SiF<sub>3</sub><sup>+</sup> after SR excited etching and after thermal etch and SR dose without etchant

Although the origins of and the relation between the TOF peak for the fast moving species and the TDS peaks are not well understood at this moment, a thick condensed Si<sub>x</sub>F<sub>y</sub> layer must be present in order for both peaks to appear under the condition that Si is irradiated by focused white SR light after a few tens of thousands dose (mA·min) at XeF<sub>2</sub> atmosphere.

## Reference

- 1) H. Ohashi, K. Tabayashi and K. Shobatake, UVSOR Activity Report (1992) 122.
- 2) H. Ohashi and K. Shobatake, UVSOR Activity Report (1993) 74.

# Beamsplitting and Polarization Properties of Cr/C Transmission Multilayers close to the Carbon K-edge

F. Schäfers

BESSY, Lentzeallee 100, 14195 Berlin, Germany

A. Furuzawa, K. Yamashita

Department of Physics, Nagoya University, Japan

M. Watanabe

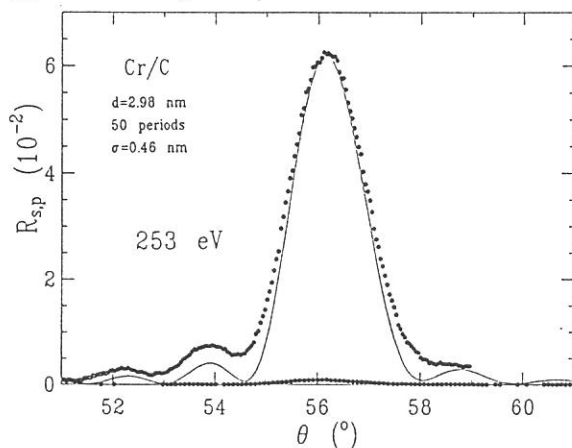
UVSOR, Institute of Molecular Science, Okazaki, Japan

J.H. Underwood

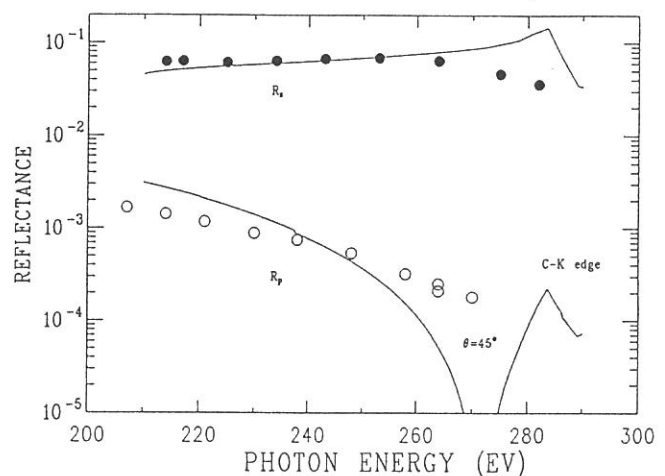
Center for X-ray Optics, LBL, Berkeley, CA 94720, USA

This paper reports on the beamsplitting (reflection and transmission) properties of a Cr/C-transmission multilayer which was optimized for use as phase retarder for polarization analysis around 270 eV /1,2/. The performance for both for s- and p-polarized light was measured at various incidence angles from near-normal incidence to the Brewster-angle. The data are compared with calculations taking into account the interfacial roughness of the multilayer used in reflection.

The experimental data have been collected at the radiometry beamline 5B of the UVSOR storage ring /3/ in a 2 weeks beamtime shift in April 1993. Two Cr/C multilayers (50 periods with a total thickness of 3.0 - 3.2 nm) were investigated: The first one used in reflection was produced on a standard Si-wafer. The second one used in transmission, also on a Si-wafer had a window of 3 by 5 mm<sup>2</sup> which was edged down to a thickness of approximately 0.2  $\mu$ m.



**Figure 1:** Measured reflectancies for s- and p-polarized light at 253 eV photon energy for the Cr/C multilayer as function of the grazing angle of incidence, in comparison with a calculation taking the roughness into account.



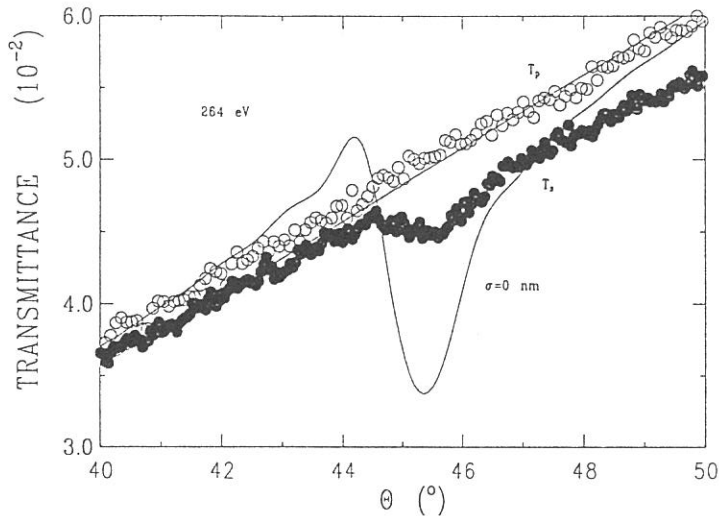
**Figure 2:** Measured peak-reflectancies for s- and p-polarized light for various photon energies. For the calculation the roughness values of Fig. 1 fitted at 253 eV were used.

Fig. 1 shows the experimental results for the BRAGG-reflected intensity for s- and p-polarized light of 253 eV photon energy. In comparison the calculated reflectance is shown also. A best fit is achieved by assuming a roughness of  $\sigma=0.46$  nm according to the parametrization given in ref. /4/. In order to reproduce the experimental data for p-polarization a slightly larger roughness and a larger d-spacing had to be used in the calculation.

Fig. 2 gives the experimental peak reflectancies for different energies between 200 eV and the C-K edge both for s- and for p-polarized light. The Bragg-peak moves from near normal

incidence to approximately  $45^\circ$ , behind the C-K edge no reflected intensity can be detected due to strong absorption in the Carbon layers. Note that a remarkable s-reflectance of 6 % in near normal incidence was measured! For comparison calculated reflectancies taking into account the fitted roughness parameters of Fig. 1 are also shown.

The corresponding reflectance for p-polarized light is only 0.2 % and is decreasing towards the quasi-Brewster-angle at  $45^\circ$  to 0.02 %. The polarizance which is defined as the ratio  $R_s/R_p$  varies in accordance to calculation between 30 and 200 so that this multilayer can be used as efficient linear analyzer when it is operated close to the Brewster-angle as was done in ref. /2/.



**Figure 3:** Measured transmittance for s- and p-polarized light at 264 eV photon energy for the Cr/C multilayer as function of the grazing angle of incidence, in comparison with a calculation for a perfect multilayer ( $\sigma=0$  nm).

The transmission behaviour of the multilayer is plotted in Fig. 3 as function of the angle of incidence for a photon energy of 264 eV which corresponds to a BRAGG-angle close to the Brewster angle of  $45^\circ$ . The results are shown for s- and for p-polarized light. The difference between s- and p-component is clearly seen though not that strongly pronounced as theoretically expected (full lines). Only the s-component is resonating in analogy to the Bragg-reflection case. The roughness was neglected in the calculation but the transmission of the Si-membrane was taken into account.

## CONCLUSION

We have presented experimental data on a high performance transmission type multilayer of Cr/C which can be used both in reflection and in transmission. It combines the properties of a beamsplitter where the incident beam is splitted into two beams of nearly equal intensity, separated by approximately  $90^\circ$ , of a linear polarizer with a polarizance of up to 200 in the Brewster minimum and of a phase retarder which can be used in polarimeters for analyzation of circularly polarized light. It can be operated in the photon energy range between 200 eV and the C-K edge at 284 eV.

## ACKNOWLEDGEMENT

The project was funded by a Grand-in-Aid from the Japanese Ministry of Education, Science, and Culture, for Scientific Research on priority areas: "X-ray imaging Optics".

## REFERENCES

1. S. Di Fonzo, W. Jark, Rev. Sci. Instr. **63**, 1375 (1992)
2. S. Di Fonzo, W. Jark, F. Schäfers, H. Petersen, A. Gaupp, to be published in Appl. Opt. **33**, (1994)
3. M. Sakurai, J. Fujita, K. Yamashita, M. Ohtani, I. Hatsukade, K. Tamura, H. Nagata, Y. Suzuki, S. Seki, Vacuum, **41**, 1234 (1990)
4. K. Yamashita, M. Watanabe, O. Matsudo, J. Yamazaki, I. Hatsukade, T. Ishigami, S. Takahama, K. Tamura, M. Ohtani, Rev. Sci. Instrum. **63**, 1217 (1992)

## Optical Properties of Compound Semiconductors in VUV Region

Qixin GUO, Yoshiaki MITSUISHI, Hiroshi OGAWA, and Akira YOSHIDA\*

*Department of Electronic Engineering, Faculty of Science and Engineering,  
Saga University, Saga 840**\*Department of Electrical and Electronic Engineering,  
Toyohashi University of Technology, Toyohashi 441*

Indium nitride, one of the III-V compound semiconductors with a wurtzite crystalline structure, has direct band gap of around 1.9 eV at room temperature, and is promising for visible light optoelectronic devices and highly efficient solar cells. Moreover, InGaN and InAlN are expected to yield light-emitting diodes and laser diodes operating in the orange to ultraviolet range of the spectrum, because in these systems it is possible to vary the energy gap between 1.9 and 6.2 eV.<sup>1-3)</sup> In spite of the prospects of the nitrides in device applications, experimental data on the optical properties are surprisingly scarce, and the understanding of these properties is far from being satisfactory. Accurate knowledge of the optical spectra over a wide range of wavelength is indispensable for many applications. In our preceding paper,<sup>4)</sup> we reported the refractive index of InN in the energy from 2 to 20 eV. The purpose of this study is to develop our previous work on the optical spectra to the higher photon energy (up to 120 eV) and to understand totally the electronic structure of InN.

InN films were grown on (0001) oriented sapphire substrates by microwave-excited metalorganic vapor phase epitaxy. Reflection high energy electron diffraction (RHEED) results showed all the films to be single crystal and to have an orientation relationship of (0001)InN // (0001)Sapphire. Visual inspection by an optical microscope showed that the films have a specular surface. Reflectance spectra were measured at BL5B of UVSOR in the Institute for Molecular Science. Reflectance data  $R(E)$  were obtained by taking the ratio  $I_r(E)/I_0(E)$ , where the intensities for incident light  $I_0(E)$  and reflected light  $I_r(E)$  were measured in sequence in a given photon energy interval. The incident angle was near normal,  $15^\circ$  from the normal axis of the sample surface. Figure 1 shows the reflectance spectrum from a specular InN single crystal. The optical constants are determined from the reflectance and the phase  $\theta(E)$  which is calculated by the Kramers-Kronig analysis of the reflectance spectra. Figure 2 gives the obtained imaginary part of the dielectric function  $\varepsilon_2$  of InN. Good agreement was found between our spectra and those reported in the calculation of pseudopotential method.<sup>5)</sup>

## References

- [1] S. Nakamura, T. Mukai, and M. Senoh, *Appl. Phys. Lett.* **64**, 1687 (1994).
- [2] Q.X. Guo and A. Yoshida, *Jpn. J. Appl. Phys.* **33**, 2453 (1994).
- [3] Q.X. Guo, H. Ogawa, and A. Yoshida, *J. Crystal Growth*, (1994). (in press)
- [4] Q.X. Guo, O. Kato, M. Fujisawa, and A. Yoshida, *Solid State Commun.* **83**, 721 (1992).
- [5] N.E. Christensen and I. Gorczyca, *Phys. Rev. B* **50**, 4397 (1994).

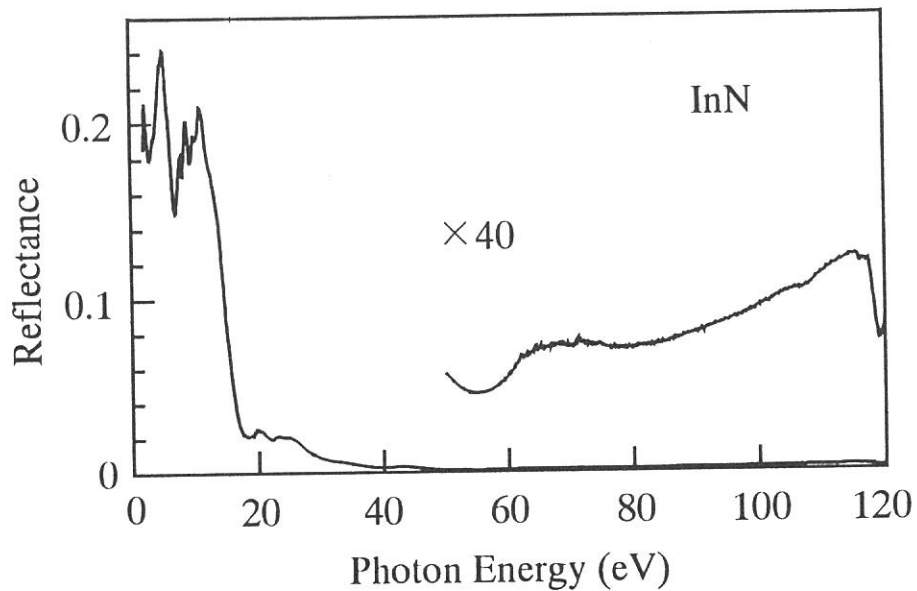


Fig. 1. Reflectance spectrum of indium nitride.

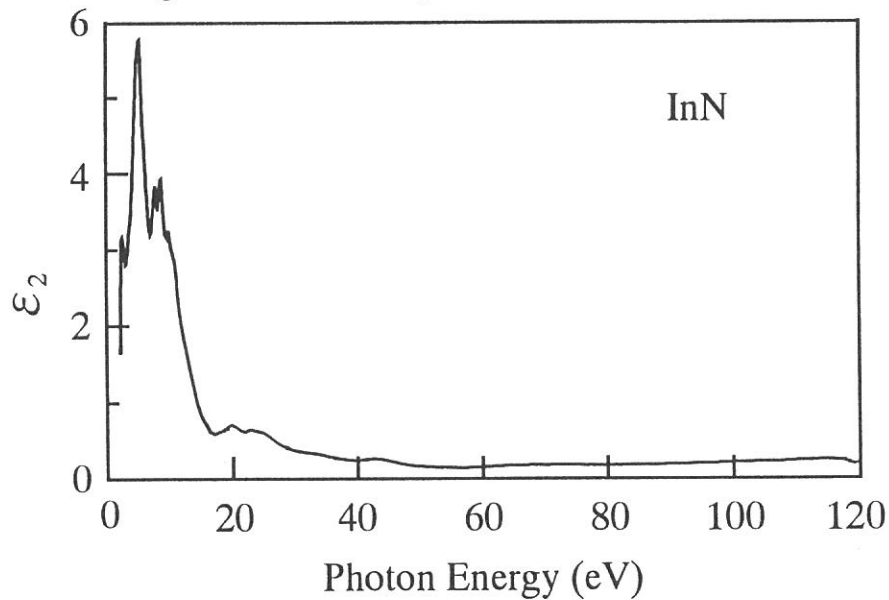


Fig. 2. Photon energy dependence of imaginary part of the dielectric function of indium nitride.

## VUV Reflection Spectra of Amorphous Chalcogenide Films

Koji HAYASHI, Daisaku KATO\*, and Koich SHIMAKAWA\*

*Institute for Molecular Science, Okazaki 444*

*\*Department of Electronics and Computer Engineering, Gifu University, Gifu 501-11*

A lot of works have been done for the characterization of the amorphous chalcogenide materials (such as a-As<sub>2</sub>S<sub>3</sub>, a-As<sub>2</sub>Se<sub>3</sub>, and a-Se etc.) These materials are expected as a potential material for photofunctional devices because these materials are presenting variety of photoinduced phenomena. However to the best of our knowledge, the vacuum ultra-violet (VUV) reflection spectra in these materials has not been studied so far. In this report, we measured the VUV spectra in these materials for the first time.

The measurements were performed at room temperature at BL5B beam line of the UVSOR facility in Okazaki. Samples (a-As<sub>2</sub>S<sub>3</sub>, a-As<sub>2</sub>Se<sub>3</sub>, and a-Se) were prepared onto Corning 7059 substrates by the conventional evaporation technique. After evaporation, samples were annealed at near those glass-transition temperature for two hours in a vacuum.

Figure 1 shows the VUV reflection spectra of a-As<sub>2</sub>S<sub>3</sub>, a-As<sub>2</sub>Se<sub>3</sub>, and a-Se in the photon energy region between 35 eV and 65 eV at room temperature. Two main peaks and interfering pattern were observed at this energy region. The peaks 1 and 2 are corresponding to the 3d core levels of As and Se, respectively.

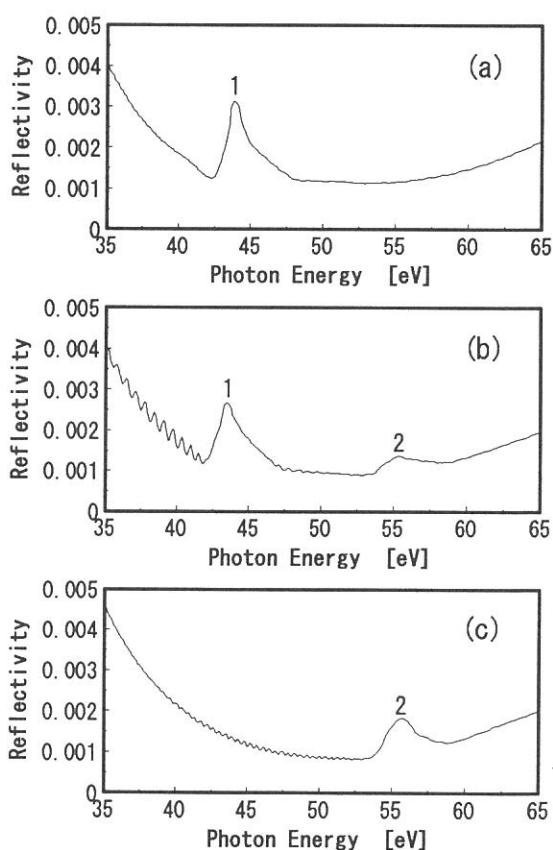
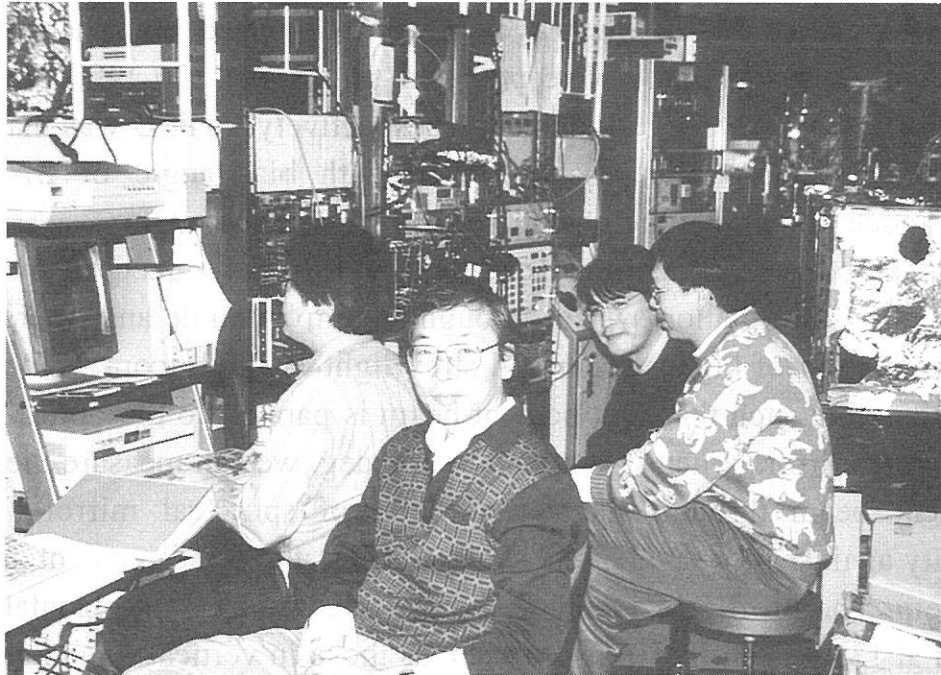


**Figure 1** The VUV reflection spectra of (a)a-As<sub>2</sub>S<sub>3</sub>, (b)a-As<sub>2</sub>Se<sub>3</sub>, and (c) a-Se.





Mr. K. Sakai (left) is preparing dry nitrogen for the 3-month shut down with Mr. E. Nakamura.



Prof. K. P. Lee (Korea, center) and Dr. Y. Q. Cai (Australia, right) are working with Dr S. Tanaka (left) and Mr. N. Takahashi at BL6A2.

## Characterization of Normal Incidence Multilayer Telescope in 100-300A Region

Koujun YAMASHITA, Hideyo KUNIEDA, Takashi YAMAZAKI,  
Kazuaki IKEDA, Kazutami MISAKI, Yoshiyuki TAKIZAWA\*,  
Masato NAKAMURA\*\* and Ichiro YOSHIKAWA\*\*

*Department of Physics, Nagoya University, Chikusa-ku, Nagoya 464-01*

*\*Institute of Space and Astronautical Science, Yoshinodai, Sagamihara 229*

*\*\*Department of Earth and Planetary Physics, University of Tokyo,  
Bunkyo-ku, Tokyo 113*

A normal incidence multilayer telescope on board a sounding rocket is aimed at observing extreme ultraviolet from celestial objects, which consists of a spherical mirror with 20 cm in diameter and focal length of 30 cm coated with Mo/Si multilayer and position sensitive detector(PSD) at the focal plane. The characterization of this telescope was carried out using monochromatized synchrotron radiation in the wavelength region 100-300A.

Three kinds of Mo/Si multilayer mirrors deposited on spherical surface with  $2d=140, 184$  and  $324\text{\AA}$  were prepared to observe 130-140, 170-180 and 270-330A band at near normal incidence, respectively. A PSD was made of CsI photocathode, tandem microchannel plate with bias angle of 27 deg and resistive anode to read out the position of an incident photon<sup>1)</sup>.

Incident beam monochromatized by PGM is introduced to the vacuum chamber with  $\theta-2\theta$  rotation system through  $0.2\text{mm}\phi$  pinhole and filters to avoid the contamination of higher order and stray light<sup>2)</sup>. A telescope is mounted on the rotation table such that the incident beam is parallel to the optical axis and normal to the mirror. When it is turned to 180 deg, we can measure the intensity of incident beam through the central hole of spherical mirror. Thus the reflectivity against the wavelength is obtained at the fixed incident angle with this system. The profile of incident and reflected beam in horizontal position observed at 133A is shown in fig.1, whereas those in vertical direction does not show any difference between them. The strange knee associated with main peak is due to the stray light which shows different spectrum. Care should be taken for the derivation of reflectivity from this measurement. We can obtain two dimensional beam profile at the fixed wavelength and incident angle by using PSD. The absolute detection efficiency of PSD was measured below 200A by

referring to that of a thin window proportional counter, which depends on the incident angle and wavelength.

The peak reflectivity of multilayer spherical mirrors was obtained to be nearly 60% for the peak wavelength of 133A and 172A and 20% for 300A at the normal incidence. This value is close to the calculated one based on the optical constant. The detection efficiency of PSD was obtained to be 30% in the wavelength region of 130-200A as expected. These results are promising for the further development of EUV multilayer optical system.

## References

- 1) K. Yamashita et al., Rev. Sci. Instrum., 63, 1513(1992).
- 2) K. Yamashita et al., UVSOR Activity Report 1990, p. 147.

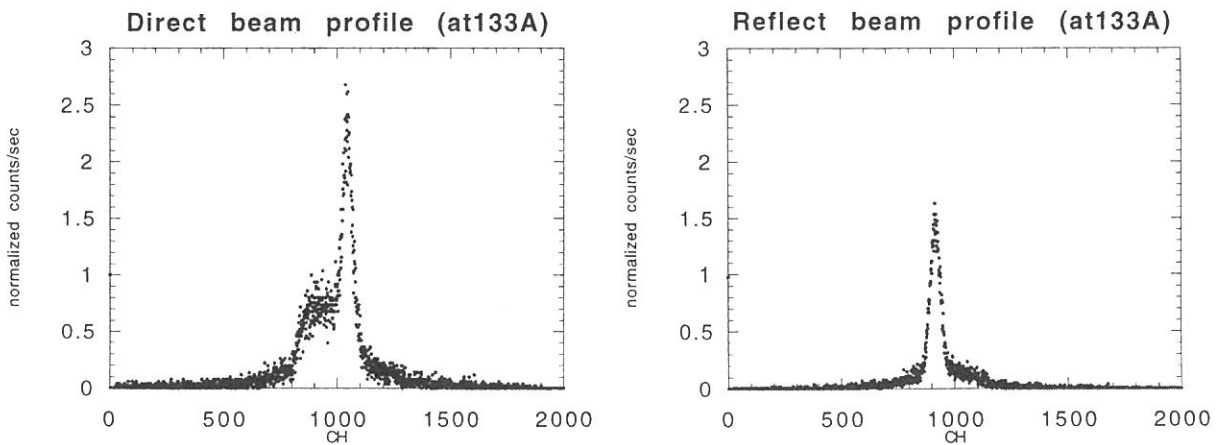


Fig.1 Profile of incident and reflected beam for the wavelength 133A at the horizontal position of PSD surface. The incident angle of reflected beam is 80 deg to the reflecting surface. 1mm on the PSD surface corresponds to 56ch in abscissa.

## Angular distribution of Ne metastable desorption induced by exciton formation at the surface of solid Ne

T. Hirayama\*, T. Nagai\*, M. Abo\*, I. Arakawa\*, M. Sakurai\*\*, and K. Mitsuke

Institute for Molecular Science, Myodaiji, Okazaki 444.

\* Department of Physics, Gakushuin University, 1-5-1, Mejiro, Toshima, Tokyo 171.

\*\* Department of Physics, Kobe University, 1-1, Rokkodai, Nada, Kobe 657.

The production of excitons in a rare gas solid (RGS) can lead to the desorption of metastable species. Two mechanisms, the cavity ejection (CE) and the excimer dissociation (ED), were proposed for these desorption phenomena<sup>1</sup>, and have been examined experimentally and theoretically. The studies of the kinetic energy and angular distributions of desorbed species can reveal the desorption mechanism and the exciton dynamics at the surface of RGS.

We have measured the kinetic energy and angular distributions of Ne metastable desorbed from solid Ne through exciton formation by the selective excitation using monochromatic synchrotron radiation. Photon stimulated desorption (PSD) experiments have been carried out at the beam line BL5B of UVSOR. Details of the experimental apparatus and the procedures have already been published elsewhere.<sup>2-4</sup>

The close correlation between the excitonic excitation in solid and the metastable desorption have been found by the wavelength dependence of the PSD metastable yield.<sup>5</sup> Figure 1 shows time-of-flight (TOF) spectra of desorbed Ne atoms in metastable excited state measured at the incident photon energies of 17.2, 17.6, 19.0 and 20.4 eV, which correspond to the excitation energies of 1st order surface exciton (S1), 1st order bulk exciton (B1), 2p<sup>5</sup>3p type surface exciton (S'), and 2nd order bulk exciton (B2), respectively. The peak at flight time  $t_f = 0$  is due to the scattered and/or emitted light from the sample surface, and is used as a standard of time. It has been already revealed<sup>1, 3</sup> that the higher kinetic energy peak A ( $E_k = 1.15$  eV), which is only observed by the excitation of the higher order excitons (S' and B2), is caused by the excimer dissociation (ED) mechanism and that the lower kinetic energy peaks D ( $E_k = 0.18$  eV)

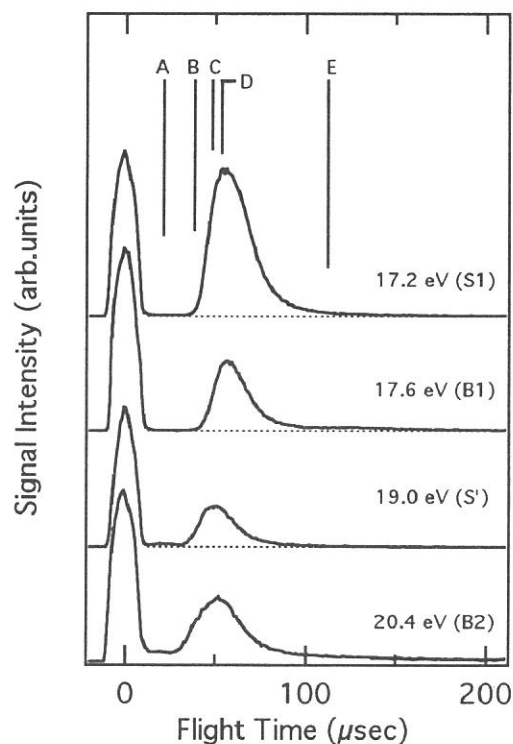


Fig.1. Time-of-flight spectra of PSD Ne\* at the excitation photon energies of 17.2, 17.6, 19.0, and 20.4 eV.

by S1 and B1 excitations and C ( $E_k = 0.23$  eV) by S' and B2 through the cavity ejection (CE) one. A broad peak or a plateau E appears ( $E_k = 0.05$  eV) by the bulk (B1 or B2) excitations and the shoulder B by the higher order (B2) excitations.

Angular distributions of the Ne\* intensities of the cavity ejection peaks at the photon energies corresponding to S1, B1 and S' excitations are shown in fig.2. Solid lines are the fitting curves using  $I(\theta) = \cos^n\theta$ . Each has a sharp angular distribution along the surface normal, however the sharpness of the distributions is different and depends on the type of the initial excitation. The remarkable sharpness of the CE peaks in these angular distributions can be explained in the framework of the cavity ejection mechanism. The reason for the obvious difference between the angular distribution of the CE peaks by S1 and S' excitation has not been clarified yet.

We have performed a simulation of the angular distributions of the desorbed metastable atoms using a simplified model.<sup>6</sup> Preliminary results show the qualitative agreement between the experiments and the simulation in the kinetic energy and the angular distributions.

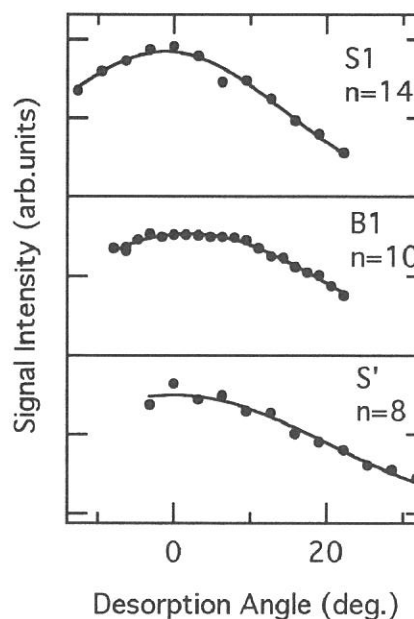


Fig.2. Polar angle dependence of the signal intensity of PSD Ne\* at the photon energies corresponding to the excitation of S1, B1, and S' excitons. Solid lines are the fitting curve using  $I(\theta) = \cos^n\theta$ .

#### REFERENCES.

1. T. Kloiber and G. Zimmerer, *Radiat. Eff. Def. Solids* **109**, 219 (1989).
2. M. Sakurai, T. Hirayama and I. Arakawa, *Vacuum* **41**, 217 (1990).
3. D. E. Weibel, A. Hoshino, T. Hirayama, M. Sakurai and I. Arakawa, in *Desorption Induced by Electronic Transitions - V*, edited by A. R. Burns E. B. Stechel and D. R. Jenninson (Springer-Verlag, 1992), p. 333.
4. D. E. Weibel, T. Nagai, T. Hirayama, I. Arakawa and M. Sakurai, *Langmuir*, accepted for publication. (1994).
5. I. Arakawa, *et al.*, *Nucl. Instrum. Meth.* accepted for publication. (1995).
6. M. Sakurai, T. Nagai, M. Abo, T. Hirayama and I. Arakawa, *J. Vac. Soc. Jpn.* submitted.

## VUV Reflectivity Spectra of Rare-Earth Sesquioxides IV

Fumitaka ARAI, Shin-ichi KIMURA\*, Mikihiko IKEZAWA and Mareo ISHIGAME

*Research Institute for Scientific Measurements, Tohoku University, Sendai 980-77*

*\* UVSOR Facility, Institute for Molecular Science, Okazaki 444*

Rare-earth compounds show characteristic behavior due to many body effect. The origin is thought to be the interaction between the localized 4f magnetic moment and the carriers. The typical ones are known to be Kondo effect, heavy fermion and valence fluctuation.

We have an interest in the mixed valence of rare-earth insulators. For instance, CeO<sub>2</sub> is known that the mean valence number of Ce - ion is about 3.5. The origin is thought that the wave number of Ce - 4f unoccupied state mixes into that of O - 2p valence bands. Actually, the 4d - 4f resonant photoemission of valence band in CeO<sub>2</sub> shows that the valence band includes the Ce - 4f or 5d character. [1] However, a photoemission induces a change of the electronic structure at the ejection of electrons. On the other hand, photo absorption at low energy is thought to reflect the initial state. So we are measuring absorption spectra, especially reflectivity spectra, for the investigation of fundamental electronic structure.

Rare-earth oxides are typical insulators of rare-earth compounds. The valence number of a rare-earth sesquioxide is almost 3, however, some materials show mixed valence like CeO<sub>2</sub> as mentioned before. Before investigation of the mixed valence materials, we must check the normal trivalent materials, whether the spectra of the materials are normal or not. The absorption due to the transition from the valence to the conduction bands has already investigated. [2] Now we measured the absorption from the 5p state in rare-earth ion in detail.

The measurement was done at two beam lines 5B and 7B. In comparison with BL7B, BL5B has high resolution above 20 eV. In addition, we can measure the reflectivity spectra in a higher energy range than BL7B. This is an advantage for the Kramers-Kronig transformation of a reflectivity spectrum.

The obtained reflectivity spectra of R<sub>2</sub>O<sub>3</sub> (R = La, Pr, Nd, Sm, Eu, Er, Tm, Yb and Lu) in the energy range from 15 to 50 eV are shown in Fig. 1. The optical conductivity spectra which are derived by the Kramers-Kronig transformation of the reflectivity in Fig. 1 are shown in Fig. 2. In the energy range, the main absorption structure is originated from R-5p and O-2s in the occupied state and R-5d, 6s in the unoccupied state. From the photoemission spectra of R<sub>2</sub>O<sub>3</sub>



[3] and a bremsstrahlung isochromat spectrum of  $\text{CeO}_2$  [4], the energies of these states from the Fermi level are known. So we can infer the origins of the absorption bands. The origins of absorption band indicated A - G are tentatively assigned as follows; A:  $\text{O-}2s \rightarrow \text{R-}5d$ , B:  $5p_{3/2} \rightarrow \text{R-}5d(t_{2g})$ , C:  $5p_{3/2} \rightarrow \text{R-}5d(e_g)$ , D:  $5p_{3/2} \rightarrow \text{R-}6s$ , E:  $5p_{1/2} \rightarrow \text{R-}5d(t_{2g})$ , F:  $5p_{1/2} \rightarrow \text{R-}5d(e_g)$  and G:  $5p_{1/2} \rightarrow \text{R-}6s$ .

Weak shoulders indicated B' and E' are observed. The origin is unclear but probably it may be due to core excitons. The detail measurements and analysis will be done in the next step.

1. M. Matsumoto *et al.*, Phys. Rev. B **50**, 11340 (1994).
2. S. Kimura *et al.*, UVSOR Activity Report 1991, 86 (1992); F. Arai *et al.*, *ibid.* 1992, 41 (1993); F. Arai *et al.*, *ibid.* 1993, 135 (1994).
3. F. Arai, Doctor Thesis, Tohoku University (1994).
4. L. K. Lang *et al.*, J. Phys. F **11**, 121 (1981).

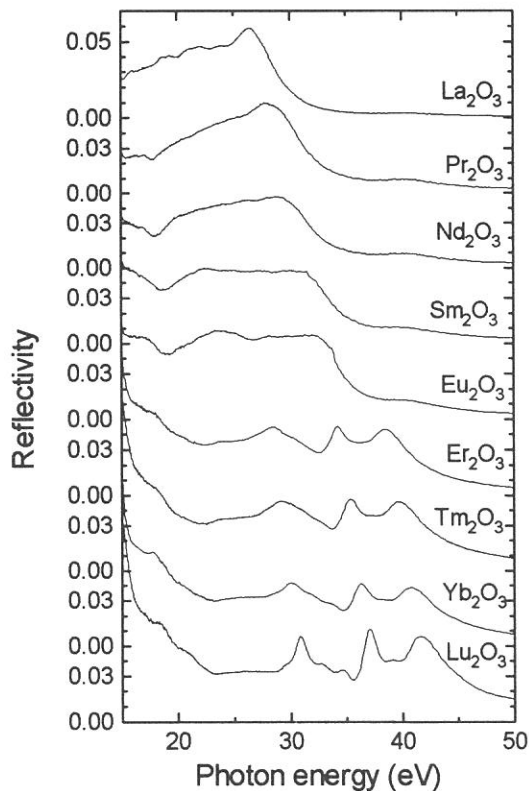


Fig. 1. Reflectivity spectra of  $\text{R}_2\text{O}_3$  ( $\text{R} = \text{La, Pr, Nd, Sm, Eu, Er, Tm, Yb}$  and  $\text{Lu}$ ) in the energy range 15 - 50 eV.

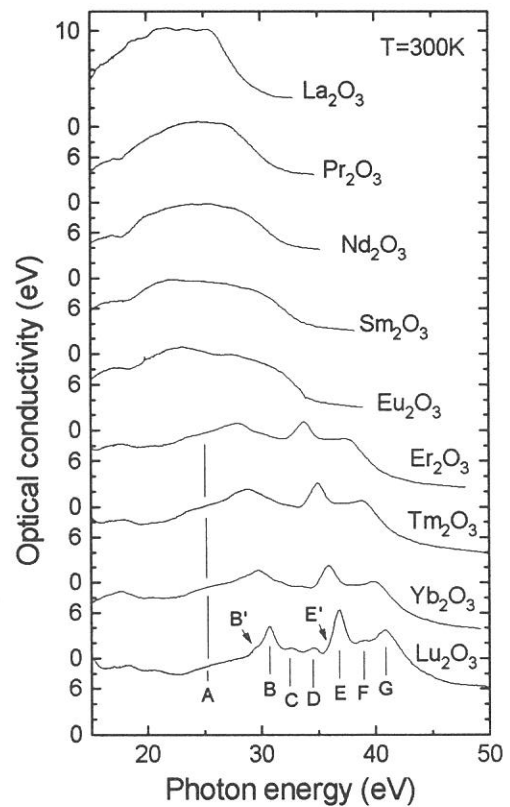


Fig. 2. Optical conductivity spectra of  $\text{R}_2\text{O}_3$  ( $\text{R} = \text{La, Pr, Nd, Sm, Eu, Er, Tm, Yb}$  and  $\text{Lu}$ ) in the energy range 15 - 50 eV derived from Fig. 1. by the Kramers-Kronig transformation.



## FAR INFRARED ABSORPTION OF ICE XI

M. KOBAYASHI and D. TAZAWA

Faculty of Engineering Science, Osaka University, Toyonaka, Osaka 560

Usual ice existing at ambient pressure below 273 K has a hexagonal lattice structure for arrangements of oxygen atoms with orientational disorders regarding hydrogen atoms. The third law of the thermodynamics demands the ordering of hydrogen at sufficiently low temperatures. Actually, the relaxation time required for the ordering is innumerably long, therefore, the ordered phase has not been realized in pure ice. However, when small amount of KOH is doped, a drastic decrease of the relaxation time was brought into and proton ordering was observed to occur [1]. The ordered phase is called phase XI. Here we report far-infrared absorption spectra in ice XI.

0.01 mol of KOH was added into 1 l H<sub>2</sub>O pure water which filled a gasket hole with a diameter of 1 mm. The gasket whose thickness was 5  $\mu$  m was set between two diamond anvils. The cell was settled at the bottom of a cryostat. In order to measure lattice vibrational spectra, we have used the far-infrared beam line of BL6A1 at UVSOR. The transmitted light signal was detected by a Ge bolometer.

Figure 1 shows absorption spectra of ice Ih and XI. A broken line was measured above 72 K which corresponds to the phase Ih (normal ice). A dotted line and a solid line were obtained below 72 K by keeping the temperature for 3 hours 40 minutes and 5 hours 50 minutes, respectively. It is seen that the absorption coefficient is larger for ice Ih than for ice XI between 60 and 230  $\text{cm}^{-1}$ . This is attributed to the breaking of the momentum conservation law because of the proton randomness in ice XI. As for the main peaks located at higher than 230  $\text{cm}^{-1}$  also change by altering temperature and keeping time. Some of the changes should reflect the Ih-XI phase transition.

## REFERENCES

- [1]Y. Tazima, T. Matsuo and H. Suga: Nature 299 (1982) 810.

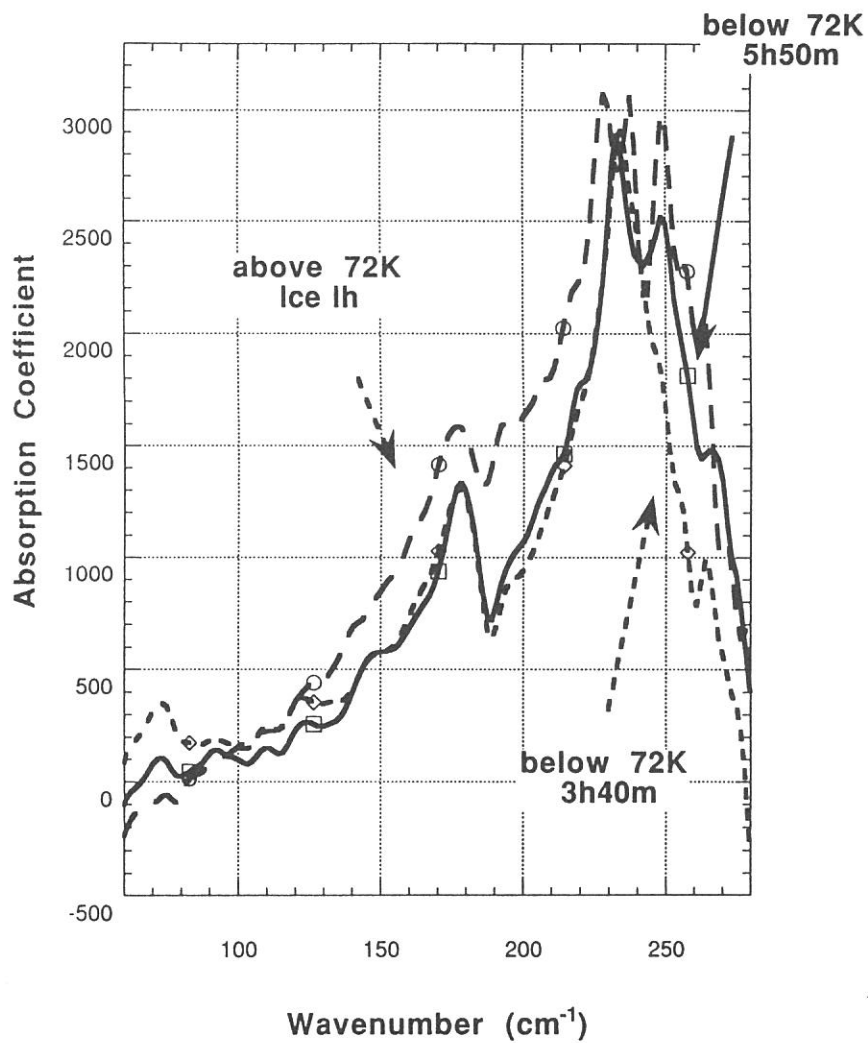


Fig. 1 Far-infrared absorption spectra of ice Ih and XI.

## Size-dependence of Phase Transition of CdS Microcrystals

Takao NANBA and Yasuhiro NOTAKE

*Department of Physics, Faculty of Science, Kobe University,  
Kobe 657*

and

Gwyn P. WILLIAMS

*National Synchrotron light Source,  
Brookhaven National Laboratory, Upton, New York 11973, USA*

A structural stability of the microcrystals related with a structural phase transition is an attractive subject. Our interest is focussed on the following two subjects, (1) if the critical pressure (" $P_c$ ") at which the phase transition occurs in the microcrystals differs from that in bulk state and (2) what is the size-dependence? No clear experimental evidence showing differences between bulk and microcrystalline states has not ever been presented.

The surface phonon of the microcrystal shows a drastic large decrease in energy and broadening at a particular pressure which corresponds to the structural phase transition. Therefore, the far infrared transmission measurement is a useful method to know the magnitude of the  $P_c$  of the phase transition.

We have done the far infrared transmission measurement on CdS microcrystals of various sizes under pressure in order to know the size-dependence of the  $P_c$  in microcrystals.

CdS microcrystals were produced by evaporating CdS powder in Ar gas at different pressures [1]. The shape and the size distribution of CdS microcrystals were determined by a transmission electron microscopic observation. Small amounts of microcrystals were mixed with a Apiezon-N grease which works as a pressure transmitting medium. The transmission measurement under high pressure up to 10 GPa in the far-infrared region was done by using a so called lever-arm type of diamond anvil cell which was installed at the far-infrared spectroscopic systems of the BL6A1 at the UVSOR of the Institute for Molecular Science (IMS) at Okazaki and also of the beamline U4-IR of the National Synchrotron Light Source (NSLS) VUV ring of Brookhaven National Laboratory (USA).

Fig.1 shows the development of the far-infrared transmission spectra of CdS microcrystal with the diameter of 890 Å with pressure at a room temperature. The sharp dip at  $270\text{ cm}^{-1}$  in the  $P=0$  spectrum is due to the surface phonon of the microcrystal. Observed energy of the  $270\text{ cm}^{-1}$  as a surface phonon in CdS is in good agreement with the value expected by the continuum model

on a surface phonon mode of a spherical microcrystal [2]. The surface phonon showed continuously a blue shift to  $290\text{ cm}^{-1}$  with pressure up to 3.7 GPa. At the pressure above 4.1 GPa the spectrum changed suddenly and a new broad band appeared at  $230\text{ cm}^{-1}$  instead of the band around  $290\text{ cm}^{-1}$ . We attributed this to a phase transition occurring at a pressure between 3.7 and 4.1 GPa. Similar experiments were done on microcrystals of various sizes.

Values obtained for  $P_c$  for each CdS microcrystal are plotted in Fig.2 as the function of the percentage of the number of the surface atoms ( $n$ ) to the number of total atoms ( $N$ ) in the microcrystal. As seen from the figure, the  $P_c$  of the microcrystals differs from the bulk state and the particles with smaller diameter give higher  $P_c$  values. The higher  $P_c$  means the hardening of the materials in the microcrystalline state and is consistent with a phenomenological explanation based on the surface tension in the microcrystals.

### Acknowledgements

The authors are grateful to the staff of the UVSOR facilities of the IMS (Japan) and of the NSLS, Brookhaven Laboratory (USA) for their experimental supports.

### References

- [1] K. Kimoto, Y. Kajima, M. Nonomiya and R. Uyeda; Jap. J. appl. Phys. 2 (1963) 702.
- [2] L. Genzel and T. P. Martin; Phys. Stat. Sol. (b) 51 (1972) 91.

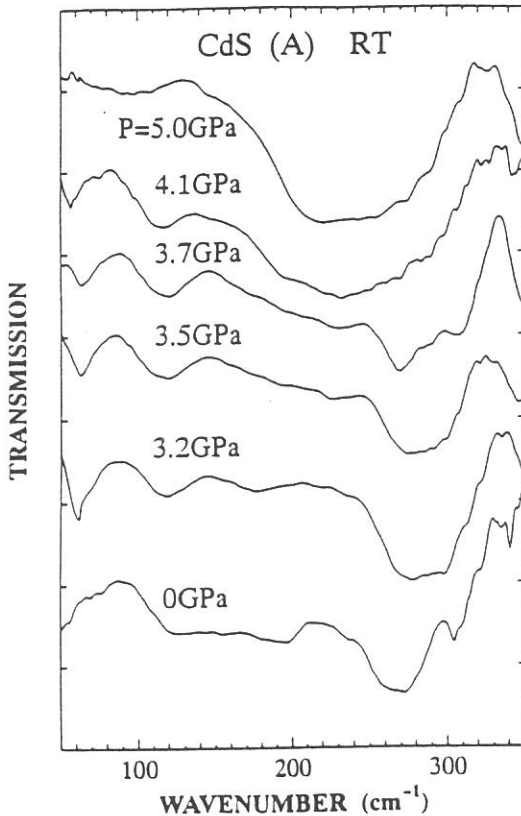


Fig.1 Spectral developments of surface phonon absorption of CdS microcrystals with the average

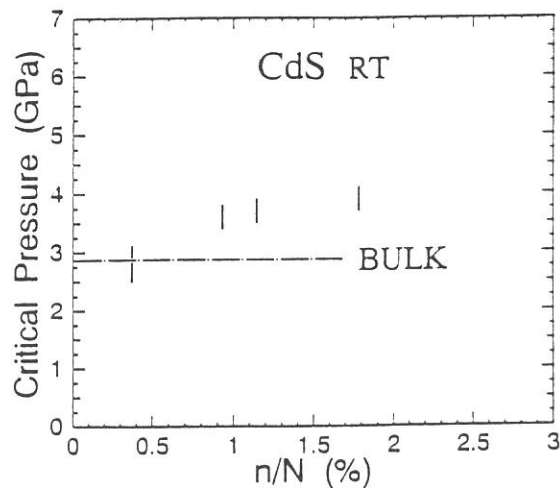


Fig.2 Measured values of critical pressure ( $P_c$ ) of CdS microcrystals of various diameters as a function of the percentage of atoms at surface. Dash-broken line corresponds to 2.8 GPa where the phase transition of bulk CdS occurs.

## Multichannel FT Spectrometer for Mid-Infrared

Shuji ASAKA and Jeung Sun AHN

Institute for Molecular Science, Myodaiji, Okazaki 444

A compact multichannel Fourier-transform (MCFT) spectrometer without mechanical moving parts had already been constructed by us for visible wavelength range<sup>1)</sup>. We have newly developed a same type of spectrometer for mid-infrared range around  $3\ \mu\text{m}$  of wavelength. The spectrometer consists of a birefringent interferometer based on a Savart plate and a CCD detector, as illustrated schematically in Figure 1, which is basically the same as the system explained in the reference 1). In the present system, we have adopted a  $\text{TiO}_2$  crystal as the Savart plate. Main features of the present system are the following.

- (1) Utilization of a birefringent common-path interferometer without moving components. This approach makes it easy to construct a compact interferometer and to circumvent the noises due to mechanical vibrations, and also provides the ability to measure transient spectrum of a single event by using a pulse source.
- (2) Use of a large solid angle as a consequence of the linearly arranged optics of the birefringent interferometer.
- (3) No requirement of the entrance and exit slits.

Features 2 and 3 serve to make the throughput of the interferometer quite large, and this is the main advantage of this spectrometer over conventional Fourier transform and dispersive spectrometer.

The sensitivity and the resolution of this spectrometer is now under investigation.

### Reference

- 1) S.TAKAHASHI, J.S.AHN, S.ASAKA, and T.KITAGAWA, *Appl.Spectrosc.* **47**, 863 (1993).

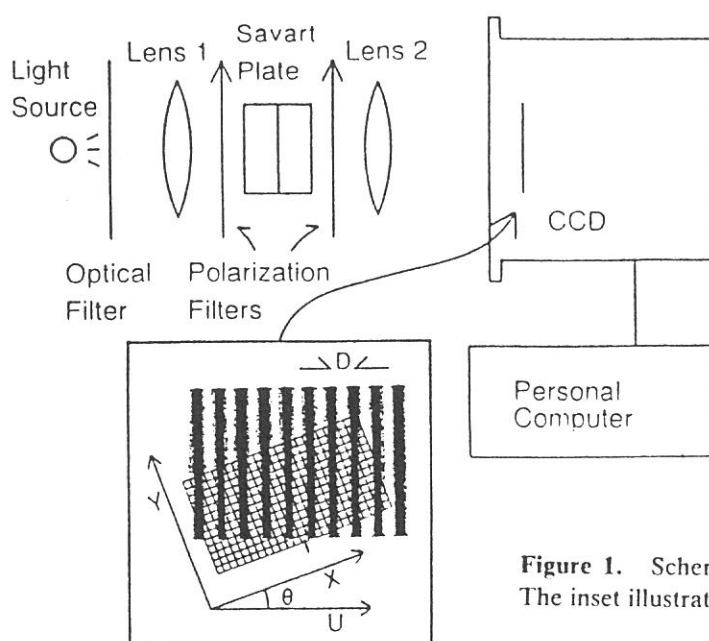


**Figure 1.** Schematic diagram of the MCFT system constructed. The inset illustrates the way of CCD arrangement.

## Far Infrared Transmission of SmTe under High Pressure

Y. S. Kwon, T. S. Park, K. S. An, I. S. Jeon, S. Kimura<sup>1</sup>, C. Y. Park,  
T. Nanba<sup>2</sup> and T. Suzuki<sup>3</sup>

*Department of Physics, Sung Kyun Kwan University, Suwon 440-746, KOREA*

<sup>1</sup> *Institute for Molecular Science, Okazaki 444*

<sup>2</sup> *Department of Physics, Kobe University, Kobe 657*

<sup>3</sup> *Department of Physics, Tohoku University, Sendai 980-77*

Sm monochalcogenides have a gap between 4f-level and conduction band. It is known from a resistivity under a pressure and the energy gap is decreased by the pressure. [1] The value has been estimated -14.8 meV / kbar in SmSe and -11.9 meV / kbar in SmTe. A transition from semiconductor to metal occurs induced by pressure. In order to investigate the pressure-induced semiconductor-metal transition, we measure a far infrared transmission under several pressures.

The measurement was done at a far infrared beam line 6A1. High pressure was created by a diamond anvil cell. [2] The transmission and reflection spectra of SmTe have been reported already. [3] The data show the insulator character of SmTe because the transmission spectrum appears. Figure shows the transmission spectra under several pressures. At 0 GPa, the spectrum shows that the state is insulator because of the strong transmission. Above 2.4 GPa, however, the state changes to a metal because the transmission is reduced in the wave number range 200 - 300  $\text{cm}^{-1}$ . The result is a direct observation of the pressure-induced semiconductor-metal transition of SmTe for the first time.

[1] C. M. Varma, Rev. Mod. Phys. **48** (1976) 219.

[2] T. Nanba, Rev. Sci. Instrum. **60** (1989) 1680.

[3] T. Nanba et al., UVSOR Activity Report 1993 (1994) 100.

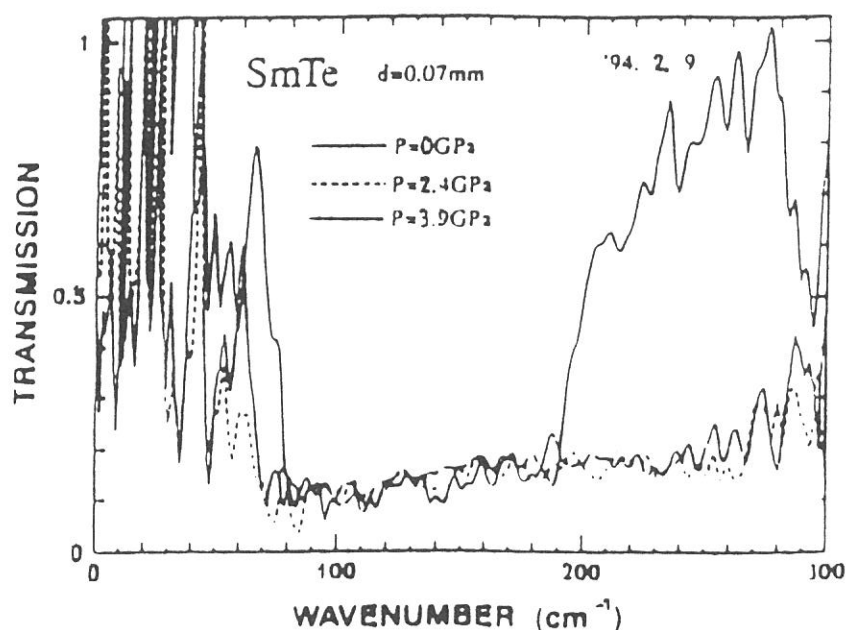


Fig. Transmission spectra under pressures 0, 2.4 and 3.9 GPa.

## Infrared Low Frequency Study of The Phase Transitions in LiKSO<sub>4</sub> and LiNaSO<sub>4</sub> Single Crystals

Fernando Rull Perez and Shin-ichi Kimura  
*Institute for Molecular Science, Okazaki 444, Japan*

Reflection spectra of single crystalline LiKSO<sub>4</sub> and LiNaSO<sub>4</sub> in the far infrared region were measured in the range of temperature 12-300 K for different crystal orientations. Compound of the family LiASO<sub>4</sub> (A= Li, Na, K, Rb, Cs, Ag, etc.) are interesting materials because they exhibit in general fast-ionic conductivity at high temperatures.[1] Among these crystals LiNaSO<sub>4</sub> and LiKSO<sub>4</sub> are specially interesting because both have hexagonal unit cell but only LiNaSO<sub>4</sub> show fast-ion-conducting behavior. On the other hand LiKSO<sub>4</sub> show a sequence of phase transitions below room temperature at 210 K, 180 K and 20 K on cooling and 30 K, 190 K and 250 K on heating which have not been observed in LiNaSO<sub>4</sub>. [2] The mechanism for these transitions seems not to be completely elucidated although is widely recognized that SO<sub>4</sub> rotations play an important role in the structural disorder of these compounds.[3] Several Raman and Infrared studies have been performed until now in these systems in which the temperature dependence of the internal SO<sub>4</sub> modes and the vibrational Li-modes have received the great attention.[2-5] But at our knowledge no such detailed study in the IR low frequency region has been performed. Figs. 1 and 2 show the temperature dependence of the far-infrared spectra of LiNaSO<sub>4</sub> and LiKSO<sub>4</sub> in the range 12-300 K for E || z-axis orientation.

From these data the temperature behavior of the position and bandwidth of the SO<sub>4</sub> librational modes are of particular interest. In Figs. 3 (a) and (b), we present the results obtained for LiNaSO<sub>4</sub> after a fitting of the experimental spectra and Figs. 3 (c) and (d) shows the same results for LiKSO<sub>4</sub>. In most of these bands a shift to lower frequencies and a broadening as the temperature increases is observed.

From the temperature dependence of the bandwidth the modes with strong rotational contribution can be distinguished and the contribution to the orientational disorder can be estimated. Work is in progress to analyze the dependence with temperature for the intensity and band profile of the different bands in the frequency and time domain using Fourier transform methods. The aim is to use these results in the interpretation of the dynamics of the SO<sub>4</sub> librational modes and in the study of their role in the phase transitions.

### References

1. D.H. Withmore, *J. Crystal Growth* **39**, 160 (1976).
2. D.- Teeters, R. Frech, *Phys. Rev. B* **26**, 5897 (1982).
3. A.J. Oliveira, F.A. Germano, J. Mendes Filho, F.E.A. Melo, J.E. Moreira, *Phy. Rev. B* **38**, 12633 (1988).
4. D. Teeters, R. Frech, *Phys. Rev. B* **26**, 4132 (1982).
5. V. Varma, R. Bhattacharjee, J.R. Fernandes, C. N. R. Rao, *Solid State Commun.* **76**, 627 (1990).



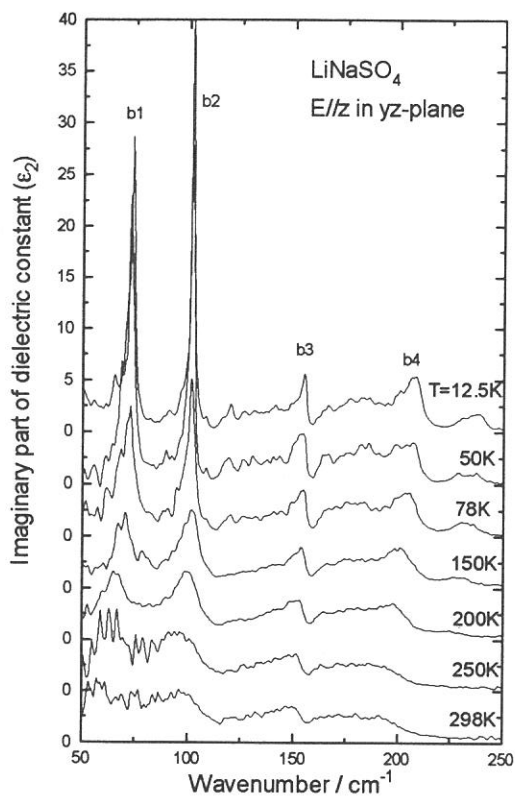


Fig. 1. Temperature dependence imaginary part of dielectric constant of LiNaSO<sub>4</sub>.

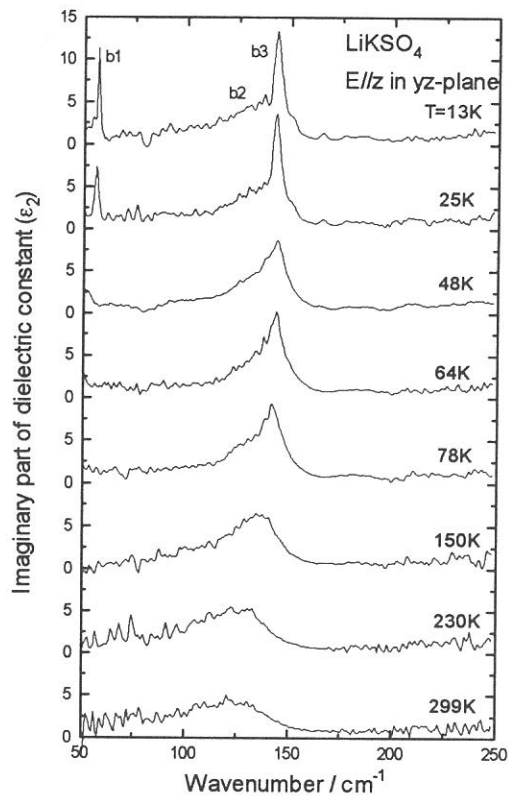


Fig. 2. Temperature dependence imaginary part of dielectric constant of LiKSO<sub>4</sub>.

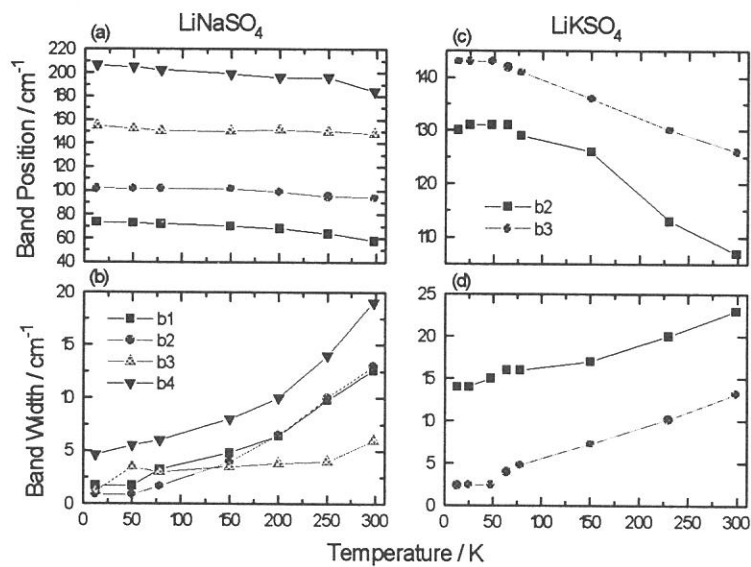


Fig. 3. Absorption band position and width of each peaks as the function of temperature.

## Optical Observation of Interaction between Low Frequency Plasma and Magnetic Field in $\text{La}_{2-x}\text{Sr}_x\text{CuO}_4$ ( $x \approx 0.1$ )

Shin-ichi KIMURA, Mikihiko IKEZAWA\*, Hironao KOJIMA\*\*, Isao TANAKA\*\*,  
Takashi WATANABE\*\* and Masashi TACHIKI\*\*\*

*UVSOR Facility, Institute for Molecular Science, Okazaki 444*

*\* Research Institute for Scientific Measurements, Tohoku University, Sendai 980*

*\*\* Faculty of Engineering, Yamanashi University, Kofu 400*

*\*\*\* Institute for Materials Research, Tohoku University, Sendai 980*

Cuprate high- $T_C$  materials are well known to show characteristic properties. All of the materials form two dimensional crystal structure. The physical properties along  $\text{CuO}_2$ -plane (c-plane) and along c-axis are perfectly different from each other. For example, the transport along the c-plane is like a metal but the transport along c-axis is like a semiconductor at the temperature above  $T_C$ .

The c-axis polarized reflectivity spectra of  $\text{La}_{2-x}\text{Sr}_x\text{CuO}_4$  (LSCO) were observed by Tamasaku *et al.*<sup>1</sup> The main structure in the normal conducting state consists of phonon peaks and the absorption due to the conduction electron is very weak because of a small number of carriers across  $\text{CuO}_2$ -plane. On the other hand, the spectra in the superconducting state show characteristic behaviors in comparison with a normal metal. The Drude like reflectivity spectrum appears and the plasma edge is located at a very low energy of a few ten wave numbers. The relaxation time of the Drude function is observed to become long as the temperature decreases. The reason is thought to be the weak interaction with phonons and other electrons. So we have an interest in the plasma with the very low concentration of carriers.

We report the first observation of the interaction between the low frequency plasma and magnetic field by optical

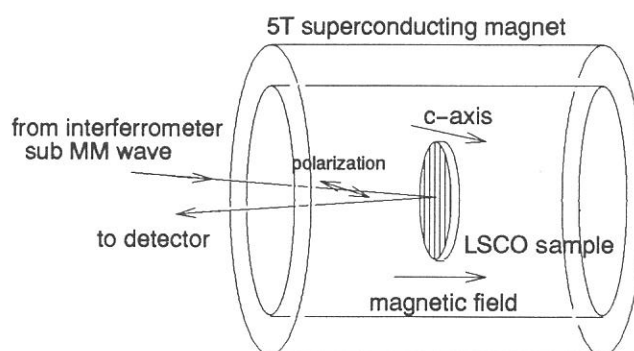


Fig.1 A schematic depiction of the reflectivity measurement of the c-axis polarized light under magnetic field which is applied along the normal direction of a sample surface.

measurements. The theory has already presented by Tachiki *et al.*<sup>2</sup> When an external magnetic field, which is stronger than the lower critical magnetic field,  $H_{c1}$ , is applied, vortices are created. If a light is introduced in the state, the vortices are driven by the light. It is expected theoretically that the relaxation time of the Drude absorption becomes short as the magnetic field increases because of the existence of the interaction between the plasma of carriers and the vortices.

The reflectivity spectra of LSCO ( $x \approx 0.1$ ) with the c-axis polarization in the wave number range of 10 - 40  $\text{cm}^{-1}$  under magnetic field up to 5 T using a superconducting magnet (SCM) were measured at an FIR beam line 6A1. The systematic figure in the case of  $H \perp E // c$ -axis is shown in Fig. 1. The advantage of the use of SR is the linear polarization and the fairly stronger light intensity than the ordinary light source below 40  $\text{cm}^{-1}$ . The light was guided to a sample by light pipes of copper with an inside diameter of 10 mm. The sample was cooled down to 14 K by contacting to the liquid helium tank of SCM.

The obtained reflectivity spectra and theoretical functions are shown in Fig. 2. It is seen that the experimental data are fitted well by the theoretical functions. Therefore it is considered that the origin of the change of spectrum by the magnetic field is consistent with the theory by Tachiki *et al.*<sup>2</sup>, i. e. the plasma of carriers is interrupted by the vortices which is driven by the incident light.

1. K. Tamasaku, Y. Nakamura, and S. Uchida, Phys. Rev. Lett. **69**,1455 (1992).
2. M. Tachiki, T. Koyama, and S. Takahashi, Phys. Rev. B (in press).

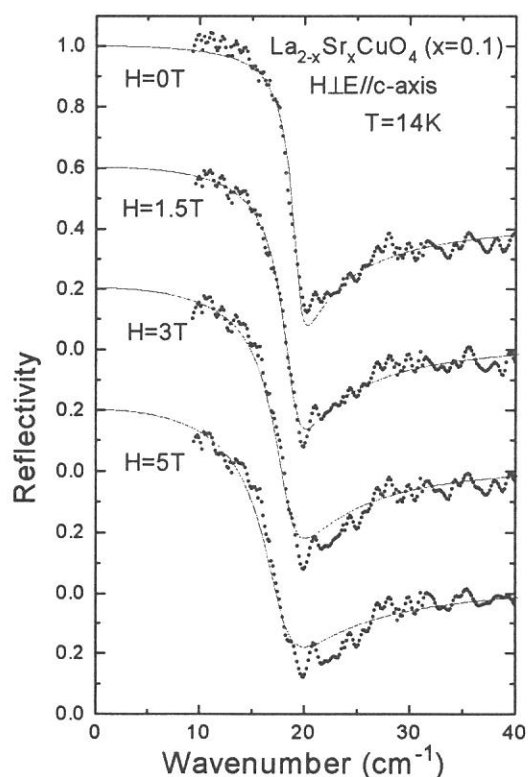


Fig. 2 The results of the curve fitting of the theoretical functions (solid lines) to the reflectivity spectra (dots).

## Far-infrared and Millimeter Wave Spectra of Superionic Glasses of AgI-AgPO<sub>3</sub>

Teruyoshi AWANO and Takao NANBA\*

*Department of Applied Physics, Tohoku Gakuin University, Tagajo 985*

*\*Department of Physics, Kobe University, Kobe 657*

Superionic conducting glasses have the advantage over superionic conducting crystals in their high ionic conductivity at room temperature<sup>1)</sup>. For example, the ionic conductivity of (AgI)<sub>0.5</sub>(AgPO<sub>3</sub>)<sub>0.5</sub> glass is about 10<sup>-3</sup> Scm<sup>-1</sup>, which is thousands times larger than that of AgI at the room temperature<sup>2)</sup>. They also have the advantages on easy synthesis and formation, for example, of fibers and films.

We have investigated far-infrared and millimeter wave spectra of some silver or copper ion conductors to study the dynamics of mobile ions. In AM<sub>4</sub>X<sub>5</sub> (A=alkali metal; M=Ag or Cu; X=halogen) crystal, a structure by "ionic plasmon" was observed in the spectral region below 10 cm<sup>-1</sup> in silver ion conductors or 30 cm<sup>-1</sup> in copper ion conductors in energy loss function spectra at temperatures of superionic conducting phase<sup>3)</sup>. We have tried to investigate in this study whether the "ionic plasmon" exists in the non-periodic structure in glass. In this investigation, we measured reflectivity spectra (and transmission spectra if it was possible) of (AgI)<sub>x</sub>(AgPO<sub>3</sub>)<sub>1-x</sub> (X=0.5, 0.25 and 0) glass in spectral region from 3 to 250 cm<sup>-1</sup>.

The mixture of AgI, NH<sub>4</sub>H<sub>2</sub>PO<sub>4</sub> and AgNO<sub>3</sub> were kept at 700 K for 12 hours and quenched rapidly to obtain glass specimen<sup>2)</sup>. Characterization of glass was done by X-ray diffraction analysis and DSC measurement.

Fig. 1 shows reflectivity spectra of the glass at 298 K. There are two broad peaks commonly in these three spectra at around 90 cm<sup>-1</sup> and 15 cm<sup>-1</sup>. Low energy tail below 8 cm<sup>-1</sup> increased in proportion to their ionic conductivity. This is due to Drude like behavior of silver ions as discussed about AM<sub>4</sub>X<sub>5</sub> in ref. 3. Optical constants were obtained by K-K analysis.

Fig. 2 shows conductivity spectra. Main peaks were observed at 110 cm<sup>-1</sup> (or 125 cm<sup>-1</sup> in AgPO<sub>3</sub>) and 18 cm<sup>-1</sup> (or 32 cm<sup>-1</sup> in AgPO<sub>3</sub>, which was not so clear). The bands around 110 cm<sup>-1</sup> are due to breathing mode of a silver ion in a cage of tetrahedron of iodine ions. The bands around 18 cm<sup>-1</sup> are due to attempt mode of it.

Fig. 3 shows energy loss function, which is the imaginary part of the reciprocal of dielectric constant. The low energy tail below 9 cm<sup>-1</sup> increased in the superionic conducting glasses. This suggests that longitudinal oscillation of the carrier ion exist. Such a broad peak as those in AM<sub>4</sub>X<sub>5</sub> crystal, which is due to the "ionic plasmon", was not clear. This seems to be due to the non-periodic structure of the glass.

This structure by this longitudinal motion of conduction ion decreased slightly at 77K. This change was not so drastically as that of AM<sub>4</sub>X<sub>5</sub> crystal. This seems to be due to the random and coarse network of the AgI<sub>4</sub> tetrahedron.

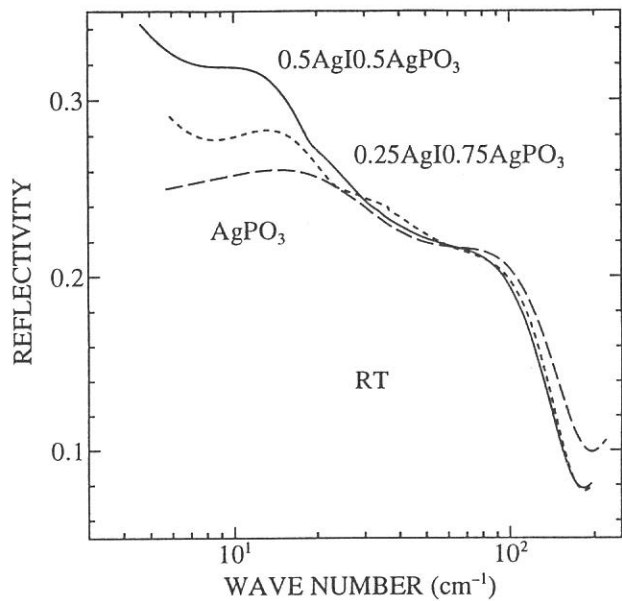


Fig. 1 Reflectivity Spectra of  $(\text{AgI})_x(\text{AgPO}_3)_{1-x}$  glass.

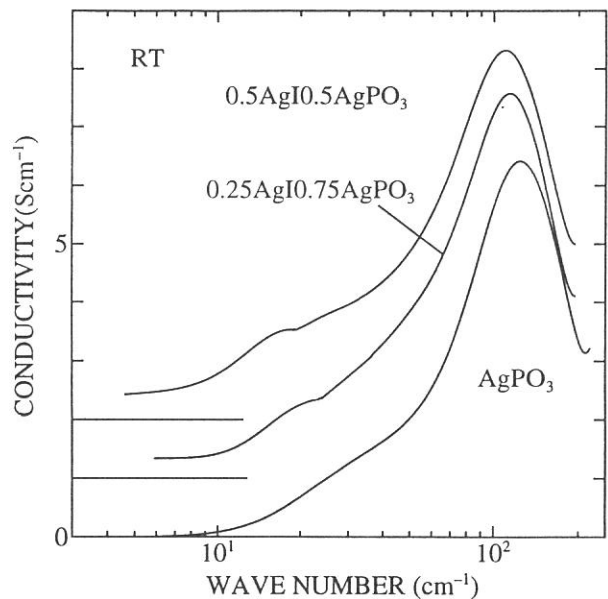


Fig. 2. Conductivity spectra of  $(\text{AgI})_x(\text{AgPO}_3)_{1-x}$  glass.

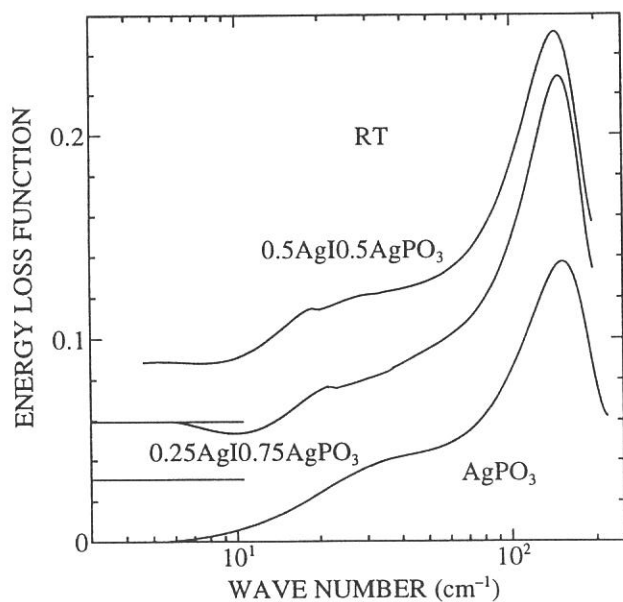


Fig. 3 Energy loss function spectra of  $(\text{AgI})_x(\text{AgPO}_3)_{1-x}$  glass.

#### References

- 1) T. Minami, J. Non-Cryst. Solids, 73 (1983) 273.
- 2) H. Takahashi, Y. Hiki, T. Sakuma and S. Funahashi, Solid State Ionics 53-56 (1992) 1164.
- 3) T. Awano, T. Nanba and M. Ikezawa, Solid State Ionics, 53-56 (1992) 1269.

## Photoemission Study of the Al-Pd-Mn F1-type Icosahedral Phase

M. MORI, M. KAMADA<sup>‡</sup>, T. MIYAZAKI<sup>‡</sup> and T. ISHIMASA<sup>†</sup>

Department of Natural Science Informatics, School of Informatics and Sciences, Nagoya University, Nagoya 464-01

<sup>†</sup>Department of Nuclear Engineering, School of Engineering, Nagoya University, Nagoya 464-01

<sup>‡</sup>Institute for Molecular Science, Myodaiji, Okazaki 444

Since the discovery of an icosahedral phase (i-phase) in Al-Mn alloys by Shechtman *et al.* [1], a large number of studies have been reported about the electronic and magnetic properties of icosahedral quasicrystal materials in spite of remaining the arrangement of the atoms in an i-phase unclear. By intuition the pseudogap structure can be interpreted in terms of the nearly-free-electron-like energy gap inferred from the strong diffraction spots, which may be related to the stability of the i-phase and decagonal quasicrystals. Friedel pointed out the possibility that the pseudogap structure can be enhanced by a crossing effect of 3d state with the nearly-free-electron-like state, and the stability would be augmented in an i-phase system containing transition metals by the crossing effect at about  $E_F$  which enhances the energy gap of the Brillouin zone. Recently a pseudogap-like anomaly in the DOS structure near  $E_F$  was directly confirmed with the photoemission study of an Al-Cu-Fe i-phase by Mori *et al.* [2]. The CIS spectra, being a kind of photoemission study, at the binding energy region between 0 – 2 eV show a resonant characteristic near the 3p-electron excitation of Fe atom in the Al-Cu-Fe i-phase. The specimen of this study, the Al-Pd-Mn i-phase, is also well known one of the stable quasicrystals and that especially has the i-phase to i-phase phase transformation temperature point. Therefore, this is considered to be the most interested materials studying the electronic structure, investigating the origin of the quasicrystal stability.

The first purpose of this experiment is to confirm the previous results by using with the angle-integrated photoemission spectrometer on beam-line BL-6A2. The second, if possible, is to observe the angle-resolved photoemission study to try the electronic band of the Al-Pd-Mn i-phase quasicrystal. The single quasicrystal sample – an Al-Pd-Mn high temperature i-phase quasicrystal – was an ingot prepared by the same method in ref. [3]. The specimen used with this study consists of only a *usually-reported F-type i-phase*. It was cut perpendicular to the 2-fold axis and filed flatly using with  $1\mu\text{m}$  alumina powder. The cleaning of the sample surface was used with the argon thinning equipment. Photoemission studies were performed with an angle-integrated spectrometer on beam-line BL-6A2. All measurements and sample treatments were carried out at room temperature. In the case of the angle-integrated photoemission study, the clean surface of the specimen was obtained by scraping with a diamond file in a vacuum of  $2 - 4 \times 10^{-8}$  Pa. Immediately after this process, the sample was transferred to the UPS experimental chamber and measured in a vacuum

of  $0.5 - 2 \times 10^{-8}$  Pa.

Using the argon thinning equipment, we tried to get the clean surface. The high voltage is 5 kV and the current is 20 mA. And the argon ions were bombed perpendicular to the sample surface for 0.5 - 5 hours. We have tried to get the clean sample surface, changing the experimental conditions of the argon thinning equipment. The decision getting the clean surface was done by the method of the photoemission spectrum. But we could not get the clean surface of the Al-Pd-Mn i-phase quasicrystal. We consider the three reasons: One is that we could not get the clean surface is got by the flaking due to the cleavage along the 5-fold plane, not getting the large single quasicrystals. The second is that we could not measured the argon ion currents to the sample. Therefore, the last is that we could not make the angle small between the sample surface and the argon ion beams.

Photoemission studies were performed with an angle-integrated spectrometer. The line shape of overall observed spectrum is like a single large peak on a plateau cut off at  $E_F$  shown in Figure. This observed spectrum was as same as the spectrum studied with the angle-resolved spectrometer.

We have tried to get the large single quasicrystals. And we hope to study the electron band with an angle-resolved spectrometer on beam-line BL-6A2, as the clean surface is got by the flaking due to the cleavage along the 5-fold plane.

- [1] Shechtman D., Blech I., Gratias D. and Cahn J. W., 1984, *Phys. Rev. Lett.*, **53**, 1951
- [2] Mori M., Matsuo S., Ishimasa T., Matsuura T., Kamiya K., Inokuchi H. and Matsukawa T., 1991, *J. Phys.: Condens. Matter*, **3**, 767 *ibid.*, 1992, *J. Phys.: Condens. Matter*, **4**, L157
- [3] Ishimasa T. and Mori M., 1992, *Phil. Mag.*, **B18**, L175

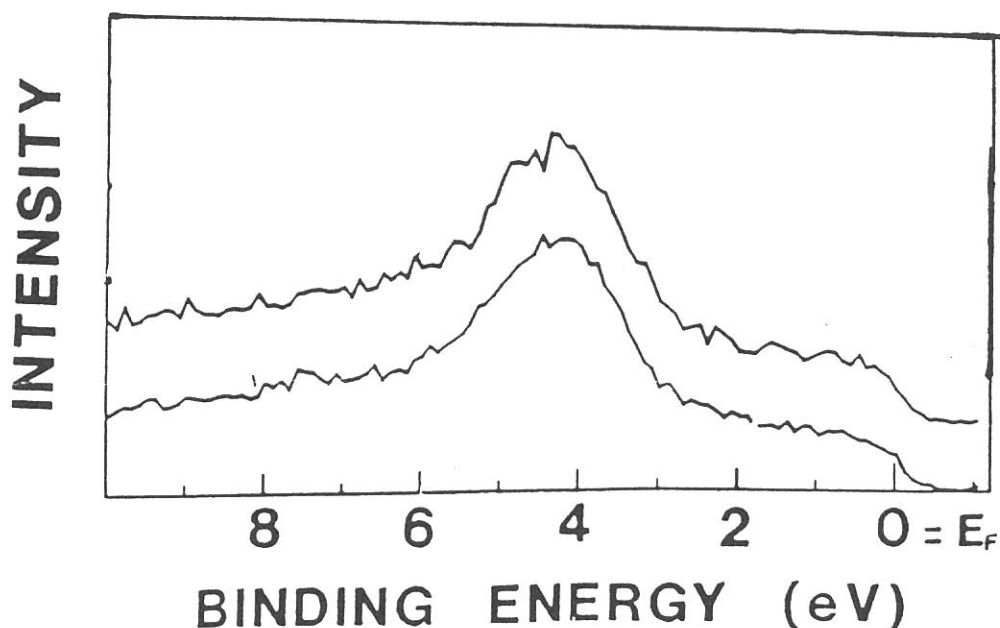


Figure. The photoemission spectra of Al-Pd-Mn F1-type i-phase measured at room temperature for incident photon energies 100 eV and 110eV.



## Decay Curves for Auger-free Luminescence from BaF<sub>2</sub> Excited near the Ba 4d Edges

S.Kubota, M.Kamada<sup>1</sup> and M.A.Terekhin<sup>2</sup>

*Rikkyo University, Nishi-Ikebukuro 3, Tokyo 171*

<sup>1</sup>*Institute for Molecular Science, Okazaki 444*

<sup>2</sup>*RRC 'Kurchatov Institute', Moscow 123182, Russia*

Above the Ba<sup>2+</sup> 4d edge in BaF<sub>2</sub> crystal the Auger-free luminescence yield decreases to a magnitude of about 60 % of that below the edge as shown in Fig.1[1]. The aim of present work is to study quenching mechanisms of Auger-free luminescence by measuring the time dependence of 220 nm emission band from BaF<sub>2</sub> during excitation of the 4d core electrons in Ba<sup>2+</sup> (90 eV) ions using monochromatized synchrotron radiation from BL6A2 of UVSOR facility. Delayed luminescence photons from the band pass filter were detected by a microchannel plate photomultiplier.

Figure 2 shows the typical decay curves from BaF<sub>2</sub> crystal at room temperature for several excitation energies  $h\nu$ . In the figure, the curves are normalized in intensity at maximum intensities. For comparison the measured decay curve for  $h\nu = 20$  eV is also shown. It is seen from the figure that the decay curves can not be fitted by a single exponential decay and its decay character after about 3 ns is almost similar for all curves.

In the region of  $h\nu > 100$  eV, a faster decrease in the decays is observed compared with those below 100 eV. It is to be noted here that a decrease in the area of the decay curve, which is proportional to the luminescence intensity, is about 10%. This decrease is much smaller than the observed decrease(60%) in the Auger-free luminescence yield above the 4d edge energy. This suggests the existence of some non-radiative process for the Ba 5p core holes. This non-radiative process should be too fast to follow in our time resolved spectroscopy; i.e. time scale of less than 100 ps.

The quenching factor  $Q(t=3 \text{ ns}) = -\ln[I(t=3 \text{ ns})/I_0(t=3 \text{ ns})]$  is introduced in Ref. [2] to demonstrate the quenching caused by the interaction with secondary electronic excited states produced by the same excitation photons. Here,  $I(t)$  and  $I_0(t)$  represent the measured time dependence of the luminescence and the decay curve without quenching effect, respectively. Figure 1 shows measured  $Q(t=3 \text{ ns})$  against  $h\nu$  together with the values in the energy region of  $30 \text{ eV} < h\nu < 90 \text{ eV}$  from Ref.[2].

As can be seen from Fig.2, no abrupt increase in  $Q(t=3 \text{ ns})$  is observed above the 4d edge energy. This suggest that the abrupt decrease in the

luminescence yield is not explainable only in terms of the quenching caused by the interaction with secondary electronic excited states.

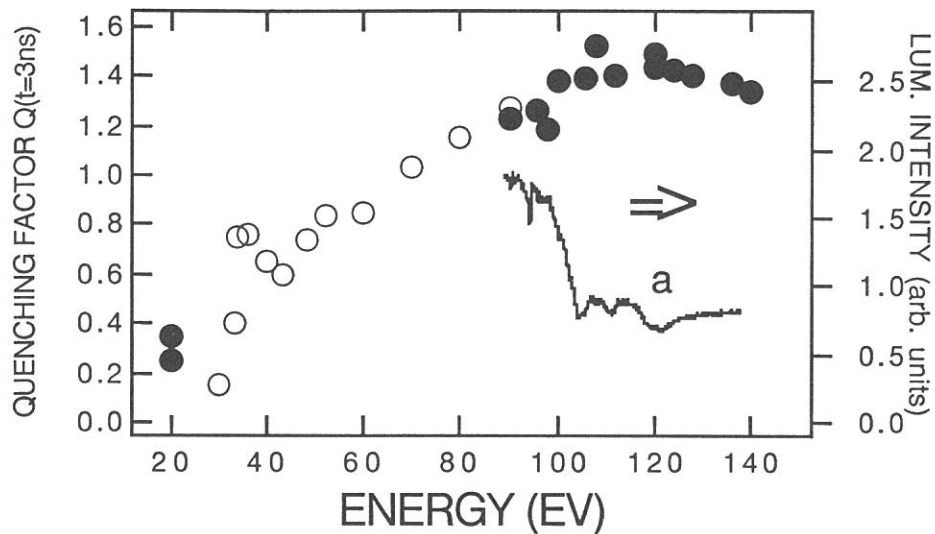


Fig.1. (a).Photo-excitation spectrum for 220 nm emission band from BaF<sub>2</sub> from [1] (a). Masured quenching factor Q(t=3 ns) (•) and refereed from [2] (o).

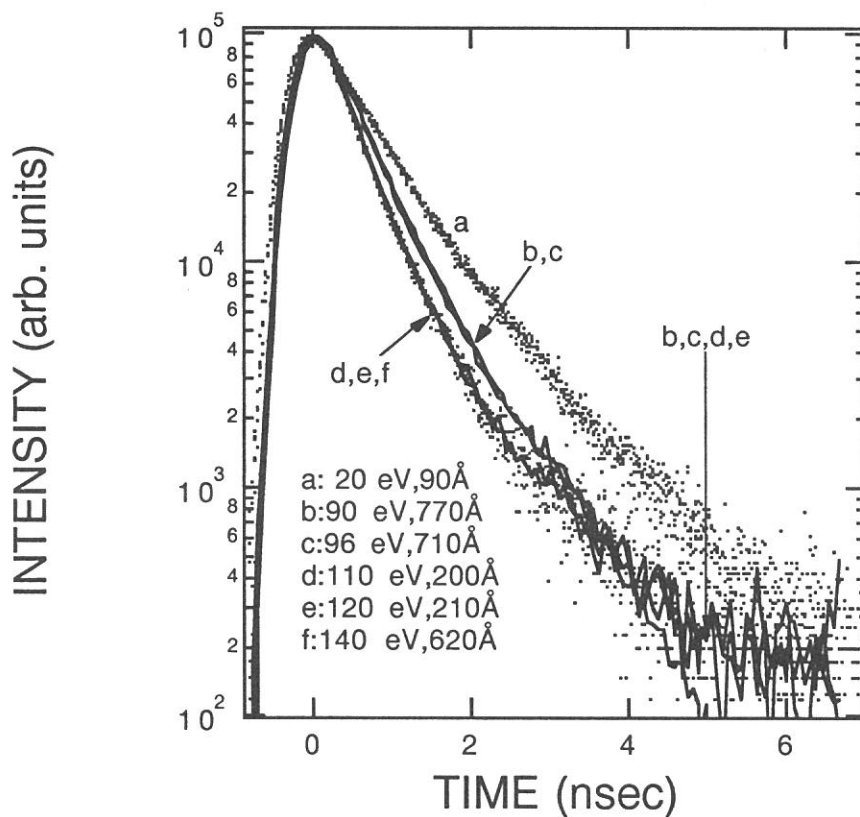


Fig. 2. Decay curves for the 220 nm band from BaF<sub>2</sub> under excitation of several photon energies.

[1] S.Kubota, M.MacDonald and I.H.Munro, to be published.

[2] M.A.Terekhin, A.N.Vasil'ev, M.Kamada, E.Nakamura and S.Kubota, Phys. Rev. B.( in press).

**Electron Spectroscopy of Stage 2 FeCl<sub>3</sub>-Graphite Intercalation Compound**

Takeshi ABE, Yasuo MIZUTANI, Eiji IHARA, Mitsuru ASANO, Toshio HARADA,  
Masaya KAWASE\*, Shunsuke NAKANISHI\*, Hiroshi ITOH\*, and  
Masao KAMADA\*\*

Institute of Atomic Energy, Kyoto University, Uji, Kyoto 611

\*Faculty of Education, Kagawa University, Sawai-cho, Takamatsu 760

\*\*Institute for Molecular Science, Myodaiji, Okazaki 444

Studies of ultraviolet photoelectron spectroscopy(UPS) of graphite intercalation compounds(GICs) have greatly contributed to obtain their density-of-states. However, these works have been usually focused on the donor type GICs, and only a few studies for the acceptor type GICs have been made so far[1].

In the present work, UPS is applied to a typical acceptor type stage 2 FeCl<sub>3</sub>-GIC and a shift of Fermi level ( $E_F$ ) for the GIC from highly oriented pyrolytic graphite(HOPG) is studied.

Stage 2 FeCl<sub>3</sub>-GIC was prepared from HOPG and anhydrous FeCl<sub>3</sub> by an ordinary two-bulb method[2]. The GIC was characterized by x-ray diffraction. The angle-integrated UPS experiments were carried out at BL6A2 equipped with a plane grating monochromator and a cylindrical retarding field analyzer. Stage 2 FeCl<sub>3</sub>-GIC and HOPG were cleaved in the preparation chamber of an ultrahigh vacuum less than  $5 \times 10^{-8}$  Pa to provide clean surfaces and then transferred in-situ to the analytical chamber with a background pressure of  $4 \times 10^{-8}$ Pa. All spectra are corrected by use of the UPS spectrum of Au as a reference.

Figure 1 shows the UPS spectra of the stage 2 FeCl<sub>3</sub>-GIC as a function of excitation energies  $h\nu = 25, 30, 35, 50$  eV. The prominent structures are labeled in the order of increasing the energies with A to D. Feature A is attributed to the Fe 3d electrons of the intercalate, and feature B is identified as the Cl 3p electrons. Features C and D represent the  $\pi$  and  $\sigma$  bands of graphite. The shapes of the spectra except for  $h\nu = 50$  eV are very similar. For the excitation energy of  $h\nu = 50$  eV, the UPS spectrum of the stage 2 FeCl<sub>3</sub>-GIC is considered to be very affected by the surfaces.

Figures 2 and 3 show the UPS spectra of the stage 2 FeCl<sub>3</sub>-GIC and HOPG for the excitation energies  $h\nu = 25$  eV and 30 eV, respectively. The  $\sigma$ - or  $\pi$ -bands in the UPS

spectra of the GIC are shifted in energy so as to be superimposed on the corresponding  $\sigma$ - or  $\pi$ -bands in those of the HOPG in Figs. 2 and 3, respectively. By this procedure, the values of the shift of  $E_F$  are determined to be 0.7 eV and 0.6 eV for the excitation energies  $h\nu = 25$  eV and 30 eV, respectively, which are in good agreement with the literature[3] measured by the optical reflectance spectroscopy.

The shift of  $E_F$  for the stage 2  $\text{FeCl}_3$ -GIC from HOPG is not affected by changing the marker structures, leading to the conclusion that the rigid band approximation is valid for the stage 2  $\text{FeCl}_3$ -GIC.

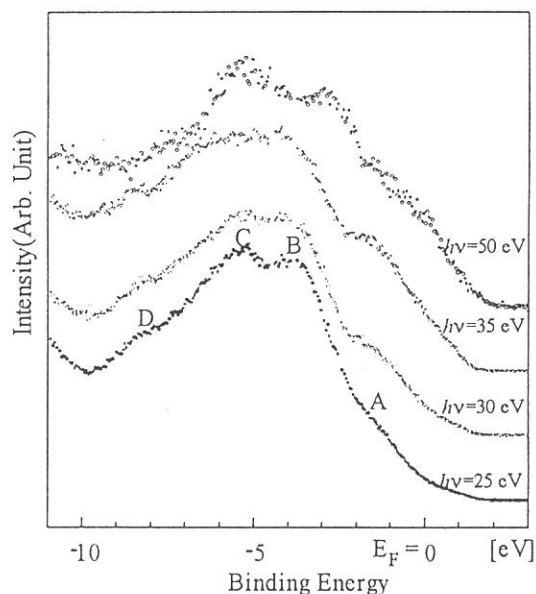


Fig. 1 UPS spectra of stage 2  $\text{FeCl}_3$ -GIC ( $h\nu = 25, 30, 35, 50$  eV).

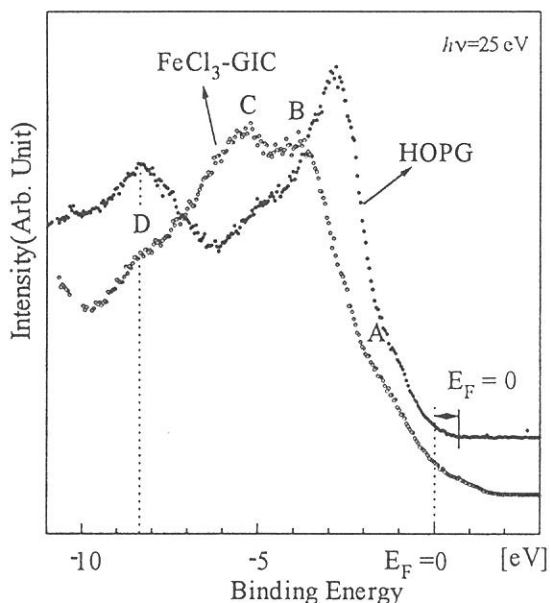


Fig. 2 UPS spectra of stage 2  $\text{FeCl}_3$ -GIC and HOPG ( $h\nu = 25$  eV). The  $\sigma$ -band in the UPS spectrum of the GIC is shifted in energy so as to be superimposed on the corresponding  $\sigma$ -band in that of the HOPG.

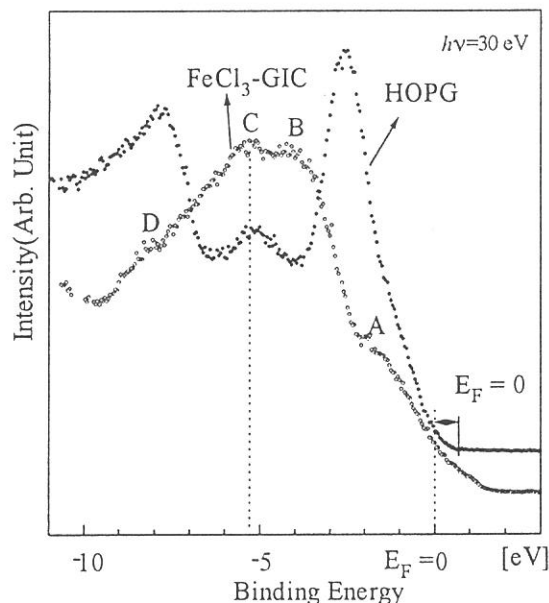


Fig. 3 UPS spectra of stage 2  $\text{FeCl}_3$ -GIC and HOPG ( $h\nu = 30$  eV). The  $\pi$ -band in the UPS spectrum of the GIC is shifted in energy so as to be superimposed on the corresponding  $\pi$ -band in that of the HOPG.

- 1) R. Schlögl, *Graphite Intercalation Compounds II*(Edited by H. Zabel and S. A. Solin)p.53. Springer-Verlag, Berlin Heiderberg New York (1990).
- 2) Y. Mizutani, T. Abe, M. Asano, and T. Harada, *J. Mater. Res.* **8**, 1586 (1993).
- 3) D. S. Smith and P. C. Eklund, *Intercalated Graphite of Symposia Proceedings*(Edited by M. S. Dresselhaus, G. Dresselhaus, J. E. Fischer, and M. J. Moran Vol. 20 )p.99. Mater. Res. Soc., Boston (1983).

**METALLIC Na FORMATION IN NaCl CRYSTALS BY ELECTRON AND VUV PHOTON IRRADIATION**

Shigehiro OWAKI\*, Shigeko KOYAMA\*, Masao TAKAHASHI\* and Masao KAMADA\*\*

\*I.S.I.R., Osaka University, Ibaraki, Osaka 567.

\*\*Institute for Molecular Science, Okazaki, Aichi 444

We reported previously that due to aggregation of F centers after dense irradiation of 21 MeV electron pulses from a linac, metallic Na particles in NaCl single crystal were formed. This was established using optical absorption and positron annihilation lifetime measurements.<sup>1</sup> However, metallic Na was not detected in the crystals by X ray photoelectron spectroscopy (XPS). We proposed that the particle size was too small and the density was too low due to a uniform distribution in the bulk.

In this paper, NaCl crystals are irradiated with electrons of low energy (30–10 KeV) or with photons in the vacuum ultraviolet (VUV) region from synchrotron radiation (SR). In both cases, metallic Na is formed on the crystal surface as determined by Auger electron spectroscopy (AES) and UV photoelectron spectroscopy (UPS). The results are compared with those using high energy electrons.

Sodium chloride crystals, cleaved in Ar gas, were installed in a XPS apparatus (Vacuum Generator microlab Mk3) in which a pressure of  $3 \times 10^{-9}$  Torr was maintained during electron irradiation. The cleavage surface was scanned within the region of  $2 \times 2 \mu\text{m}^2$  by a thin focused electron beam (30 KeV,  $1.6 \mu\text{A}$ ) from a high luminosity gun.

The results of AES near Na KLL peaks are shown in Fig.1 with curve fits. In Fig.1 (a) obtained at the initial stage of the measurements, there is a single peak corresponding to KLL Auger line of ionic Na (peak (1) at 978 eV). In Fig.1 (b) of the spectrum after the electron irradiation for 10 min., a new peak (2) appears at 4–5 eV higher energy than that of ionic Na. The kinetic energy of the new peak corresponds to that of metallic Na.<sup>2,3</sup> It is important to note that this peak was not observed in a sample irradiated with 21 MeV electrons from a linac.

With the higher current or longer irradiation time, the peak of ionic Na shifted to 981 eV and the new peak also shifted 8 eV to the higher energy side than that of ionic Na. Moreover, another broad peak (3) was observed on the lower energy side as shown in Fig.1 (c) and it seems to correspond to isolated atomic Na, because of the kinetic energy of KLL of Na vapor, 977 eV.<sup>4</sup>

As another radiation sources for metal formation on NaCl surface and an analysis method, intense photon fluxes in the VUV region of SR and UPS were used at the UVSOR. The irradiation was performed on powdered crystals of NaCl with a photon flux diameter of 1 mm of white light (0 order light of grating monochromator); the analyzing light was monochromatic at 100 or 130 eV at BL6A2.

The peak analysis near the Na 2p line by UPS of a sample before and after VUV irradiation for 30 min. is shown in Fig. 2 (a) and (b). Peak (2) in Fig.2 (b) is consistent with metallic Na and peak (3), with a satellite due to plasmon loss from metallic Na (energy of bulk plasmon; 5.8 eV, energy of surface plasmon; 4.1 eV).<sup>2</sup> In the UPS vacuum system, electrons of 10 KeV were used for irradiation and the surfaces were analyzed by UPS for comparison of radiation effects between VUV photons and electrons of low energy. The former appears to be more effective than the latter, though it is difficult to compare the two flux intensities.

---

\*Present address: S. Owaki, College of Int. Arts & Sciences, University of Osaka Prefecture, Sakai, Osaka 593. S. Koyama, The Kansai Electric Power Co., Inc. Ohi, Fukui.

It is easily found from the broadening of the ionic Na KLL peak in AES that irradiation of high currents of low energy electrons damage NaCl crystal surfaces. As one of the results, formation of metallic Na was confirmed with separation of the metallic peak from the ionic peak. With further exposure to electrons, the metallic peak shift to 8 eV on the higher energy side than that of ionic Na and neutral Na (vapor state) was observed during irradiation.

The line broadening and shift of the Na 2p peak in UPS shows that the irradiation by VUV photon produces similar radiation damage to that of low energy. Exposure of NaCl to VUV may be a more effective method to create metallic Na than by electron. The observation of the bulk plasmon loss peak in a sample after VUV exposure of 30 min. means that there is metallic layer of thickness sufficient to produce the bulk plasmon. Irradiation by 21 MeV electron creates only particles of metallic Na with a size on the order of 10 nm and a bulk mole fraction less than  $10^{-3}$  estimated from the optical absorption.

Dense metal formation due to surface damage in high vacuum seems to depend on that fact that Cl ions (H center) can escape from the surface more easily than aggregation of F centers which is competitive with recombination of Frenkel pairs in the bulk.

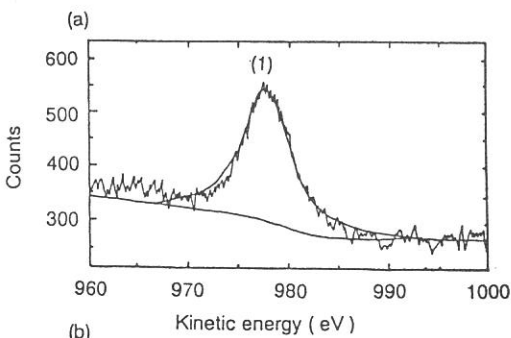


Fig.1

Auger electron spectra of a region near Na KLL in NaCl crystals: (a) before irradiation, (b) after irradiation of electrons of 30 KeV and (c) after the longer irradiation. Peak (1); ionic Na, (2); metallic Na and (3); atomic Na. Smooth curves are calculated fitting curves.

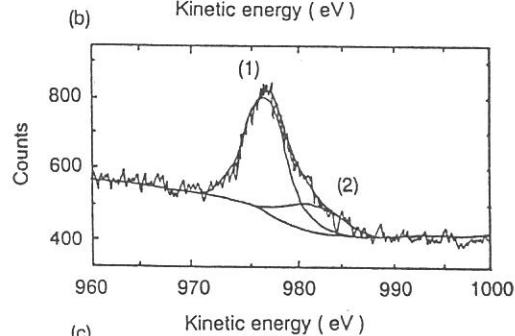
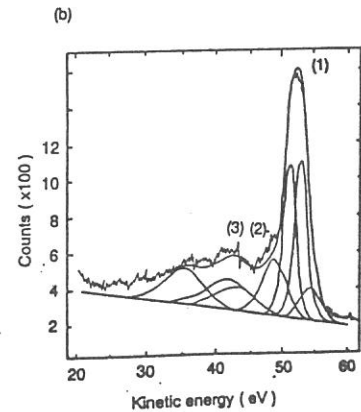
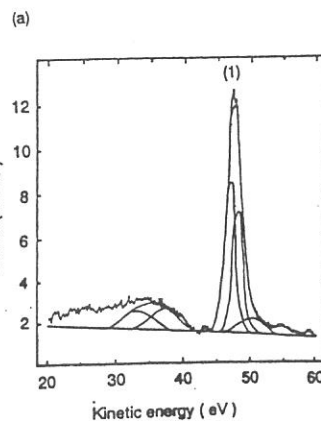
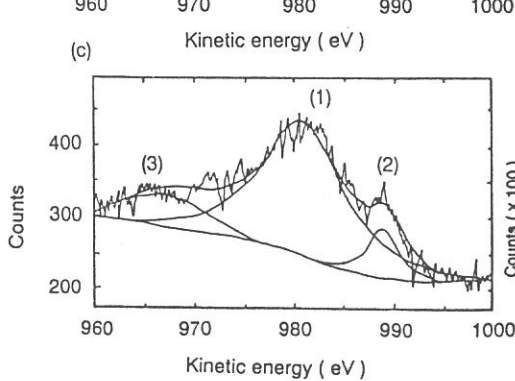


Fig.2

Photoelectron spectroscopy of a region of near Na 2p in NaCl powdered crystals:(a) before exposure, and (b) after exposure to VUV of SR for 30 min.. Peak (1); ionic Na, (2); metallic Na, (3); bulk plasmon loss from metallic Na. Smooth curves are calculated fitting curves.



#### REFERENCES:

1. S.Owaki, S.Koyama, K.Nobugai, T.Okada, K.Inabe, and Y.Fukuda, *Proc. 12th Int. Conf. Defects in Insulating Materials* (World Scientific 1993) pp853
2. A.Barrie and F.J.Street, *J. Electron Spectrosc. Relat. Phenom.*, 7,1 (1975)
3. C.D.Wagner, *Disc. Faraday Soc.*, 60, 291(1975)
4. H.Hilling, B.Cleff, W.Mehlbom and Schmitz, *Z. Physik*, 268, 225(1974)



## Photon-Energy Dependence of Excited-State Na Desorption from Na Halides

Sayumi Hirose and Masao Kamada

*Institute for Molecular Science, Myodaiji, Okazaki 444*

Photon-stimulated desorption (PSD) and electron-stimulated desorption (ESD) of constituent ions and atoms from solids have aroused considerable interest, because of their close relation to fundamental interaction between incident beams and solid surfaces, and also because of their applicability to microfabrication. There are most desorption studies of ions and ground-state atoms from alkali halides, while several works are reported about the PSD of excited-state atoms.<sup>1)</sup> There is a famous desorption mechanism for ions which is due to the core-level excitation (Knotek-Feibelman model),<sup>2)</sup> but it is not clear whether the KF model is valid for excited-state alkali desorption or not. Therefore, we have investigated the photon-energy dependence for PSD of excited-state alkali atoms in order to know quantitatively the contribution from core-level excitations.

The experiments were carried out at a plane-grating monochromator (PGM) beam line 6A2. Monochromatized lights by PGM were used as an excitation source. Single crystals of NaF and NaCl were cleaved with a knife edge in a sample chamber, base pressure of which was about  $5 \times 10^{-8}$  Pa.

Figure 1 shows excitation spectra of the broad luminescence band (a) and the excited-state Na desorption (b) as well as the absorption spectrum (c)<sup>3)</sup> in NaCl. The broad luminescence band may be attributed to the recombination luminescence originating from defects in the bulk. The prominent peak observed around 33 eV in the absorption spectrum is due to the Na  $L_{2,3}$ -core excitons. Although the excitation spectra in the vicinity of Na

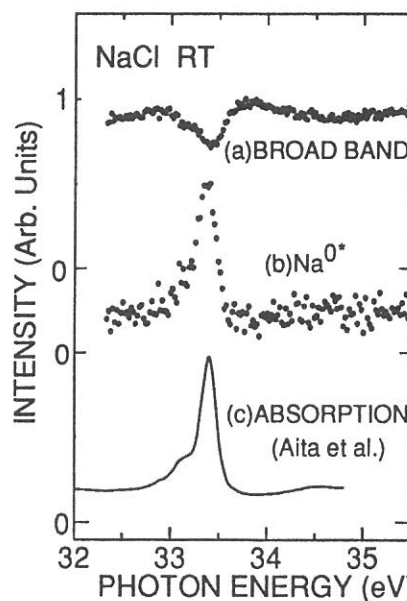


Fig. 1. Excitation spectra of broad luminescence band (a) and excited-state Na desorption (b) from NaCl. Curve (c) is absorption spectrum taken from ref. 3.



$L_{2,3}$ -core exciton band are different in lineshapes, a peak and a dip, between the excited-state Na desorption and the broad luminescence band, we can estimate the ratio of the luminescence and desorption yields for core-level to valence-band excitations ( $\eta_C/\eta_V$ ). On the basis of the results shown in Fig. 1, the ratios were found to be about 0.7 and 1.0 for the bulk luminescence band and excited-state Na desorption, respectively. This indicates that there is no special contribution from core-level excitation to the excited-state alkali desorption.

The ion desorption from the surface has been explained in terms of the KF model above core-level threshold, where Auger transition plays an important role. If the KF model is valid for the desorption of excited-state Na atoms, we may expect that the ratio for the excited-state alkali desorption is larger than that for the bulk luminescence band. However, this is not the case; the ratios  $\eta_C/\eta_V$  are almost the same between the excited-state alkali desorption and the bulk luminescence band. Therefore, it can be concluded that the contributions of core-level excitation to the bulk luminescence band and the excited-state Na desorption are in the same order as those of valence-band excitation, even in the photon energy corresponding to the excitation energy of core-excited states. Moreover, the excited-state Na desorption from NaF was observed below the threshold of core-level excitation. Therefore, the KF model is not valid for the excited-state alkali desorption. We suppose that the core-level excitation produces the secondary electronic excitations of valence electrons, which contribute the desorption of excited-state alkali atoms.

## References

- 1) Desorption Induced by Electronic Transitions (DIET IV), edited by G. Betz and P. Varga (Springer, Berlin, 1990).
- 2) P. J. Feibelman and M. L. Knotek, Phys. Rev. B18, 6531 (1978).
- 3) O. Aita, K. Ichikawa, and K. Tsutsumi, Phys. Rev. B38, 10079 (1988).

## Photoemission Study of Indium Nitride

Kazutoshi FUKUI, Masao KAMADA\*

Dept.Elec.Elec.Engi., Fac.Engi., Fukui Univ., FUKUI 910

\* UVSOR, IMS, OKAZAKI 444

Indium Nitride (InN) is one of the member of III-V compound semiconductors. The crystal structure of InN is either wurtzite or zinc-blende type. The minimum bandgap locates at  $\Gamma$  point in  $k$ -space and is about 2 eV. Since it is very difficult to grow InN single crystals, there is probably no experimental investigation about band structure of InN. However, recently thin films are fabricated by metalorganic chemical vapor deposition (MOCVD)[1], metalorganic vapor phase epitaxy (MOVPE)[2], and RF plasma sputtering [3] methods. To investigate the quality of InN thin films and the band structure of InN, both the photoelectron and the Auger spectra have been measured.

Thin films were fabricated on  $\alpha$ -Al<sub>2</sub>O<sub>3</sub> by MOCVD method [1]. All were  $n$ -type semiconductors and the thickness was about 0.1 ~ 1  $\mu$ m. They were all poly-crystalline films which have a wurtzite structure ( $c$ -axis was perpendicular to the substrate and  $a$ -axis was almost oriented to one direction). Xe ion sputtering (2 keV) was carried out to remove surface contamination [3]. Before Xe sputtering, Carbon, Nitrogen, and Oxygen were only detected on the Auger spectra. After etching, 1) Carbon was almost removed, 2) Indium and Nitrogen were dominant elements 3) Oxygen was still detected. Similar result for the composition ratio in thin films was obtained by the ESCA(XPS) measurements with Ar ion sputtering. Thus, it is concluded that the Oxygen atoms were incorporated in the thin films from the beginning stage of the fabrication. The investigation of the incorporation of Oxygen into the GaN thin films, which are fabricated by MOCVD method [4], suggests that Oxygen comes from the water vapor in the NH<sub>3</sub> gas which is used as the source of Nitrogen. The Oxygen incorporated in the present case may be due to the same problem.

Figure 1(a), (b), and (c) show the energy distribution curves (EDCs) of InN thin films before Xe sputtering (a), on the way of sputtering (b), and after sputtering (c). The excitation photon energy was about 60 eV. After sputtering, samples were annealed up to 150 C, but the EDC did not change with this annealing procedure. The spectra consist of valence band (VB) and In 4*d* levels.

The broad peak at about 18 eV in Fig. 1(a) is due to the In 4*d* levels, which consist of the various components which reflect bonding states between In and N, O, or C. After the surface contamination was removed, two peaks due to the spin-orbit interaction of In 4*d* levels are shown clearly. Furthermore, the line width of these two peaks in Fig.1(c) becomes narrower relative to those in Fig.1(b). It suggests that In 4*d* levels are very sensitive to the surface conditions. The energy position of the top of the VB is also different between before and after (on the way of) sputtering. Fermi edge can be seen clearly after sputtering (Fig. 1(c)). In

the case of InN, carrier electrons are created by the defects of Nitrogen, and in fact the carrier densities of the samples are in the order of  $10^{20} \text{ cm}^{-3}$ . The energies of donor levels due to Nitrogen defects were calculated [6]. They locate just under the bottom of the conduction band (CB) or in the CB. The main VB edge is about  $2 \sim 3 \text{ eV}$  below the Fermi edge in Fig. 1(c) so that Fig. 1(c) may show the EDC of the degenerate semiconductor. We have to do further investigation to discuss the band structure in more details.

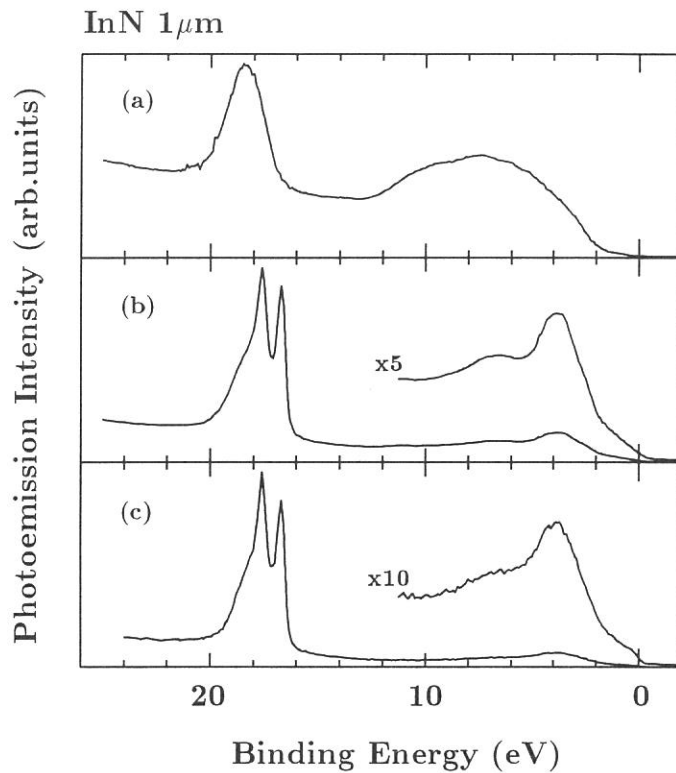


Fig.1 Photoemission Spectra of InN thin film: (a) before Xe sputtering, (b) after the sputtering for 40 minites, (c) after the sputtering for 60 minites

#### Refereces

- [1] A.Yamamoto et al., J. Cryst. Growth 37 (1994) 415-20.
- [2] A.Wakahara and A.Yoshida, Appl. Phys. Lett. 54 (1989) 709-11.
- [3] T.L.Tansley and C.P.Foley, J. Appl. Phys. 59 (1986) 3241.
- [4] C.P.Foley and J.Lyngdal, J. Vac. Sci. Technol. A 5 (1987) 1708-12
- [5] B.C.Chung and M.Gershenson, J. Appl. Phys. 72 (1992) 651-9
- [6] D.W.Jenkins and J.D.Dow, Phys. Rev. B 39 (1989) 3317-29

## Resonant Photoemission of $R_3Au_3Sb_4$ (R=La, Ce and Pr)

Shin-ichi KIMURA, Masao KAMADA, Kenichi KATOH<sup>1</sup> and Mitsuo KASAYA<sup>1</sup>

*UVSOR Facility, Institute for Molecular Science, Okazaki 444*

<sup>1</sup>*Department of Physics, Faculty of Science, Tohoku University, Sendai 980-77*

Recently, insulators of strongly correlated electron systems are investigated. They are called Kondo insulators. The origin of the energy gap is thought to be due to many body effect between carriers and localized magnetic moments. We have an interest in the hybridization between the valence band and the localized magnetic moments such as 4f bands in rare-earth ion and also in the origin of the energy gap. So we measured a resonant photoemission of valence band and estimated the hybridization intensity using a cluster model.

We measured one of Kondo insulators,  $Ce_3Au_3Sb_4$ , and the reference materials  $La_3Au_3Sb_4$  and  $Pr_3Au_3Sb_4$ . As the reference of the transport data, the energy gap of  $Ce_3Au_3Sb_4$  is 45 meV and that of  $La_3Au_3Sb_4$  is 70 meV. [1]  $Pr_3Au_3Sb_4$  has no gap. As the reference of the optical conductivity, the energy gap of  $Ce_3Au_3Sb_4$  originates from the 4f<sup>d</sup> state and 5d conduction band [2]. The hybridization between Ce - 4f<sup>d</sup> state and Sb-5p was concluded to be weak. So we measured the resonant photoemission of these materials and estimated the hybridization intensity for confirmation of the conclusion from the optical data.

The measurement was done at the beam line 6A2 with a plane grating monochromator and a cylindrical mirror electron analyzer. The energy of the 4d - 4f giant absorption band of  $R^{3+}$  ion (R = La, Ce and Pr) is in the range 110 - 130 eV. The energy resolution of the energy range was about 0.6 eV. The clean surface was obtained by scraping using a diamond filer.

The obtained photoemission spectra are shown in Figs. (a) - (c). From the difference spectrum of  $La_3Au_3Sb_4$ , the intensity of the Sb-5p valence band has weak resonant enhancement of the La 4d - 4f absorption. This means that the Sb-5p valence band weakly mixes to the La-5d band. In all materials, Au-5d band does not mixes to the rare-earth ion because of no evidence of the resonant enhancement. This means that the Au-5d band does not contribute to the bonding.

The back ground and fitted Lorentz functions are shown in the figure. After fitting, we got the informations of the hybridization energy  $V_0$ , which is independent on the number of occupied 4f, and the binding energies of the 4f electron ( $-E_f$ ) and the ligand band ( $-E_v$ ) in the

initial state by using a cluster model. [3] The obtained parameters are shown in Table. In  $\text{Ce}_3\text{Au}_3\text{Sb}_4$ ,  $V_0 = 0.76$  eV. The value is smaller than other Ce-compounds. The typical value of  $V_0$  is about 1 eV. The result is qualitatively consistent with the reflectivity data.

[1] K. Katoh and M. Kasaya, *Physica B* **186-188** (1993) 428.

[2] S. Kimura et al., *J. Phys. Soc. Jpn.* **62** (1993) 4174.

[3] A. Fujimori et al., *Phys. Rev. B* **38** (1988) 7789.

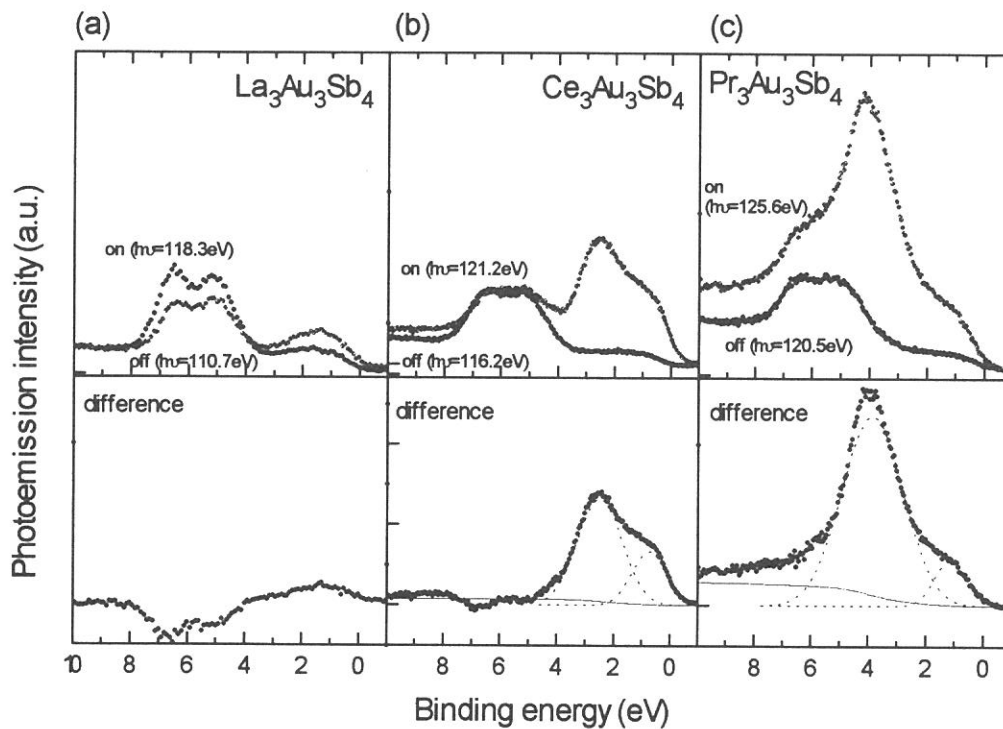


**Fig.** On- and off- resonant photoemission and the difference spectra of  $\text{R}_3\text{Au}_3\text{Sb}_4$  ( $\text{R} = \text{La}, \text{Ce}$  and  $\text{Pr}$ ).

	$\text{Ce}_3\text{Au}_3\text{Sb}_4$	$\text{Pr}_3\text{Au}_3\text{Sb}_4$
$V_0$ (eV)	0.76	0.95
$-E_f$ (eV)	1.9	3.6
$-E_v$ (eV)	1.2	1.4

**Table** Obtained parameters after analysis of cluster model.

## Far-infrared reflectance of $\beta''$ -(BEDT-TTF)<sub>2</sub>AuBr<sub>2</sub>: coexistence of free carriers and a single-particle gap at $2\Delta=130\text{cm}^{-1}$

Akito Ugawa,<sup>a,b</sup> David B. Tanner,<sup>b</sup> and Kyuya Yakushi<sup>a</sup>

<sup>a</sup>*Department of Molecular Assemblies, Institute for Molecular Science, Okazaki, Aichi 444, Japan*

<sup>b</sup>*Department of Physics, University of Florida, 215 Williamson Hall, Gainesville, Florida 32611-2085, U.S.A.*

Recent studies concerning Fermi-surface topology (so-called *fermiology*) of organic conductors have been extensively developed by electromagnetic measurements such as Shubnikov-de Haas (SdH) and de Haas-van Alphen (dHvA) effect. These phenomena are based on quantized cyclotron motion of electrons[1], so that a closed Fermi surface is at least necessary for the object. Among reported organic conductors (BEDT-TTF)<sub>2</sub>X system is very appropriate for this condition because a number of salts are predicted to have a two-dimensional, closed Fermi surface through tight-binding band calculations[2]. In most cases the SdH and/or the dHvA oscillations have been observed in good agreement with the above band picture, suggesting the efficiency of this calculation. Since this approximation, however, completely neglects Coulomb interaction between conduction electrons as well as electron-phonon interaction, the model cannot describe SDW and CDW state, which situations become more conspicuous if the band is highly anisotropic.

The  $\beta''$ -type BEDT-TTF salt, which retains metallic properties down to mK regions, is just a instance for the above case. The band calculation predicts two kinds of Fermi surface[3]: one is based on a one-dimensional band along the  $\Gamma \rightarrow Z$  direction, and another is a small pocket around the X point in the first Brillouin zone. This picture is inconsistent with the SdH and dHvA results which suggest the presence of three closed parts in the Fermi surface[4-6]. The reconstruction of the Fermi surface is then necessary to explain the quantum oscillations, which driving force should be related to the neglected interactions. We measured the temperature dependence of reflectance of  $\beta''$ -(BEDT-TTF)<sub>2</sub>Cl<sub>2</sub> to investigate the band structure of this type salt: the spectra down to 25 K and  $500\text{cm}^{-1}$  did not show any sign for the occurrence of SDW or CDW transition[7]. We here present the far-infrared results on  $\beta''$ -(BEDT-TTF)<sub>2</sub>AuBr<sub>2</sub>. We have found a single-particle gap at  $2\Delta=130\text{cm}^{-1}$  besides free carrier absorption below  $20\text{cm}^{-1}$ . The details of the electronic structure are discussed in comparison with (TMTSF)<sub>2</sub>X salts.

Single crystals of  $\beta''$ -(BEDT-TTF)<sub>2</sub>AuBr<sub>2</sub> were prepared by a conventional electrochemical method using tetra-*n*-butylammonium dibromoaurate(I) as a supporting electrolyte. Temperature dependence of far-infrared reflectance was measured on Bruker IFS-113v spectrometers (both at UF and IMS *UVSOR* BL6B[8]) with a reflectance unit and a Hi-tran cryostat over the wave-number region of 20-700  $\text{cm}^{-1}$  at temperatures among 5-300 K. The absolute reflectivity at a given temperature was determined from four measurements:  $R(\omega, T) = [P_s(\omega, T)/P_r(\omega, T)]/[P_{Au}(\omega, 300)/P_r(\omega, 300)]$ , where  $P_x(\omega, T)$  is the power spectrum at temperature  $T$  and the suffixes  $x=s, r, Au$  represent the spectrum from a sample, reference (Au mirror), the sample coated with Au, respectively.

In the  $\beta''$ -type crystal BEDT-TTF molecules are arranged uniformly along the  $c$  axis while dimerized along the  $a$  axis (nearly  $\perp c$ ;  $\beta=103^\circ$ ), forming two-dimensional layers parallel to the (010) face. The room temperature reflectance (not presented here) looks like a Drude type for both polarizations  $\parallel c$  and  $\perp c$ , the latter spectrum having some vibrational structures at 250, 310 and around  $450\text{cm}^{-1}$ . These bands are due to  $A_g$  modes of BEDT-TTF molecule resulting from the strong dimerization along the  $a$  axis.

Figure 1 shows the polarized reflectance at 7.0 K. The data below  $20\text{cm}^{-1}$  are linear-extrapolated as  $R \rightarrow 1$  on  $\omega \rightarrow 0$ , shown with dotted lines. The  $E_{\parallel c}$  reflectance is high and gradually increases as frequency down to  $150\text{cm}^{-1}$ . The structures appeared at nearly the same positions as in the  $E_{\perp c}$  spectrum, are also assignable to  $A_g$  modes of BEDT-TTF. This seems unreasonable because the molecules are not dimerized in the  $\parallel c$  direction, that is,  $A_g$  modes are infrared-inactive. The x-ray results have also indicated that no structural change corresponding to a formation of CDW occurs down to 4 K[7]. The vibrational structures in the  $E_{\parallel c}$  spectrum are then regarded as the component of  $\parallel a$  polarization, whose direction is not completely orthogonalized to  $\parallel c$ . These vibrational features are extremely pronounced in the  $E_{\perp c}$  spectrum at low temperatures.

We now turn our interest to a reflectance dip below  $150\text{cm}^{-1}$  in both spectra. This infers the presence of energy gap, which become more obvious through Kramers-Krönig analysis. Figure 2 shows the  $E_{\parallel c}$  conductivity spectra at temperatures 7.0 K and 300 K (Note that the spectrum of 300 K is drawn in tenfold scale). The conductivity at 7.0 K demonstrates a very strong and sharp peak at  $130\text{cm}^{-1}$ . These spectral features including its line-shape quite resemble the case in (TMTSF)<sub>2</sub>AsF<sub>6</sub> at 6 K, where the material is in the SDW state[9], suggesting that the peak comes from an optical transition across a single-particle gap on the one-dimensional band. The possibility of a CDW collective mode is denied by the reason mentioned above. Considering the EPR result which indicates the occurrence of magnetic transition below 20 K[10], the origin of the gap is probably due to the SDW nesting along the  $\parallel c$ . This assignment also suits the SdH/dHvA results[4-6] because the Fermi surface is predicted to consist of three pockets after the nesting transition[11]. The temperature dependence of the  $E_{\parallel c}$  reflectance among 5-40 K, however, scarcely changed over  $20\text{-}700\text{cm}^{-1}$ , meaning that the pseudo-gap exists above the EPR transition temperature. We here remark that the conductivity spectrum at 300 K is far from a typical line-shape of free-carrier absorption: the spectrum demonstrates a broad peak around  $170\text{cm}^{-1}$ , accompanying a dip

below  $100\text{ cm}^{-1}$ . This suggests that the nesting fluctuation of SDW is present even at room temperature. The similar results have been reported in the chain-axis conductivity of  $(\text{TMTSF})_2\text{PF}_6$ [12]. As discussed in this section the electronic structure of  $\beta''\text{-(BEDT-TTF)}_2\text{X}$  is proved to quite resemble that of  $(\text{TMTSF})_2\text{X}$  in spite of the large difference of donor molecule arrangement. The calculated band structure of  $(\text{TMTSF})_2\text{X}$  yields a one-dimensional Fermi surface with small warp[13], which is also very similar to the one-dimensional part in  $\beta''\text{-(BEDT-TTF)}_2\text{X}$ . In both cases the band dispersion is dominated by the largest overlap(s) along the particular direction ( $\parallel a$  for the TMTSF salt and  $\parallel c$  for the BEDT-TTF salt), the overlap(s) being much stronger than in other directions. The major part of the Fermi surface, as a result, consists of open planes in both salts, and the optical transitions near the Fermi level then become similar.

The superconductivity in  $\beta''\text{-(BEDT-TTF)}_2\text{X}$  has not been found yet down to  $44\text{ mK}$ [6] in spite of the quite resemblance to  $(\text{TMTSF})_2\text{X}$ . This is an interesting problem in the future.

## REFERENCES

- 1 See, for example, D. Shoenberg, *Magnetic oscillations in metals* (Cambridge Univ. Press, 1984).
- 2 T. Mori *et al.*, Bull. Chem. Soc. Jpn. **57**, 627 (1984).
- 3 T. Mori *et al.*, Chem. Lett. 1037 (1986).
- 4 F. L. Pratt *et al.*, Phys. Rev. Lett. **61**, 2721 (1988).
- 5 A. G. Swanson *et al.*, in *Organic Superconductivity*, edited by V. Z. Kresin and W. A. Little, pp.191 (Plenum Press, New York, 1990).
- 6 S. Uji *et al.*, Physica **B194-196**, 1307 (1994).
- 7 A. Ugawa *et al.*, Synth. Met. **27**, A407 (1988).
- 8 A. Ugawa *et al.*, Rev. Sci. Instrum. **63**, 1551 (1992).
- 9 J. E. Eldridge and G. S. Bates, Phys. Rev. **B34**, 6992 (1986).
- 10 M. Kurmoo *et al.*, Solid State Commun. **61**, 459 (1987).
- 11 F. L. Pratt *et al.*, Physica **B177**, 333 (1992).
- 12 C. S. Jacobsen *et al.*, Phys. Rev. **B28**, 7019 (1983).
- 13 T. Mori *et al.*, Chem. Lett. 1923 (1982).

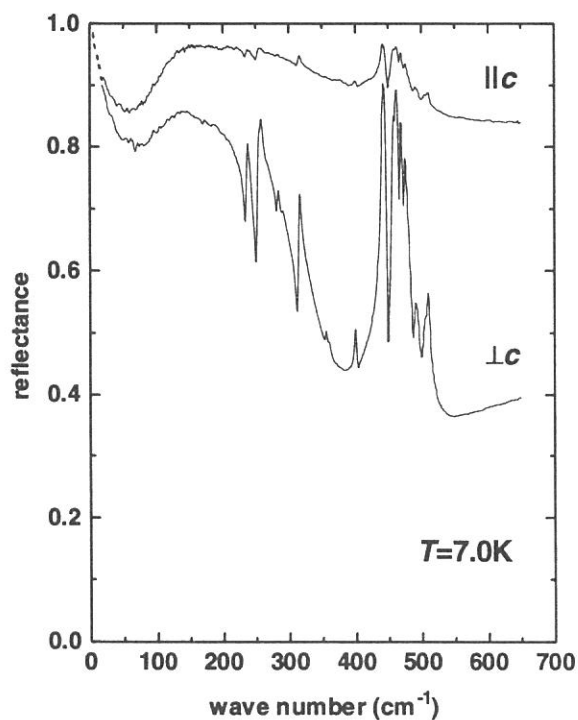


Figure1. Polarized reflectance at 7.0K.

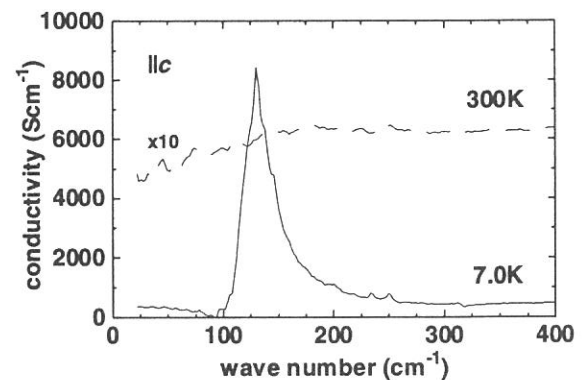


Figure 2. Conductivity spectra for  $\parallel\parallel\parallel c$  at 7.0K and 300K.



## Mo $L_{III}$ -edge and Mg $K$ -edge XANES Study of Local Structure of MoO<sub>3</sub>-MgO binary oxide

H.Aritani<sup>1)</sup>, T.Tanaka<sup>1)</sup>, T.Funabiki<sup>1)</sup>, S.Yoshida<sup>1)</sup> and S.Hasegawa<sup>2)</sup>

1) Division of Molecular Engineering, Kyoto University, Sakyo-ku, Kyoto 606-01, Japan

2) Department of Chemistry, Tokyo Gakugei University, Koganei, Tokyo 184, Japan

### Introduction

Supported and mixed molybdenum oxides have been studied and applied widely as heterogeneous catalysts. For instance, Bi<sub>2</sub>O<sub>3</sub>-MoO<sub>3</sub> catalyst is used in practice for the partial oxidation of olefins to produce unsaturated aldehydes or dienes<sup>1)</sup>. In the structural study of Bi-Mo oxide system, the catalytic activity depends on the phases of bismuth-molybdate (Bi<sub>2</sub>O<sub>3</sub>- $n$ MoO<sub>3</sub>)<sup>2)</sup>. Antonio *et. al.* reported that Mo  $K$ -edge XANES can provide structural insights for the three phases of  $\alpha$ - ( $n=3$ ),  $\beta$ - ( $n=2$ ) and  $\gamma$ - ( $n=1$ ) Bi<sub>2</sub>O<sub>3</sub>- $n$ MoO<sub>3</sub><sup>3)</sup>.

MoO<sub>3</sub>-MgO binary oxide exhibits catalytic activity for partial oxidation. We also found the metathesis activity for propene by relatively higher-content of pre-reduced MoO<sub>3</sub>-MgO<sup>4)</sup>. With respect to Mo-Mg oxide system, Mo  $L_{III}$ -edge XANES study was applied recently to MgO-supported MoO<sub>3</sub><sup>5)</sup>. In this study, it is suggested that supported-molybdena at low Mo content are stabilized in an octahedral structure on MgO, and tetrahedral one was generated at relatively higher contents. This result is inconsistent with the studies from UV-visible spectroscopy<sup>6)</sup>. Thus, the structural information of Mo-Mg oxide system is still unclear.

In this report, we describe the local structure around Mo and Mg ions in MoO<sub>3</sub>-MgO binary oxides by Mo  $L_{III}$ -edge and Mg  $K$ -edge XANES spectroscopy.

### Experimental

The MoO<sub>3</sub>-MgO samples [Mo/(Mo+Mg)=0.1~0.9] were obtained by solution-evaporation method of (NH<sub>4</sub>)<sub>6</sub>Mo<sub>7</sub>O<sub>24</sub> · 4H<sub>2</sub>O and MgCl<sub>2</sub> · 6H<sub>2</sub>O mixed solution, followed by drying the mixture overnight and calcination at 873K for 3 hs. The XANES experiment was carried out at BL-7A in UVSOR. Two-crystal monochromator of beryl and Ge(111) were used for Mg  $K$ - and Mo  $L_{III}$ -edge respectively. Each spectrum was collected in an electron yield mode.

### Results and Discussion

Fig. 1 shows the Mo  $L_{III}$ -edge XANES spectra of authentic samples. The white lines due to  $2p$ - $4d$  transition are split corresponding to the ligand field splitting of the  $d$ -orbitals<sup>4)</sup>. In case of MgMoO<sub>4</sub> having tetrahedral [MoO<sub>4</sub>] unit, the white lines are attributed to the electron transition from  $2p_{3/2}$  to split  $t_2$ - $e$  of  $4d$  state. For MoO<sub>3</sub> having octahedral [MoO<sub>6</sub>] unit is due to the transition of  $2p_{3/2} \rightarrow t_{2g}$ - $e_g$  of  $4d$  atomic orbitals. It is noted that transition cross sections are different between tetrahedral and octahedral molybdena. In case of MoO<sub>3</sub>, the white line at lower energy side (to  $t_{2g}$ ) was larger than that at higher (to  $e_g$ ) one, and a gap between two white lines was 3.1eV, while in case of MgMoO<sub>4</sub>, the white line at lower energy side (to  $e$ ) is smaller than higher (to  $t_2$ ) one, and the gap is 2.3eV. Such an energy gap between these white lines are consistent with  $d$ - $d$  gap, although, the energy resolution of XANES measurement was poor. On the other hand, XANES spectra of MoO<sub>3</sub>-MgO were shown in Fig. 2. At a low content less than 0.5, a feature of

two white lines over XANES spectrum were similar to  $\text{MgMoO}_4$ , indicating that tetrahedral  $[\text{MoO}_4]$  unit is stabilized at lower content. At the higher Mo content above 0.5, the relative intensity of a white line at lower energy side became gradually larger with an increase in Mo ratio. This is explained by co-existence of octahedra and tetrahedra, and suggests the generation of octahedral  $[\text{MoO}_6]$  unit at higher content. But, the energy gap of white lines are not in agreement with that for  $\text{MoO}_3$ . Formed  $[\text{MoO}_6]$  unit in high content of Mo is distorted more than  $\text{MoO}_3$ . This is supported by the XRD result that  $\text{Mg}_2\text{Mo}_3\text{O}_{11}$  and  $\text{MgMo}_2\text{O}_7$  phases were observed around 0.7 of Mo ratio.

From Mg  $K$ -edge XANES, mixture of  $\text{MgO}$  and  $\text{MgMoO}_4$  phases were found at less than 0.4 of Mo ratio, and fraction of  $\text{MgMoO}_4$  phase increased the increase in Mo ratio. At higher than 0.5 of Mo ratio,  $\text{MgMoO}_4$  phase was only observed.

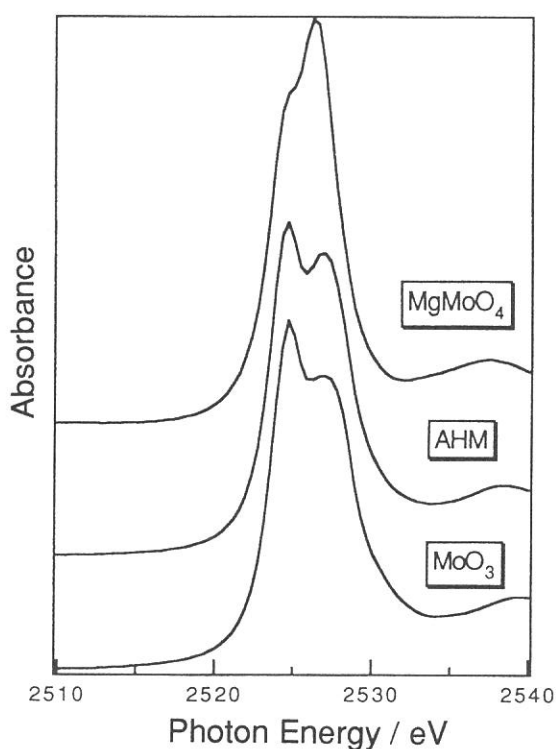


Fig. 1 Mo  $L_{\text{III}}$ -edge XANES of authentic samples. (AHM=ammonium heptamolybdate)

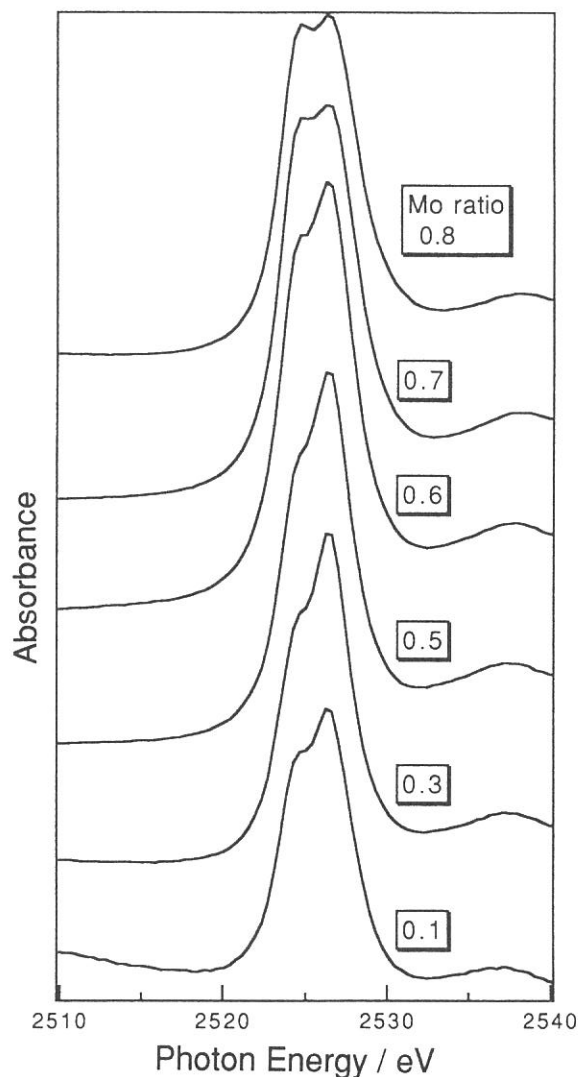


Fig. 2 Mo  $L_{\text{III}}$ -edge XANES of  $\text{MoO}_3$ - $\text{MgO}$ .

- 1) L.C.Glaeser, J.F.Brazdil, M.A.Hazle, M.Mehicic, R.K.Grasselli, *J. Chem. Soc. Faraday Trans. 1*, 81 (1985) 2903.
- 2) M.Egashira, K.Matsuo, S.Kagawa, T.Seiyama, *J. Catal.*, 58 (1979) 409.
- 3) M.R.Antonio, R.G.Teller, D.R.Sandstorm, M.Mehicic, J.F.Brazdil, *J. Phys. Chem.*, 92 (1988) 2934.
- 4) S.Hasegawa, T.Tanaka, M.Kudo, H.Mamada, H.Hattori, S.Yoshida, *Catal. Lett.*, 12 (1992) 255.
- 5) B.Hedman, P.Frank, S.F.Gheller, A.L.Roe, W.E.Newton, K.O.Hodgson, *J. Am. Chem. Soc.*, 110 (1988) 3798.
- 6) M.Che, F.Figueras, M.Forisser, J.McAtter, M.Perrin, J.L.Portefaix, H.Praliaud, *Proc. 6th Intern. Congr. Catal.*, London (1976) 261 ; J.M.M.Llorente, V.Rives, P.Malet, F.J.Gil-Llanbias, *J. Catal.*, 135 (1992) 1.

## A XANES Study on the Dehydration Process of Magnesium Hydroxide<sup>1</sup>

Tomoko YOSHIDA, Tsunehiro TANAKA, Hisao YOSHIDA, Takuzo FUNABIKI,  
Satohiro YOSHIDA and Takatoshi MURATA\*

*Department of Molecular Engineering, Kyoto University, Kyoto 606-01*

*\*Department of Physics, Kyoto University of Education, Kyoto 612*

The dehydration process of  $\text{Mg}(\text{OH})_2$  to  $\text{MgO}$  has been widely studied by means of X-ray diffraction (XRD),<sup>2</sup> electron and optical microscope,<sup>3</sup> and kinetics,<sup>4,5</sup> etc. However, it has been left unclear whether nucleation of  $\text{MgO}$  crystallite commences on the surface or inside of  $\text{Mg}(\text{OH})_2$ . To clarify this, it is necessary to observe the dehydration process directly at an atomic level by other techniques than those mentioned above. In the present study, we carried out analysis of phases included in  $\text{Mg}(\text{OH})_{2-2x}\text{O}_x$  by deconvolution of Mg K-edge XANES.<sup>6</sup>

X-ray absorption spectra were recorded at the beam line 7A station attached with a beryl two-crystal monochromator of UVSOR of Institute for Molecular Science, Okazaki, Japan. Energy calibration was made by Al K-edge absorption of Al in beryl. The samples were mixed with active carbon in dry hexane and were put on the first photocathode made of Au of the electron multiplier. Data were collected in a total electron yield mode, which monitors energy dependence of Mg KLL Auger electron yield mainly. Taking into account the escape depth of the Auger electron being about 30 Å, spectra can provide information of the surface state of samples.

$\text{Mg}(\text{OH})_2$  powder samples (600 mg) were dehydrated *in vacuo* at various temperatures (373 K - 673 K) for 5 h. The degree of dehydration was determined from the weight loss of samples. Dehydration of  $\text{Mg}(\text{OH})_2$  occurred drastically *in vacuo* at around 573 K. XRD pattern showed that the main phase was  $\text{Mg}(\text{OH})_2$  in the samples evacuated below 573 K, while above 583 K, small crystallite of  $\text{MgO}$  was formed dominantly. We have estimated the molar fractions of  $\text{MgO}$  and  $\text{Mg}(\text{OH})_2$  crystals in the samples by evaluation of integrated intensities of (200) diffraction peak of  $\text{MgO}$  and that of (101) of  $\text{Mg}(\text{OH})_2$  using silicon powder as an internal standard. The result is shown in Fig. 1(a). We found that the ratio of  $\text{MgO}$  crystal phase determined by XRD is lower than that expected from the degree of dehydration up to 583 K.

Fig. 2 shows Mg K-edge XANES of samples evacuated at 373 K - 623 K and  $\text{MgO}$ . The XANES spectrum of the sample evacuated at 373 K was identical with that of  $\text{Mg}(\text{OH})_2$ . The feature of XANES changes from that of  $\text{Mg}(\text{OH})_2$  to that of  $\text{MgO}$  with increase in the evacuation temperature. The sample evacuated at 623 K exhibited the same XANES as that of  $\text{MgO}$ . It is very likely that  $\text{Mg}(\text{OH})_2$  and  $\text{MgO}$  crystallites coexist in the samples evacuated at

around 573 K. To estimate the composition of MgO and Mg(OH)<sub>2</sub>, we have attempted the simulation of XANES spectra by superposition of XANES of Mg(OH)<sub>2</sub> and that of the sample evacuated at 623 K with a suitable ratio. All of the spectra were able to be reproduced sufficiently. The fractions of MgO determined by this procedure is also shown in Fig. 1(b). When the sample was evacuated at around 573 K, the fraction of MgO crystal phase determined by XRD was 33%, which was lower than that expected from the degree of dehydration 43%. On the other hand, the fraction of the local structure of MgO estimated by XANES analysis was higher (63%). Taking into account that XANES reflects the information of surface layers, Fig. 1 clearly suggests that the formation of MgO by dehydration occurs in the surface layers at first.

We also examined the time-course of the dehydration *in vacuo* at 573 K until 10 h. The results also indicated that nucleation of MgO crystallite starts in the surface layers. In addition, XANES analysis indicated that the fraction of MgO existing in the surface layers increases gradually with evacuation time and Mg(OH)<sub>2</sub> is still left in the surface even after 87% of dehydration. We conclude here that the MgO phase is formed in some part of surface layers at first and then the crystallization of MgO proceeds both in the surface layers and in the inside of the sample.

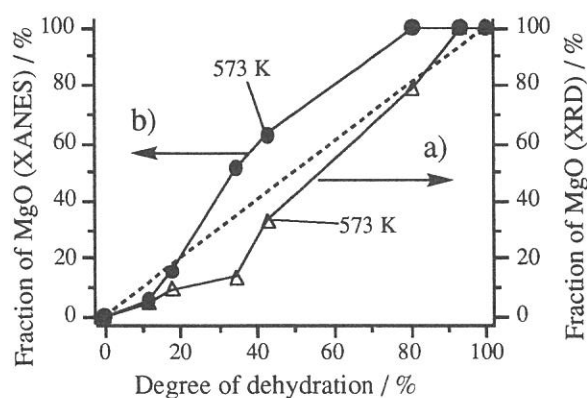


Fig. 1 Fractions of MgO vs. degree of dehydration. The fractions were estimated by the analyses of a) XRD and b) XANES.

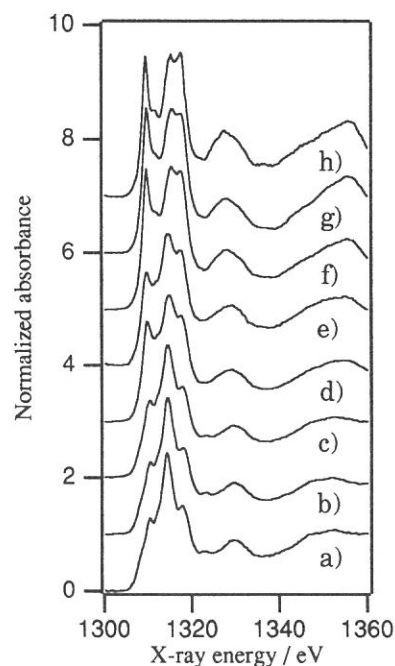


Fig. 2 Mg K-edge XANES of Mg(OH)<sub>2</sub> evacuated at a) 373 K, b) 523 K, c) 553 K, d) 563 K, e) 573 K, f) 583 K, g) 623 K and h) MgO.

- [1] T. Yoshida, T. Tanaka, H. Yoshida, S. Takenaka, T. Funabiki, S. Yoshida, *Physica B*, *in press*.
- [2] H. Terauchi, T. Ohga, H. Naono, *Solid State Commun.*, 35 (1980) 895.
- [3] R. S. Gordon, W.D. Kingery, *J. Amer. Ceram. Soc.*, 49 (1966) 654.
- [4] P. J. Anderson, R.F. Horlock, *Trans. Faraday Soc.*, 58 (1962) 1993.
- [5] R. S. Gordon, W.D. Kingery, *J. Amer. Ceram. Soc.*, 50 (1967) 8.
- [6] S. Yoshida, T. Tanaka, T. Hanada, T. Hiraiwa, H. Kanai, T. Funabiki, *Catal. Lett.*, 12 (1992) 277.

# Nb L-edge XANES Study of Nb compound catalysts

Yasuyuki Nishino, Masato Aida, Sumie Matsuhara, Kentaro Nakamura  
and Sadao Hasegawa

*Department of Chemistry, Tokyo Gakugei University, Koganei, Tokyo 184*

## 1. Introduction

In the recent catalyst, chemistry we have often turned the X-ray absorption spectrum to good account in characterizing catalysts. XANES which turn up before and after the absorption edge have used for fingerprintic analysing approach.

In general, it is known that niobium pentoxide,  $\text{Nb}_2\text{O}_5$ , crystallizes at room temperature in a monoclinic structure of which the niobium ion is octahedrally surrounded by oxygen ions. Sugiura *et al.* have studied that the Nb  $L_3$  and  $L_2$  X-ray absorption-edge spectra of  $\text{Nb}_2\text{O}_5$  and  $\text{NH}_4\text{NbF}_6$  interpreted in terms molecular orbital (MO) theory<sup>1</sup>.

We have measured the Nb  $L_3$  and Nb  $L_2$  absorption-edge spectra of  $\text{Nb}_2\text{O}_5$ , Nb/ZnO and Nb/MgO and reported about the change of Nb L-edge XANES due to the difference of the supports.

## 2. Experimental

Nb-loaded MgO was prepared by impregnating MgCl dissolved in water with oxalic acid solution of niobium oxalate. The product was treated by calcining at 673K and 873K for 2h in air.

Nb-loaded ZnO was also prepared by impregnation ZnO with oxalic acid solution of niobium oxalate, and was treated by calcining in previous condition.

The Nb L-edge adsorption spectra of the catalysts were measured at BL-7A soft X-ray beam line with UVSOR facilities, when used a Ge(1,1,1) two-crystal monochrometer.

## 3. Results and Discussion

The Nb  $L_3$  and  $L_2$  absorption-edge spectra of  $\text{Nb}_2\text{O}_5$  and Nb-loaded metal oxide are shown Fig.1 and 2. All the samples are observed a strong doublepeaked edge structure on the  $L_3$  and  $L_2$  absorption-edge spectra. The strong peaks A and B can be attributed to the transitions from the Nb  $2p_{3/2}$  to the Nb  $4d_{3/2}$  and to the Nb

4d  $5/2$  respectively. The observed  $A-B$  separations ( $\Delta E_{AB}$ ) corresponds to the ligand-field splitting ( $\Delta$ ) of the 4d state of  $Nb^{5+}$ . The photon-energy values of their absorption peaks are given in Table.1 and 2.  $\Delta E_{AB}$  of Nb-loaded metal oxide catalysts calcined at 673K are larger than that of  $Nb_2O_5$  in spite of content.

The relative intensity of peak- A and B ( $A/B$ ) for Nb/MgO, Nb/ZnO are increased in the increasing of Nb contents. The Nb  $L_2$  absorption-edge spectra for Nb/MgO, Nb/ZnO, and  $Nb_2O_5$  are quite similar to their respective  $L_3$  spectra, since the  $L_2$  and  $L_3$  spectra are spin-orbit components (Fig.2). Only the initial state ( $2p^{1/2}$  or  $2p^{3/2}$ ) for transitions is different. On the other hand, the peak separations in the  $L_3$  absorption-edge spectra are somewhat larger than those in the  $L_2$  absorption-edge spectra.

Table 1 The photon-energy values (in eV) the maxima in the Nb  $L_2, L_3$  absorption spectra of  $Nb_2O_5/Mg^{1)}$ ,  $Nb_2O_5/ZnO^{1)}$  and  $Nb_2O_5$

Notion	Nb $L_2$ absorption			Nb $L_3$ absorption		
	$Nb_2O_5$	$Nb_2O_5/MgO$	$Nb_2O_5/ZnO$	$Nb_2O_5$	$Nb_2O_5/MgO$	$Nb_2O_5/ZnO$
A	2469.2	2466.5	2466.5	2374.9	2372.6	2372.6
B	2471.3	2468.7	2469.0	2377.0	2375.0	2375.4
A-B	2.1	2.2	2.5	2.1	2.4	2.8

1) Sample was calcined at 673K for 2h.

Table 2 The photon-energy values (in eV) the maxima in the Nb  $L_2, L_3$  absorption spectra of  $Nb_2O_5/MgO^{1)}$ ,  $Nb_2O_5/ZnO^{1)}$  and  $Nb_2O_5$

Notion	Nb $L_2$ absorption			Nb $L_3$ absorption		
	$Nb_2O_5$	$Nb_2O_5/MgO$	$Nb_2O_5/ZnO$	$Nb_2O_5$	$Nb_2O_5/MgO$	$Nb_2O_5/ZnO$
A	2469.2	2466.2	2466.5	2374.9	2372.6	2372.6
B	2471.3	2469.4	2469.4	2377.0	2375.7	2375.7
A-B	2.1	3.2	2.9	2.1	3.1	3.1

1) Sample was calcined at 873K for 2h.

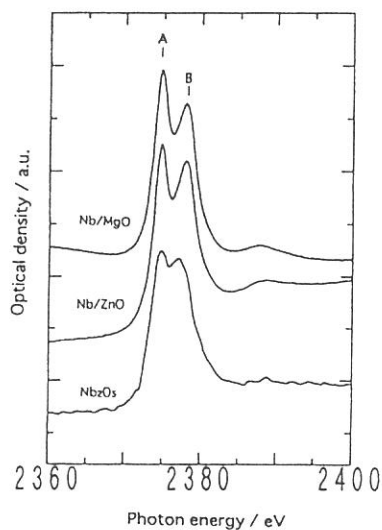


Fig.1 Nb  $L_2$ -edge XANES of Nb-loaded on metal oxide  $Nb_2O_5$

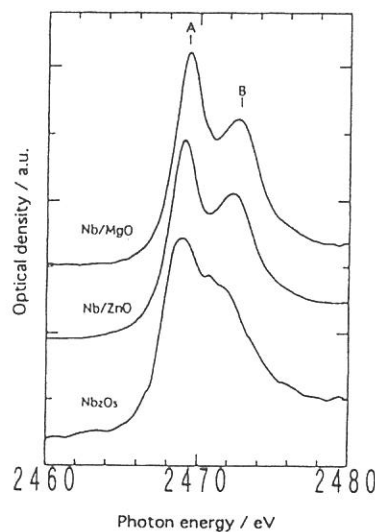


Fig.2 Nb  $L_3$ -edge XANES of Nb-loaded on metal oxide  $Nb_2O_5$

1) C. Sugiura, M. Kitaura and S. Muramatsu, *Phys. Chem. Solid.*, 49, 9, 1095 (1988)



## Throughput at BL7A Using Wiggler Operated at 2 T and 4 T

M. Watanabe<sup>1)</sup> and O. Matsudo<sup>2)</sup>

1. Research Institute for Scientific Measurements, Tohoku University, Sendai 980
2. UVSOR, Institute for Molecular Science, Okazaki 444

For spectroscopic studies above 2 keV, the synchrotron radiation (SR) from the wiggler operated at 4 T is introduced through the bending magnet B<sub>7</sub> to the beam line BL7A equipped with a double crystal monochromator (DXM) and monochromatized by a pair of germanium crystals. Below 2 keV however, the SR from the bending magnet (bending light) is used, because beryl crystals which monochromatized the light below 2 keV are damaged by the SR from the wiggler (wiggler light) operated at 4 T. In this case, the DXM of BL7A should be aligned again on the direction of the bending light. This is a tiresome procedure. Therefore, it is required that the wiggler is operated at 2 T (or 1.5 T) for experiments below 2 keV, so that it may be needless to align the beam line again.

The distance between the first crystal of the DXM and the source point is about 4.5 m and 6.7 m in the case of the bending light and the wiggler light, respectively. The slit in front of the first crystal is 2 mm high and 10 mm wide. Taking into account of these parameters, we calculated the photon number on the first crystal for the wiggler light (2 T, 4 T) and the bending light (1.1 T) as shown in Figure 1.

Figure 2 shows the throughput of the DXM at BL7A. The bending light and the wiggler light (2 T, 4 T) are monochromatized by a pair of germanium crystals. The intensity of the wiggler light at 2 T is almost same around 2 keV and strong between 2 and 3.7 keV in comparison with that of the bending light. The intensity of the bending light is spuriously stronger than that from the wiggler light above 3.7 keV. It may be due to the scattered light not monochromatized with the germanium crystals. We have demonstrated that the operation of the wiggler at 2 T (or 1.5 T) is promising, because the wiggler light not only at 4 T but 2 T can be introduced to BL7A. However the beam positions of the SR at two beam lines (BL3A1, BL3A2) moved. Further study for correction of the orbit is required. The radiation damage on the beryl crystal have also to be investigated.

We would like to sincerely thank Dr. Hama and other members of Machine Group for the laborious trial of the correction of the orbit. It is greatly appreciated that the experimentalists at the whole beam lines took part in checking the beam positions before and after the operation of the wiggler.



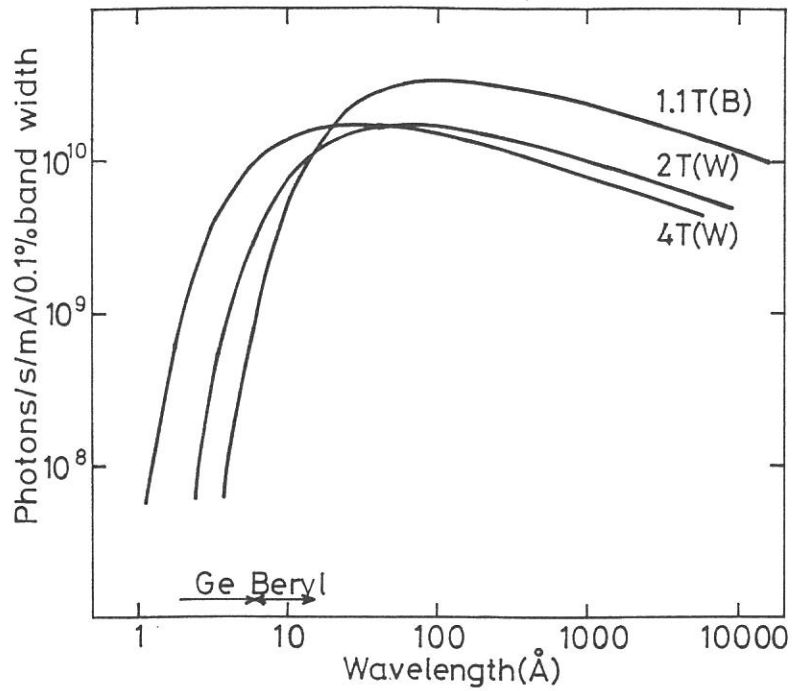


Fig. 1 Calculated photon number on the first crystal. B: bending magnet, W: wiggler.

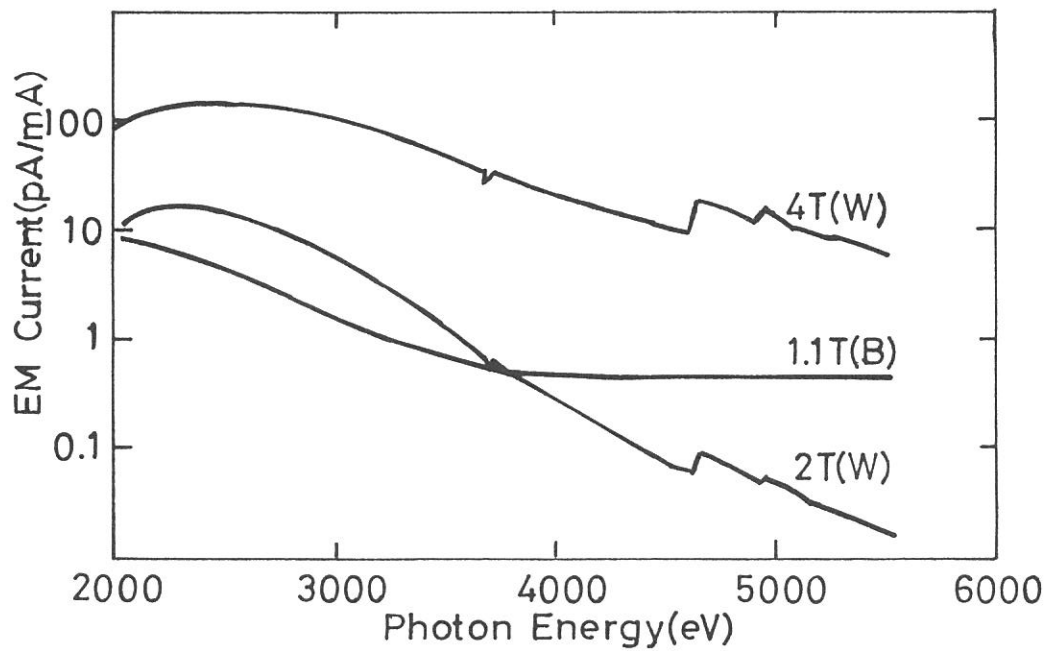


Fig. 2 Throughput of the DXM at BL7A normalized by a stored current of 1 mA. Monochromatized light is detected by an electron multiplier (EM) with the first dinode made of Be-Cu.

## Na K XANES Spectra of Silicate Crystals and Glasses

Takatoshi Murata, Shigeru Hayashi and Gordon E. Brown Jr.\*

Department of Physics, Kyoto University of Education, Fushimi, Kyoto 612, Japan

\*Department of Geological and Environmental Sciences,  
Stanford University, Stanford, CA 94305-2115, USA

Silicate minerals are compounds of Na-Al-Si-O. The coordination number of Na atom which is 8 in mineral crystals changes into 6 to 7 in glasses. X-ray absorption spectra of Na K edge region for silicate minerals and glasses have been measured using total yield of photoelectron on the JUMBO line in SSRL.<sup>1</sup> From the analysis of EXAFS data, Na-O distances for three compounds, albite, jadeite, and nepheline were determined. In albite, for example, they are ranging from 2.37 to 3.26Å. However, due to heavy damage of Beryl crystal used to monochromatize the white SR beam in JUMBO beam line in SSRL, the resolution of the spectra are not good enough. Therefore, it is necessary to investigate again the x-ray absorption spectra of these silicate minerals in more stable condition, i.e., without the effect of radiation damage of monochromator crystal of Beryl. We have measured the Na K XANES spectra of the same materials which were measured in the SSRL. Measurements were done on the soft x-ray beamline BL7A in the UVSOR. The absorption spectra were measured using total yield of photoelectron. Samples were ground into a fine powder in a agate mortar. and were spread as a fine film on a piece of adhesive graphite tape. The tape is stucked onto the first photocathode of electron multiplier (Hamamatsu R595). The total yield of the emitted photoelectrons from the sample is measured as the output current of the electron multiplier. The entire monochromator-sample system is held in a vacuum chamber at  $1 \times 10^{-7}$  Torr.

Figures 1 to 3 show the results for three minerals. Clear differences between crystal and glass for each material is shown in the spectra. The spectra reflect the difference in coordination environments in each material. Simulation of the spectra using FEFF program is in progress.

### Reference

1. D.A. McKeown, G.A. Waychunas, and G.E. Brown Jr., *J. Noncrystal. Solids*, **74**, 335 (1985).

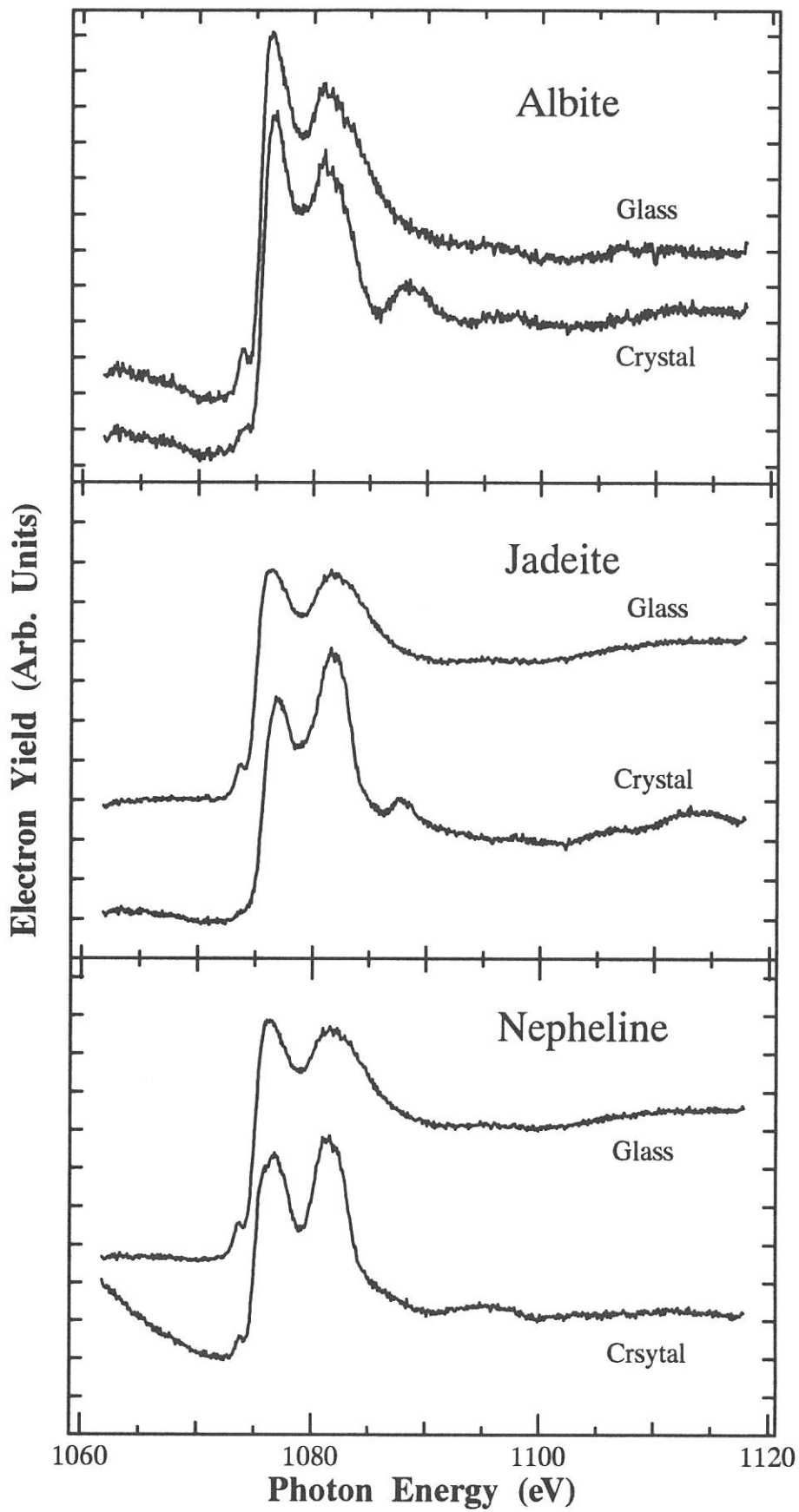


Figure 1. Na K XANES spectra of crystals and glasses of Albite, Jadeite, and Nepheline.

## S-K and P-K polarized absorption spectra of layered thiophosphates MPS<sub>3</sub> (M=Mn,Fe,Ni,Zn,Mg)

Atsushi KAMATA, Shun-ichi NAKAI, Takayuki KASHIWAKURA, Noriyoshi KOZUKA

Takaya YOKOHAMA, Hiroshige TEZUKA and Osamu MATSUDO\*

Faculty of Engineering, Utsunomiya University, Utsunomiya 321

\*Institute for Molecular Science (UVSOR), Okazaki 444

MPS<sub>3</sub> (M=Mn, Fe, Ni, Zn, Mg) are largely studied by many workers because of their low dimensional electrical, magnetic and optical characters. The crystal structure is similar to the CdCl<sub>2</sub> structure, and each layer is weakly bonded by van der Waals forces. Foreign atoms or molecules can be intercalated into van der Waals gaps (in the cationic forms). For example, in the case of Li is intercalated, it is expected to work as a good secondary battery. Characters are similar to each other material (MPS<sub>3</sub> (M=Mn, Fe, Ni)), while NiPS<sub>3</sub> has predominantly large electric resistivity among them<sup>1)</sup>, and only NiPS<sub>3</sub> has the magnetization axis lying in the ab-plane<sup>2)</sup>. From many studies, it is cleared that the transition metal included in MPS<sub>3</sub> (M=Mn, Fe, Ni) is strongly ionized<sup>3,4)</sup>. Further more from the Near-normal-incident reflectivity measurement, it is revealed that these band structures are closely similar to each other<sup>1)</sup>. It is considered that the first peak of S-K, P-K absorption spectra arise mainly from the transitions to the P-S antibonding states which contain s(P), p(P), p(S) characters, and it is also revealed that p-like partial densities of states of the unoccupied energy levels of a [P<sub>2</sub>S<sub>6</sub>]<sup>4-</sup> clusters are similar to each other materials (MPS<sub>3</sub> (M=Mn, Fe, Ni))<sup>5)</sup>. In this study, we have measured the S-K and P-K polarized absorption spectra of MPS<sub>3</sub> (M=Mn, Fe, Ni, Zn, Mg) to investigate the spatial asymmetry of p-like unoccupied states of these materials.

All samples were synthesized by means of Chemical Vapor Transport (CVT) method. We carried out polarized absorption measurement by using synchrotron radiation at the BL-7A line of the Ultraviolet Synchrotron Radiation Facility (UVSOR), Institute for Molecular Science. The double crystal monochromator mounted Ge(111) crystal was used for measurement. The sample was cleaved in a vacuum by peeling off with Scotch tape along the sample surface (ab-plane). The S-K and P-K polarized absorption spectra were measured by means of p-polarized light from soft x-ray Wiggler beam line with rotating the sample around the axis which stands perpendicularly with the c axis of MPS<sub>3</sub>.

Figure 1 shows the S-K absorption spectra of MPS<sub>3</sub> (M=Mn, Fe, Ni, Zn, Mg). The solid curve was taken for the polarization of electric field of incident beam parallel to the ab-plane (E//ab), and the dotted curve was taken for nearly parallel to the c-axis (E//c). All spectra were normalized at the background of absorption threshold. The (E//ab) spectra shows predominant peaks around at 2472 eV for all samples, and have a broad peak at about 7eV higher than the first peak. Except for MgPS<sub>3</sub>, all materials show large polarization dependency at the first peak. Among them, the spectra of MnPS<sub>3</sub> and FePS<sub>3</sub> are very similar. While NiPS<sub>3</sub> indicates somewhat different features in the polarization dependency. Figure 2 shows P-K absorption spectra of MPS<sub>3</sub> (M=Mn, Fe, Ni, Zn, Mg). Solid line and dotted one denote same orientations

as in the case of Fig. 1. In the (E//ab) spectra, the first peak is appeared at 2147.5eV for all materials, and shoulder structure is appeared at 2eV higher energy region of the first peak. Polarization dependency is also observed at the first peak between (E//ab) and (E//c) spectra except for MgPS<sub>3</sub>. The (E//ab) spectra in both of the S-K and P-K absorption exhibit similar structures, while the (E//c) spectra show large difference between in these materials. In this experiment, spectra show spatial asymmetry of density of states of 3p (S and P) unoccupied states. Especially NiPS<sub>3</sub> shows large differences between (E//ab) and (E//c) spectra than the other materials, it can be said that NiPS<sub>3</sub> has large spatial asymmetry of 3p (S) unoccupied density of states. The interpretation of this polarization dependency is now on progress.

## References

- 1) F. S. Khumalo and H. P. Hughes, Phys. Rev. **B23** 5375 (1981)
- 2) P. A. Joy and S. Vasudevan, Phys. Rev. **B46** 5425(1992)
- 3) M. Piacentini et al, Chem. Phys. **65** 289 (1982)
- 4) M. Piacentini et al, Chem. Phys. **72** 61 (1982)
- 5) Y. Ohno and K. Hiram, J. Solid State Chem. **63** 258 (1986)

Figure 1

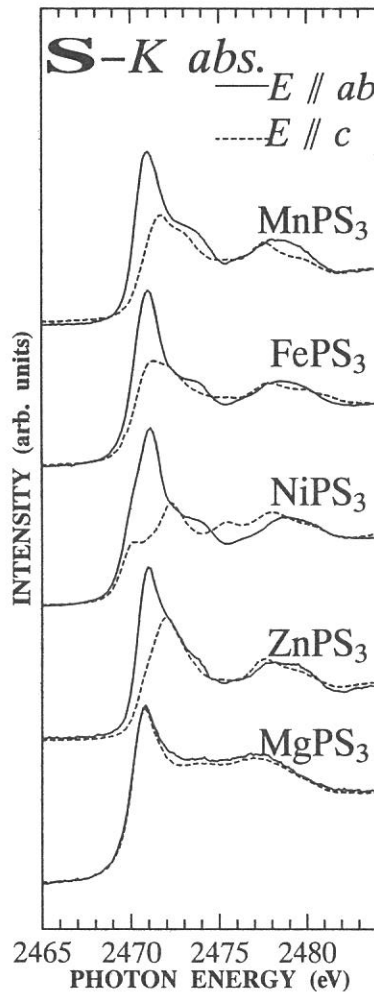
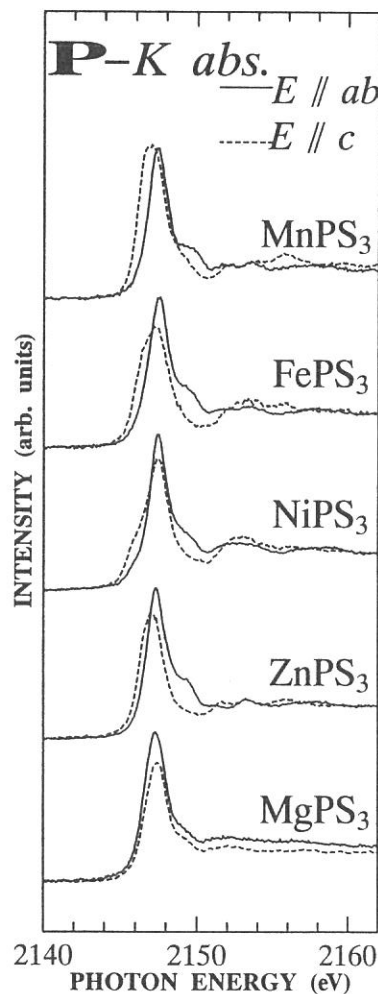


Figure 2



## VUV Reflection Spectra of Electrically Polarized TiO<sub>2</sub>-Containing Silicate Glass with Optical Second Harmonic Generation Activity

Kiyoshi KURACHI, Jun MATSUOKA, Hiroyuki NASU and Kanichi KAMIYA  
*Faculty of Engineering, Mie University, Tsu 514*

Second harmonic generation (SHG) of light should not be theoretically observed for the materials such as glasses because of their macroscopic inversion symmetry. However, since Myers et al.<sup>1)</sup> reported the permanent SHG activity in strongly electrically polarized SiO<sub>2</sub> glasses in 1991, SHG from glass have been investigated vigorously. Recently, we also observed SHG from electrically polarized SiO<sub>2</sub> glasses, and found that SHG intensity strongly depended on OH concentration of the glasses<sup>2)</sup>. Furthermore, we observed SHG from electrically polarized TiO<sub>2</sub>-containing silicate glass<sup>3)</sup>. However, the origin of SHG activity in this glass has not been clarified yet.

In this study, measurement of the VUV reflection spectra of the TiO<sub>2</sub>-containing glasses was carried out in order to examine the poling effect on the electronic structure of glass.

The glass with a composition of 7.5K<sub>2</sub>O·7.5Cs<sub>2</sub>O·26.5TiO<sub>2</sub>·58.5SiO<sub>2</sub> (mol%) was prepared by melting method at 1550°C for 1 hour in an alumina crucible. Dc voltage (500V–3kV) was applied to the glass plates at various temperatures ranging from 200°C to 300°C for 2 hours in air, and then cooled to room temperature under the application of dc electric field. The glass plates both having and without having SHG activity were served for the VUV reflection measurements.

Figures 1 and 2 show the VUV reflection spectra of 7.5K<sub>2</sub>O·7.5Cs<sub>2</sub>O·26.5TiO<sub>2</sub>·58.5SiO<sub>2</sub> glass plates poled at 3kV at 200–300°C for 2 hours, and at 0.5–3kV at 300°C for 2 hours, respectively. All of the spectra have a peak around 5.4 eV which is confirmed by Izumitani and Hirota<sup>4)</sup> to originate from the Ti<sup>4+</sup>-related transition. Samples which show SHG activity are a, b, d, e and f. The spectra show that the peak shifts to the lower energy side on the application of dc voltage, and the shift increases with the increase in poling temperature and applied dc voltage. So, this shift may be related to some structural change of the glass around Ti<sup>4+</sup> such as the decrease of Ti–O bond distance and some distortion of TiO<sub>n</sub> polyhedra. Howev-



er, since the  $\text{Ti}^{4+}$ -related reflection peak of sample c and g which have no SHG activity also shifts to the lower energy side, not whole these changes would be responsible for the SHG activity.

In summary, VUV reflection spectra of  $\text{TiO}_2$ -containing silicate glasses electrically poled under various conditions were measured, and the application of dc voltage was found to cause the electronic structural change in  $\text{TiO}_2$ -containing silicate glass although the relation between the structure change and SHG activity was not simple.

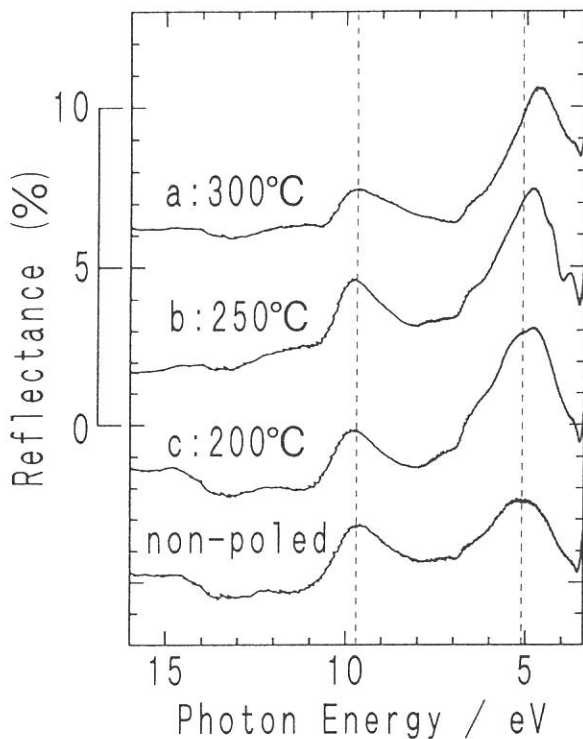


Fig. 1 Vacuum ultraviolet reflection spectra of  $7.5\text{K}_2\text{O}\cdot 7.5\text{Cs}_2\text{O}\cdot 26.5\text{TiO}_2\cdot 58.5\text{SiO}_2$  (mol%) glasses poled at 3kV at 200-300°C for 2 hours and non-poled glass.

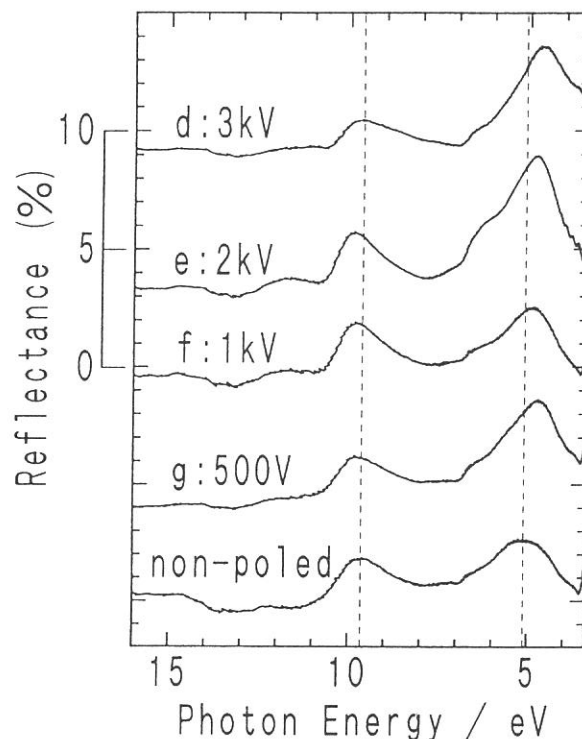


Fig. 2 Vacuum ultraviolet reflection spectra of  $7.5\text{K}_2\text{O}\cdot 7.5\text{Cs}_2\text{O}\cdot 26.5\text{TiO}_2\cdot 58.5\text{SiO}_2$  (mol%) glasses poled at 0.5-3kV at 300°C for 2 hours and non-poled glass.

#### References

1. R. A. Myers, N. Mukherjee and S. R. J. Brueck, *Opt. Lett.*, **16** (1991), 1732.
2. H. Nasu, H. Okamoto, A. Mito, J. Matsuoka and K. Kamiya, *Jpn. J. Appl. Phys.*, **32** (1993), L406.
3. H. Nasu, K. Kurachi, A. Mito, H. Okamoto, J. Matsuoka and K. Kamiya, *J. Non-Cryst. Solids*, in press.
4. T. Izumitani and S. Hirota, *J. Non-Cryst. Solids*, **80** (1986), 460.

# OPTICAL CHARACTERISTICS OF FLUORINE-DOPED SiO<sub>2</sub> FORMED BY PLASMA-ENHANCED CHEMICAL VAPOR DEPOSITION

Keisuke ISHII and Yoshimichi OHKI

Department of Electrical Engineering, Waseda University,  
3-4-1 Ohkubo, Shinjuku-ku, Tokyo 169

Silicon dioxide films formed by chemical vapor deposition from Tetraethoxysilane (TEOS) begin to be used widely as interlevel dielectric layers in ultra-large-scale integrated circuits (ULSI). In order to secure high-speed operation of ULSI, it is necessary to lower the capacitance of interlevel dielectric layers. It has been reported that the dielectric constant can be decreased by addition of fluorine into SiO<sub>2</sub> [1]. Together with this decrease in dielectric constant, change in etching rate and hygroscopicity is also reported. This suggests that some structural change is caused by the fluorine addition. Although such structural change may affect the reliability of the dielectric layers, little attention has been given to the structure of F-doped SiO<sub>2</sub>. Based on such a background, F-doped SiO<sub>2</sub> films were formed by plasma-enhanced chemical vapor deposition of TEOS and tetrafluoromethane (CF<sub>4</sub>), and their optical characteristics were studied using synchrotron radiation.

Samples were deposited using an apparatus described in our previous paper [2]. Oxygen (flow rate: 10 sccm) and CF<sub>4</sub> (10 sccm) or oxygen (10 sccm) was introduced from the top of a glass bell-jar and excited with an RF power of 13.56 MHz through capacitive coupling. The TEOS (1 sccm) gas was vaporized and transported at 70 °C into the 'tail-flame' of the oxygen/CF<sub>4</sub> or oxygen plasma. For other measurements, silicon wafers were used. The photoluminescence was observed using synchrotron radiation at the Institute for Molecular Science.

When the F-doped sample deposited at 600 °C was irradiated

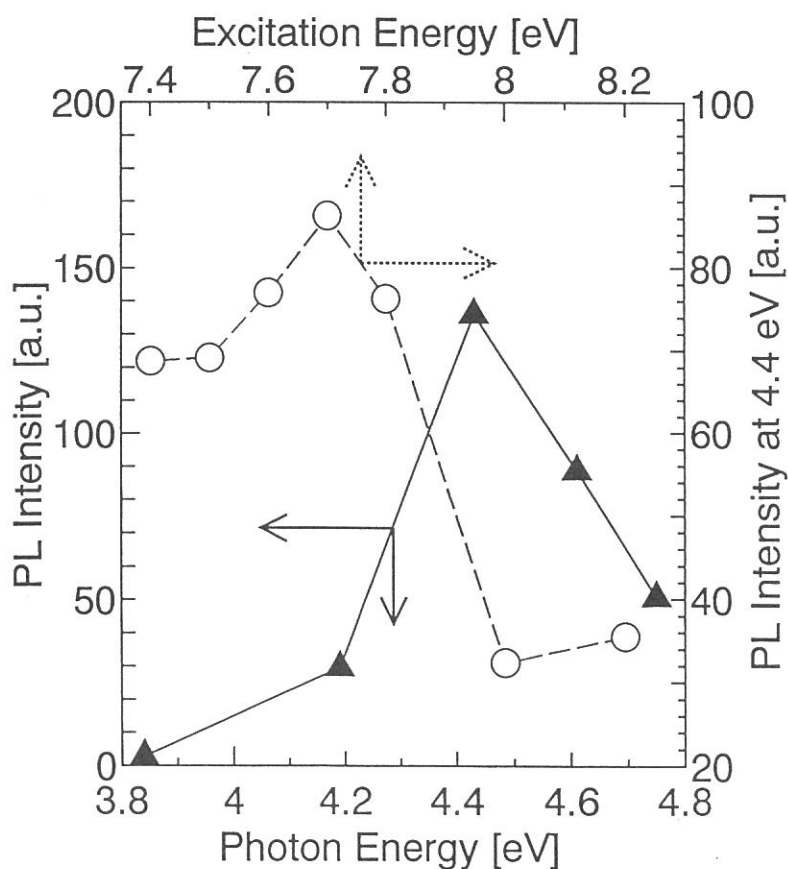


Fig. 1. Photoluminescence spectrum excited by 7.6-eV photons and excitation spectrum of the 4.4-eV luminescence obtained at 10K for F-doped SiO<sub>2</sub>.

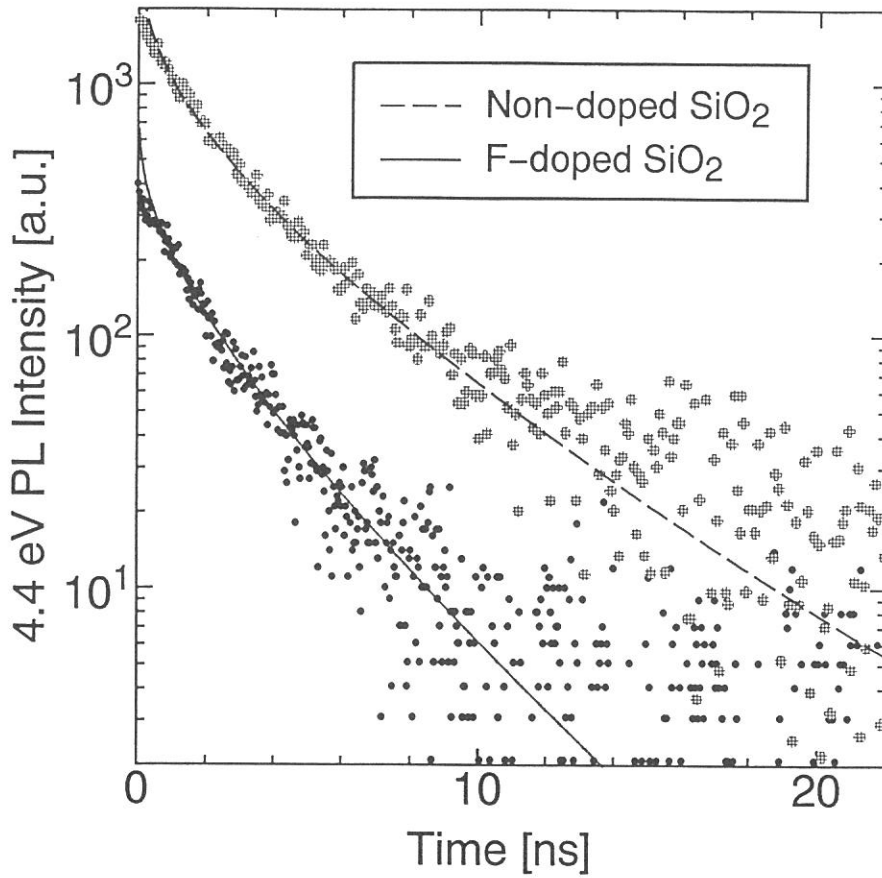


Fig. 2. Semilog plot of the decay of 4.4-eV luminescence excited by 7.6-eV photons. The solid and broken curves are drawn by assuming the stretched-exponential function:

$$I(t) \propto \left(\frac{\beta}{\tau}\right) \left(\frac{\tau}{t}\right)^{1-\beta} \exp\left[-\left(\frac{t}{\tau}\right)^\beta\right]$$
. The  $\beta$  parameters is 0.82 for F-doped SiO<sub>2</sub> and 0.78 for non-doped SiO<sub>2</sub>.

obtained by the least-squares fit to the data using the following

equation:  $I(t) \propto \left(\frac{\beta}{\tau}\right) \left(\frac{\tau}{t}\right)^{1-\beta} \exp\left[-\left(\frac{t}{\tau}\right)^\beta\right]$  Here,  $\tau$  is the effective decay constant, and  $\beta$  is a

parameter which takes a value of  $0 < \beta < 1$ . Lower  $\beta$  means that the function deviates more from a single-exponential decay and indicates that the sample structure is more highly distorted [2].

While  $\beta$  is 0.78 for the non-doped sample, it is 0.82 for the F-doped sample. This indicates that the degree of the structural distortion is smaller in F-doped SiO<sub>2</sub>. The fluorine addition is considered to relax the structural distortion of SiO<sub>2</sub> films synthesized by plasma-enhanced chemical vapor deposition.

### References

- [1] for example: T. Fukada and T. Akahori, Extended Abstract (The 40th Spring Meeting, 1993), The Japan Society of Applied Physics and Related Societies, 31pZV1 (in Japanese).
- [2] K. Ishii, Y. Ohki, and H. Nishikawa, J. Appl. Phys., Vol. 76, p. 5418 (1994).
- [3] H. Nishikawa, E. Watanabe, D. Ito, and Y. Ohki, Phys. Rev. Lett., Vol. 72, p. 2101 (1994).

by 7.6-eV photons at 10 K, photoluminescence was observed around 4.4 eV. Figure 1 shows the luminescence intensity as a function of the emitted photon energy by the 7.6-eV photon irradiation and the excitation spectrum of this luminescence. The luminescence spectrum has a peak around 4.4 eV, while the emission spectrum has one around 7.6 eV. Referring to the studies on high-purity silica [3], this luminescence is assumed to be due to the oxygen vacancies ( $\equiv \text{Si}-\text{Si} \equiv$ ).

Figure 2 shows the decay of the 4.4-eV luminescence of the 600 °C deposited samples excited by 7.6-eV photons. The solid and broken curves were

Reflection Spectra of Nonequilibrium Solid Solutions  
in Alkali Bromides

Satoshi HASHIMOTO and Masami INABA

Department of Physics, Kyoto University of Education,  
Fukakusa, Fushimi-ku, Kyoto 612

It is well known that formation of solid solution depends on materials in many binary systems of alkali halides. This is interpreted in terms of lattice misfit between two materials. Recently we have successfully produced thin crystals of solid solutions with a large value of the misfit in a nonequilibrium state.<sup>1)</sup>

Thin crystals with about 1  $\mu\text{m}$  thickness of alkali bromides which do not form solid solutions in growing bulk crystals have been prepared through the method using quartz cell<sup>2)</sup>. In Figure 1 reflection spectrum of  $\text{Rb}_{0.5}\text{Cs}_{0.5}\text{Br}$ (a) measured at 12 K is shown and absorption spectra of  $\text{CsBr}$ (b) and  $\text{RbBr}$ (c) taken for evaporated thin films<sup>3)</sup> are also shown for comparison. Distinct doublet peaks with a 0.51-eV splitting ( $4p^6 \rightarrow 4p^55s$ ) is seen on the curve (a). This value is almost equal to the splitting energy of spin-orbit interaction of bromine p-electrons in pure  $\text{RbBr}$  and  $\text{CsBr}$ . Two peaks in  $\text{CsBr}$  ( $4p^6 \rightarrow 4p^54d$ ) at 7.09 and 7.18 eV, being characteristic to  $\text{CsCl}$ -type, disappears on the curve (a). From these results, thin crystal of  $\text{Rb}_{0.5}\text{Cs}_{0.5}\text{Br}$  forms a solid solution in the  $\text{NaCl}$ -type. If the thin crystal occurs phase separation as expected from phase diagram of bulk crystals, two peaks of lowest excitons must appear on the reflection spectrum of  $\text{Rb}_{0.5}\text{Cs}_{0.5}\text{Br}$ . In Fig. 2 reflection spectrum of  ${}^{\text{K}}\text{Rb}_{0.5}\text{Cs}_{0.5}\text{Br}$  is shown on the curve (a) together with absorption spectra of  $\text{CsBr}$ (b) and  $\text{KBr}$ (c).<sup>2)</sup> Two peaks similar to Fig. 1(a) can be seen except some structures around the second peak.

#### References

- 1) M.Inaba and S.Hashimoto: to be submitted to J.Phys.Soc.Jpn.
- 2) S.Hashimoto and M.Itoh: Jpn.J.Appl.Phys. 27(1988)726.
- 3) K.Teegarden and G.Baldini: Phys.Rev. 155(1967)896.

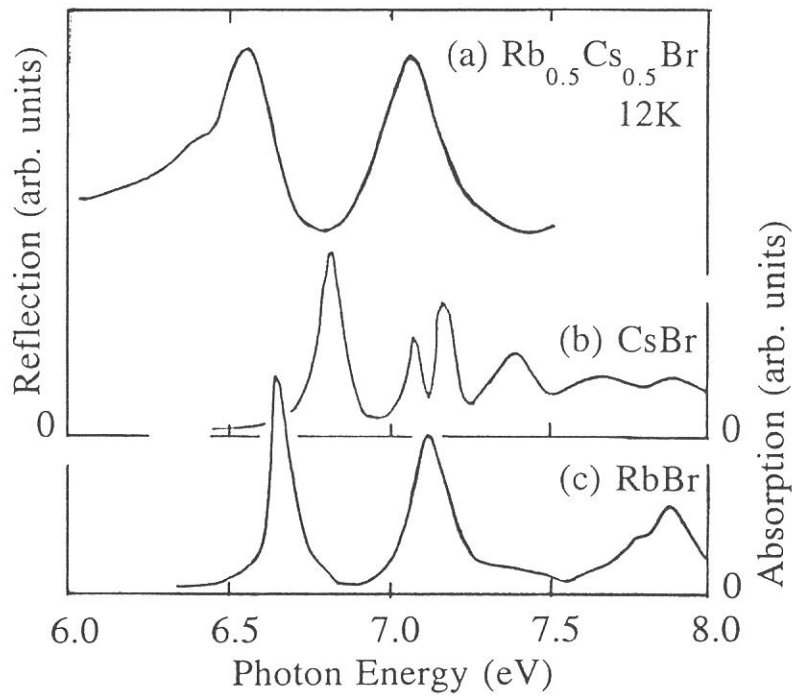


Fig.1 Reflection spectrum of thin  $\text{Rb}_{0.5}\text{Cs}_{0.5}\text{Br}$  crystal(a) measured at 12 K. Absorption spectra of CsBr(b) and RbBr(c) taken for thin evaporated films at 10K are also shown for comparison.

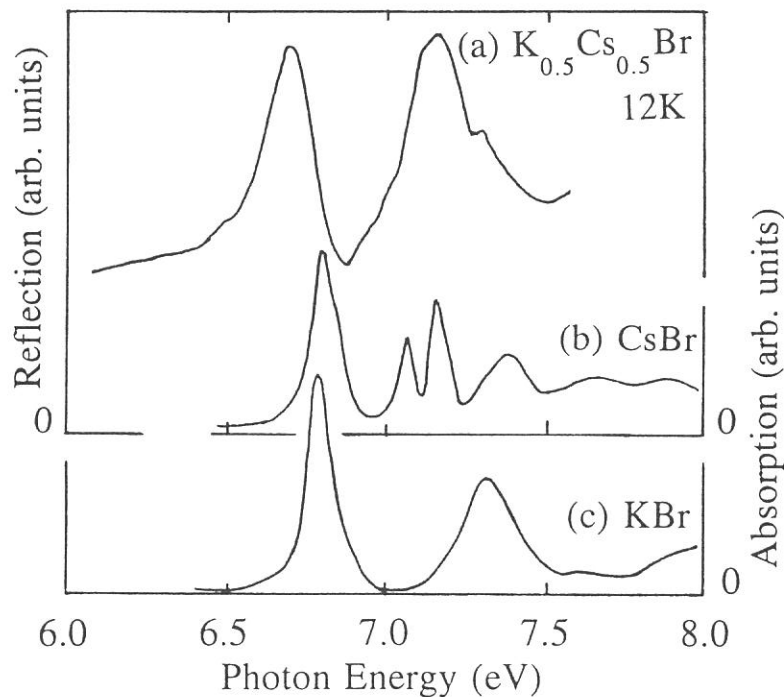


Fig.2 Reflection spectrum of thin  $\text{K}_{0.5}\text{Cs}_{0.5}\text{Br}$  crystal(a) measure at 12K. Absorption spectra of CsBr(b) and KBr(c) taken for thin evaporated films at 10 K are also shown for comparison.

## Dispersion Properties of Excitons in Thin Alkali Bromide Crystals

N. Ohno,<sup>1</sup> I. Iwaki,<sup>1</sup> S. Hashimoto<sup>2</sup> and M. Itoh<sup>3</sup>

<sup>1</sup>*Department of Solid State Electronics,  
Osaka Electro-Communication University, Neyagawa 572*

<sup>2</sup>*Department of Physics, Kyoto University of Education, Kyoto 612*

<sup>3</sup>*Department of Applied Science, Shinshu University, Nagano 380*

Dispersions of the refractive index near the excitonic resonance have been investigated extensively in semiconducting materials by using novel experimental techniques. They have been well understood in the framework of the exciton-polariton theory. However, few investigations have been made for ionic crystals with a strong exciton-photon interaction. This is mainly because these materials have a large band-gap energy usually in the VUV region. In the present study, we have investigated the dispersion properties of the refractive index near the exciton resonance in alkali bromides using thin single crystals for the first time.

The sample crystals were grown from the melt inside a narrow gap of a cell composed of two quartz plates.<sup>1)</sup> The crystal thickness  $d$  could be changed within a range from 0.05 to 50  $\mu\text{m}$ .

Figure 1 shows an example of the reflection spectrum of RbBr with  $d = 0.540 \mu\text{m}$  measured at 10 K. The pronounced doublet peaks at 6.60 eV and 7.09 eV are ascribed to the  $\Gamma(3/2,1/2)$  and  $\Gamma(1/2,1/2)$  exciton transitions, respectively, split by the spin-orbit interaction.<sup>2)</sup> On the low-energy side of the first exciton band, we can observe well-pronounced Fabry-Perot interference fringes.

Since the refractive indices of alkali bromides are available in the visible region,<sup>3)</sup> we can estimate the spectral variation of the refractive index  $n$  from the analysis of Fig. 1. The result obtained for RbBr is shown in Fig. 2. The arrow in the figure is the peak energy of the first exciton band in the reflection spectra. The refractive index shows a strong dispersion in the vicinity of the exciton resonance. We get the refractive index up to 6.50 eV which is close to the first-exciton resonance energy.

The analysis of the dispersion curves of alkali bromides is now in progress in terms of the exciton-polariton model to determine the transverse-exciton energy, the longitudinal-transverse splitting energy, the background dielectric constant and so on.

## References

- 1) S. Hashimoto and M. Itoh: Jpn. J. Appl. Phys. **27** (1988) 726.
- 2) G. Baldini and B. Bosacchi: Phys. Rev. **166** (1968) 863.
- 3) A. Kublitzky: Ann. Phys. (5) **20** (1934) 793.

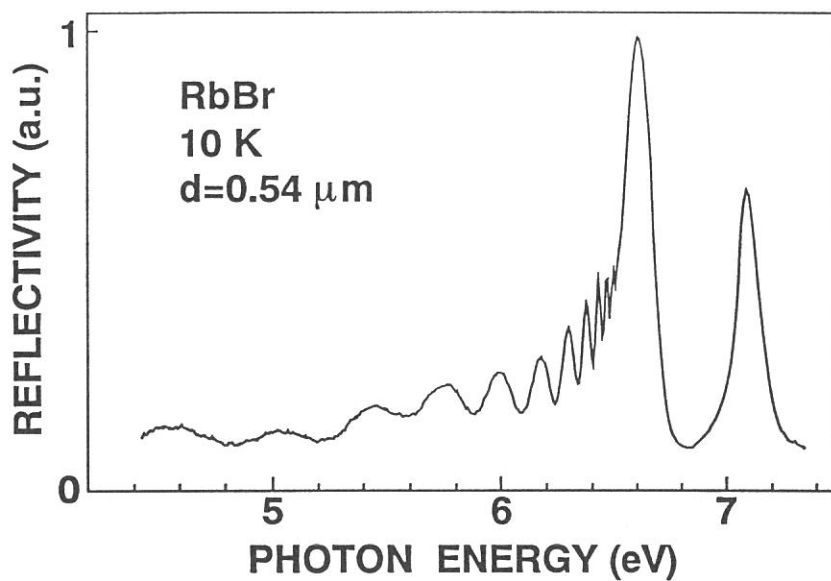


Fig. 1. Reflection spectrum of a thin RbBr crystal with  $d = 0.54 \mu\text{m}$  thickness measured at 10 K.

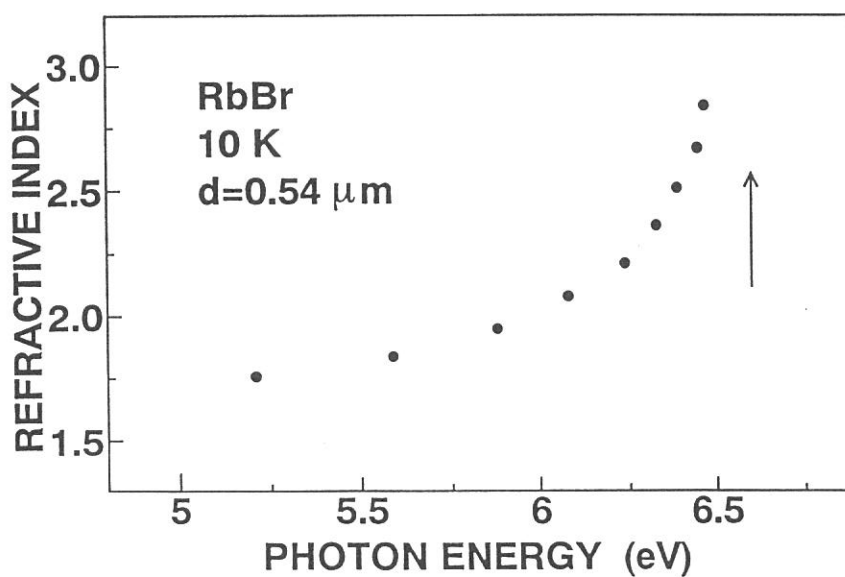


Fig. 2. Refractive index dispersion of RbBr at 10 K. The arrow indicates the peak energy of the first exciton band in the reflection spectra.



# VUV reflection spectra of LiF doped fluoroaluminate glasses

Naoyuki Kitamura, Kohei Fukumi, Kohei Kadono and Hiroshi Yamashita

Osaka National Research Institute, AIST, 1-8-31 Midorigaoka, Ikeda, Osaka 563, Japan

Fluoroaluminate glass, which contains aluminum fluoride as the only glass network former, have been studied from the view points of the glass formation<sup>1-3</sup>, glass structure<sup>4-6</sup>, optical<sup>7,8</sup> and chemical<sup>9</sup> properties, and so on. The glass consisting of aluminum fluoride and alkaline earth fluorides has excellent ultraviolet (UV) transmitting property with a cutoff wavelength at around 170 nm.<sup>8</sup> Therefore, it is of interest for application to optical components or laser matrices in UV to vacuum UV region as well as silica glass. Lithium fluoride is a candidate for improving transmittance because its cutoff energy is highest among all fluorides. In this report, we shall deal with the transmission and reflection properties of  $\text{BaF}_2\text{-CaF}_2\text{-AlF}_3$  glass system in the vacuum UV region. Anomalous band shift found in these spectra by doping lithium fluoride has been discussed.

An  $18\text{BaF}_2\cdot 37\text{CaF}_2\cdot 45\text{AlF}_3$  (BCA) glass, and 5 and 10 mol% LiF doped BCA glasses were used in this study. Transmittance and reflectivity in the vacuum UV region were measured at the beam line BL7B. The measurements were performed at 300 K and 105 K in the 6-8 eV (transmittance) and 8-12 eV (reflectivity) region. An incident angle on the reflectivity measurement was about  $10^\circ$ . A lithium fluoride single crystal was used for the relative calibration of photon energy.

Absorption coefficient at 300 and 105 K for non-doped  $18\text{BaF}_2\cdot 37\text{CaF}_2\cdot 45\text{AlF}_3$  (BCA) glass is shown in fig. 1 by thick and thin solid lines, respectively. A weak broad band is observed at around 6.8 eV in this glass. Absorption edge shifts toward higher energy side by about 0.1 eV under cooling from 300 to 105 K. Absorption coefficient at 300 K for LiF doped BCA glasses are also shown in fig. 1. The absorption edge shifts by about 0.2 and 0.4 eV toward high energy side with 5 and 10 mol% doping of lithium fluoride, respectively. According to additivity of physical property a 0.02 eV shift is expected with 10 mol% LiF doping at most, even if absorption coefficient of the dopant (LiF) is assumed to be zero. Therefore, this anomalous shift induced by the LiF additive suggests that the electronic state of the glass is

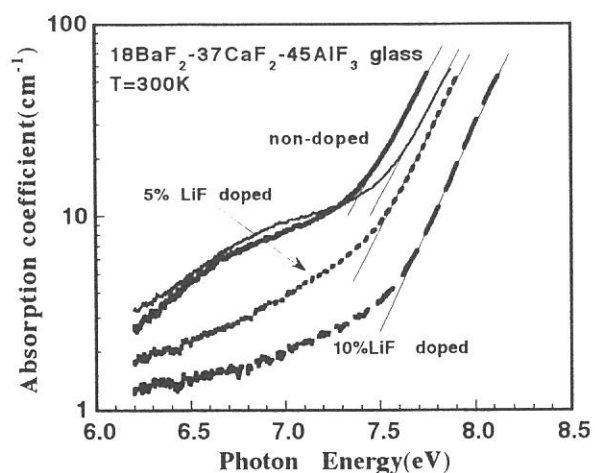


Fig. 1 Absorption spectra of LiF doped  $18\text{BaF}_2\cdot 37\text{CaF}_2\cdot 45\text{AlF}_3$  glasses at 300K. Thin solid line shows a spectrum for the non-doped glass at 105K.

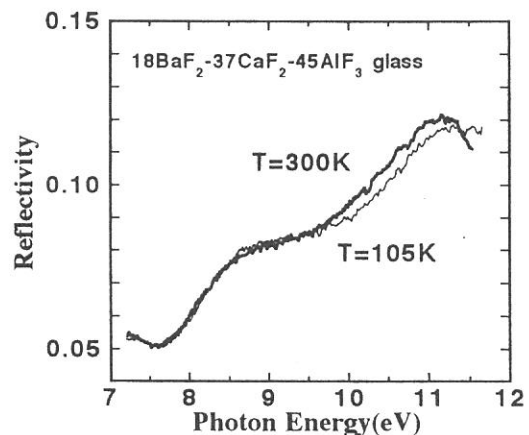


Fig. 2 Temperature dependence of reflectivity for  $18\text{BaF}_2\cdot 37\text{CaF}_2\cdot 45\text{AlF}_3$  glass.

modified by the LiF dopant. The weak band at around 6.8 eV is not clear yet.

Remarkable decrease in absorption coefficient at lower energy side and anomalous shift of the absorption edge mean a modification of the electronic state induced by LiF doping. Spectral changes related to this modification should be also observed in a reflection spectrum at higher energy region because it should give information of the electronic state for the glass. Fig. 2 shows reflectivity at 300 K (thick line) and 105 K (thin line) for the non-doped BCA glass. A strong band at around 11.2 eV and a weak shoulder at around 8.9 eV are found in the spectrum. Peak position of the strong band shifts toward higher energy side by 0.2 eV under cooling from 300 to 105 K, while that of the weak band at 8.9 eV does not show remarkable shift. Therefore the shift of the strong band is a dominant origin for the shift of the absorption edge under cooling as shown in fig. 1. The discrepancy in the magnitude of the shifts between the absorption edge and the 11.2 eV band will be due to that the steady band at 8.9 eV against cooling contributes to the absorption edge. Reflectivity at 300 K are shown in fig. 3 for the 5 and 10 mol% LiF doped BCA glasses. The strong bands of 5 and 10 mol% doped glasses have peaks at higher energy side by about 0.3 and 0.5 eV, respectively, than that of the non-doped glass. Since these values of peak positions are fairly in agreement with the shift of absorption edge induced by the LiF doping, the assumption of the origin for the shift is supported. The strong bands also shift toward higher energy side with cooling from 300 to 105 K. The weak band at 8.9 eV may not be of intrinsic because intensity of this band is less reproducible among the samples of same composition.

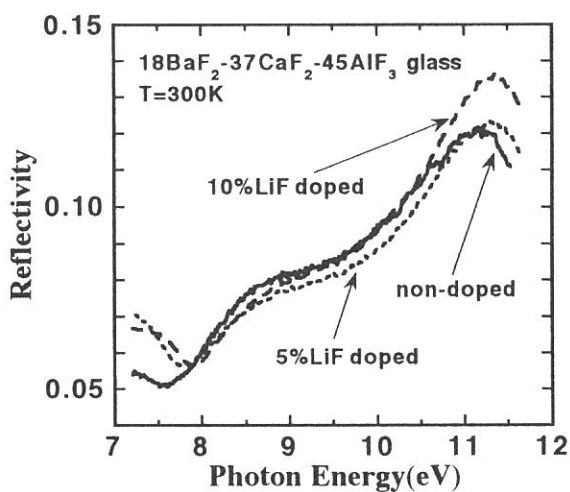


Fig. 3 Reflection spectra of LiF doped  $18\text{BaF}_2\text{-}37\text{CaF}_2\text{-}45\text{AlF}_3$  glasses at 300K.

## References

- <sup>1</sup>M. Imaoka, *Yogyo-Kyokai-shi*, **62**, 24 (1954).
- <sup>2</sup>J. J. Videau, J. Portier and B. Piriou, *Rev. Chim. Min.*, **16**, 393 (1979).
- <sup>3</sup>I. Yasui, H. Hagihara and Y. Arai, Extended abstracts for the 5th international symposium on halide glasses, Shizuoka, Japan, 1988, p.497.
- <sup>4</sup>Y. Kawamoto and A. Kono, *J. Non-Cryst. Solids*, **85**, 335 (1986).
- <sup>5</sup>D. Ehrt, C. Erdmann and W. Vogel, *Z. Chem.*, **23**, 37 (1983).
- <sup>6</sup>D. Ehrt and W. Vogel, *Z. Chem.*, **23**, 111 (1983).
- <sup>7</sup>D. Ehrt, M. Krauß, C. Erdmann and W. Vogel, *Z. Chem.*, **22**, 315 (1982).
- <sup>8</sup>N. Kitamura, J. Hayakawa and H. Yamashita, *J. Non-Cryst. Solids*, **126**, 155 (1990).
- <sup>9</sup>A. B. Seddon, "Fluoride Glasses", ed. by A. E. Comyns, John Wiley & Sons, 1989, p.158.

## Crystallization Processes of Amorphous $\text{CdI}_2$ Thin Films

Kazutoshi FUKUI, Ken-ichi NIIMI, Takanobu YAMADA and Hideyuki NAKAGAWA  
Dept.Elec.Elec.Engi., Fac.Engi., Fukui Univ., FUKUI 910

We have been studying the crystallization processes of the amorphous  $\text{CdI}_2$  thin films by using both optical absorption and luminescence measurements. Cd halide ( $\text{CdI}_2$ ,  $\text{CdBr}_2$ ,  $\text{CdCl}_2$ ) single crystals, layered ionic crystals which belong to the hexagonal  $\text{CdI}_2$  structure and the rhombohedral  $\text{CdCl}_2$  structure ( $\text{CdBr}_2$ ,  $\text{CdCl}_2$ ), have wide band gap and are insulators. Cd layer is sandwiched by the halogen (X) layers and an unit layer consists of these X-Cd-X layers. The bonding force between Cd and X layers is ionic. However, the bonding force between unit layers is van der Waals force. This fact is useful for application to fabricating multilayer (wide band gap superlattice), since the condition of the van der Waals epitaxy technique is satisfied. That is one of our main motivation to investigate the properties of  $\text{CdI}_2$  thin films. On the other hand, it is known that  $\text{CdI}_2$  becomes amorphous when it is evaporated onto substrates held at liquid nitrogen temperature (LNT). The investigation of crystallization processes of amorphous  $\text{CdI}_2$  by using optical method are interesting not only for application but also for basic science, because the structural phases reflect to optical spectra. The purposes of the present study are i) to examine good evaporation condition (ultra high vacuum, pre-annealing of substrate), ii) to perform detailed optical absorption measurements, especially for very thin films by using the brightness and the stability of SR.

$\text{CdI}_2$  thin films were evaporated onto both  $\text{SiO}_2$  plate and  $\text{CdBr}_2$  flake-like single crystal substrates by Pt basket evaporators. The substrates were annealed about upto 420 K (6 hours) and 520 K (2 hours) before evaporations and kept at LNT during evaporations. Vacuum pressure was in the range of  $10^{-9}$  Torr. The absorption spectrum of *as-deposited* film was measured at LNT just after evaporation. Then, *as-deposited* film was annealed *in situ* to 140 K and kept at 140 K. After 10 minutes, this film was again cooled to LNT and the absorption spectrum of the 140 K annealed film was measured. The annealing temperatures were increased step by step from 140 K to 400 K (step was 20 K). The 10 minutes annealing at each annealing temperature was applied to the same film again and again. All absorption spectra were measured at LNT.

Figure 1 shows the annealing effects on the absorption spectra of the  $\text{CdI}_2$  film evaporated onto the  $\text{CdBr}_2$  substrate. The thickness is estimated at less than 50 Å, so that the S/N ratio is not so well. The parameters in the figure indicate the annealing temperatures. At 77 K, the peak at 3.8 eV can be found, which is the typical peak in the amorphous phase. Since energy range around 3.8 eV corresponds to the forbidden excitonic transition region in the crystalline phase, the 3.8 eV peak in the amorphous phase becomes allowed due to the structural disordering. Annealing effects are not clear till the annealing temperature increases to 180 K. Above 180 K, the 3.8 eV peak gradually moves to 3.9 eV and becomes sharp. In the previous work, we found that this sharp peak corresponds to the so-called  $X_1$  excitonic peak in the crystalline phase. The

$X_1$  peak is observed only when the electric vector of light is perpendicular to the crystallographic  $c$ -axis<sup>1)</sup>, in other words, the electric vector is parallel to the layers. Therefore, sharp  $X_1$  peak indicates that the  $CdI_2$  layers are almost parallel to the substrate plane, so that there is two dimensional crystalline phase at 280 K  $\sim$  340 K. At 360 K, the spectrum is drastically changed and quite similar to that of the bulk single  $CdI_2$  crystal,

Annealing effects shown in Fig. 1 is quite same as the results of our previous work, which were carried out under medium vacuum (about  $10^{-5}$  Torr) with substrates not annealed before evaporation. The crystallization process of  $CdI_2$  on  $CdBr_2$  has well reproduction without thickness dependence, and the quality of thin films in the crystalline phase are good. It is interesting that the good quality  $CdI_2$  thin films are able to be fabricated even though under the not-so-good evaporation conditions.

The annealing effects on the absorption spectra of  $CdI_2$  thin film on  $SiO_2$  substrate in present work are almost the same as those shown in Fig. 1. These results are quite different from our previous work. In the previous work, the drastic blue shifts ( $> 0.5$  eV) of the lowest excitonic absorption edge, which is due to the quantum size effect by the formation of the  $CdI_2$  micro-crystals in the amorphous  $CdI_2$ , was observed. This difference probably is caused by the difference of the evaporation conditions. Further study is now on progress.

In conclusion, the annealing effects on the absorption spectra of  $CdI_2$  thin films on  $SiO_2$  and  $CdBr_2$  were observed and the results for films on  $CdBr_2$  are well understood, while these on  $SiO_2$  are not clear at present.

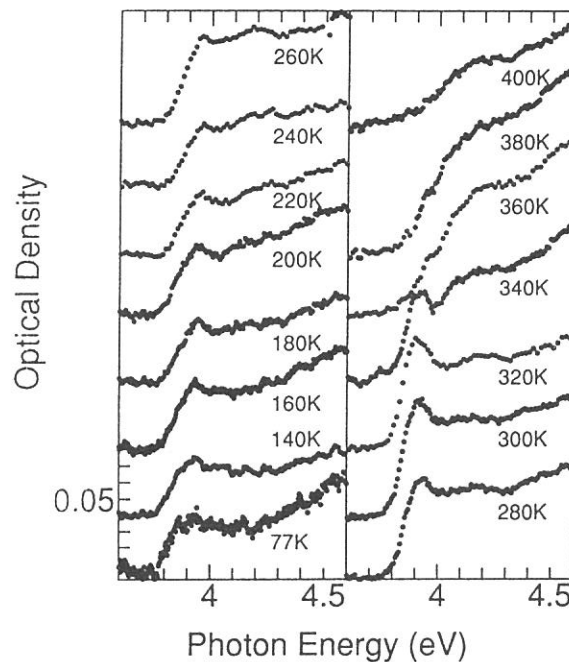


Fig.1

## Reference

- 1) M.Fujita, H.Nakagawa, K.Fukui et al. : J. Phys. Soc. Jpn 59 (1990) 338-47.

**Time-resolved Tryptophan Fluorescence of  
Glycerinated Muscle Fibers**

Mieko TANIGUCHI and Isao YODA

Department of Physics, Faculty of Science,  
Nagoya University, Nagoya 464-01, Japan

Effects of magnesium and ATP on glycerinated crab muscle fibers were investigated by time-resolved fluorescence microspectroscopy. The fluorescence lifetimes were measured at the single-bunch modes of UVSOR. The pulsed light source from the storage ring of synchrotron radiation ( 750 MeV, 60 mA ) was passed through a 1 m Seya-Namioka monochromator and collimated a silica lens to a spot in a fused quartz cell. The emission was collected by a quartz lens and passed through a monochromator or a filter. Fluorescence lifetimes were measured by the time-correlated single photon counting system under the single bunch operation. A bundle of glycerinated muscle was used. The lifetimes of the fibers in rigor solutions have three components (  $\tau_1 = 0.1$  ns,  $\tau_2 = 1.7$  ns and  $\tau_3 = 4.9$  ns ), as shown in Fig.1. The lifetimes of the fibers in relax solutions were almost same as those of rigor muscles. These values did not change with magnesium ion concentrations. The ratios of the fractional intensities of rigor and relax muscles were constant and changed with various magnesium concentrations, respectively. These changes were coupled with spectral changes ( Ref.1 ).

## References

- 1) M. Taniguchi, I. Yoda and N. Watanabe ; UVSOR Activity Report 1993, p161-162 (1994).
- 2) M. Taniguchi, I. Yoda and N. Watanabe; Int. Conf. on Electrooptp 94, Germany (1994).

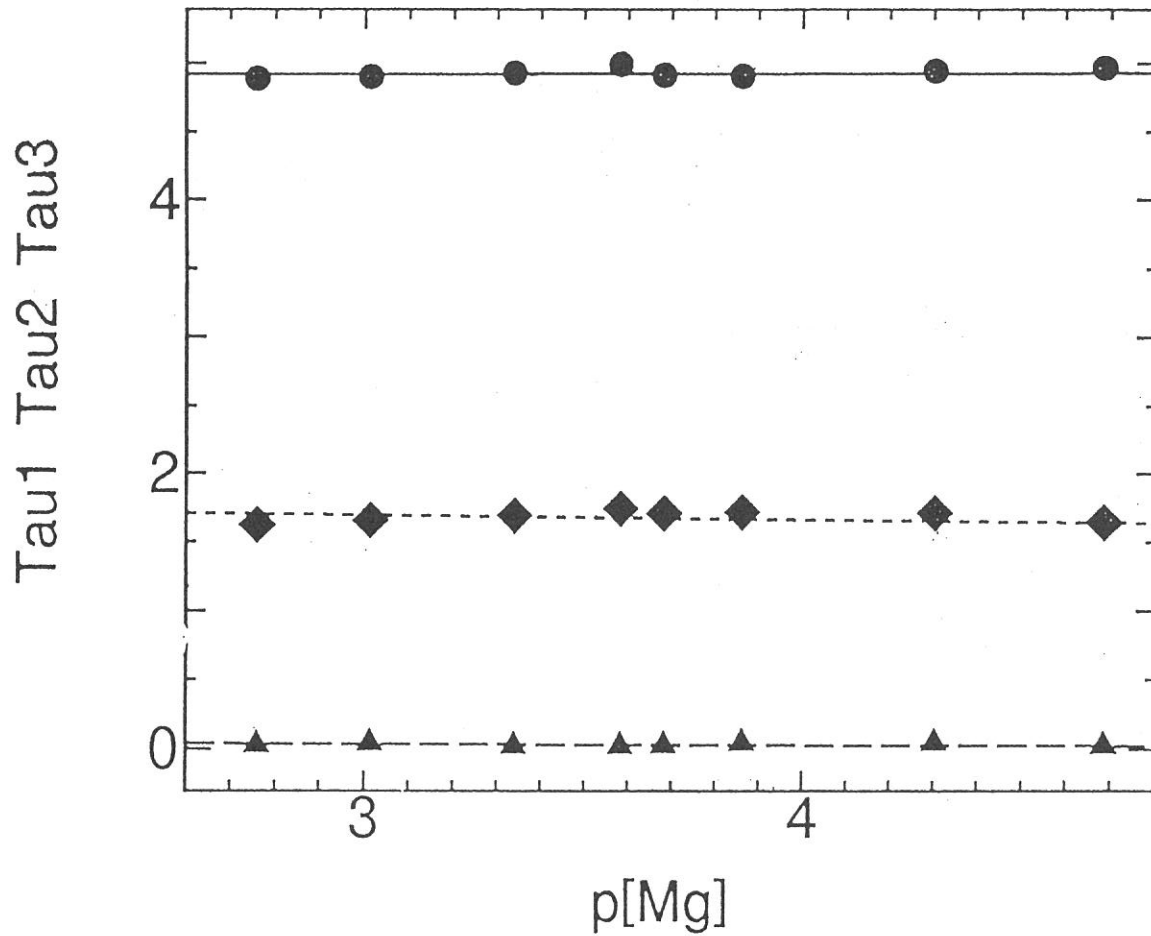


Fig. 1 The fluorescence lifetimes of rigor muscle fibers as a function of magnesium ion concentrations. Excitation at 280 nm. Emission at 350 nm.

**SOR Patterning of Plasma Polymerized  
HMDS Resist with 0.2 Micron Mask**  
Shinzo Morita, Georgy K.Vinogradov, Yuri Koval,  
Chunlin Shao, Ryoichi Inanami and Kenji Senda  
Nagoya university, CCRAST  
Nagoya 464-01, JAPAN

Recently, several successful works have been done on a synthesis of deep UV sensitive silicon containing dry resists[1,2]. The resists were patterned under oxygen ambient with 0.3  $\mu\text{m}$  line & space features. Here we tried to pattern silicon containing plasma polymerized resist with a 0.2  $\mu\text{m}$  mask by means of SOR lithography.

Hexamethyldisilazane (HMDS) was used as silicon containing monomer. Resist film was deposited on n-type silicon wafers ( $\langle 100 \rangle$ , Sb doped, conductivity 0.01–0.02  $\Omega\cdot\text{cm}$ ), by pulse discharge plasma polymerization in a reactor shown in Fig.1. Film sickness during the deposition was monitored by a quartz crystal microbalance. The deposition conditions were — discharge frequency 13.56 MHz, discharge power 5 W, monomer gas pressure 0.15 Torr, pulse duration 1 sec, ON/OFF ratio 1/1, and substrate temperature around 0°C. And the deposition was stopped when the monitoring thickness was 0.15  $\mu\text{m}$ .

The 0.2  $\mu\text{m}$  mask pattern was fabricated by gold evaporation onto 0.5  $\mu\text{m}$  tall vertical walls of polyimide, which is known as a convenient method of X-ray mask fabrication.

HMDS resist has been irradiated with an SOR beam through 15  $\mu\text{m}$  beryllium foil in a reaction chamber, as shown in Fig.2. The chamber was connected to the synchrotron ring through the diaphragm supplied with a differential pumping system providing a possibility to irradiate samples at a relatively high oxygen gas pressure. The resist film was exposed to SOR beam, irradiated 180 mA·min (10 J) in the presence of oxygen at a pressure of 0.2 Torr through the mask.



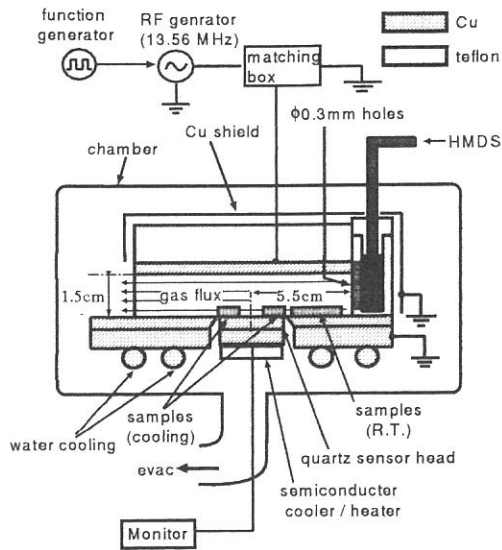


**Fig.1** The plasma polymerization reactor.

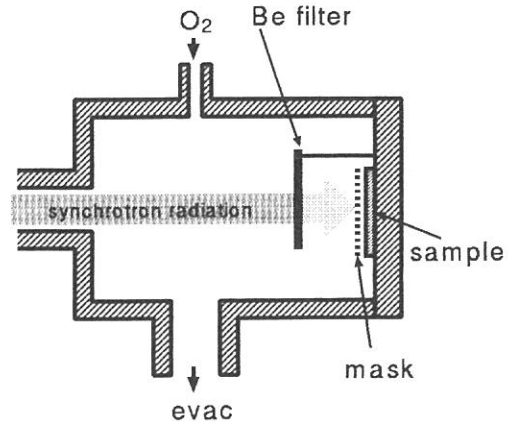


**Fig.2** SOR exposure chamber and sample.

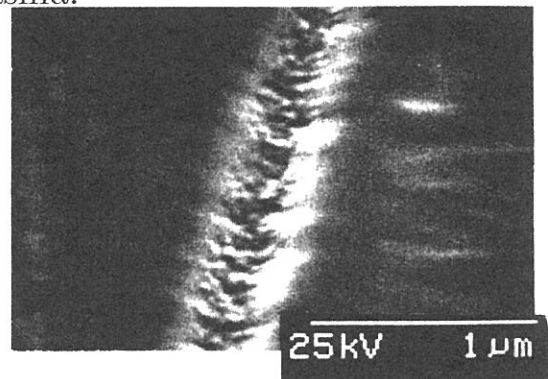
SOR exposed resists were developed by means of  $\text{Cl}_2$  RF plasma etching at 0.3 Torr for 2 minutes. Because the exposed area is undergone photo-oxidative crosslinking to stable Si-O-Si crosslinked network, only Si-Si bond part was etched off by the plasma.

Fig.3 shows a SEM photograph of the developed resist on silicon wafer, which has  $0.2 \mu\text{m}$  width lines. We succeeded transferring the  $0.2 \mu\text{m}$  gold patterns to the plasma polymerized silicon containing resist, by the SOR lithography.

A finer patterning below  $0.1 \mu\text{m}$  features by the SOR lithography will be aimed to be realized in a future experiment.

## REFERENCES

- [1] T.W.Weidman and A.M.Joshi: SPIE Vol.1925 (1993) 145
- [2] A.M.Joshi, T.W.Weidman, A.D.Johnson, J.F.Miner and D.E.Ibbotson: SPIE Vol.1925 (1993) 709



**Fig.3** SEM photograph of the developed resist surface by  $\text{Cl}_2$  RF plasma etching.

SiC nucleation on Si substrate for diamond formation  
using synchrotron radiation enhanced chemical vapor deposition  
employing methanol and H radical

(BL-8A)

Masanobu Ikeda, Masaru Hori, Toshio Goto, \*Muneto Inayoshi, \*Mineo Hiramatsu,  
\*Masahito Nawata and \*\*Atsunari Hiraya

Department of Quantum Engineering, School of Engineering, Nagoya University,  
Chikusa-ku, Nagoya 464-01, Japan

\*Department of Electrical and Electronic Engineering, Faculty of Science and Technology,  
Meijo University, Shiogamaguchi, Tempaku-ku 1-501, Nagoya 468

\* \*\*Institute for Molecular Science, Myodaiji, Okazaki 444

Diamond has the excellent properties such as high thermal conductivity, high electrical insulation and optical transparency. These properties are expected to be applied for the heat sink of semiconductor, electrical insulator and so on. The technology of diamond thin film formation has been developed actively using plasma enhanced chemical vapor deposition (P-CVD) and a hot filament method.<sup>1,2)</sup>

Synchrotron radiation (SR) is the unique white light source in the wavelength region from vacuum ultra violet to soft X-ray and so corresponds to wavelength region to dissociate the reactive gases such as hydrocarbon and hydrogen gases. It is expected that fine pattern deposition of thin film can be carried out using SR beam because of the high spatial resolution of this beam.

In this study, we developed a unique SR CVD system shown in Fig. 1 and tried to synthesize the diamond thin films on Si substrate. This system consisted of three parts; a hydrogen (H) radical source generated by the microwave H<sub>2</sub> discharge, a SR beam for the excitation of source gases in the gas phase as well as on surface of the substrate and a CO<sub>2</sub> laser for the substrate heating. Methane (CH<sub>4</sub>) diluted by hydrogen molecule (H<sub>2</sub>) and methanol (CH<sub>3</sub>OH) diluted by H<sub>2</sub> were used for the source gases,<sup>3,4)</sup> because these gases have been generally used for the diamond formation using P-CVD and also the absorption bands of CH<sub>4</sub> and CH<sub>3</sub>OH correspond to the spectrum of SR.<sup>5)</sup>

The experiments were carried out at the beam line 8 A (BL-8A) of UVSOR. The main reaction chamber was evacuated to  $1.0 \times 10^{-4}$  Pa using a turbo-molecular pump and a rotary pump. The Si substrate was scratched by the diamond powder with the size of 30-40  $\mu$ m in the ultrasonic vibrator for 1 hour in order to enhance the diamond nucleation density.<sup>1)</sup> During the irradiation of the SR beam to the substrate, the partial pressure of CH<sub>4</sub> or CH<sub>3</sub>OH was maintained at 21.3 Pa and the partial pressure of H<sub>2</sub> was 5.3 Pa, respectively in the main reaction chamber, the substrate temperature was maintained at 800 °C, the dosage of SR to the substrate was  $1.0 \times 10^5$  mA.min and supplied microwave power was 100 W.

It was observed that the film was deposited only at the area of SR irradiation on the substrate, when we only employed the CH<sub>3</sub>OH and H radical. Figure 2 shows the image of the atomic force microscope (AFM) of the deposited film on the substrate. The grain size of the film was estimated to be about 20 nm.

The deposited films were also characterized by Fourier transform infrared (FT-IR) absorption spectroscopy. Figure 3 shows the FT-IR spectra of the deposited film. The absorption peaks near 1000-1100 cm<sup>-1</sup>, 1070 cm<sup>-1</sup> and 800cm<sup>-1</sup> were attributed to the Si-O, C=C and Si-C bonds, respectively. From the results of FT-IR spectra, the deposited film was estimated to be SiC

containing oxygen and carbon. Some experiments were carried out without irradiation of SR beam and/or microwave H<sub>2</sub> discharge. In both cases, the FT-IR absorption peaks attributed to SiC as shown in Fig. 3 were not observed. From these results, we consider that H radical is important for the nucleation of SiC on Si substrate using SR employing CH<sub>3</sub>OH and H<sub>2</sub> gases.

References

- 1) M. Kamo, Y. Sato, S. Matsumoto and N. Setaka: *J. Cryst. Growth* 62 (1983) 642
- 2) I. Watanabe and K. Sugata: *Jpn. J. Appl. Phys.* 27 (1988) 1397
- 3) Y. Mitsuda, Y. Kojima, T. Yoshida and K. Akashi: *J. Mater. Sci.* 22 (1987) 1557
- 4) T. Yara, M. Yuasa, J. S. Ma, J. Suzuki, S. Okada and A. Hiraki: *Appl. Surf. Sci.* 60/61 (1992) 308
- 5) J. Berkowitz, *Photoabsorption Photoionization and Photoelectron Spectroscopy*. Academic Press, 1979
- 6) S.I. Shah and M.M. Waite, *Appl. Phys. Lett.* 61, 3113 (1992)

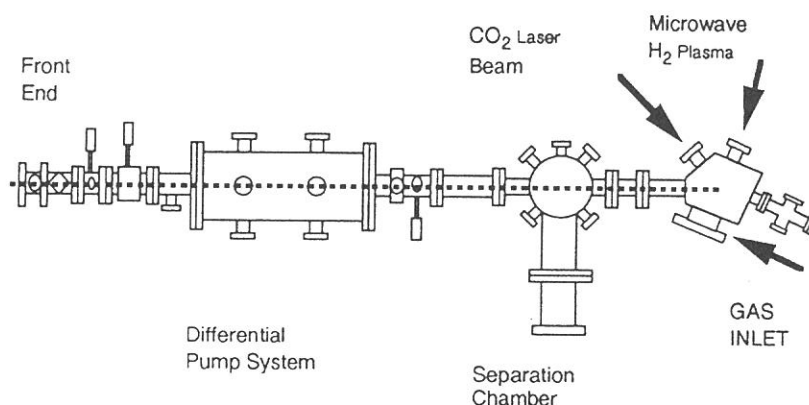


Figure 1 Schematic diagram of SR CVD system.

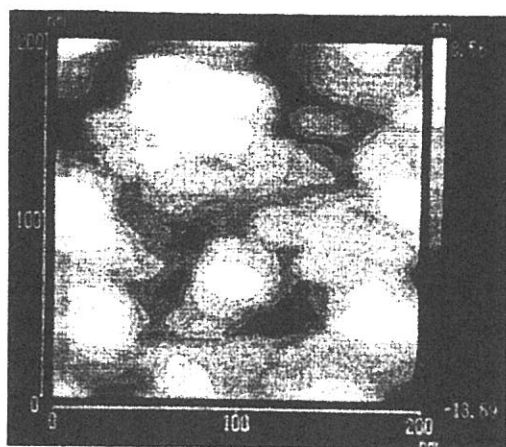


Figure 2 Image of AFM of the deposited film at the pressure of CH<sub>3</sub>OH / H<sub>2</sub> = 21.3 / 5.3 Pa, the substrate temperature of 800 °C, dosage of SR of 1 × 10<sup>5</sup> and the microwave power of 100 W.

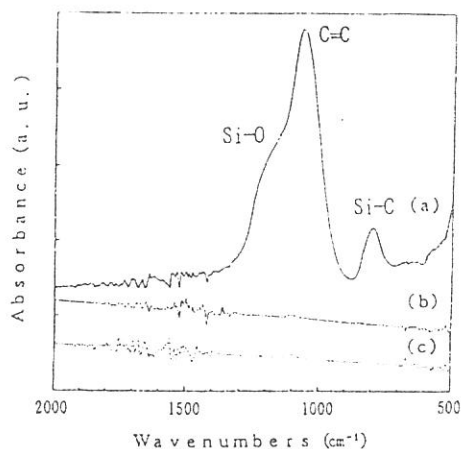


Figure 3 FT-IR absorption spectra of deposited film at the pressure of CH<sub>3</sub>OH / H<sub>2</sub> = 21.3 / 5.3 Pa, the substrate temperature of 800 °C, (a) dosage of SR of 1 × 10<sup>5</sup>, and the microwave power of 100 W, (b) without microwave power and (c) without irradiation of SR beam.

## Soft X-Ray Microscope with Zone Plate at UVSOR

N. Watanabe<sup>1)</sup>, S. Aoki<sup>1)</sup>, Y. Shimanuki<sup>2)</sup>, K. Kawasaki<sup>2)</sup>, M. Taniguchi<sup>3)</sup>, E. Anderson<sup>4)</sup>, D. Attwood<sup>4)</sup>, D. Kern<sup>5)</sup>, S. Shimizu<sup>6)</sup>, H. Nagata<sup>6)</sup>, Y. Horikawa<sup>7)</sup>, S. Mochimaru<sup>7)</sup> and H. Kihara<sup>8)</sup>

1) Institute of Applied Physics, Tsukuba University, Tsukuba 305

2) Department of Oral Anatomy, Tsurumi University, Yokohama 230

3) Department of Physics, Nagoya University, Nagoya 464

4) Lawrence Berkeley Laboratory, Berkeley, CA

5) IBM Research Center Yorktown Heights, NY

6) Nikon Corp., Nishi-ooi, Shinagawa-ku, Tokyo 140

7) Olympus Optical Co. Ltd., Hachioji-shi, Tokyo 192

8) Physics Laboratory, Kansai Medical University, Hirakata 573

An imaging microscope with zone plates was constructed at UVSOR BL8A. The microscope is basically the same with the last type. Fig.1 shows a schematic of the optical system, and Table 1 shows the characteristics of the condenser zone plate (CZP) and the objective zone plate (OZP) used. The soft x-ray from the storage ring was monochromatized and condensed by CZP at a properly placed pinhole ( $\approx 20\mu\text{m}$ ). A specimen downstream from the pinhole was imaged by OZP on a microchannel plate (MCP) monitored by a SIT camera or a photographic film (Kodak T-max 400).

The resolution test was performed at 3.2nm using a zone plate with the outermost zone width of 45nm as a specimen. Fig.2(a) shows an image of the zone plate taken by MCP as a detector, and Fig.2(b) by the film. Almost the outermost zone (45nm width) could be resolved in Fig.2(b).

An environmental chamber (wet cell) using SiN windows (Fig.3) as vacuum seals was made and wet biological specimens (rabbit myofibrils, lettuce and soybean protoplasts, *Deinococcus radiodurans* strain, tubulin of COS cell stained by immunogold labeling) were observed at 2.4nm. Fig.4 shows a lettuce protoplasts image.

In the present microscope, the numerical aperture of CZP was much smaller than that of the OZP. To adjust both the numerical apertures, an ellipsoidal condenser mirror system was made (Fig.5), and imaging test was performed at 3.2nm. Fig.6 shows an image of Cu mesh (#2000).

### Acknowledgements

The authors are grateful for the help and encouragements from A. Prof. M. Kamada, Mr. K. Sakai and other staffs of the Institute for Molecular Science.

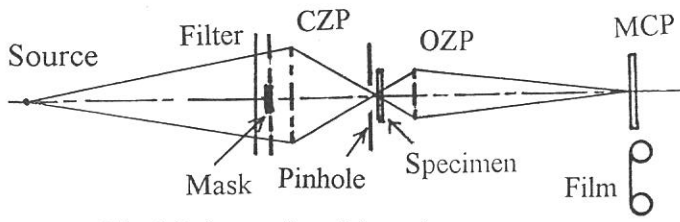
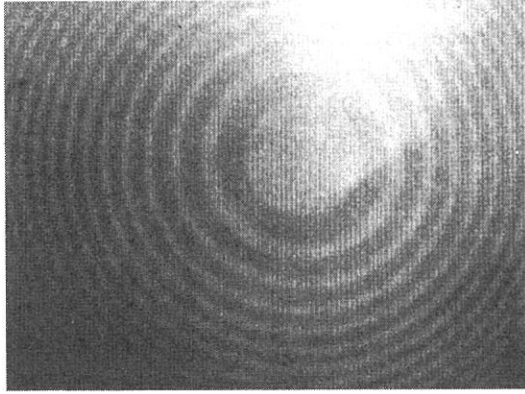


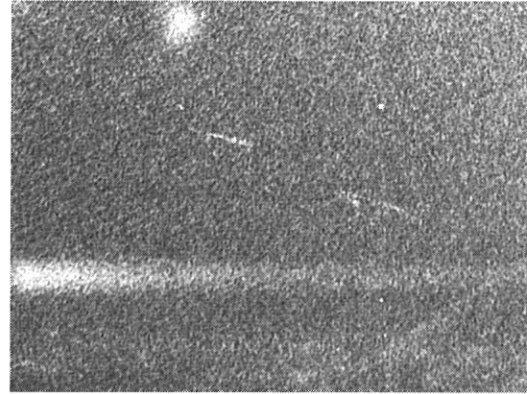
Fig.1 Schematic of the microscope

Table 1 Characteristics of zone plates

	CZP	OZP
Diameter( $\mu\text{m}$ )	4300	50
Outermost zone width(nm)	250	45
Zone material	Au	Ni



(a)  $2\mu\text{m}$



(b)  $1\mu\text{m}$

Fig.2 Zone plate image at 3.2nm. (a)MCP and SIT camera, accumulation:8s. (b)Film(T-max 400) used as a detector, exposure:2min.

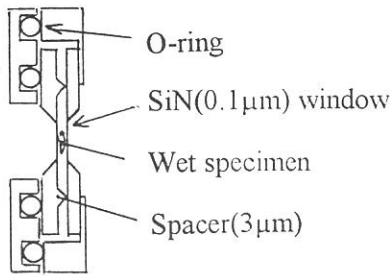


Fig.3 Schematic of the wet cell

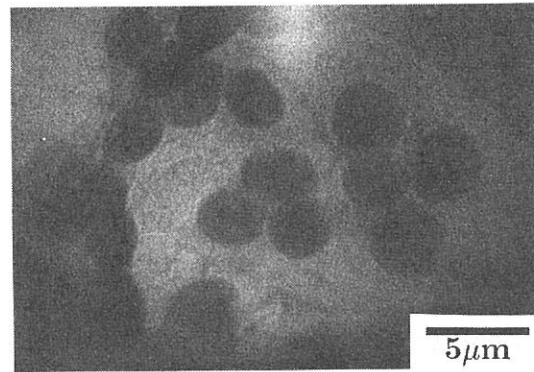


Fig.4 Lettuce protoplast image at 2.4nm. Exposure:5min. Film:T-max 400.

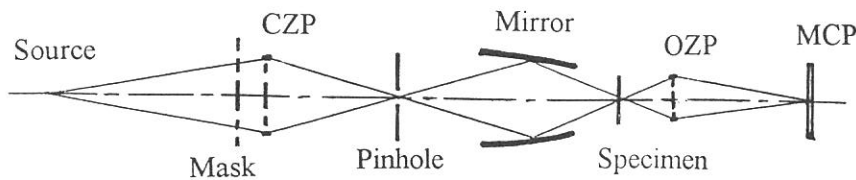


Fig.5 Ellipsoidal condenser mirror system

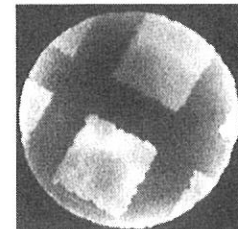


Fig.6 #2000 mesh image. Exposure:16s.

## Accumulated photon echoes in UV by using dispersion compensation

Hiroshi ITOH<sup>1</sup>, Shunsuke NAKANISHI<sup>1</sup>, Masaya KAWASE<sup>2</sup>,  
Hitoshi FUKUDA<sup>3</sup>, Noriaki TSURUMACHI<sup>3</sup>, Hideyuki INOUE<sup>3</sup>,  
Hiroki NAKATSUKA<sup>3</sup>, and Masao KAMADA<sup>4</sup>

<sup>1</sup>*Department of Physics, Kagawa University, Takamatsu 760*

<sup>2</sup>*Department of Chemistry, Kagawa University, Takamatsu 760*

<sup>3</sup>*Institute of Applied Physics, University of Tsukuba, Tsukuba 305*

<sup>4</sup>*UVSOR, Institute for Molecular Science, Okazaki 444*

We have applied synchrotron radiation (SR) to investigate accumulated photon echo signals of an organic molecule (Aniline) doped in polyvinyl alcohol (PVA) in ultraviolet (UV) wavelength region. There are a lot of difficulties to conquer for getting the signals in UV region because of the very short phase relaxation. One of the most serious effects preventing the detection is dispersion effect of optical elements. In this time, a phase relaxation time of about 200 fs was observed by compensating the dispersion of the plate beam splitter (PBS).

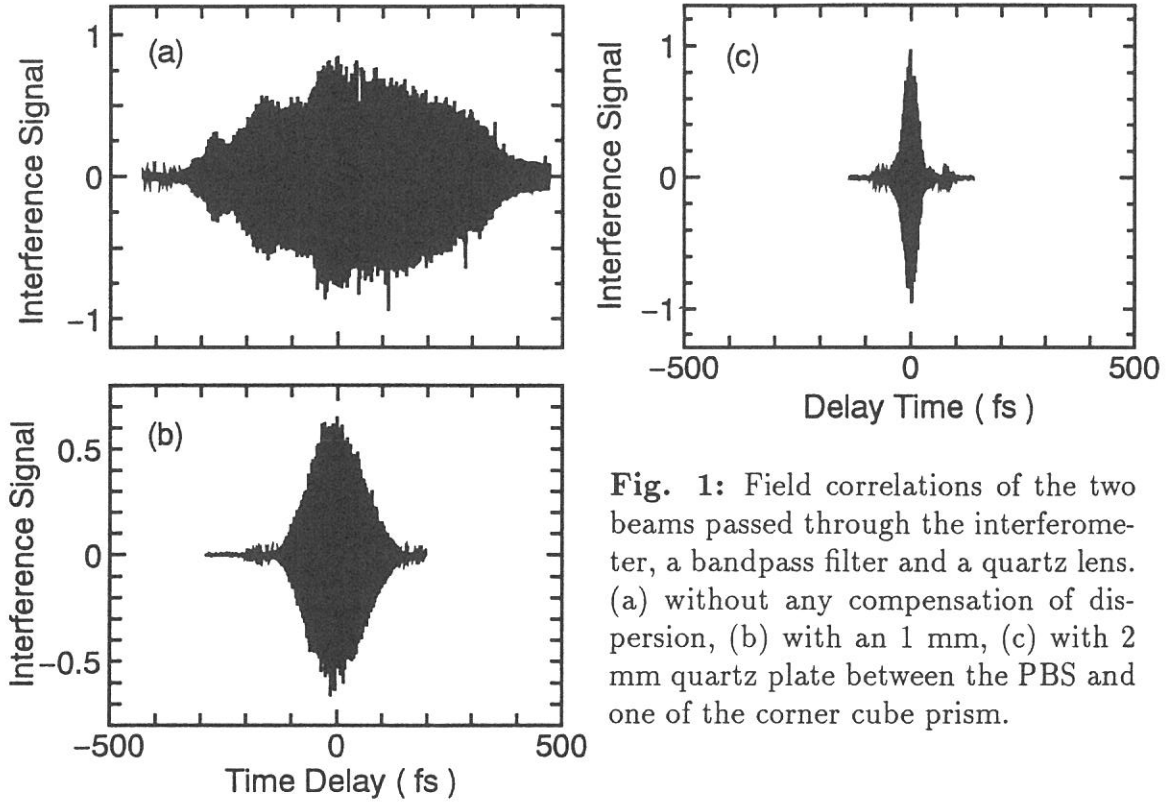
The experiment was performed at the BL-8A. The SR beam was filtered by the bandpass filter with the center wavelength of 310 nm and the bandwidth of about 10.5 nm. The SR beam was split into two beams, the pump and probe beam, by the PBS in the Michelson interferometer, and the probe beam was temporally delayed relative to the pump beam. The pump and probe beam were aligned to collinearly overlap. The pump beam was phase modulated with a piezoelectric transducer at  $f=5.8$  kHz. The pump and the probe beam were focused by 60 mm focal length quartz lens onto the sample, aniline doped in PVA at 4.3 K. The transmitted beam was detected by a PIN photodiode and fed into a lock-in amplifier.

The field correlation trace of the two excitation beams was recorded to determine the time resolution of the echo experiment. Since one of the two beams divided by the PBS passes three times through the plate PBS in the interferometer while another one passes only one time, the dispersion of the PBS in UV affects the field correlation. Figure 1 shows the observed interferograms of the SR passed through the bandpass filter and the quartz lens mentioned before. When any dispersion due to the PBS was not compensated, we obtained the time resolution of 557 fs as shown in Fig. 1(a). By inserting a quartz plate of 1 mm thickness between the PBS and one of the quartz corner cube prism of the interferometer, the temporal width of the correlation was greatly improved to 127 fs as shown in Fig.1(b). With further compensation by another quartz plate of 2 mm thickness instead of the 1 mm thick plate, the time resolution of 35 fs was obtained as shown in Fig.1(c). In this manner, if we use a quartz plate of 2.4 mm thickness, more short time correlation (30 fs) would be obtained by perfectly compensating the dispersion of the PBS.

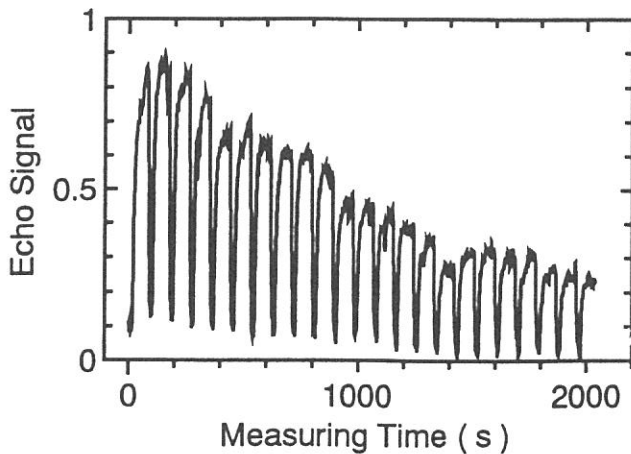


Figure 2 shows an accumulated photon echo decay data obtained in the aniline doped in PVA. In the data acquisition, the signals were accumulated during 70 sec at a fixed delay time, and then the phase grating was erased by slowly changing the delay time until the next sampling delay time by taking 20 sec with the two excitation beams on. The echo signal intensity was taken into a microcomputer every 1 sec. The actual delay time between two beams in Fig. 2 was scanned from 180 to 520 fs and the dephasing time  $T_2$  obtained is 181 fs at 4.3 K.

In conclusion, the SR beam have been shown to apply accumulated photon echoes in UV region. It is successfully shown that the SR has potential to time resolve the echo decay in UV with time resolution of 30 fs.



**Fig. 1:** Field correlations of the two beams passed through the interferometer, a bandpass filter and a quartz lens. (a) without any compensation of dispersion, (b) with an 1 mm, (c) with 2 mm quartz plate between the PBS and one of the corner cube prism.



**Fig. 2:** An accumulated photon echo signal of the Aniline doped in PVA at 4.3 K.



## Performance Test of Constant-Deviation Constant-Length Spherical Grating Monochromator at BL8B1

Atsunari HIRAYA, Eiken NAKAMURA, Jun-ichi Adachi, Masami HASUMOTO,  
Toshio KINOSHITA, Kusuo SAKAI, Eiji ISHIGURO\*, and Makoto WATANABE\*\*

*Institute for Molecular Science, Myodaiji, Okazaki 444*

*\*Department of Applied Physics, Osaka City University, Sumiyoshi-ku, Osaka 558*

*\*\*Research Institute for Scientific Measurements, Tohoku University, Sendai 980*

In order to cover the 30 - 800 eV photon energy range, a constant-deviation constant-length spherical grating monochromator (CDCL-SGM) has been constructed at the bending magnet beamline BL8B1 of the UVSOR<sup>1)</sup>. The monochromator has three laminar type gratings G1(1080 l/mm: R=15m), G2 (540 l/mm: R=15m), and G3(360 l/mm: R=7.5m) that can be interchanged in vacuum.

After the final adjustment of the monochromator, absolute photon flux behind the postfocusing mirror was evaluated for three gratings from drain current of Au-foil, with assuming constant quantum efficiency (photoelectrons / photon) of gold to be 0.073. As shown in Fig. 1, photon flux in the order of  $10^8$  -  $10^9$  photons / sec (at 100 mA) was obtained with 10  $\mu$ m slits in the whole energy range. Figure 2 shows energy resolutions for three gratings calculated by ray-tracing, as well as observed energy resolutions at several photon energies. Observed resolutions were deduced from absorption spectra of gaseous N<sub>2</sub>, Ar, and Kr (Figs. 3 - 5). Observed resolutions for both G1 ( $E/\Delta E \approx 4000$  at 400 eV) and G2 ( $E/\Delta E \approx 3000$  at 245 eV) gratings with 10  $\mu$ m slits are in good agreement with calculated values. On the other hand, observed resolution for G3 grating ( $E/\Delta E \approx 1000$  at 91 eV) is three times

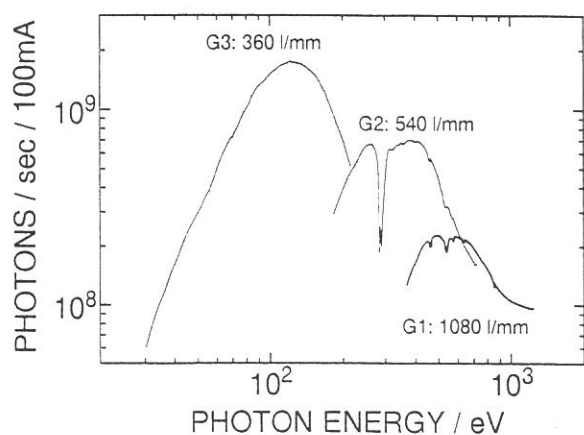


Fig. 1. Throughput spectra (absolute photon flux) of CDCL-SGM for three gratings with 10  $\mu$ m slits and at 100 mA ring current.

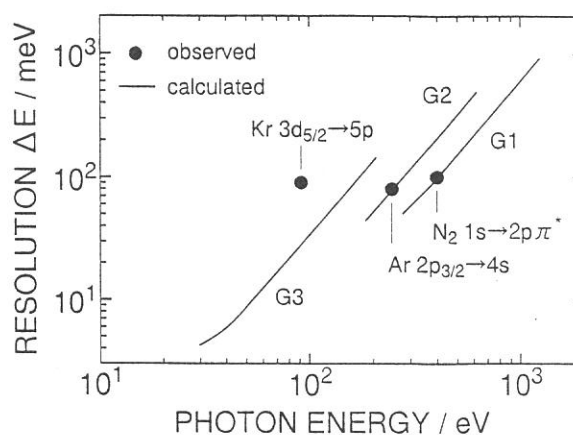


Fig. 2. Energy resolution of CDCL-SGM for three gratings with 10  $\mu$ m slits. Solid lines: calculated values, filled circle: observed values.

wider than the calculated value. This is possibly caused by the misalignment in the constant deviation angle for G3 grating.

An experimental chamber, equipped with a photoelectron detector (total- or threshold-) and a time-of-flight (TOF) ion detector, is connected to the beamline. As a preliminary test for the experimental chamber and the detection system, fragment-ion mass spectrum of  $N_2$  was measured. Figure 6 shows the mass spectrum of  $N_2$  excited at 401 eV ( $1s \rightarrow 2p\pi^*$  resonance) with setting the TOF detection angle perpendicular to the linear polarization axis and with correcting total-electrons. Double peak feature observed for  $N^+$  and  $N^{++}$  around their  $m/e$  values arises from kinetic energy release in the ionic fragmentation of parent  $N_2$ .

## Reference

- 1) A. Hiraya et al., Rev. Sci. Instrum. (in press: Feb. 1995)

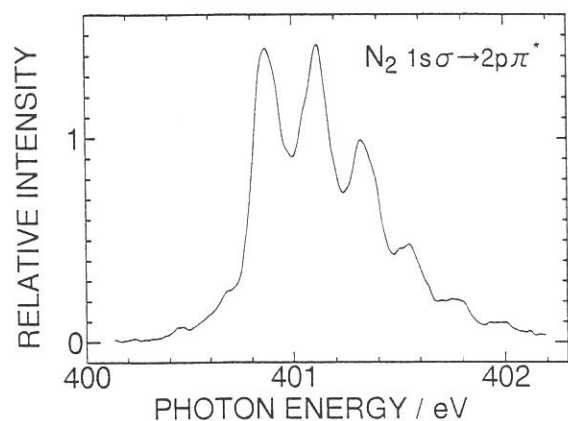


Fig. 3. Nitrogen  $K$ -Absorption spectrum of gaseous  $N_2$  at  $1s \rightarrow 2p\pi^*$  region measured with using G1 grating and  $10\mu\text{m}$  slits.

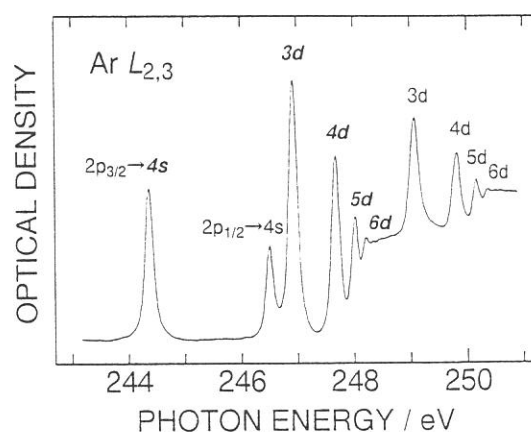


Fig. 4.  $L$ -absorption spectrum of gaseous Ar measured with using G2 grating and  $10\mu\text{m}$  slits.

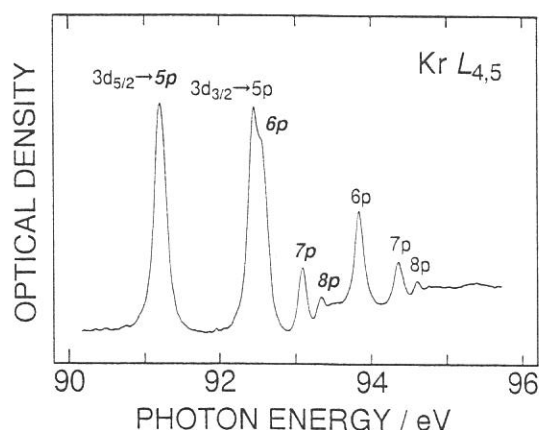


Fig. 5.  $M$ -absorption spectrum of gaseous Kr measured with using G3 grating and  $10\mu\text{m}$  slits.

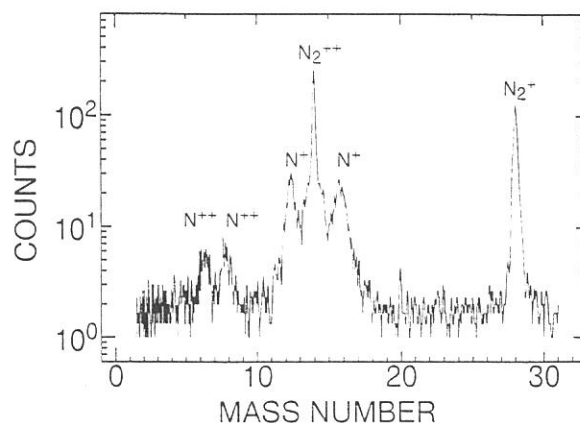


Fig. 6. TOF-mass spectrum of  $N_2$  excited at 401 eV ( $1s \rightarrow 2p\pi^*$  resonance).

## The Electronic Structure of Porphyrin/Metal Interfaces Studied by Ultraviolet Photoelectron Spectroscopy

D.Yoshimura<sup>a)</sup>, S.Narioka<sup>a)</sup>, M.Sej<sup>a)</sup>, H.Ishii<sup>a)</sup>, Y.Ouchi<sup>a)</sup>, T.Miyazaki<sup>a),b)</sup>, S.Hasegawa<sup>b)</sup>  
Y.Harima<sup>c)</sup>, K.Yamashita<sup>c)</sup> and K.Seki<sup>a)</sup>

a) Department of Chemistry, Faculty of Science, Nagoya University, Nagoya 464-01

b) Institute for Molecular Science, Myodaiji, Okazaki 444

c) Faculty of Integrated Arts and Sciences, Hiroshima University, 1-7-1 Kagamiyama, Higashi-Hiroshima 724

Recently the applications of various organic semiconductors to electric devices have been extensively studied. The elucidation of the electronic structure of organic semiconductor/metal interface is indispensable for understanding and refining the performance of such devices. However there have been few studies with direct observation of the interfacial electronic structure. In most studies on organic devices, the interfacial electronic structure has been estimated by lining-up separately observed energy levels of the two components, assuming one of the traditional models: a) vacuum level alignment occurs at the organic/metal interface ( $\Delta=0$ ) and energy levels in space charge layer bend to achieve Fermi level alignment ( $\varepsilon_v^F=\text{const}$ ) like inorganic semiconductor/metal interface (Fig.1a). b) The vacuum level of organic layer coincides with that of metal without band bending ( $\Delta=0, \varepsilon_v^F \neq \text{const}$ ) like insulator/metal interface (Fig.1b) But the validity of these models is not yet well examined for organic semiconductor.

In this work, we investigated the electronic structure of the interface between four metals (Mg, Al, Ag, Au) and 5,10,15,20-tetraphenylporphyrinatozinc (ZnTPP, Fig. 2) which are known to work as solar cells [1], using ultraviolet photoelectron spectroscopy (UPS). We discussed the energy level alignment at the interface on the basis of the observed electronic structure.

UPS spectra were measured by using the angle-resolved UPS system at BL8B2 of UVSOR at Institute for Molecular Science. Thin ZnTPP films (5 nm thick) were prepared on the metal substrates by vacuum evaporation in ultra high vacuum. The work functions of the samples were determined by the low energy cut-off of the UPS spectra.

Table 1 summarizes the observed work functions of the metals ( $\Phi_m$ ), onset energy of HOMO ( $\varepsilon_v^F$ ) and the energy of the vacuum level of ZnTPP films relative to the Fermi level of substrate metal. The labels of UHV and OX indicate results measured in ultrahigh vacuum (UHV) condition and after oxygen exposure (4 Torr, 5 minutes), respectively. Fig.1c shows the energy diagram of the interface obtained from our results. If Fermi-level alignment occurs across the interface,  $\varepsilon_v^F$  should be constant irrespective of substrates (Fig.1a). On the other hand, vacuum-level alignment requires  $\Delta \equiv \varepsilon_{\text{vac}}^F - \Phi_m = 0$  (Fig.1b). Presently observed results show that neither of these cases holds at ZnTPP/Metal interface and that the energy level of ZnTPP are fixed to the vacuum level of the substrate metal with non-zero constant interface dipole ( $\Delta \varepsilon_{\text{vac}}^F - \Phi_m = 0.7$  eV). This is also supported by the results for oxygen exposure.

After exposure to oxygen, energy shift of HOMO and vacuum level of ZnTPP were observed. The extent and direction of the shift were strongly dependent on the substrate (see  $\varepsilon_{\text{vac}}^F(\text{ox}) - \varepsilon_{\text{vac}}^F(\text{UHV})$  in Table 1). It is known that the work function of most metal surface is increased by

exposure to oxygen due to large electronegativity of oxygen atom. On the other hand, the work function of Au surface is insensitive to oxygen exposure and that of Al surface is slightly decreased by oxygen exposure. This tendency of work function change qualitatively corresponds with the observed shift  $\varepsilon_{\text{vac}}^{\text{F}}(\text{ox}) - \varepsilon_{\text{vac}}^{\text{F}}(\text{UHV})$ , when we assume "constant D" condition.

In conclusion, we found that the energy levels of ZnTPP are fixed to the vacuum level of the substrate metal with constant difference of vacuum level between ZnTPP and metal at interface. This requires the modification for traditional models of energy level alignment at interface.

Figure 1

Energy diagram of organic/metal interface. (a) Fermi level alignment case, (b) vacuum level alignment case, (c) presently observed results.

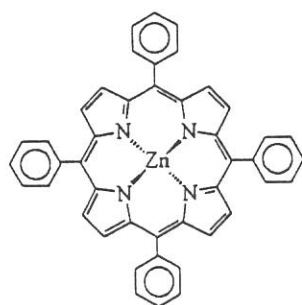
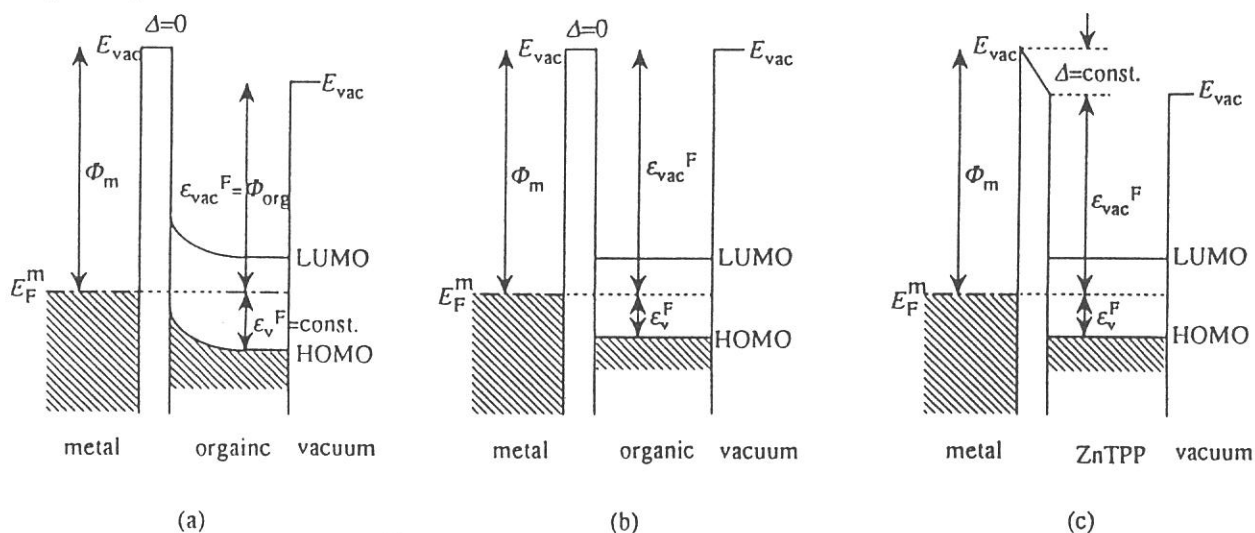


Figure 2 Chemical structure of ZnTPP

Table 1. Summary of the observed energy parameters (in eV)

Metal	In UHV condition					After oxygen exposure				
	$\Phi_m$	$\varepsilon_v^{\text{F}}(\text{UHV})$	$\varepsilon_{\text{vac}}^{\text{F}}$	$\Delta \equiv \varepsilon_{\text{vac}}^{\text{F}} - \Phi_m$	$I_s^{\text{th}}$	$\varepsilon_v^{\text{F}}(\text{ox})$	$\varepsilon_{\text{vac}}^{\text{F}}(\text{ox})$	$\varepsilon_v^{\text{F}}(\text{ox}) - \varepsilon_v^{\text{F}}(\text{UHV})$	$I_s^{\text{th}}$	
Mg	3.8 <sub>8</sub>	2.1 <sub>0</sub>	3.2 <sub>3</sub>	-0.6 <sub>5</sub>	5.3 <sub>3</sub>	1.8 <sub>5</sub>	3.5 <sub>2</sub>	-0.25	5.3 <sub>7</sub>	
Al	4.3 <sub>0</sub>	1.7 <sub>3</sub>	3.6 <sub>3</sub>	-0.6 <sub>7</sub>	5.3 <sub>6</sub>	1.9 <sub>8</sub>	3.3 <sub>0</sub>	+0.2 <sub>5</sub>	5.2 <sub>8</sub>	
Ag	4.3 <sub>0</sub>	1.7 <sub>3</sub>	3.6 <sub>1</sub>	-0.6 <sub>9</sub>	5.3 <sub>4</sub>	1.0 <sub>3</sub>	4.3 <sub>6</sub>	-0.7 <sub>0</sub>	5.3 <sub>9</sub>	
Au	4.7 <sub>8</sub>	1.1 <sub>6</sub>	4.0 <sub>8</sub>	-0.5 <sub>7</sub>	5.3 <sub>7</sub>	1.1 <sub>4</sub>	4.2 <sub>1</sub>	-0.0 <sub>2</sub>	5.3 <sub>5</sub>	

#### Reference

[1] K.Yamashita, Y.Harima, and T.Matsubayashi, J.Phys.Chem. **93**, 5311 (1989)

## Determination of azimuthal orientation of metal-free phthalocyanine on MoS<sub>2</sub> surface

K. KAMIYA, M. MOMOSE, Y. HARADA, and N. UENO,  
Faculty of Engineering, Chiba University, Inage-ku, Chiba 263, Japan  
T. MIYAZAKI, S. HASEGAWA, and H. INOKUCHI,  
Institute for Molecular Science, Okazaki 444, Japan  
S. NARIOKA, H. ISHII, and K. SEKI,  
Faculty of Science, Nagoya University, Chikusa-ku, Nagoya 464-01, Japan

The determination of the molecular orientation in thin films of functional organic molecules is of fundamental importance, since the surface structure of the substrate affects the molecular orientation to give a new intermolecular interaction. Therefore, the determination of the molecular orientation with respect to the surface crystal axes of the substrate is greatly required. The angular distribution of photoelectrons from thin films of organic crystals involves information on the molecular orientation in the film as well as on the electronic state. The quantitative analysis of the photoelectron angular distribution of thin films of large organic molecules is usually difficult, and no quantitative analysis has been performed after the challenging work by Permien et al.<sup>1</sup> Recently, we have found that the angular distributions calculated by the independent-atomic-center (IAC) approximation combined with molecular orbital calculation agree excellently with observed ones for thin films of BTQBT,<sup>2</sup> and succeeded in determining the tilt angles of these molecules.

In the present study, we determined the azimuthal orientation of metal-free phthalocyanine (H<sub>2</sub>Pc) molecules on MoS<sub>2</sub> surface orientation by the quantitative analysis of the observed angular distribution using the IAC method.

ARUPS measurements were performed at the beam line BL8B2 of the UVSOR at Institute for Molecular Science.<sup>3</sup> The photoelectron spectra were recorded under the total resolution of about 0.2eV. The electric vector of photons and the momentum vector of photoelectrons are on a plane perpendicular to the substrate surface. The azimuthal angle ( $\phi$ ) dependence of photoelectron spectra was measured at normal incidence [incident angle of photon( $\alpha$ )=0°] with the photon energy of 40eV. The direction of the surface crystal axes of the MoS<sub>2</sub> substrate was determined by low energy electron diffraction (LEED) measurements. The azimuthal angle  $\phi$  is measured from the  $[11\bar{2}0]$  direction of the MoS<sub>2</sub> crystal.

The  $\phi$  dependence of HOMO band intensity of the ARUPS spectrum of a thin film (3 Å) of the H<sub>2</sub>Pc on the MoS<sub>2</sub> substrate is plotted in Fig. 1. Two large maxima at  $\phi \approx 8^\circ$  and  $-25^\circ$  and two small maxima at  $\phi \approx 42^\circ$  and  $-50^\circ$  are clearly seen. This strong  $\phi$  dependence can be ascribed to an epitaxial growth of H<sub>2</sub>Pc on the MoS<sub>2</sub> substrate.

We carried out quantitative analysis of the  $\phi$  dependence of the photoelectron intensity of the HOMO band to determine the molecular orientation. The theoretical model in calculating the photoelectron angular distribution with the IAC approximation was described in the previous paper.<sup>2</sup> In the calculation, D<sub>4h</sub> symmetry was assumed for H<sub>2</sub>Pc structure except center H<sub>2</sub>. The molecular azimuthal angle  $\phi_s$  and the inclination angle  $\beta$  at which the molecular plane is inclined to the substrate surface are introduced for

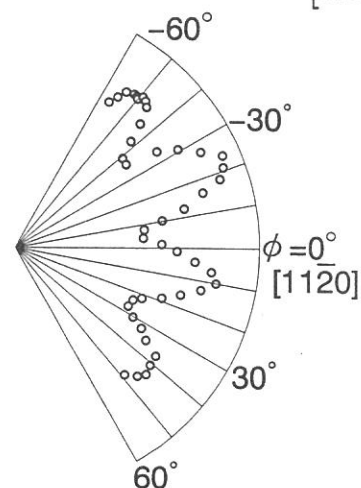


FIGURE 1 Azimuthal angle  $\phi$  dependence of the HOMO band intensity ( $h\nu=40\text{eV}$ ,  $\alpha=0^\circ$ ,  $\theta=34^\circ$ ) of the H<sub>2</sub>Pc thin film (3 Å) on the MoS<sub>2</sub> substrate.



the calculation of the  $\phi$  dependence of the photoelectron intensity. The calculated  $\phi_s$  dependence of the HOMO band intensity for  $\beta=0^\circ$  is displayed in Fig. 2, where the corresponding molecular orientation is also shown. In the calculation we summed up six  $\phi_s$ -dependencies corresponding to the six fold symmetry of the MoS<sub>2</sub> surface. It is seen that there are six large maxima and six small ones in the  $\phi_s$  dependence.

For the determination of the H<sub>2</sub>Pc molecular orientation in the ultrathin film on the MoS<sub>2</sub> surface, we compared the observed results with the calculated  $\phi$  dependencies for various  $\beta$ . The best agreement between the calculated and observed  $\phi$  dependencies was obtained for  $\beta=0^\circ$  as shown in Fig. 3, where the experimental results are shown by extending the observed  $\phi$  range ( $-60^\circ < \phi < 60^\circ$ ) to  $0^\circ < \phi < 360^\circ$  on the basis of the 6 fold crystal symmetry of the MoS<sub>2</sub> substrate. The calculated results for other values of  $\beta$  little agree with the observed ones. From these results it is concluded that the H<sub>2</sub>Pc molecules lie flat ( $\beta=0^\circ$ ) on the substrate and that the film grows epitaxially with respect to the three equivalent directions of the MoS<sub>2</sub> surface. Furthermore the analysis of the take-off angle  $\theta$  dependence of the photoelectron intensity of the HOMO band gave the flat orientation of H<sub>2</sub>Pc molecules. As a summary, three equivalent molecular orientations are displayed in Fig.4. It is notable that the symmetry axes of the H<sub>2</sub>Pc molecule are not parallel to the crystal axes of MoS<sub>2</sub>.

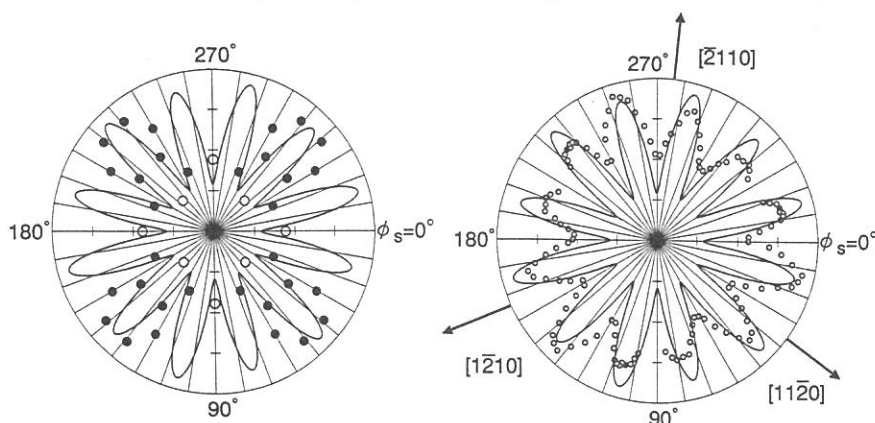


FIGURE 2 The calculated  $\phi_s$  dependence (—) of the photoelectron intensity of the HOMO band of oriented H<sub>2</sub>Pc. The molecular orientation (one of six orientations) which shows the origin of  $\phi_s$  is also shown. (see text) The symbols ● and ○ represent the position of the carbon and nitrogen atom, respectively.

FIGURE 3 Comparison of the calculated (—) and observed (○)  $\phi$  dependencies. Three arrows indicate the direction of the three equivalent crystal axes of the MoS<sub>2</sub> surface. The origin of the experimental  $\phi$  is on [1120] direction.

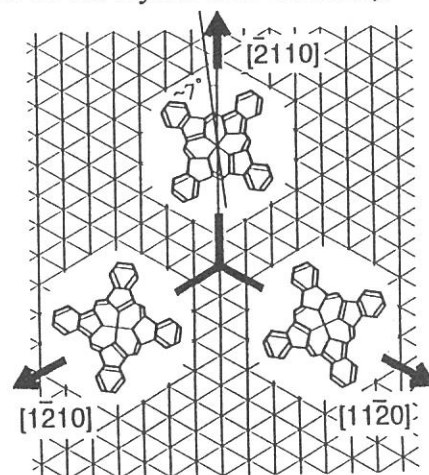


FIGURE 4 Orientation of H<sub>2</sub>Pc molecules on the MoS<sub>2</sub> substrate. Three arrows represent the three equivalent crystal axes of the MoS<sub>2</sub> surface. The molecular plane is parallel to the MoS<sub>2</sub> surface.

## REFERENCES

1. T.Permien, R.Engelhardt, C.A.Feldmann, and E.E.Koch, Chem.Phys.Lett., **98**, 527(1983).
2. S.Hasegawa, S.Tanaka, Y.Yamashita, H.Inokuchi, H. Fujimoto, K.Kamiya, K.Seki, and N.Ueno, Phys. Rev. **B48**, 2596(1993).
3. K.Seki, H.Nakagawa, K.Fukui, E.Ishiguro, R.Kato, T.Mori, K.Sakai, and M.Watanabe, Nucl.Instrum.Methods, **A 246**, 264(1986).

## UPS Study of NiPS<sub>3</sub> and FePS<sub>3</sub> Crystals by Using Synchrotron Radiation

T. Miyazaki, H. Inokuchi, S. Hasegawa, K. P. Lee<sup>1</sup>, K. Ichimura<sup>2</sup>,  
and H. Fujimoto<sup>3</sup>

*Institute for Molecular Science, Myodaiji, Okazaki 444, Japan*

<sup>1</sup>*Department of Chemistry Education, Kyungpook National University  
Taegu 702-701, Korea*

<sup>2</sup>*Department of Chemistry, Faculty of Science, Kumamoto University,  
Kumamoto 860, Japan*

<sup>3</sup>*Department of Environmental Science, The Graduate School of Science and  
Technology, Kumamoto University, Kumamoto 860, Japan*

Among the layered transition metal trichalcogeno-phosphates MPX<sub>3</sub>, FePS<sub>3</sub> and NiPS<sub>3</sub> have attracted much attention due to their capability of intercalation with application to Lithium based batteries. The transition metal atoms occupy lattice planes and are octahedrally coordinated by chalcogen atoms. The phosphorus is covalently bonded to form P<sub>2</sub> pairs which occupy sites in the plane of the transition metal ions and are also octahedrally coordinated by chalcogen atoms forming a P<sub>2</sub>S<sub>6</sub> trigonal bipyramidal structure. The intercalation capability of the MPX<sub>3</sub> compounds depends on the metal M, and it seems to be related strongly with its ionicity and with the number of empty *d* states. In order to understand the origin of these differences and the changes upon intercalation, a detailed study of the electronic states of the MPX<sub>3</sub> compounds is essential. The valence bands of NiPS<sub>3</sub>, FePS<sub>3</sub>, and ZnPS<sub>3</sub> have been investigated by means of X-ray photoemission spectroscopy (XPS). The common features of all three compounds were assigned to states of (P<sub>2</sub>S<sub>6</sub>)<sup>4-</sup> and the other structures to the transition metal 3*d* levels. The satellite structure were also suggested from the comparison with the metal core level spectra. In these study, the observed spectra were aligned by one of the valence band structures. Moreover, the photoemission from 3*d* level is predominant by comparison with those of 3*s* and 3*p* levels in XPS. Accordingly, this interpretation of the valence bands may not be univocal. The resonant-photoemission (RPS) and constant-initial-state (CIS) spectroscopies have applied to investigate the valence band of FePS<sub>3</sub> and NiPS<sub>3</sub>. These works confirm that the several features of the valence band are attributed to the metal 3*d* state splitted by the crystal field and the final state effect. In addition, the satellite structure are also observed in the higher-binding-energy side of the main valence band. However, the observed photon energy region is confined to the M<sub>2,3</sub> (3*p*) absorption edge. In this report, we carried out a study of NiPS<sub>3</sub> and FePS<sub>3</sub> crystals by ultraviolet photoemission spectroscopy (UPS) with using synchrotron radiation to get further insight by carefully investigating the valence band structures. We used RPS and CIS to identify the contributions of each element to the valence band of NiPS<sub>3</sub> and FePS<sub>3</sub>.

Figure 1 and 2 show the incident photon energy dependence of photoemission spectra for NiPS<sub>3</sub> and FePS<sub>3</sub> crystals scraped in vacuum, respectively. The obtained energy distribution curves (EDCs) are shown for exciting energies at 20 ~ 90 eV. All of EDCs are aligned with E<sub>F</sub> of gold, and the abscissa are the binding energy



from  $E_F$ . Seven features are seen in the EDCs of  $\text{NiPS}_3$  at 1.2, 2.2, 3.2, 4.4, 6.8, 8.0, and 10.0 eV below  $E_F$ , while those of  $\text{FePS}_3$  are seen at 1.6, 2.5, 3.3, 5.0, 7.0, 8.1, and 9.9 eV below  $E_F$ . The spectral onset of  $\text{NiPS}_3$  locates at 0.8 eV, while that of  $\text{FePS}_3$  is close toward  $E_F$  and situated at 0.5 eV. The size of band gap for  $\text{NiPS}_3$  is getting larger than that for  $\text{FePS}_3$ . Thus, these results are enough to compare the electronic conductivity of  $\text{NiPS}_3$  and  $\text{FePS}_3$ . Figure 3 and 4 show the CIS spectra of  $\text{NiPS}_3$  and  $\text{FePS}_3$  for the incident photon energy of 20 ~ 90 eV, respectively. In  $\text{NiPS}_3$ , the structures located at 2.2, 3.2, 6.8, 8.0, and 10.0 eV show strong resonance at the 3d threshold energy of Ni and no resonance occurs in the features at 1.2 and 4.2 eV. Therefore, the structures at 2.2, 3.2, 6.8, 8.0, and 10.0 eV are mainly from Ni 3d orbitals. Moreover there are no 3d character in the 1.2 and 4.2 eV bands. In  $\text{FePS}_3$ , the resonant enhancement occurs mostly in the features of 1.6, 2.5, 3.3, 5.0, 7.0, 8.1, and 9.9 eV at the 3d threshold energy of Fe. Therefore, these structures at 1.6, 2.5, 3.3, 5.0, 7.0, 8.1, and 9.9 eV are mainly from Fe 3d orbitals.

From these observations, we concluded that the highest occupied molecular orbital of  $\text{NiPS}_3$  is mainly from  $(\text{P}_2\text{S}_6)^{4-}$  cluster states, while that of  $\text{FePS}_3$  contains contribution from Fe atoms.

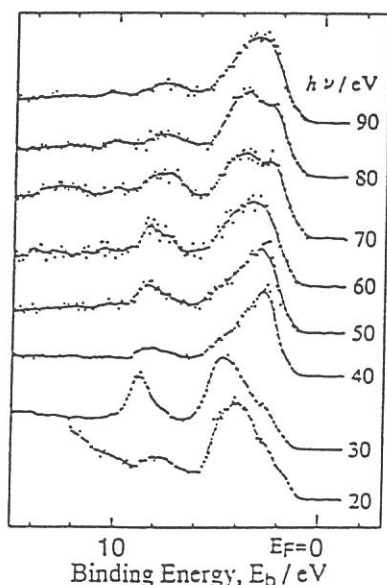


Fig.1 UPS spectra of the scraped  $\text{NiPS}_3$  crystal.

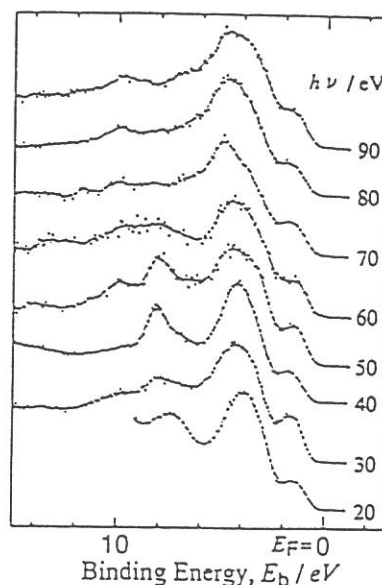


Fig.2 UPS spectra of the scraped  $\text{FePS}_3$  crystal.

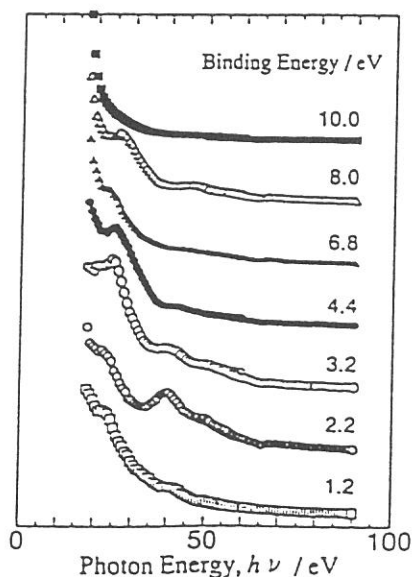


Fig.3 CIS spectra of valence band structures.

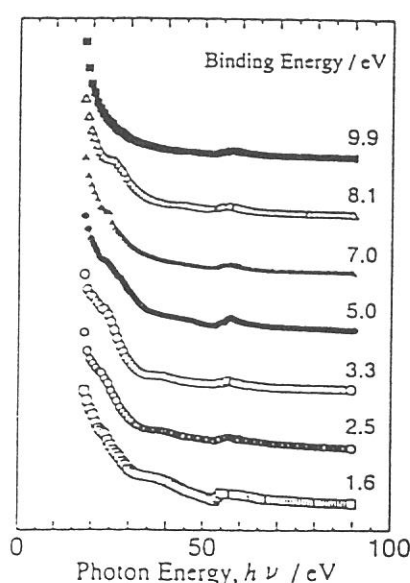


Fig.4 CIS spectra of the valence band structures.

## Photoemission Study on Poly(pyridine-2,5-diyl), Poly(2,2'-bipyridine-5,5'-diyl), and their K-doped States [1].

T. Miyamae<sup>a)</sup>, D. Yoshimura<sup>a)</sup>, H. Ishii<sup>a)</sup>, Y. Ouchi<sup>a)</sup>, T. Miyazaki<sup>a,b)</sup>, T. Koike<sup>c)</sup>, T. Yamamoto<sup>d)</sup>, and K. Seki<sup>a)</sup>

<sup>a)</sup> Department of Chemistry, Faculty of Science, Nagoya University, Nagoya 464-01

<sup>b)</sup> Institute for Molecular Science, Myodaiji, Okazaki 444

<sup>c)</sup> Chemical Synthesis Laboratories, Mitsui Petrochemical Industries, LTD., Chiba 299-02

<sup>d)</sup> Research Laboratory of Resources Utilization, Tokyo Institute of Technology, Yokohama 227

$\pi$ -Conjugated conducting polymers are the subject of recent interest, which initiated from the discovery that many polymers can be doped with either electron acceptors or donors to increase their conductivity. Recently we have found that poly(pyridine-2,5-diyl) (PPy, Fig. 1a) and poly(2,2'-bipyridine-5,5'-diyl) (PBPY, Fig. 1b) exhibit n-type electrically conducting properties [2]. In this work, we report UPS studies of PPy and PBPY, and discuss their electronic structures using the observed results. Analysis of the observed spectra was carried out with the aid of semiempirical PM3 molecular orbital (MO) calculations for oligomers. We also studied the changes in electronic structures of PPy and PBPY upon *in situ* doping with potassium by UPS.

Photoelectron spectroscopic measurements were carried out at BL8B2 of UVSOR Facility, Institute for Molecular Science. Thin films of PPy and PBPY were prepared on this gold-coated substrate by vacuum evaporation. Potassium doping was carried out *in situ* at  $125 \text{ }^\circ\text{C} \pm 5 \text{ }^\circ\text{C}$  using a SAES K-getter source in the preparation chamber.

Figure 2 shows the UPS spectra of polymers, the calculated orbital energies of four-ring pyridine oligomers by vertical lines, and the simulated spectra by convoluting the delta functions at each orbital energy with a Gaussian function of 0.5 eV FWHM. From the UPS spectra of PPy and PBPY, the threshold energies  $I_{\text{th}}$  for photoemission were found to be 6.3 and 6.35 eV, respectively. Principally these two spectra resemble each other, indicating analogous electronic structures. The simulated spectra are also similar, indicating that the difference in *head-to-head* and *head-to-tail* connections of bipyridine units do not significantly affect the electronic structures of neutral polymers.

In Fig. 3, we show the UPS spectra of K-doped PBPY for increasing doping levels. At the initial stage of doping, two new states X and Y appear in the energy gap region. With increasing K content, the peak X gradually grows up. Also the peak B shows decrease of intensity and a shift to higher binding energy side with increasing K content. This shift relative to  $E_{\text{F}}$  appears also for all the UPS structures as a shift of the peak position. We also observed a large change of work function,  $\phi$ , determined from the low-energy cutoff of the UPS spectra as shown in Fig. 4. At the initial stage of doping,  $\phi_{\text{PBPY}}$  shows a fairly large decrease of 0.83 eV.

Following the calculation of Brédas *et al.* for alkali-metal doped quarterphenyl [3], the gap state at 0.65 eV (peak X) below  $E_{\text{F}}$  can be assigned to the LUMO filled by electron donated from K atoms and stabilized by geometric relaxation, and the state at 2.54 eV (peak Y) to the destabilized HOMO. The UPS spectra of K-doped PBPY are in good correspondence with predicted bipolaron states of Brédas *et al.* [3]. The formation of bipolaron states should lead to a substantial shift of  $E_{\text{F}}$  relative to the vacuum level.

Figure 3 also shows the change of  $\phi_{\text{PPY}}$  for K-doped PPy. The doping steps and conditions were carefully controlled to be similar to the corresponding stages of doping of PBPY film in Fig. 2. At the initial stage of doping, the  $\phi_{\text{PPY}}$  decreased only by 0.36 eV, which is much smaller than the case of

PBPpy. At the highly doping stage (Fig.4f), two gap states X and Y appear at the same positions with those of PBPpy, and they can be assigned to bipolaron bands. The peak B still appears with significant intensity, while peak B in PBPpy almost disappears at this doping stage. Thus we can summarize that PPy is slow in changing by K-doping, although the heavily doped state is similar to that of PBPpy.

As for the reason why PPy needs higher dopant concentration to create bipolarons than PBPpy, it is suggestive that Yamamoto *et al.* found that PBPpy forms electrochemically active transition metal complex due to the chelating ability accompanied by the *head-to-head* structure of PBPpy [2]. In contrast to PBPpy, PPy has only a weak coordinating ability toward the metals, presumably because of the mainly *head-to-tail* structure of PPy. Thus we can conclude that more effective doping to PBPpy comes from its strong ability to coordinate with potassium ion, while it is almost absent in PPy.

## References

- [1] T.Miyamae, D.Yoshimura, H.Ishii, Y.Ouchi, K.Seki, T.Miyazaki, T.Koike, and T.Yamamoto, *Submitted to J. Chem. Phys.*
- [2] T.Yamamoto, T.Maruyama, Z.-H.Zhou, T.Ito, T.Fukuda, Y.Ypneda, F.Begum, T.Ikeda, S.Sasaki, H.Takezoe, A.Fukuda, and K.Kubota, *J. Am. Chem. Soc.*, **116**, 4382 (1994).
- [3] J.L.Brédas, B.Thémans, J.G.Fripiat, J.M.André, and R.R.Chance, *Phys. Rev. B* **29**, 6761 (1984).

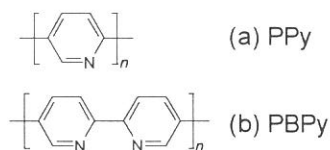


Fig. 1 The molecular structure of PPy (a) and (b) PBPpy.

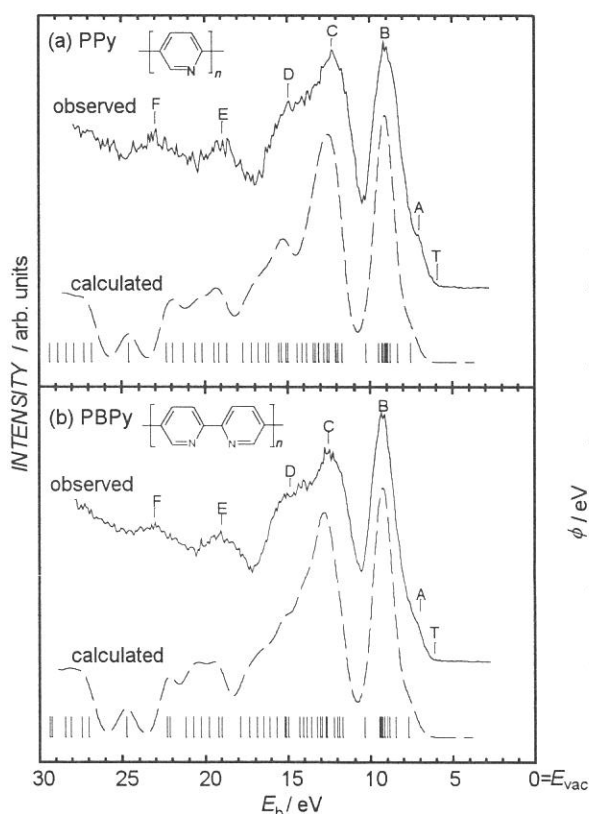


Fig. 2 UPS spectra of PPy (a) and PBPpy (b) at the incident photon energy of 40 eV. The vacuum level ( $E_{vac}$ ) is taken as the origin of the energy scale.

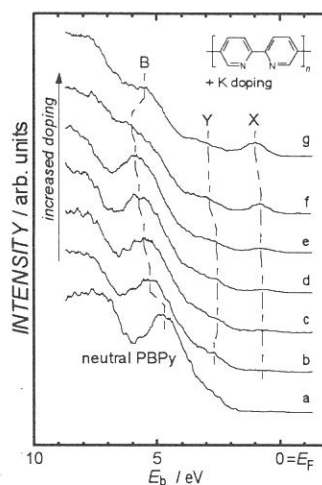


Fig. 3 UPS spectra of neutral and increasingly K-doped PBPpy. The abscissa is the binding energy from the Fermi level.

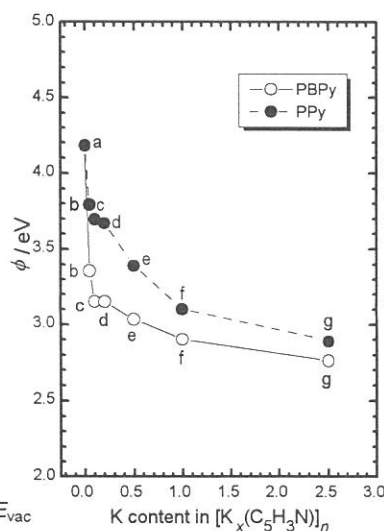


Fig. 4 Change of the work function  $\phi$  of PBPpy (open circles) and PPy (filled circles) upon K doping. The K content ( $x$ ) was estimated from the exposure time to K vapor.

## Synchrotron-Radiation Photoemission Study of *in-situ* Synthesized DCNQI(*N,N'*-Dicyanoquinonediimine)-Cu Salts

Akinori TANAKA, Ashish CHAINANI, Tatsushi MIURA, Takashi TAKAHASHI,  
Takahumi MIYAZAKI\*, Shinji HASEGAWA\*, and Takehiko MORI\*\*

*Department of Physics, Tohoku University, Aoba-ku, Sendai 980-77*

*\*Institute for Molecular Science, Myodaiji, Okazaki 444*

*\*\*Department of Organic and Polymeric Materials, Tokyo Institute of Technology,  
Meguro-ku, Tokyo 152*

The series of organic conductors  $(2,5-R_1, R_2\text{-DCNQI})_2\text{Cu}$ , where DCNQI is *N,N'*-dicyanoquinonediimine and  $R_1, R_2 = \text{CH}_3, \text{CH}_3\text{O}, \text{Br}, \text{Cl}, \text{etc.}$ , have attracted much attention because of their interesting structural, electrical, and magnetic properties. In these salts, the interaction between the  $p\pi$  orbitals of the DCNQI molecules and the Cu  $3d$  orbitals is expected to bring about a substantial deviation from a simple one-dimensional material. In this report, we present a photoemission study using synchrotron radiation on two different DCNQI-Cu salts;  $(\text{DMe-DCNQI})_2\text{Cu}$  and  $(\text{MeBr-DCNQI})_2\text{Cu}$ .

Since photoemission spectroscopy is very sensitive, we synthesized the DCNQI-Cu salts *in-situ* in a vacuum glove box directly connected to the photoemission spectrometer and measured the valence band spectra without exposing the samples to air. Photoemission measurements were carried out at BL8B2 of UVSOR, Institute for Molecular Science. The incident photon energy used in this experiment was varied from 15 to 75 eV. The total energy resolution was about 150 meV. The photoemission spectra were recorded at room temperature and no degradation of the samples was observed during the measurements.

Figures 1 and 2 show the photoemission spectra measured with various photon energies of  $(\text{DMe-DCNQI})_2\text{Cu}$  and  $(\text{MeBr-DCNQI})_2\text{Cu}$ , respectively. The overall features such as the peak position and the photon energy dependence are very similar each other. As shown in Figs. 1 and 2, the valence band spectra exhibit two major features around 3.5 and 7.5 eV binding energy, and their relative intensity changes as a function of the photon energy. This systematic change of the relative intensity of the two bands is due to the photon energy dependence of photoionization cross-section of the constituent atomic orbitals. From the photon energy dependence of the spectra profile, we successfully assigned the bands in the valence band spectra; the Cu  $3d$  states mixed with the C and N  $2p$  state in the cyano group appear around 3.5 eV binding energy while the C and N  $2p$  state originating in the quinone ring is seen at 7.5 eV. The Br  $4p$  state in  $(\text{MeBr-DCNQI})_2\text{Cu}$  is observed at about 5 eV. We found no resonant behavior at the photon energy of Cu  $3p$  threshold. Our measurements show that

the states near the Fermi level do not exhibit an enhancement in intensity, while the intensity of the feature around 3.5 eV binding energy follows the photon energy dependence of the photoionization cross-section of Cu 3*d* electrons. This difference in intensity-dependence shows that the states near the Fermi level have a substantial C and N 2*pπ* character, justifying the classification of the DCNQI-Cu salts as  $\pi$ -acceptor systems.

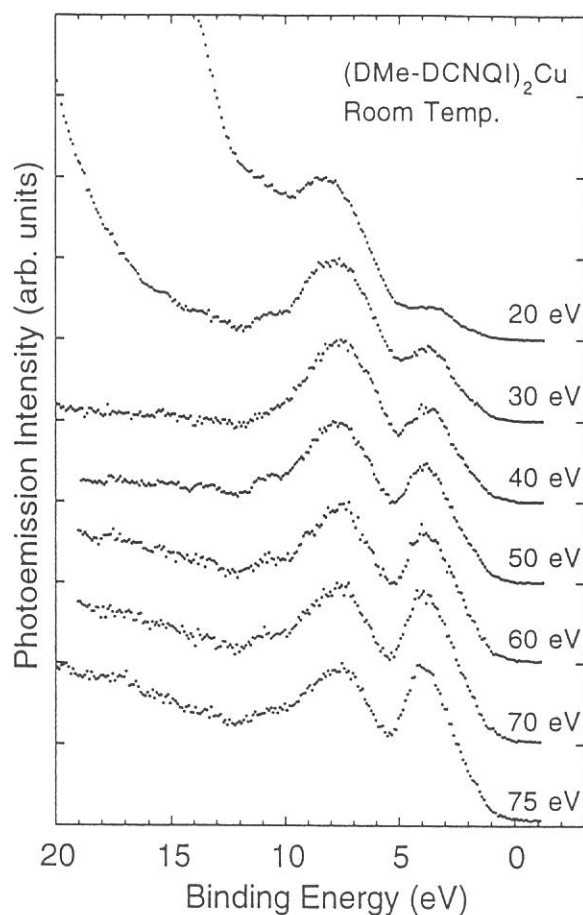


Fig. 1 Valence band photoemission spectra of (DMe-DCNQI)<sub>2</sub>Cu measured at room temperature as a function of incident photon energy. Photon energies used are indicated on each spectrum.

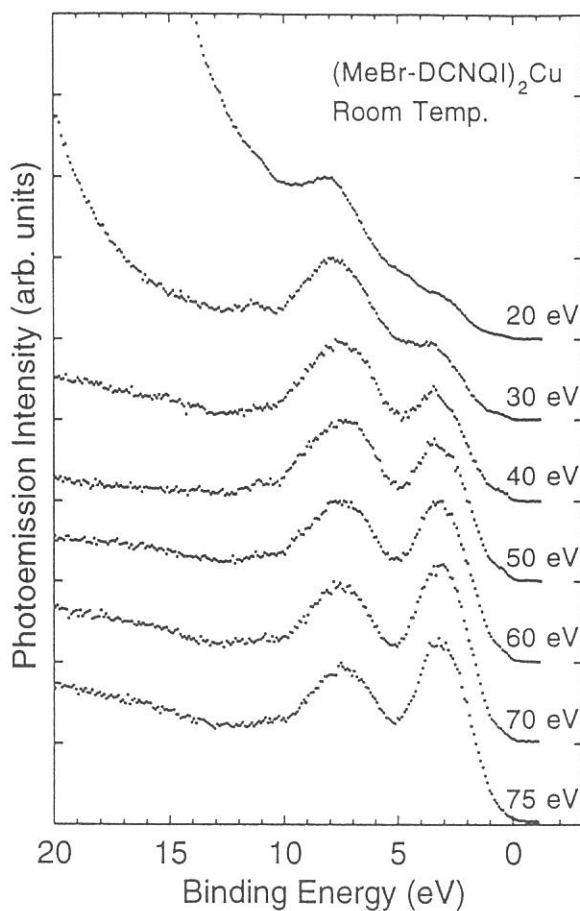


Fig. 2 Valence band photoemission spectra of (MeBr-DCNQI)<sub>2</sub>Cu measured at room temperature as a function of incident photon energy. Photon energies used are indicated on each spectrum.

## Ultraviolet Photoelectron Spectra of C<sub>78</sub> and C<sub>96</sub>

Shojun Hino\*, Hiroaki Takahashi, and Kentaro Iwasaki,

*Department of Image Science, Faculty of Engineering,  
Chiba University, Yayoi-cho, Inage-ku, Chiba 263 Japan*

Takafumi Miyazaki

*Institute for Molecular Science, Okazaki 444 Japan*

Koichi Kikuchi and Yohji Achiba,

*Department of Chemistry, Faculty of Science,  
Tokyo Metropolitan University, Hachioji, Tokyo 192-03 Japan*

The higher fullerenes have geometrical isomers [1], and NMR is often used to determine the symmetry group of fullerene. However, the precise structure cannot be determined by the NMR measurement alone, when there are plural possible structures belonging to the same symmetry. Combined studies of the ultraviolet photoelectron spectra and the theoretical calculation on the density of states of fullerenes are helpful to estimate their exact structures.

The NMR spectrum of C<sub>78</sub> indicates two or three isomers of different symmetry,  $C_{2v}$ - and  $D_3$ - C<sub>78</sub> [1,2]. When the carbon soot is prepared at high temperature, two  $C_{2v}$  and one  $D_3$  isomers are produced with an intensity ratio of 5 : 2 : 2 [3]. The structure or the symmetry group of C<sub>96</sub> has not been determined yet.

Figure 1 shows an excitation photon energy dependence of the photoelectron spectra of C<sub>78</sub>. Structures A - F are clearly observed in all spectra. An existence of structure G that was observed in the spectra of C<sub>76</sub> [4] is uncertain due to a poor signal to noise ratio. When the photon energy is changed, some structures shift their positions and the intensity of the peaks oscillates. The origin of the intensity oscillation of the first few bands might be attributed to the difference of the cross sections of the electronic states belonging to different azimuthal angular quantum numbers,  $l$  [5], which is conducted by an approximation of fullerenes as a pseudo atom [6]. Comparison of our spectra with the DOS obtained theoretically with different geometries [7] reveals that  $C_{2v}$  structure (one of the two structures belonging to  $C_{2v}$  symmetry that satisfy the isolated pentagon rule) gives the best fit with the spectra.

Figure 2 shows an excitation photon energy dependence of the photoelectron spectra of C<sub>96</sub>. The spectral onset is 1.0 eV below the E<sub>F</sub>, which is



the lowest one among the fullerenes reported up to now. There are 7 distinct structures and a vague one (denoted A - H) in the spectra. The intensity oscillates and the peak positions of the first few bands shift when the incident photon energy is changed, as in the case of  $C_{78}$ . As the calculated DOS [8] of  $C_{1-}C_{96}$  is able to reproduce the present result very well, the geometry of  $C_{96}$  might be  $C_1$ .

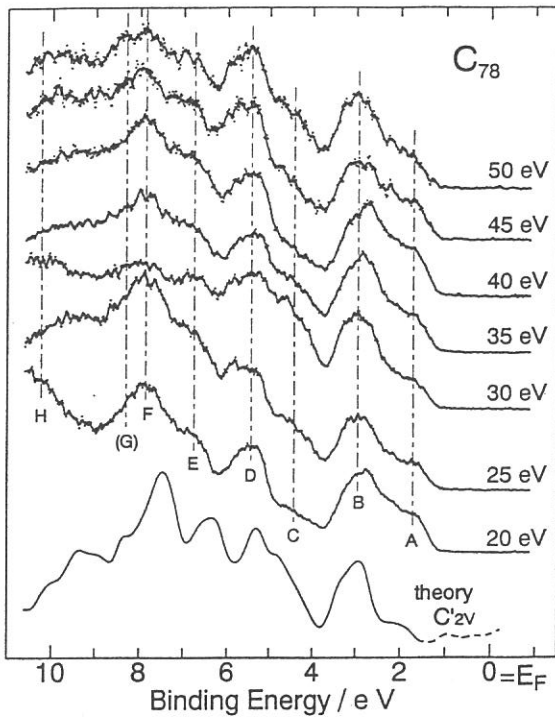


Fig. 1  
UPS of  $C_{78}$  with the calculated DOS [7].  $C_{2v}$  shows the best fit.

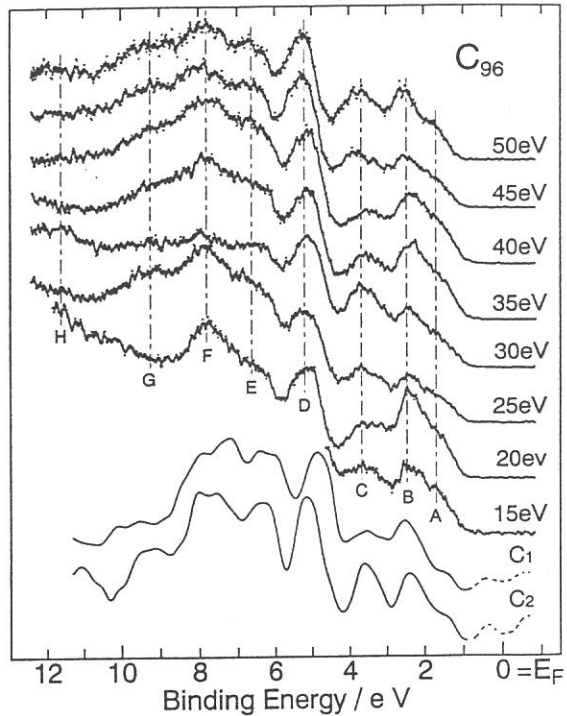
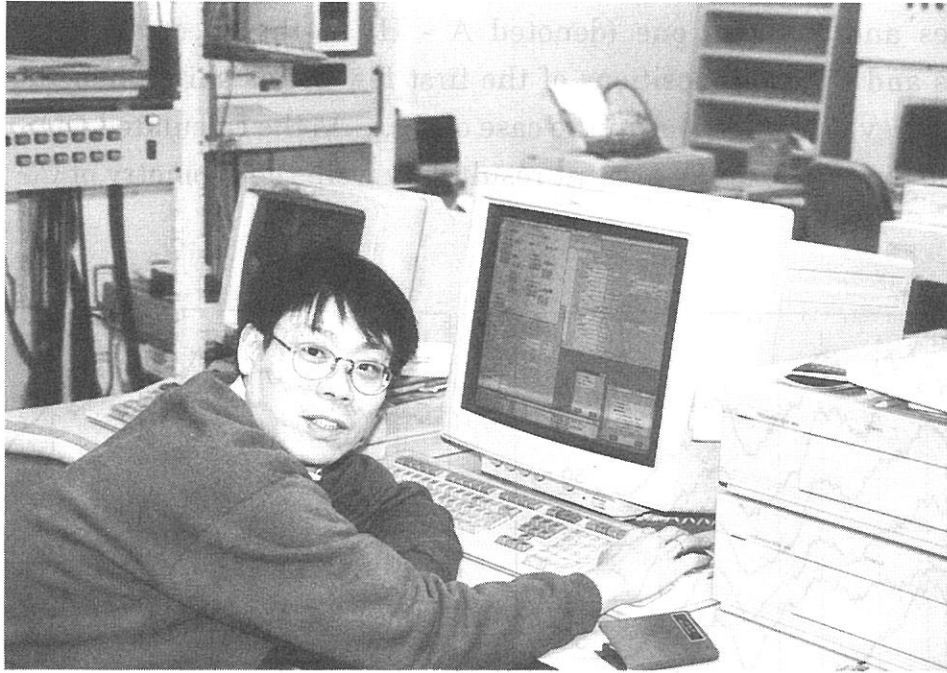


Fig. 2  
UPS of  $C_{96}$  with the calculated DOS [8].  $C_1$  gives the best fit and  $C_2$  the second.

#### REFERENCES

1. K. Kikuchi *et al.*, Nature 357 (1992) 142.
2. F. Dierich *et al.*, Science 254 (1991) 1768.
3. T. Wakabayashi *et al.*, J. Phys. Chem. 98 (1994) 3090.
4. S. Hino *et al.*, Chem. Phys. Letters 197 (1992) 38.
5. S. Saito *et al.*, Phys. Rev. B 45 (1992) 13845.
6. N. Troullier *et al.*, Phys. Rev. B 46 (1992) 1754.
7. X. Q. Wang *et al.*, Chem. Phys. Letters 200 (1992) 35.
8. X. Q. Wang *et al.*, Chem. Phys. Letters 214 (1993) 193.



Prof. H. Hama is operating the VAX system to inject electron beams.



Mr. K. Kimura is adjusting optical system for free electron laser.